Multiobjective Optimization of Parallel Robots and Optimal Path Placement

Raza Ur-Rehman

Ecole Centrale de Nantes

ÉCOLE DOCTORALE

SPIGA

Année 2009…….. N° B.U. : (laisser l'espace prévu ici)

Thèse de DOCTORAT

Spécialité : MENTION DE LA SPÉCIALITÉ

Présentée et soutenue publiquement par :

UR-REHMAN Raza

le 17 décembre 2009
à Nantes

TITRE

MULTIOBJECTIVE OPTIMIZATION OF PARALLEL ROBOTS AND OPTIMAL PATH PLACEMENT

JURY

Président : …… . M Vigen Arakélyan, Professeur, INSA, Rennes

Rapporteurs : …….. M Romdhane Lotfi, Professeur, Laboratoire de Génie Mécanique, Sousse
M Zeghloul Saïd, Professeur, Laboratoire de Mécanique des Solides, Poitiers

Examinateurs : …… M Olivier Company, MCF LIRMM, LIRMM, Montpelier
M Philippe Wenger, Directeur de recherche, IRCCyN, Nantes
M Chablat Damien, Chargé de recherche HDR, IRCCyN, Nantes
M Caro Stéphane, Chargé de recherche, IRCCyN, Nantes

Directeur de thèse : Philippe Wenger
Laboratoire : IRCCyN
Co-directeur : D. Chablat
Co-encadrant : S. Caro

N° ED …à demander après soutenance

Acknowledgment

On conclusion of three years of research work at IRCCyN, I am indebted in gratitude to The Almighty and my colleagues, whose contribution in this research in assorted ways has realised this dream. During this time, I have worked with many people and it is a pleasure to convey my gratitude to them in my humble acknowledgment.

In the first place I would like to express my gratitude to my thesis director Philippe Wenger for his guidance and valuable advices throughout this research work as well as his support in all other affairs.

I gratefully acknowledge my supervisor Damien Chablat for his supervision and important contributions. His sincere involvement with his originality has fostered my intellectual maturity that I regard as a lifetime asset. I am obliged for this generosity and wish to have collaboration in future as well.

Many thanks go to my co-supervisor Stéphane Caro whose close supervision, guidance and support enabled me to develop an understanding of the subject. His wise comments helped me to excel in generation and presentation of results and also progress as a student, a researcher and a scientist. He also put me on the road to LaTeX for my publications and thesis report, thanks to which I succeeded to have encouraging remarks from the jury members. Thanks Stéphane!

The work presented in this dissertation was supported in part by the Higher Education Commission (HEC), Government of Pakistan. Thanks should also be extended to the HEC and particularly to the Ex-Chairman HEC, Dr. Atta-ur-Rehman founder of this research program.

On a personal note, I would like to thank my friends and colleagues in Pakistan and in France for their prayers, encouragements and concerns, particularly my best friend Shafqat Waqar Ahmad for his tireless help for all of my matters in Pakistan. Here in Nantes, I have been blessed with a friendly and cheerful group of fellows. Their company made my stay memorable and lessened the work stress and gave me a support in my good and bad times. Thanks buddies!

Most importantly, I owe a huge debt of gratitude to my family: my mother whose love is

boundless, my sisters, my brothers and especially my father, who is no longer with us, as he used to be the happiest person on earth on my any accomplishment. Special thanks go to my parents-in-law and my wife who suffered a three years forced-separation (probably forced by French Embassy in Pakistan) right after our marriage because of French visa problem. Her love, understanding, patience and support are the most important things to me. Love to my two-year old daughter, Simaal Bint-e-Raza, whose birth brought me much joy and comfort.

Finally, I would like to thank everybody who was important to the successful realization of thesis, as well as expressing my apology that I could not mention personally one by one.

This work is dedicated to all of them.

Table of Contents

Introduction 1

1 Introduction to the Parallel Robots and Design Optimization 5
- 1.1 Introduction . . . 5
- 1.2 Parallel Robots . . . 6
- 1.3 Design Aspects of Parallel Robots . . . 13
- 1.4 Design Optimization . . . 17
- 1.5 Conclusion . . . 23

2 Multiobjective Design Optimization of Parallel Kinematics Machines 25
- 2.1 Introduction . . . 26
- 2.2 Performance Measures and Indices . . . 28
- 2.3 Case Study: 3–PRR Manipulator . . . 36
- 2.4 Multiobjective Design Optimization of PKMs Problem Formulation . . . 45
- 2.5 Multiobjective Optimization Problem Formulation for 3–PRR . . . 47
- 2.6 Conclusion . . . 55

3 Kinematics, Dynamics and Motors Selection of Orthoglide 5-axis 59
- 3.1 Orthoglide 5-axis . . . 59
- 3.2 Trajectory Planning . . . 63
- 3.3 Kinematics and Dynamics of the 2-dof Spherical Wrist . . . 66
- 3.4 Kinematics and Dynamics of the Orthoglide 3-axis . . . 93
- 3.5 Conclusion . . . 104

4 Single and Multiobjective Path Placement Optimization 107
- 4.1 Introduction . . . 108
- 4.2 Path Placement Optimization . . . 110
- 4.3 Case Study: Application to the Orthoglide 3-axis . . . 120
- 4.4 Results and Discussions . . . 128
- 4.5 Conclusions . . . 139

Conclusions 143

Publications 147

References 149

A Orthoglide Wrist Kinematics and Dynamics Relations 163

B Position and Acceleration of the Orthoglide Leg Elements 167

List of Figures

1.1 Schematic of a serial robot 6
1.2 Schematic of a Parallel robot 7
1.3 A 2-dof planar parallel manipulator 8
1.4 A 3-dof planar parallel manipulator 9
1.5 Star Architecture 10
1.6 3-UPU Tsai Architecture 10
1.7 Hybrid robot 11
1.8 Basic Delta architecture 12
1.9 FlexPicker (ABB)–Delta Robot 13
1.10 General Stewart Platform Structure 14
1.11 Stewart Platform 15
1.12 Biglide-parallel singular configuration 17
1.13 Biglide-serial singular configuration 17
1.14 General design optimization process 21
1.15 Graphical representation of the Pareto frontier 22

2.1 Design network of parallel kinematics mechanisms 26
2.2 3–PRR architecture 36
2.3 3–PRR planar parallel manipulator 39
2.4 Schematic diagram of a 3-PRR 42
2.5 Flexible model of a single kinematic chain of 3-PRR 42
2.6 3-PRR workspace 49
2.7 modeFRONTIER model for 3-PRR Optimization 53
2.8 Pareto frontier for 3-PRR design 54
2.9 Design variables evolution with R_w 55
2.10 CAD Designs of three Pareto-optimal solutions 56
2.11 Scatter matrix for 3-PRR 57

3.1 Prototype of the Orthoglide-5axis (IRCCyN) 60
3.2 Orthoglide 3-axis 61

3.3 Spherical wrist of Orthoglide 5-axis . . . 61
3.4 Orthoglide 5-axis workspace . . . 62
3.5 Orthoglide 5-axis cubic workspace . . . 63
3.6 Orientation of vector **v** (Traj I) . . . 64
3.7 Orientation of vector **v** (Traj II) . . . 65
3.8 Definition of reference frames for Orthoglide Wrist . . . 69
3.9 Definition of **v** in frames R_1 and R_5 . . . 72
3.10 Flow chart of wrist dynamic model . . . 73
3.11 CAD model and FBD of terminal . . . 74
3.12 CAD model and FBD of Distal . . . 75
3.13 CAD model and FBD of Proximal-1 . . . 77
3.14 CAD model and FBD of Proximal-2 . . . 77
3.15 Compatibility Free body diagrams . . . 78
3.16 Orthoglide Wrist Parameters . . . 81
3.17 Wrist kinematics-Traj-I, R=0.200 m, $\phi = 90°$ . . . 83
3.18 Wrist kinematics-Traj-I, R=0.200 m, $\phi = 45°$ . . . 84
3.19 Wrist kinematics-Traj-II, R=0.200 m, $\gamma = 45°$ . . . 85
3.20 Actuators torques vs time (Traj-I & II) . . . 85
3.21 Actuators maximum torques and powers vs R & γ . . . 86
3.22 Actuators torques for different values of γ . . . 87
3.23 Energy balance for wrist dynamics . . . 88
3.24 Terminal FBD with machining forces . . . 89
3.25 Actuators torques vs Time with machining forces . . . 90
3.26 Actuators maximum torques with machining forces . . . 91
3.27 Schematic of the Orthoglide 3-axis . . . 94
3.28 Simplified model of the Orthoglide 3-axis . . . 95
3.29 Prismatic joints position and rates for Traj-I ($\phi = 90°$) . . . 95
3.30 Prismatic joints position and rates for Traj-I ($\phi = 45°$) . . . 96
3.31 Prismatic joints position and rates for Traj-II ($\gamma = 45°$) . . . 96
3.32 Orthoglide leg parameterization for the dynamic analysis . . . 97
3.33 Orthoglide 3-axis actuators forces for Traj-I and II (R=0.2 m) . . . 98
3.34 Max power requirement with four motors (Traj-II, $\eta = 2$) . . . 102
3.35 Max Power Requirement with four motors (Traj-II, $\eta = 4/3$) . . . 103

4.1 Path placement characterization . . . 111
4.2 Flowchart of mono-objective path placement optimization process . . . 118
4.3 Flowchart of multiobjective path placement optimization process . . . 121
4.4 Orthoglide 3-axis cubic workspace . . . 122
4.5 Definition of the reference frames . . . 123

4.6 Orthoglide 3-axis i^{th} leg . . . 124
4.7 Test path characterization . . . 126
4.8 Test trajectory for a rectangular path of size $0.05 \times 0.10\,\mathrm{m}^2$ . . . 127
4.9 Cutting forces . . . 128
4.10 Locations of rectangular path with minimum energy consumption . . . 130
4.11 Locations of rectangular path with maximum energy consumption . . . 131
4.12 E_{min} and E_{max} and percentage saving for the rectangular test paths . . . 131
4.13 Energy as a function of x_{Op} and z_{Op} for a $30\,\mathrm{m} \times 60\,\mathrm{m}$ rectangular path . . . 132
4.14 Energy vs x_{Op} and y_{Op} for $30\,\mathrm{m} \times 60\,\mathrm{m}$ rectangular path . . . 132
4.15 Energy as a function of x_{Op} and y_{Op} for different orientations ($z_{Op} = 0$) . . . 133
4.16 Energy as a function of x_{Op} and ϕ for $y_{Op} = z_{Op} = 0$ . . . 133
4.17 Comparison of trajectory parameters for E_{min} and E_{max} locations . . . 134
4.18 modeFRONTIER model . . . 135
4.19 Pareto frontier for the Orthoglide 3-axis path placement . . . 137
4.20 Path locations for minimum and maximum objective functions . . . 138
4.21 Shaking forces experienced by three actuators for E_{min} and $I_{\delta f min}$ . . . 139
4.22 Scatter matrix for objective functions and design variables . . . 140

List of Tables

1.1 General comparison of serial and parallel robots . . . 8
1.2 Classification of optimization problems . . . 22

2.1 Summary of performance measures . . . 35
2.2 Lower and upper bounds of the design variables . . . 52
2.3 *modeFRONTIER* algorithm parameters . . . 52
2.4 Three Pareto optimal solutions . . . 54

3.1 Orthoglide 5-axis workspace parameters . . . 63
3.3 DH-parameters for Orthoglide wrist . . . 70
3.4 Relations of θ_1, θ_2, θ_3, θ_4 . . . 71
3.5 Summary of θ_1, θ_2, θ_3, θ_4 relations . . . 71
3.6 Orthoglide wrist parameters . . . 82
3.7 Motors parameters of the Orthoglide Wrist . . . 83
3.8 Wrist kinematics and dynamics peak values for Traj.-II . . . 84
3.9 Maximum actuators torques and powers with machining forces . . . 92
3.10 Maximum prismatic joints rates and accelerations for test trajectories . . . 94
3.11 Parameters of the Orthoglide 5-axis arm . . . 98
3.12 Ball screw calculation for Orthoglide 5-axis . . . 99
3.13 Motors Parameters from Catalogue . . . 99
3.14 Preliminary Motors Tests . . . 100
3.15 Power requirements with different motors ($\eta = 2$) . . . 101
3.16 Power requirements for M3 and M4 motors ($\eta = 4/3$) . . . 102
3.17 Effect of the variation of wrist mass for M3 ($\eta = 2$) . . . 103
3.18 Effect of the variation of wrist mass for M4 ($\eta = 2$) . . . 104

4.1 Orthoglide 3-axis workspace parameters . . . 122
4.2 Orthoglide 3-axis actuators parameters . . . 122
4.3 Parameters of the Orthoglide 3-axis Leg . . . 124
4.4 Minimum and maximum energy used for a given rectangular path . . . 130
4.5 *modeFRONTIER* algorithm parameters . . . 135
4.6 Design parameters for the Pareto solutions . . . 136

Introduction

In the competitive world of today, the industries are overwhelmed with the high demand that the human being himself cannot achieve. It is is apparent that faster, more efficient, more productive and reliable systems are required. That is one of the reasons why more efficient robotic systems have to be developed.

Traditional robotic manipulators can be classified into two families: the serial and the parallel manipulators. Serial manipulators are distinguished by the fact that they have only one independent kinematic chain between the base and the end-effector of the manipulator whereas the parallel manipulators have more than one kinematic chains connecting the base and the end-effector.

Parallel manipulators, also known as Parallel Kinematics Machines (PKMs), have attracted attention for their high speed, better accuracy, low mass/inertia properties and high structural stiffness. These are attractive features for the innovative machine-tool architectures; however practical utilization for the potential benefits requires an extensive and efficient analysis of their structure, kinematics and dynamics.

PKMs design, like any other product design, goes through many phases and requires, as a prerequisite, a designer's knowledge as well as years long experience for a design to be appreciable. A designer is faced with a great amount of variables and parameters, each one needed to be analyzed carefully. While some are more important than others, to know how important they are with respect to each other can be an exhaustive task. Still, there are times when less important variables play the most important role in the failure of an engineering structure. It is only natural that while dealing with a very complex design of enormous proportions, it is not possible for a designer to take into account all the variables simultaneously. An optimization process, however, does not require such an experience and it is faster than conventional design processes. Design optimization based on numerical algorithms and techniques can be applied to various engineering systems to help a designer come out with a proposal that is more efficient, light weight, reliable, safe, cost effective and that satisfies the user too. This requires not only the final product to

be optimized but also the optimization of manufacturing process as well as the optimum use/application of the product.
Conventional design techniques may be used for a trivial design of PKMs with a limited capability of considering the performance measures and constraints. However, for complex designs, with a large set of objectives and constraints, these techniques cannot adequately address the problem. A multiobjective optimization approach, on the other hand, can be used to identify a set of optimal trade-off solutions (called a Pareto set) between the conflicting design objectives/constrains, to gain a better understanding of the complexity of the PKMs design problem. Accordingly, in this thesis, some multiobjective optimization approaches are proposed for the design optimization of PKMs.

Research Directions and Contributions

The major contributions of this research work are listed as follows.

- A multiobjective optimization approach to determine the optimal design parameters of a PKM is proposed in order to maximize its regular workspace and minimize the mass in motion. The performance of the mechanism within the workspace is guaranteed by constraining the condition number of the kinematic Jacobian matrix and stiffness characteristics.
- An approach to select proper actuators/motors is presented based on the kinematic and dynamic analysis of a parallel manipulator. Some test trajectories are proposed to analyze the mechanism and motors performance.
- A novel concept of single and multiobjective optimum path placement based on the electric energy consumption, shaking forces and actuators torque is introduced that deals with optimum use of a pre-designed in-use PKM.

Thesis Organization

This thesis report is composed of four chapters. The first chapter provides a state of the art of parallel manipulators and design optimizations. The other three chapters address three separate but inter-linked design optimization issues of PKMs.
The first issue addressed in the second chapter is that of dimensional synthesis of parallel manipulators. A multiobjective optimization problem is proposed to determine optimum structural and geometric parameters of parallel manipulators in order to minimize the mass of the components in motion and to maximize its workspace with desired manipulability and stiffness characteristics. The proposed approach is applied to the optimum design of a three-degree-of-freedom planar parallel manipulator.
The second topic addressed in the third chapter is the important issue of the actuators selection based on the dynamic model of the manipulators. The process focuses on the

kinematic and dynamic analysis of the Orthoglide 5-axis, a spatial PKM developed for high speed operations. The analysis is carried out firstly for the 2-dof spherical wrist of the Orthoglide 5-axis and then for the 3-dof translational parallel manipulator, the Orthoglide 3-axis. Some test trajectories are used to analyze the results and finally, a procedure of motors selection is proposed.

The fourth chapter deals with the optimal use of a PKM. Single and multi-objective path placement optimization approaches for PKMs are presented based on electric energy consumption, actuators torques and shaking forces. It proposes a methodology to determine the optimal location of a given test path within the workspace of a PKM in order to minimize the electric energy used by the actuators, actuators maximal torques and the shaking forces subject to the geometric, kinematic and dynamic constraints. The proposed methodology is applied to the Orthoglide 3-axis, as an illustrative example.

1 Introduction to the Parallel Robots and Design Optimization

1.1 Introduction **5**

1.2 Parallel Robots **6**

1.2.1 Classification of Parallel Robots 7

1.2.2 Planar Parallel Manipulators 8

1.2.3 Spatial Parallel Manipulators 9

1.2.4 Hybrid Manipulators 10

1.2.5 Some Basic Parallel Architectures 11

1.3 Design Aspects of Parallel Robots **13**

1.3.1 Kinematics 14

1.3.2 Dynamics 16

1.3.3 Singularities 16

1.4 Design Optimization **17**

1.4.1 Optimization Process 19

1.4.2 Classification of Optimization Process 20

1.4.3 Multiobjective Optimization and Pareto Optimality 20

1.5 Conclusion **23**

This chapter presents a brief overview of the parallel kinematic machines or parallel robots. It covers general introduction, some of the design aspects and performance measures of the parallel manipulators. Some typical parallel architectures are also presented. At the end, an introduction to the optimization process addressing single and multiobjective optimizations formulations is presented.

1.1 Introduction

Parallel mechanisms have attracted attention for high speed and accuracy applications due to their conceptual potentials in high motion dynamics and accuracy combined with low mass/inertia properties, high structural stiffness (i.e. stiffness-to-mass ratio) due to their closed kinematic loops (Brogårdh, 2007; Weck and Staimer, 2002; Chanal *et al.*, 2006; Merlet, 2006c). This growing attention is inspired by their essential advantages over serial

manipulators that have already reached the dynamic performance limits (Pashkevich *et al.*, 2009b). These features are induced by their specific kinematic structure, which resists to the error accumulation in kinematic chains and allows convenient actuator location close to the manipulator base. Besides, the links work in parallel against the external force/torque, eliminating the cantilever-type loading and increasing the manipulator stiffness (Pashkevich *et al.*, 2009b; Tsai, 1999). Parallel robots are attractive for the innovative machine-tool architectures (Tlusty *et al.*, 1999; Wenger *et al.*, 1999), but practical utilization for the potential benefits requires development of efficient kinematic and dynamic analysis, which satisfy the computational speed and accuracy requirements of relevant design procedures (Pashkevich *et al.*, 2009b).

1.2 Parallel Robots

Traditional robotic manipulators can be classified in two families: the serial and the parallel manipulators. Serial manipulators are distinguished by the fact that they have only one independent kinematic chain between the base and the end-effector of the manipulator. These are opened-loop mechanisms, namely, composed of an open kinematic chain with each intermediate link coupled with two other links by means of two actuated joints. One end of this chain is fixed to the base while the other end is the end-effector. The presence of single kinematic chain and the absence of any passive joint make the serial manipulators simpler to design and to analyze.

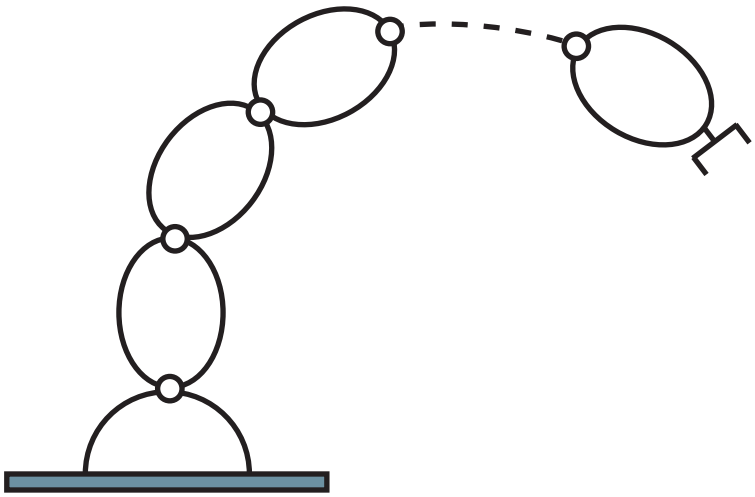

Figure 1.1 – *Schematic of a serial robot*

On the contrary, the parallel manipulators have several legs connecting the base and the end-effector (EE), also called moving platform (MP). Each leg is a kinematic chain whose end links are connected to the two platforms, i.e. base and end-effector. Contrary to serial manipulators, where all joints are actuated, parallel manipulators also contain passive joints. The inclusion of passive joints causes their analysis more complex than the

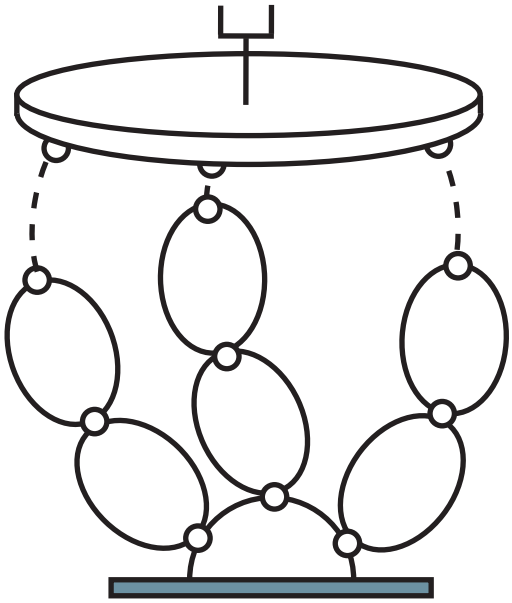

Figure 1.2 – *Schematic of a Parallel robot*

analysis of their serial counterparts. Parallel manipulators are closed-loop mechanisms presenting very good performance in terms of accuracy, velocity, stiffness and ability to manipulate large loads. They have already been used for many applications like machining (Bruzzone *et al.*, 2002), medical robotics (Pisla *et al.*, 2008), space (Rojeski, 1972; Thompson and Campbell, 1997), astronomy (Su *et al.*, 2003), flight-simulators (Baret, 1978) for the design of earthquake simulators (French *et al.*, 2004).
Serial manipulators are more common in industry due to their simple kinematics and accessibility of well developed and matured technical design and analysis material. Another advantage of serial manipulators is the availability of large workspace compared to their own size. However serial manipulators have many limitations some of which include low stiffness, low payload, low accuracy, high inertia etc. Major drawbacks of parallel manipulators are their limited workspace and difficult kinematic analysis. A summary of the comparison of the general features of serial and parallel manipulators presented in (Kuen, 2002) is given in Table 1.1.

1.2.1 Classification of Parallel Robots

The parallel robots can be compared based on several criteria. For instance,(Company, 2006) used the following criteria to compare some parallel robots:

- Mechanism number of degrees of freedom (dof)
- Type of dof
- Mechanism features (constant legs length, variable legs length,...)
- Mechanism dimensions (as for Gough-like platforms)

Table 1.1 – *General comparison of serial and parallel robots (Kuen, 2002)*

Feature	Serial Robots	Parallel Robots
Workspace	large	small
Stiffness	low	high
Singularity Problems	some	abundant
Payload	low	high
Inertia	large	small
Structure	simple	complex
Accuracy	error accumulated	error average out
Speed	low	high
Acceleration	low	high
Forward Kinematics	simple	complex
Inverse Kinematics	complex	usually simple
Dynamics	relatively simple	complex
Design Complexity	low	high

- Actuators placement and number regarding mechanism dof
- Number of kinematic chains (fully parallel, kinematics redundancy, actuation redundancy, hybrid mechanisms...)

A detailed survey of the different classifications of parallel manipulators can be found in (Company, 2000)

1.2.2 Planar Parallel Manipulators

As their name indicates, planar parallel manipulators (PPMs) generate planar motions. Usually, their kinematics and control are simple. A Two-dof and a three-dof PPMs are shown in Figs. 1.3 and 1.4, respectively.

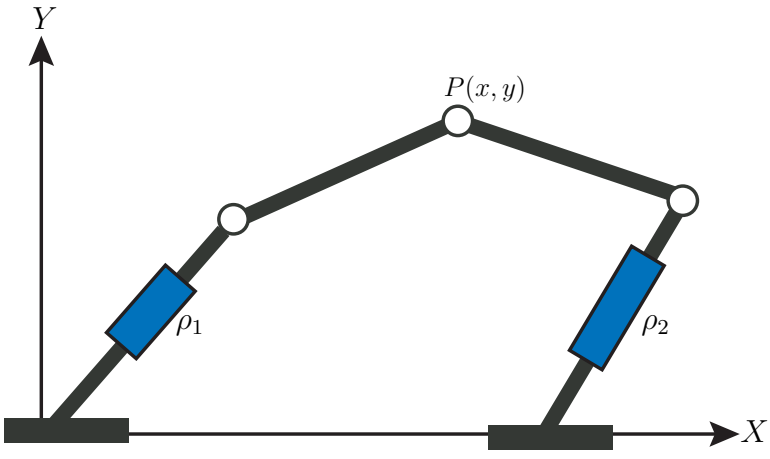

Figure 1.3 – *A 2-dof planar parallel manipulator*

PPM can find their uses in stand alone applications, particularly, when planar motions are required with high speed and precision, like laser or water jet cutting and pick-and-place operations. They can also be used as simple sub-elements in more complex mechanisms (Company, 2006). Some machining applications with such devices are given in (Katz *et al.*, 2001).

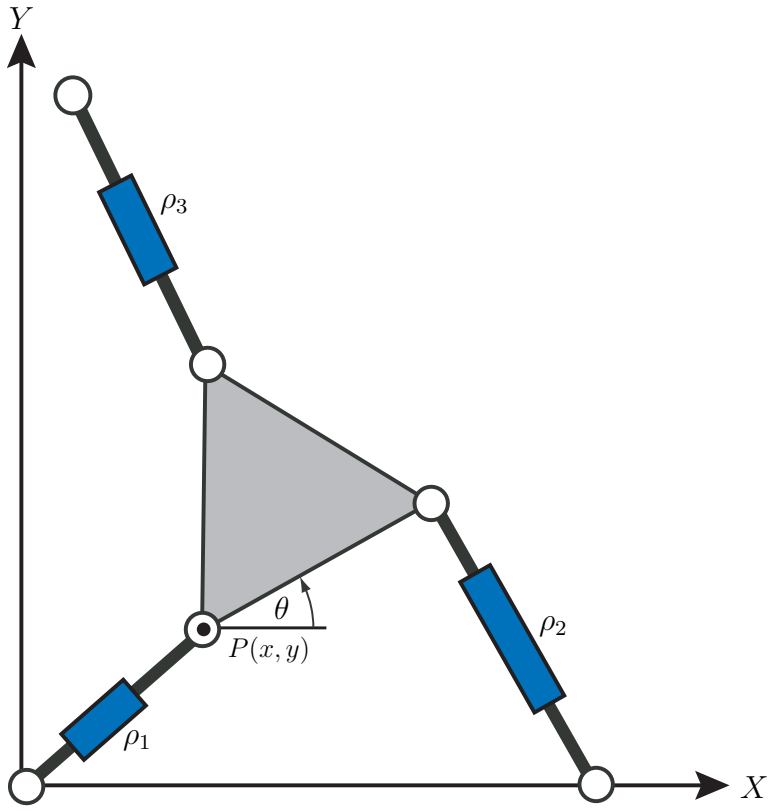

Figure 1.4 – *A 3-dof planar parallel manipulator*

1.2.3 Spatial Parallel Manipulators

Spatial parallel manipulators (SPMs) can have more than 3-dof and have the ability to move in the three dimensional space. These manipulators have various architectures and can be used in a vast milieu of robotic applications. We can find a great amount of SPMs in the literature (Stewart, 1965; Clavel, 1988; Kong and Gosselin, 2002, 2004; Liu *et al.*, 2005; Gogu, 2006). Some of the famous architectures of spatial robots are Delta architecture (Clavel, 1988), Star architecture (Hervé and Sparacino, 1992), Tsai architecture (Tsai, 1996) and Stewart platform (Stewart, 1965). Star and 3-UPU Tsai architectures are shown in Figs. 1.5 and 1.6, respectively, whereas Delta robot and Stewart platform are briefly presented in the coming sections.

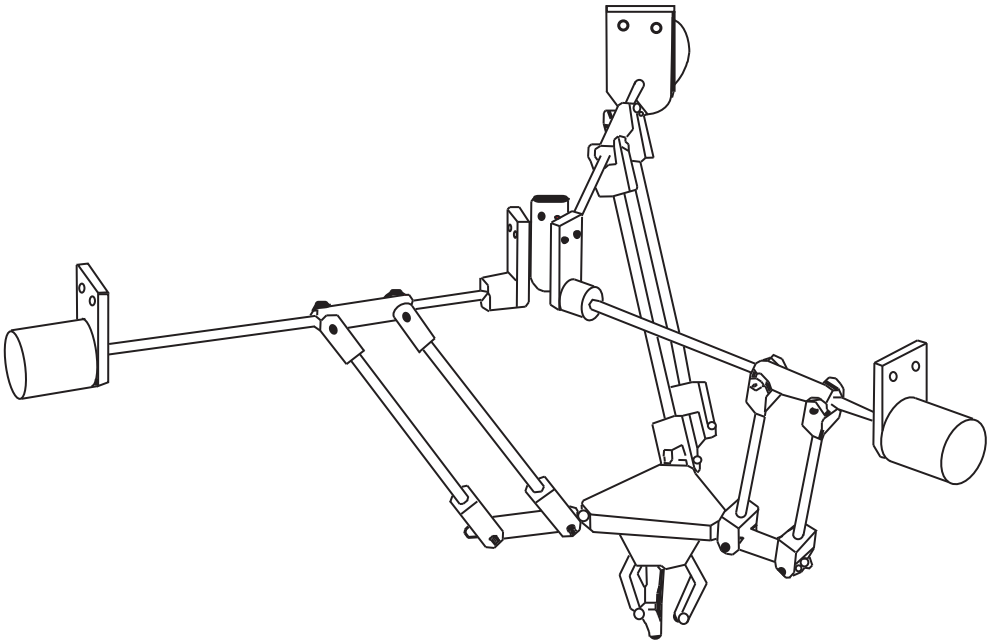

Figure 1.5 – *Star Architecture (Hervé and Sparacino, 1992)*

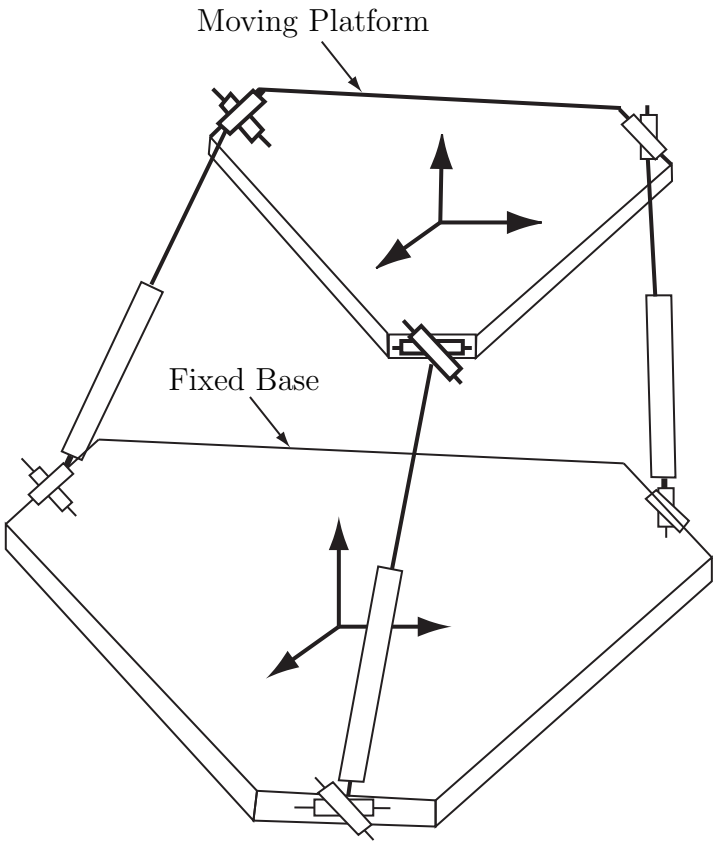

Figure 1.6 – *3-UPU Tsai Architecture (Tsai, 1996)*

1.2.4 Hybrid Manipulators

Hybrid manipulators are usually a concatenation of serial and parallel architectures where only a part of the mechanism is based on parallel kinematics. According to Krut (2003),

a mechanism is hybrid if it has several kinematic chains between the base and the platform with at least one of them including more than one actuator. For example, parallel manipulators with a serial wrist and serial manipulators with a parallel wrist can be classified as hybrid manipulators. These hybrid manipulators can gather the advantages of both serial and parallel manipulators. For example a hybrid manipulator can have large workspace thanks to the serial architecture and a good accuracy and stiffness thanks to the parallel chain. Figure 1.7 depicts a concatenation of a Delta type manipulator and 3-UPS platform, namely, a hybrid manipulator (Gallardo-Alvarado, 2005).

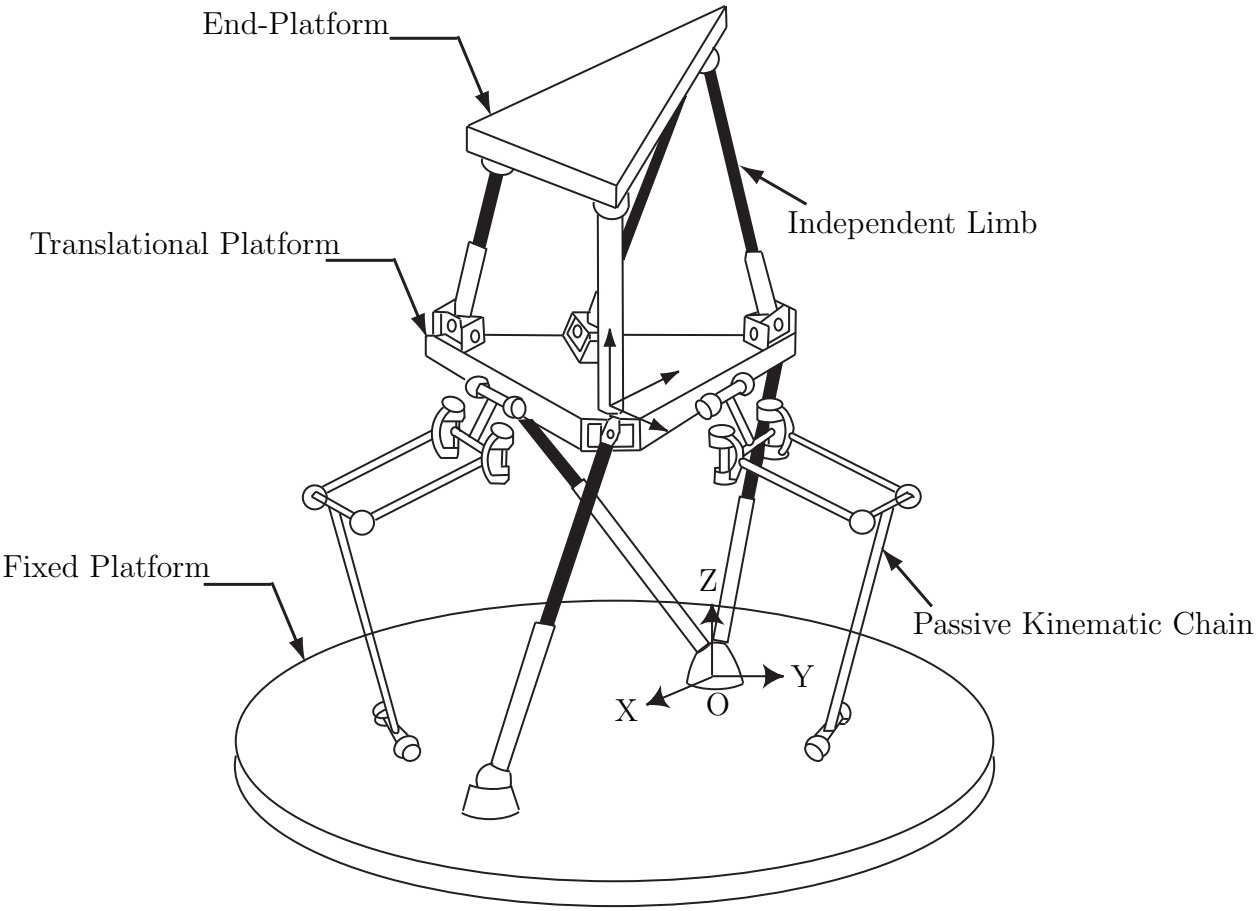

Figure 1.7 – *Hybrid robot (Gallardo-Alvarado, 2005)*

1.2.5 Some Basic Parallel Architectures

1.2.5.1 Delta Architecture

The Delta manipulator, designed by Clavel (1988), is a well known 3-dof translational parallel manipulator. It is composed of three identical limbs connecting the moving platform to the base as illustrated in Fig. 1.8. Each limb contains a revolute joint and a parallelogram joint and another revolute joint.

The distinguishing feature of the Delta robot is the use of parallelograms. It has three

Figure 1.8 – *Basic Delta architecture*

kinematics chains of type $R-R-P_a-R$ where R and P_a stand for revolute and parallelogram joints respectively. These parallelograms constrain some rotation of the moving platform and enable it to move in pure translation along X, Y and Z directions. Actuators are fixed and are located at the base of the robot. Actuators can be of linear or of rotational type. Three kinematic chains connect the base with the platform or end-effector. An additional actuator and a central telescopic bar can be added to provide a rotational degree of freedom about the axis of symmetry of the robot, hence yielding a four-dof robot. This is the case of commercially available Delta robot devoted to pick and place operation like the Flexpicker robot from ABB shown in Fig. 1.9.

As the actuators are located at the base and the moving parts are light, Delta robots have small inertia hence have good dynamic performance. As a matter of fact, they can achieve a velocity equal to 10m/s and accelerations up to 20g (Krut, 2003). Due to high speed of the Delta robot, it is widely used in packaging, medical, pharmaceutical and electronic industry.

1.2.5.2 Stewart Platform

Stewart platform, also known as Gough-Stewart platform or Hexapod,is a PKM having six degrees of freedoms, developed by Gough and Whitehall (1962) and Stewart (1965). The mechanism consists of a stationary base platform and a mobile platform connected with each other with six kinematics chains or legs. The legs have actuated prismatic joints allowing the change of the length of each leg. The legs are connected to the base and the

Figure 1.9 – *FlexPicker (ABB)–Delta Robot*

mobile platform by means of universal joints, (Figs. 1.10 and 1.11).

The desired position and orientation of the mobile platform can be achieved by varying the lengths of the six legs, i.e., transforming six translational motions of prismatic joints into three positional (x, y, z) and three rotational (pitch, yaw, roll) degrees of freedom of the mobile platform.

Stewart platform or its counterparts (Hexapods etc) are widespread in the literature. The Stewart platforms are mainly used in the design of flight simulators, for virtual reality, machine tool technology, crane technology, satellite dish positioning, telescopes and medical applications.

1.3 Design Aspects of Parallel Robots

Parallel robots offer promising advantages over their serial counterparts like high stiffness, high accuracy, high dynamic capacity, low inertia and a better payload-to-weight ratio (Merlet, 2006c; Tlusty *et al.*, 1999; Wenger *et al.*, 1999; Majou *et al.*, 2001). However, the closed-loop nature of the mechanism leads to complex kinematics, difficult trajectory planning, small and complicated workspace with singularities and non linear input/output relations (Angeles, 2002).

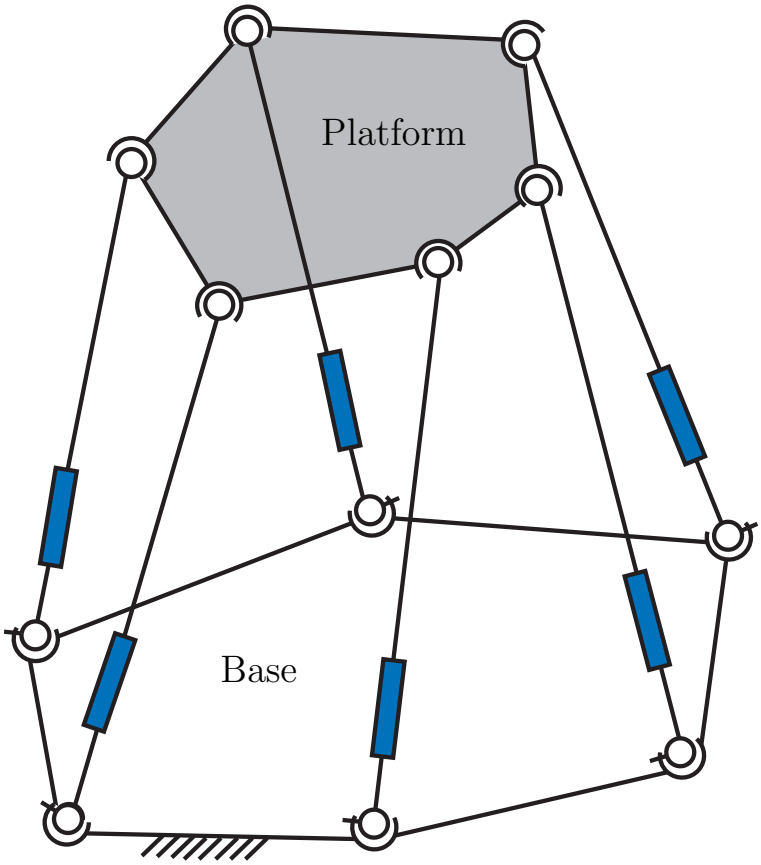

Figure 1.10 – *General Stewart Platform Structure*

1.3.1 Kinematics

Robot kinematics is the study of the relationship between the joint parameters and the corresponding pose of the end-effector. Inverse kinematic model (IKM) determines the required joint parameters for a given end-effector pose whereas direct or forward kinematic model (DKM) determines the end-effector pose for a known set of joint coordinates. The IKM is expressed as follows:

$$\mathbf{x}_p = f(\mathbf{q}) \tag{1.1}$$

and the DKM as:

$$\mathbf{q} = f^{-1}(\mathbf{x}_p) \tag{1.2}$$

where $\mathbf{q}$ is the vector of active joints variables and $\mathbf{x}_p$ is the vector of operational coordinates of the end-effector.
Similarly, direct velocity model (DVM) defines the Cartesian velocities of the end-effector in terms of joint rates, i.e.,

$$\dot{\mathbf{x}}_p = \mathbf{J}_p \dot{\mathbf{q}} \tag{1.3}$$

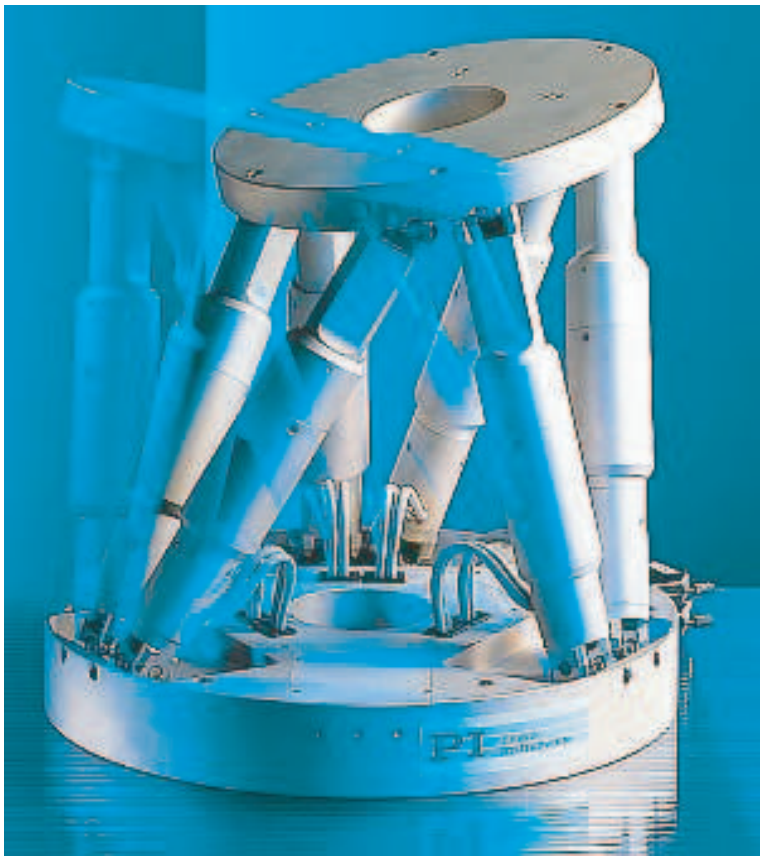

Figure 1.11 – *Stewart Platform*

And, inverse velocity model (IVM) determines joint rates as a function of the Cartesian velocities of the end-effector, i.e.,

$$\dot{\mathbf{q}} = \mathbf{J}_p^{-1}\dot{\mathbf{x}}_p \tag{1.4}$$

where, $\mathbf{J}_p$ is the robot Jacobian matrix, $\dot{\mathbf{x}}_p$ is the end-effector velocity vector comprising of linear and angular velocity components and $\dot{\mathbf{q}}$ is the actuated joints velocity vector.

Eq. (1.3) can also be written as:

$$\mathbf{A}\dot{\mathbf{x}}_p = \mathbf{B}\dot{\mathbf{q}} \tag{1.5}$$

where $\mathbf{A}$ and $\mathbf{B}$ are the parallel and serial Jacobian matrices (Gosselin, 1990b). As long as matrix $\mathbf{A}$ is not singular, we have, $\mathbf{J}_p = \mathbf{A}^{-1}\mathbf{B}$.

Finally, the second order velocity model (or acceleration model) expresses the acceleration of the end-effector in terms of the accelerations and velocities of the actuated joints variables which can be derived upon differentiation of Eq. (1.3):

$$\ddot{\mathbf{x}}_p = \mathbf{J}_p\ddot{\mathbf{q}} + \dot{\mathbf{J}}_p\dot{\mathbf{q}} \tag{1.6}$$

■

The kinematics of parallel robots along with various practical examples and applications have been thoroughly presented by Merlet (2006c) and Angeles (2002). Besides, we can find the kinematic model of a general Stewart-Gough platforms in (Husty, 1996), the kinematic analysis of the Delta robot in (Clavel, 1988) and the one of the Orthoglide, a 3-dof translational PKM, in (Wenger and Chablat, 2000). A state of the art of the kinematics of the PKMs is given by Zentner (2005), Nielsen (1999) and Erdman (1993).

1.3.2 Dynamics

Forces and torques acting on the robot are related to the resulting robot motion by its dynamics. Robot dynamics deals with the determination of the relations between joint forces and the generalized accelerations, velocities and coordinates of the end-effector. The Inverse Dynamic Model (IDM) gives the relation between the actuated joint forces/torques for a given trajectory, velocities and acceleration of the end-effector whereas the Direct Dynamic Model (DDM) gives the relation between the end-effector trajectory, velocities and acceleration for a known or given actuated joints forces/torques. The knowledge of robots dynamics is of prime importance to understand the robot performance and for the command and control. Particularly, dynamics plays an important role in the control of PKMs, high bandwidth robots and structurally sensitive robots (Merlet, 2006c).
The dynamics of PKMs has been an area of interest of several researchers (Fichter, 1986; Lee and Shah, 1988; Sugimoto, 1989; Reboulet and Berthomieu, 1991; Sklar and Tesar, 1998). To develop the dynamic model of parallel robots, several approaches have been proposed, including the Newton-Euler formulation (Sugimoto, 1989; Dasgupta and Choudhury, 1999), Lagrange approach (Miller and Clavel, 1992), principle of virtual work (Tsai, 2000), screw theory (Gallardo-Alvarado *et al.*, 2003) or principle of Hamilton (Miller, 2004). An introduction to different approaches to derive the IDM and DDM of PKMs can be found in (Merlet, 2006c; Angeles, 2002; Ibrahim, 2006).

1.3.3 Singularities

Singularities is one of the major issues of parallel robots and has been a prime focus of research of several roboticians. At singular configurations, robots are exposed to unusual behaviors as loss or gain of degrees of freedom, unattainable directions of motion, existence of motion while the actuators are locked (Pashkevich *et al.*, 2009b). Merlet (2006c) defines the singular configurations as *the particular poses of the end-effector, for which parallel robots lose their inherent infinite rigidity, and in which the end-effector will have uncontrollable degrees of freedom.*
One of the earlier singularity analysis of a closed-loop kinematic chain is that of Hunt (1978). Other pioneers to define and study singularities of closed-loop kinematic chains are Gosselin (1990b); Gosselin and Sefrioui (1991); Merlet (2006c, 1989); Ma and Angeles

(1991a); Zlatanov *et al.* (1994, 1995); Mohammadi Daniali *et al.* (1995) and Park and Kim (1999).

In general kinematic singularities of mechanisms can be classified into six different classes (Zlatanov *et al.*, 1994), whereas there are two basic types of singularities (Gosselin, 1990b), namely, parallel and serial singularities.

A parallel singularity occurs when the determinant of the parallel Jacobian matrix, $\mathbf{A}$, vanishes, i.e. $|\mathbf{A} = 0|$ (Gosselin, 1990b). At this configuration, end-effector can move with locked actuated joints, which results in an absence of control of the end-effector or tool-point P. Figure 1.12 shows a parallel singular configuration of 2-dof mechanism, Biglide. These singularities can damage the mechanism and have to be eliminated from the workspace (Majou and Chablat, 2007).

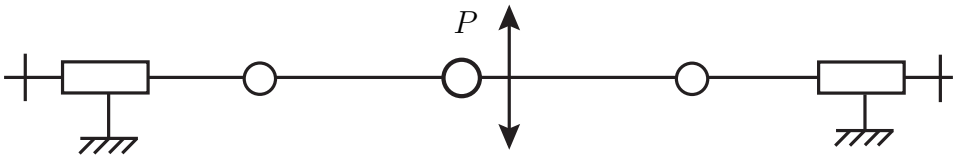

Figure 1.12 – *Biglide-parallel singular configuration*

A serial singularity occurs when the determinant of the serial Jacobian matrix, $\mathbf{B}$, vanishes, i.e. $|\mathbf{B} = 0|$ (Gosselin, 1990b). This type of singularity results in a loss of degree of freedom of the mechanism, i.e. at this configuration, there exists a direction along which no motion can be produced. Figure 1.13 represents the serial singular configuration of the Biglide. Serial singularities define the boundary of the Cartesian workspace of the parallel kinematic machines (Merlet, 2006c).

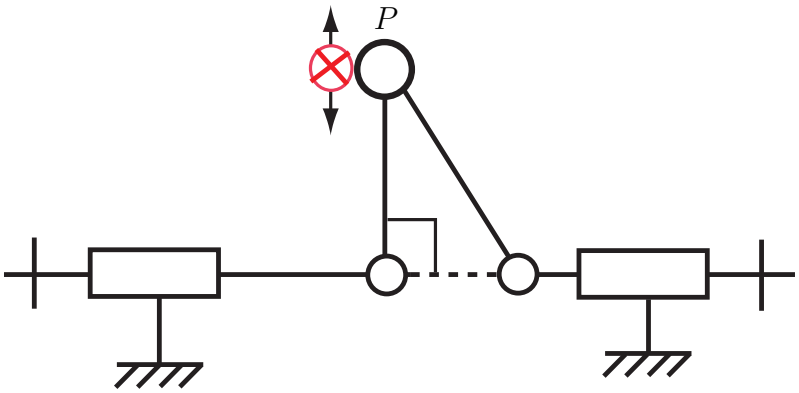

Figure 1.13 – *Biglide-serial singular configuration*

1.4 Design Optimization

Humans have been exploiting and manipulating their knowledge, experience and resources since pre-historic times to maker their living better and easier. In other words they have

been optimizing their resources for better yields. In simple words, optimization is a process of increasing the overall output while reducing the input at the same time. Development of industrial tyres is just one good example to realize the humans' desire to improve their usage of resources, from a very inefficient triangular to very efficient circular one, it has gone through many phases gradually reducing the effort and hence increasing the mechanical efficiency. In order to increase the strength to weight ratio, the use of hollow cylindrical shafts compared to solid ones is another good example.

Off course, optimization is not just limited to tyres or shafts; it now encompasses whole range of engineering applications in every field of endeavour. From automobiles to aircrafts and satellites, watercrafts to trains, housing projects to giant bridges, simple objects like needles to state of the art robots, and from civil to military applications, optimization has been a key area of interest in all applied fields.

Humans are consuming the resources made available to them by the nature in growing numbers. To say the obvious; not all of these resources are renewable, it is therefore increasingly important, logically and environmentally, to optimize our use of these resources. Optimization may therefore be rightly said as one of the most crucial tools in humans' battle for survival.

Engineering design process goes through many phases and requires, as a prerequisite, a designer's knowledge as well as years long experience for a design to be appreciable. A designer is confronted with myriad variables and parameters, each seeking careful attention and indulgence. While some are more important than others, the very designation of the level of importance can itself be an exhaustive task. Still, there are times when "less important" variables play the most important role in the failure of an engineering structure. It is only natural that while dealing with a very complex design of enormous proportions, it is not possible for a designer to take into account all the variables simultaneously. An optimization process, however, does not demand this much experience and yet it is faster than a conventional design process. Design optimization based on numerical algorithms and techniques can be applied to varied engineering systems to help a designer come out with a proposal that is more efficient, light weight, reliable, safe, cost effective and that satisfies the end user too. This requires not only the final product to be optimized but also the optimization of manufacturing process as well as the tools to manufacture those products at every level of production. A lot of research has been done in the field of optimization, proposing different approaches, techniques and methodologies. They span a large range of problems such as linear programming, constrained/unconstrained non-linear optimization, single and multi-objective optimization.

1.4.1 Optimization Process

Optimization process in design is a tool of conceptualization and analysis used to achieve better designs or design improvements. It is a mathematical procedure for determining optimal solutions by representing all the complexities of the design in the form of design variable(s), objectives function(s) and/or constraint(s). The basic elements of any constrained optimization problem are:

Objective function. An objective function or vector of objective functions is the mathematical expression that expresses the optimization goal in terms of design variables. Optimization process is required to either minimize or maximize the objective function. For instance, in robotics, maximization of the workspace or minimization of inertia/mass of a manipulator can be the objective functions.

Design variables. Also known as decision variables, are the "unknowns" of the optimization problem which are to be determined. From the point of view of the designer, these are the controllable numeric values which affect the value of the objective function. Design variables can be continuous (such as a length/diameter/cross-section of the robot links) or discrete (such as the number of links/joints in a robot).

Constraints. A set of constraints that must be satisfied in order for the design to be feasible. These are mathematical expressions that combine the variables to express limits on the possible solutions. Constraints allow the design variables to take certain values but exclude others. In addition to physical laws; constraints can reflect resource limitations, user requirements, or bounds on the validity of the analysis models.

Variable bounds. Design variables are not usually permitted to take any value. Instead, these are usually have lower and upper limits, known as variable bounds. Variable bounds limits the design space and along with constraints, used to distinguish the solutions as feasible or unfeasible.

The optimization problem is then:
Find the values of the design variables that minimize or maximize the objective function while satisfying the constraints. Remembering that variables describe all situations and constraints describe all feasible situations Mathematically, an single-objective optimization problem can be expressed as:

$$\min_{\mathbf{x}} f \qquad \text{subject to:} \begin{cases} g_i(\mathbf{x}) \leqslant 0 & i = 1, \cdots m \\ h_j(\mathbf{x}) = 0 & j = 1, \cdots n \\ \mathbf{x}_l \leqslant \mathbf{x} \leqslant \mathbf{x}_u \end{cases} \tag{1.7}$$

Where, $\mathbf{x}$ is the vector of design variables, f is the objective function to be minimized subject to m inequality and n equality constraints given by $g_i(\mathbf{x})$ and $h_j(\mathbf{x})$, respectively.

■

Optimization is an iterative process and involves at least some degree of trial and errors. As the problem complexity is increased, the search procedure becomes tedious and may not guarantee a solution in all cases. The main steps involved in solving an optimization problem can be cited as (Arora, 1989):

- understand the problem, by drawing a diagram or flow chart which represents the problem;
- write a problem formulation in words, including decision variables, objective function, and constraints;
- write the algebraic formulation of the problem;
  - o define the decision variables;
  - o write the objective function(s);
  - o write the constraints;

  develop a spreadsheet model;
- set up the Solver settings and solve the problem;
- examine the results and make corrections to the model;
- analyze and interpret the results.

The overall structure of an optimization approach is presented in Fig. 1.14.

1.4.2 Classification of Optimization Process

There are many optimization algorithms available to solve an optimization problem. Many methods are appropriate only for certain types of problems. Thus, it is important to be able to recognize the characteristics of a problem in order to identify an appropriate method to solve the problem. Within each class of problems there are different minimization methods, varying in computational requirements, convergence properties, and so on. Optimization problems are classified according to the mathematical characteristics of the objective function, the constraints, and the control variables. Other classifications are summarized in Table 1.2. Normally, optimization problems found in engineering are the combinations of different classifications. For instance, a problem may be of the type "constrained nonlinear multiobjective optimization"

1.4.3 Multiobjective Optimization and Pareto Optimality

In numerous real life optimization applications, there exist many targets or objectives that should be optimized simultaneously. However, these targets often conflict and it is not possible to satisfy all of them at the same time. Thus one has to make compromises. Such types of optimization problems are called multiobjective optimization problems.

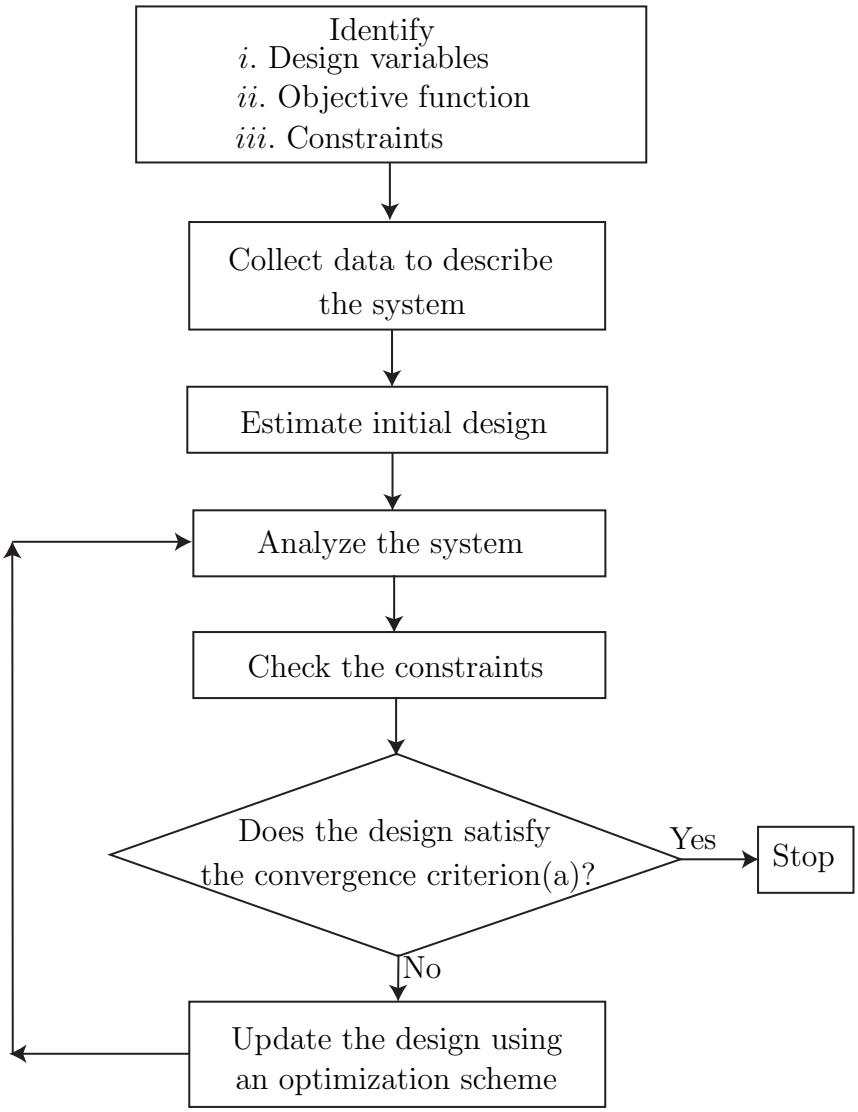

Figure 1.14 – *General design optimization process (Arora, 1989)*

A general multiobjective optimization problem is to find design variables that optimize a vector objective function subject to a number of constraints and bounds. It is often formalized as follows (Shan and Wang, 2005):

$$\min_{\mathbf{x}} F(\mathbf{x}) = (f_1(\mathbf{x}), \ldots, f_m(\mathbf{x}), \ldots f_k(\mathbf{x})) \tag{1.8}$$

$$\text{subject to:} \quad \begin{array}{ll} g_k(\mathbf{x}) \leqslant 0 & k = 1, \cdots p \\ h_j(\mathbf{x}) = 0 & j = 1, \cdots q \\ \mathbf{x}_r^l \leqslant \mathbf{x}_r \leqslant \mathbf{x}_r^u & r = 1, \cdots n \end{array}$$

where the components of the multiobjective function $F(\mathbf{x})$, are usually in conflict with one another with respect to their own optimum point. The design variable vector, $\mathbf{x} = [x_1, \cdots x_r, \cdots, x_n]$, consists of n design variables of the problem bounded by $\mathbf{x}_l$ and $\mathbf{x}_u$. $h_j(\mathbf{x})$ and $g_k(\mathbf{x})$ are equality and inequality constraints, respectively.

■

Table 1.2 – *Classification of optimization problems (Jilla, 2002)*

Characteristic	Property	Classification
Number of Control variables	One	Single variable
	More than one	Multivariable
Type of control variables	Continuous real number	Continuous
	Integers	Discrete
	Continuous real number and integers	Mixed Integer
Problem functions	Linear function of control variables	Linear
	Quadratic functions of the control variables	Quadratic
	nonlinear functions of the control variables	Nonlinear
Problem formulation	Subject to constraints	Constrained
	Not subject to constraints	Unconstrained
Number of Objective function	One	Mono objective
	More than one	Multiobjective

Contrary to the traditional mono-objective optimization, multiobjective optimization problems have several objective functions to optimize at the same time. In addition, there is not a unique solution, but instead there can be a number of mathematically equivalent good solutions. Best solution means a solution not worst with respect to any of the objectives and at least better in one objective than the other. An optimal solution is the solution that is not dominated by any other solution in the search space. Such an optimal solution is called Pareto optimal and the entire set of such optimal trade-offs solutions is called Pareto optimal set (Abraham *et al.*, 2005).

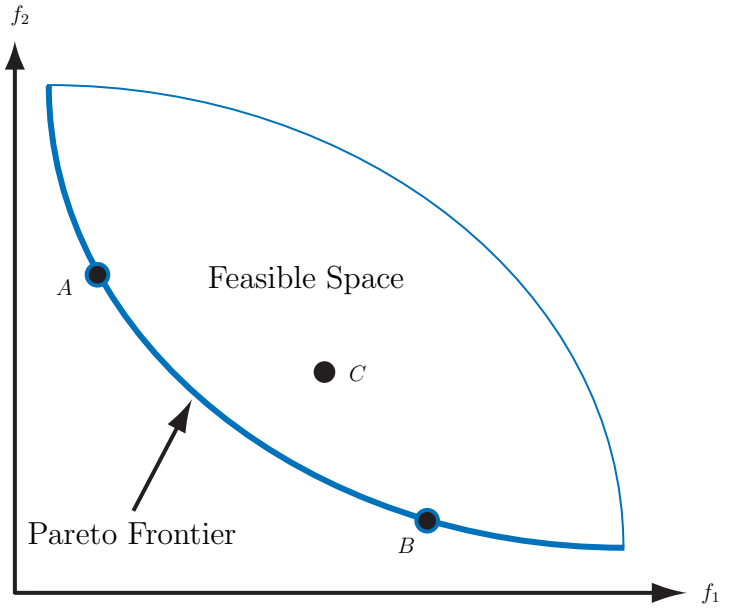

Figure 1.15 – *Graphical representation of the Pareto frontier*

Pareto optimal can be defined as (Marler and Arora, 2004), *A point $x^* \in X$ is Pareto optimal if and only if there does not exist another point $x \in X$, such that $f_i(x) \leqslant f_i(x^*)$ and $f_i(x) < f_i(x^*)$ for at least one function.* Pareto optimal points are also known as efficient, non-dominated, or non-inferior points. Even though there are several ways to approach a multiobjective optimization problem, most work is concentrated on the approximation of the Pareto set (Abraham *et al.*, 2005). Determination of some Pareto subsets, where the solution or its part must lie, decreases the design space which results a reduction of the overall computational complexity of the design task. The storage of any design variant, computed intermediately, can be used for numerical determination of the Pareto set (Valasek and Sika, 2003; Caro *et al.*, 2007; Bouyer *et al.*, 2007).
There are several approaches to solve multiobjective optimization problems. Some examples of these approaches are weighted sum method, weighted product method, weighted min-max method, exponential weighted criterion, Lexicographic method, goal programming methods, physical programming, genetic algorithms and simulated annealing. A survey of these and others multiobjective optimization approaches can be found in (Marler and Arora, 2004; Andersson, 2001).

1.5 Conclusion

The parallel kinematics machines are getting more and more attention in modern industrial applications for their potential benefits of high speed, good accuracy, low mass/inertia properties and high structural stiffness. However, practical utilization for these added benefits requires an extensive and efficient analysis of their structure, kinematics and dynamics. On the design front, use of optimization techniques is a prime area of interests of the researchers in order to optimize the existing designs or to explore new design prospects. The use of computer aided design (CAD), computational fluid dynamic (CFD) and finite element methods (FEM) has reduced the time-consuming design and analysis process with better results. Conventional design techniques may be used for a trivial design of PKMs with a limited capability of considering the performance measures and constraints. Numerical optimization techniques, on the other hand, can be very useful to obtain solution variants, i.e., set of reliable and acceptable solutions obtained by following a systematic approach instead of hit and trail or heuristics approaches.
In the next chapter, various performance measures of PKMs will be discussed and subsequently a multiobjective optimization approach will be presented in order to determine optimum design parameters of a PKM.

2 Multiobjective Design Optimization of Parallel Kinematics Machines

2.1 Introduction . . . 26

2.2 Performance Measures and Indices . . . 28

2.2.1 Workspace . . . 28
2.2.2 Manipulability . . . 29
2.2.3 Condition Number of the Kinematic Jacobian Matrix . . . 30
2.2.4 Accuracy . . . 31
2.2.5 Robustness and Sensitivity . . . 32
2.2.6 Stiffness . . . 32
2.2.7 First Natural Frequency . . . 34
2.2.8 Summary of Performance Measures and Indices . . . 35

2.3 Case Study: 3–PRR Manipulator . . . 36

2.3.1 Architecture of 3-PRR . . . 37
2.3.2 Inverse and Direct Kinematic Model of 3-PRR . . . 37
2.3.3 Jacobian Matrices of 3–PRR . . . 38
2.3.4 Dexterity of 3-PRR . . . 41
2.3.5 Stiffness Matrix . . . 41

2.4 Multiobjective Design Optimization of PKMs Problem Formulation 45

2.4.1 Optimization objectives . . . 45
2.4.2 Optimization Constraints . . . 46
2.4.3 Problem Statement . . . 47

2.5 Multiobjective Optimization Problem Formulation for 3–PRR 47

2.5.1 Optimization Design Parameters . . . 48
2.5.2 Optimization objectives . . . 48
2.5.3 Optimization constraints . . . 49
2.5.4 Problem Statement for 3–PRR . . . 51
2.5.5 Optimization Results . . . 51

2.6 Conclusion . . . 55

This chapter addresses the dimensional synthesis of parallel kinematics machines. A multiobjective optimization problem is proposed in order to determine optimum structural and geometric parameters of a parallel manipulator. The proposed approach is applied to the optimum design of a three-degree-of-freedom planar parallel manipulator in order

to minimize the mass of the mechanism in motion and to maximize its regular shaped workspace.

2.1 Introduction

The design of parallel kinematics machines is a complex subject. The fundamental problem is that their performance heavily depends on their geometry (Hay and Snyman, 2004) and the mutual dependency of almost all the performance measures. This results computational complexity of the problem and makes the traditional solution approaches inefficient. As reported by Merlet (2006c), since the performance of parallel manipulators depends on their dimensions, customization of these manipulators for each application is absolutely necessary. Furthermore, numerous design aspects contribute to the PKM performance and an efficient design will be that which takes into account all or more of these design aspects. For instance, a simplified design network of a parallel kinematics machine is shown in Fig. 2.1 (Valasek *et al.*, 2005). In this figure, eight design criteria are considered, namely, workspace, collision avoidance, dexterity and force transmission evaluation, stiffness and eigen-frequency (modal) evaluation, dynamic capability evaluation, kinematic and elastostatic accuracy evaluation and finally control system dynamics and accuracy evaluation. The design process has been decomposed into three levels of design conflicts and related structural and parametric optimizations (Valasek *et al.*, 2005):

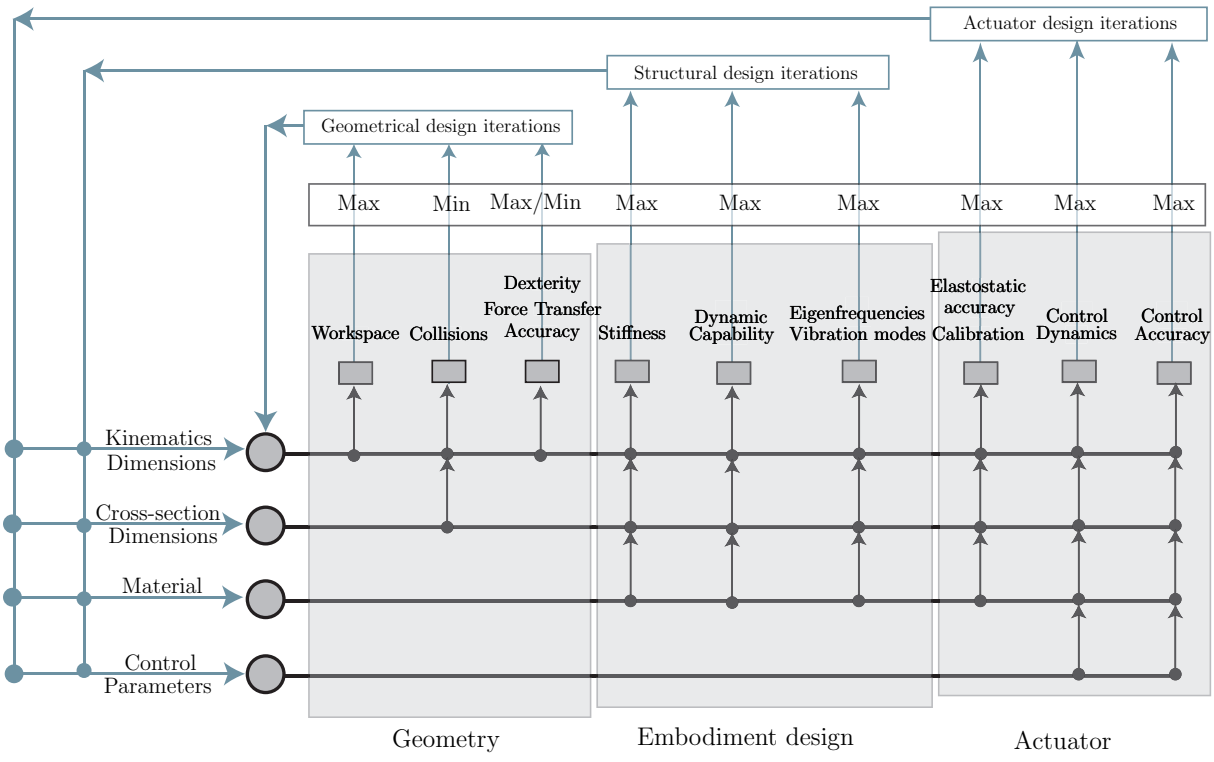

Figure 2.1 – *Design network of parallel kinematics mechanisms (Valasek et al., 2005)*

- geometric design conflicts: workspace, collision versus necessary dimensions for stiffness, accuracy, dexterity and other requirements.
- structural design conflicts: stiffness, accuracy, eigen-frequencies versus mass, dynamics, acceleration etc;
- actuator design conflicts: drive torque versus drive inertia, the influence of control system.

From this general description of a PKM design process, it is obvious that it is an iterative process and an efficient design requires a lot of computational effort and capability for mapping design parameters into design criteria (objectives, constraints) and hence following a multiobjective design procedure. The design parameters of a PKM can be determined by using multiobjective optimization techniques where the design variants can be obtained from the generated Pareto frontiers. Modern optimization techniques can serve the purpose of this customization process and can facilitate the designer to come up with more efficient and cost-effective solutions. Therefore, design optimization of parallel mechanisms has become a key issue for their development and has gained more and more attention of the researchers in the recent years. Several researchers have addressed the optimization problem of parallel mechanisms to optimize their performance with respect to a single or several design objectives.

Lou *et al.* (2005, 2008) presented a general approach for the optimal design of parallel manipulators to maximize the volume of an effective regular-shaped workspace while subject to dexterity constraints. Effective regular workspace reflects simultaneously the requirements on the workspace shape and quality. Hay and Snyman (2004) considered the optimal design of parallel manipulators to obtain a prescribed workspace whereas Ottaviano and Ceccarelli (2001) proposed a formulation for the optimum design of 3-dof spatial parallel manipulator architectures for given position and orientation workspaces. Hao and Merlet (2005) discussed a multi-criteria optimal design methodology based on interval analysis to determine the possible geometries satisfying two compulsory requirements of the workspace and accuracy. Ottaviano and Ceccarelli (2000) based their study on the static analysis and the singularity loci of a manipulator in order to optimize the geometric design of the Tsai manipulator for a given free from singularity workspace. Similarly, Ceccarelli *et al.* (2005) dealt with the multi criteria optimum design of both parallel and serial manipulators with the focus on the aspects of workspace, singularity, and stiffness. Gosselin and Angeles (1988, 1989) studied the design of a planar and a 3-dof spherical parallel manipulators by maximizing the workspace volume while taking into account the condition numbers of these manipulators. Pham and Chen (2003) suggested maximizing the workspace of a parallel flexure mechanism with the constraints on a global and uniformity measure of manipulability. Stamper *et al.* (1997) used the global condition index based on the integral of the inverse condition number of the kinematic Jacobian

matrix over the workspace, to optimize a spatial 3-dof translational parallel manipulator. Stock and Miller (2003) formulated a weighted sum multi-criteria optimization problem with manipulability and workspace as two objective functions. Menon *et al.* (2009) used the maximization of the first natural frequency as an objective function for the geometrical optimization of the parallel mechanisms. Similarly, Li *et al.* (2009) proposed dynamics and elastodynamics optimization of a 2-dof planar parallel robot to improve the dynamic accuracy of the mechanism. They proposed a dynamic index to identify the range of natural frequency with different configurations. Krefft and Hesselbach (2005) also presented multi-criteria elastodynamic optimization of parallel mechanisms while considering workspace, velocity transmission, inertia, stiffness and first natural frequency as optimization objectives. Chablat and Wenger (2003) proposed an analytical approach for the architectural optimization of a 3-dof translational parallel mechanism, Orthoglide 3-axis, based on prescribed kinetostatic performance in a given Cartesian workspace.
In this chapter, we propose a methodology to deal with the multiobjective design optimization of PKMs. The mechanism mass, conditioning number of the kinematic Jacobian matrix and accuracy characteristics are considered as objective functions. The proposed approach is highlighted by means of a 3-dof planar parallel manipulator and Pareto frontiers are obtained using a multiobjective genetic algorithm.

2.2 Performance Measures and Indices

The estimation of the manipulators performance is very important for proper manipulators application, design and selection. Angeles (2002) defines a performance index of a robotic mechanical system as a scalar quantity that measures how well the system behaves with regard to force and motion transmission. Different authors have proposed various performance characteristics and indices to compare and evaluate manipulators' performance. Workspace (Wenger and Chablat, 2000; Liu *et al.*, 2004; Stamper *et al.*, 1997; Kosinska *et al.*, 2003), dexterity (Merlet, 2006c), manipulability (Yoshikawa, 1985; Merlet, 2006b; Kucuka and Bingulb, 2006), accuracy (Merlet, 2006b), stiffness (Pashkevich *et al.*, 2009b) are widely used performance characteristics of robot manipulators.

2.2.1 Workspace

Workspace is one of the most important issues as it defines the working volume of the robot/manipulator and determines the area that can be reached by a reference frame located on the moving platform or end-effector (Liu *et al.*, 2004; Stamper *et al.*, 1997; Kosinska *et al.*, 2003). The size and shape of the workspace are of primary importance for the global geometric performance evaluations of the manipulators (Wenger and Chablat, 2000). Merlet and Mouly (1998) have defined different types of workspaces which include,

constant orientation workspace, maximal or reachable workspace, inclusive orientation workspace, total orientation workspace and finally the dextrous workspace. The constant orientation workspace is the region which can be reached by the end-effector with constant orientation. The region which can be reached by the end-effector with at least one orientation is the maximal or reachable workspace. The inclusive workspace is the region that can be attained by the end-effector with at least one orientation in a given range. Total orientation workspace defines the region which can be reached by the end-effector with every orientation of the end-effector in a given range and finally the dextrous workspace describes the region that can be reached by the end-effector with any orientation of the end-effector. Chablat *et al.* (2004) introduced the concept of regular dextrous workspace, which is defined as regular-shaped workspace within the Cartesian workspace in which the velocity amplification factors remain within a predefined range. This ensure good and homogeneous kinematic performance throughout the dextrous workspace.

In the literature, different methods to determine workspace of parallel manipulators have been proposed (Gosselin, 1990b; Merlet and Mouly, 1998; Merlet, 1995). These include, analytical methods (Kohli and Spanos, 1985; Abdel-Malek and Yeh, 1997), numerical, iterative and statistical methods mainly based on the discretization of the pose parameters (Lee and Yang, 1983; Rastegar, 1990; Alciatore and Ng, 1994; Cleary and Arai, 1991; Ferraresi *et al.*, 1995; Kumar and Waldron, 1981), optimization methods (Lee and Cwiakala, 1985) etc. Some of the research works on the workspace analysis can be reported as (Merlet, 2006c; Gosselin, 1990b; Merlet and Mouly, 1998; Chablat *et al.*, 2004; Gosselin, 1990a; Tsai and Soni, 1981; Gupta and Roth, 1982).

2.2.2 Manipulability

The concept of manipulability of a manipulator was introduced by Yoshikawa (1985). The manipulability quantifies the manipulator velocity transmission capabilities or, equivalently, dexterity of the robot (Merlet, 2006c). The manipulability μ is defined as the square root of the determinant of the product of the manipulator kinematic Jacobian matrix, $\mathbf{J}$, by its transpose (Yoshikawa, 1985).

$$\mu = \sqrt{det\left(\mathbf{J}\mathbf{J}^T\right)} \tag{2.1}$$

The manipulability measures how much the end-effector moves for a given infinitesimal joint angles motion. Manipulability measure is very useful for manipulator design, task planning and fast recovery ability from the singular points for robot manipulators (Kucuka and Bingulb, 2006).

The manipulability is equal to the absolute value of the determinant of the Jacobian in case of square Jacobian matrix (Angeles, 2002). Hence, using the singular value decomposition,

the manipulability can be written as,

$$\mu = \sigma_1 \sigma_2 \cdots \sigma_i \cdots \sigma_n \tag{2.2}$$

where σ_i are the singular values of the Jacobian matrix.
Since the value of the determinant depends on the used units, the manipulability will have different values for different units, i.e. it is not units invariant. Another shortcoming of manipulability is that it mixes translational and rotational motions. Consequently, it has been proposed to calculate the manipulability index for translational and rotational motions by splitting the Jacobian into corresponding parts (Merlet, 2006b).

2.2.3 Condition Number of the Kinematic Jacobian Matrix

In numerical analysis, the condition number of a matrix is used to estimate the error generated in the solution of a linear system of equations by the error in the data (Strang, 1976). Salisbury and Craig (1982) are the pioneer to use the condition number of the Jacobian matrix to design mechanical fingers of the articulated hands. Later on, Angeles and Rojas (1987) used it as a kinetostatic performance index of the robotic mechanical system and applied it to the design of a 3-dof spatial manipulator and a 3-dof spherical wrist. In terms of the Jacobian matrix of a robot manipulator, the condition number is an error amplifying factor of actuators affecting the accuracy of the Cartesian velocity of the end-effector (Kucuka and Bingulb, 2006).
According to Angeles (2002), for a Jacobian matrix $\mathbf{J}$, whose all entries have the same units, condition number $\kappa(\mathbf{J})$, based on the 2-norm, can be defined as the ratio of the largest σ_l to the smallest σ_s singular values of $\mathbf{J}$, i.e.,

$$\kappa(\mathbf{J}) = \frac{\sigma_l}{\sigma_s} \tag{2.3}$$

$\kappa(\mathbf{J})$ ranges from 1 to infinity, 1 for isotropic postures and infinity at singularity.
The conditioning index (CI), bounded between zero and unity, is defined as the reciprocal of the condition number, i.e., $1/\kappa$, is also used to evaluate the control accuracy, dexterity and isotropy of the mechanism (Gosselin, 1990b; Kucuka and Bingulb, 2006; Angeles, 2002). It can be used to evaluate the distance to the singular configurations. $CI = 1$ when the robot reaches an isotropic configuration and $CI = 0$, when it reaches a singular configuration. Therefore, the larger the CI, the further the distance to singularity. The main advantage of the condition number or conditioning index is that it is a single number used to describe the overall kinematic behavior of a robot. It is used as an index to describe (Merlet, 2006b),

– the accuracy and dexterity of a robot;

- the closeness of a pose to a singularity. It is, in general, not possible to define a mathematical distance to a singularity for robots whose dof is a mix between translation and orientation; hence, the use of the condition number is as valid as any other index;
- a performance criterion for optimal robot design and robots comparison;
- a criterion to determine the useful workspace of a robot.

Condition number is also used for trajectory planning and gross motion capability of a robot manipulator in the workspace (Kucuka and Bingulb, 2006)
However, a major drawback of the condition number is that, for a robot having both translational and rotational dof, the matrix involved in its calculation will be heterogeneous with respect to units used (Merlet, 2006c). Hence, the value of the condition number for a given robot and pose will change according to the unit, while clearly the kinematic accuracy is constant (Kucuka and Bingulb, 2006; Merlet, 2006b). Ma and Angeles (1991b) suggested to use a normalized inverse Jacobian matrix by dividing the rotational elements of the matrix by a length, called the *characteristic length*, such as the length of the links in a nominal position or the natural length, defined as that which minimizes the condition number for a given pose. However, the choice of the *characteristic length* remains arbitrary as it just allows us to define a correspondence between a rotation and a translation (Merlet, 2006b). For planar robots, Chablat *et al.* (2002); Alba-Gomez *et al.* (2005) selected a characteristic length that makes sense geometrically.

2.2.4 Accuracy

One of the promising feature of parallel mechanisms over their serial counterparts is their high accuracy owing to their closed kinematic chains (Brogårdh, 2007; Chanal *et al.*, 2006). Therefore, the accuracy, reflecting the maximum position and orientation errors over a given portion of the workspace (Merlet, 2006a), is a pertinent performance measure for PKM. The accuracy of a PKM can be affected by several factors, like, manufacturing errors, backlash, components compliance and active-joint errors (Briot and Bonev, 2008; Caro *et al.*, 2009). For a properly designed, manufactured and calibrated PKM, active-joint errors also known as input errors are the most significant source of accuracy decline (Merlet, 2006a).
Accuracy analysis is closely related to the singularity (Merlet, 2006b), therefore, singularity performance measures can also be used to reflect the accuracy of a PKM. For example, dexterity index (Gosselin, 1992), the condition numbers (Pittens and Podhorodeski, 1993; Rao *et al.*, 2003), and the global conditioning index (Gosselin and Angeles, 1991) can be used to optimize the accuracy of a PKM. Merlet (2006b) discussed these performance indices in order to examine the positioning accuracy of the end-effector while using the Jacobian and inverse Jacobian matrices of a PKM. Others main sources of positioning

errors for PKMs are listed in (Merlet, 2006c).

2.2.5 Robustness and Sensitivity

According to Taguchi (1993), robust design is a technique that reduces variations in a product by reducing the sensitivity of the design of the product to sources of variations rather than by controlling their source. A design is said to be robust when its performance are as least sensitive as possible to the variations in their design variable and design environment parameters (Caro *et al.*, 2005).
Sensitivity analysis is used to determine the sensitivity of a model to the variations in the design and structural parameters of the model. Sensitivity analysis helps to determine the parameters or factors contributing to the variability of the performance of the system and allow the designer to determine the design tolerances of the parameters to make the system more accurate and sufficiently robust.
Inspired by the Taguchi idea, several researchers put their efforts for the robust design and sensitivity analysis of different PKMs (Caro *et al.*, 2006, 2009; Binaud *et al.*, 2008; Bai and Caro, 2009). A state of the art of robust design is presented in (Caro, 2003). Han *et al.* (2002) described the gross motion of a 3-UPU parallel mechanism by kinematic sensitivity analysis whereas Fan *et al.* (2003) analyzed the sensitivity of a 3-PRS parallel kinematic spindle of a serial parallel kinematics machine. Wang and Masory (1993) studied the effect of manufacturing tolerances on the accuracy of Stewart Platform. Caro *et al.* (2006) introduced two complementary methods to analyze the sensitivity of a 3-dof translational parallel kinematic machine (PKM) with orthogonal linear joints: the Orthoglide. On the one hand, a linkage kinematic analysis method is proposed to have a rough idea of the influence of the length variations of the manipulator on the location of its end-effector. On the other hand, a differential vector method is used to study the influence of the length and angular variations in the parts of the manipulator on the position and orientation of its end-effector. Besides, this method takes into account the variations in the parallelograms. It turns out that variations in the design parameters of the same type from one leg to another have the same effect on the position of the end-effector. Moreover, the sensitivity of its pose to geometric variations is a minimum in the kinematic isotropic configuration of the manipulator. On the contrary, this sensitivity is a maximum close to the kinematic singular configurations of the manipulator. In a recent work, Caro and Wenger (2008) developed the sensitivity coefficients of a 3-RPR manipulator in algebraic form.

2.2.6 Stiffness

Higher stiffness of parallel robots is one of the major merit over their serial counter parts. The stiffness of a PKM mainly depends on its geometric configuration and the

stiffness of its components. (Weck and Staimer, 2002) PKMs are claimed to offer better accuracy, lower mass/inertia properties and higher structural stiffness (Merlet, 2006c). These features are induced by their specific kinematic structure, where the links act in parallel against the external force/torque, eliminating the cantilever-type loading and increasing the manipulator stiffness (Pashkevich *et al.*, 2009b; Tsai, 1999).

Generally, the stiffness analysis evaluates the effect of the applied external torques and forces on the compliant displacements of the end-effector. This property is defined through the "stiffness matrix" $\mathbf{K}$, which gives the relation between the translational/rotational displacement and the static forces/torques applied to the robot end-effector. The inverse of $\mathbf{K}$ is called the "compliance matrix". As follows from mechanics, $\mathbf{K}$ is a 6×6 semi-definite non-negative matrix, where structure may be non-diagonal to represent the coupling between the translation and rotation motions (Pashkevich *et al.*, 2009b; Duffy, 1996).

The stiffness of a PKM depends on the force/torque direction and on the manipulator configuration. Hence, to provide the designer with integrated performance criteria, various scalar indices are usually computed (such as the best/worst/average stiffness with respect to the rotation or translation). They are typically derived using the singular-value decomposition of $\mathbf{K}$. Furthermore, since matrix $\mathbf{K}$ varies throughout the workspace, corresponding global benchmarks must be computed (Pashkevich *et al.*, 2009b).

The actuators forces/torques, $\mathbf{F}$, required to cause a change in the position $\delta\mathbf{X}$ (angular/translational) of the end-effector can be written as:

$$\mathbf{F} = \mathbf{K}\delta\mathbf{X} \tag{2.4}$$

Several approaches exist for the computation of the stiffness matrix, which differ in the modeling assumptions and computational techniques. Examples can be the finite element analysis (FEA), the matrix structural analysis (MSA), and the virtual joint method (VJM) approach.

Recently, Pashkevich *et al.* (2009b) introduced new stiffness modeling method, which combines advantages of the traditional approaches. It is based on a multidimensional lumped-parameter model that replaces the link flexibility by localized 6-dof virtual springs that describe both the linear/rotational deflections and the coupling between them. The spring stiffness parameters are evaluated using FEA-modeling to ensure higher accuracy. In addition, it employs a new solution strategy of the kinetostatic equations, which allows computing the stiffness matrix for the over-constrained architectures, including the singular manipulator postures. This approach gives almost the same accuracy as FEA but with essentially lower computational effort because it eliminates the model re-meshing through the workspace (Pashkevich *et al.*, 2009b).

This model states that the deformations $\delta\mathbf{t}_i$ of the extremity of the i^{th} leg of the manipu-

lator are related to the efforts $\mathbf{f}_i$ applied on its extremity by the relation:

$$\begin{bmatrix} \mathbf{S}_\theta^i & \mathbf{J}_q^i \\ \mathbf{J}_q^i & \mathbf{0} \end{bmatrix} \begin{bmatrix} \mathbf{f}_i \\ \delta\mathbf{q}_i \end{bmatrix} = \begin{bmatrix} \mathbf{t}_i \\ \mathbf{0} \end{bmatrix}, \qquad \mathbf{S}_\theta^i = \mathbf{J}_\theta^i \left(\mathbf{K}_\theta^i\right)^{-1} \mathbf{J}_\theta^{iT} \tag{2.5}$$

where the sub-matrix $\mathbf{S}_\theta^i$ describes the spring compliance relative to the end-effector, $\delta\mathbf{q}_i$ represents the passive joints displacements of the i^{th} leg, $\mathbf{K}_\theta^i$ is the stiffness matrix corresponding to the stiffness of all the elements of the i^{th} leg and $\mathbf{J}_\theta^i$, $\mathbf{J}_q^i$ are the Jacobian matrices relating the displacements of the extremity of the leg i to the spring deflections $\delta\boldsymbol{\theta}_i$ and passive joint displacements $\delta\mathbf{q}_i$, such as,

$$\delta\mathbf{t}_i = \mathbf{J}_q^i \delta\mathbf{q}_i, \qquad \mathbf{J}_q^i = \left[\frac{\partial\mathbf{t}_i}{\partial\mathbf{q}_i}\right], \qquad \mathbf{J}_\theta^i = \left[\frac{\partial\mathbf{t}_i}{\partial\boldsymbol{\theta}_i}\right] \tag{2.6}$$

Matrices $\mathbf{K}_\theta^i$, $\mathbf{J}_q^i$ and $\mathbf{J}_\theta^i$ can be obtained with the help of modified virtual joint method (VJM), based on the lump modeling approach. According to this approach, each kinematic leg can be decomposed into a sequence of rigid links and virtual springs. Virtual springs describe elastic deformations of the links or joints and take into account the stiffness of the mechanical transmissions and the control loop.
Finally, the stiffness matrix, $\mathbf{K}_i$, of the i^{th} leg, relates the deformations $\mathbf{t}_i$ to the force $\mathbf{f}_i$ as

$$\mathbf{f}_i = \mathbf{K}_i \mathbf{t}_i \tag{2.7}$$

The stiffness matrix of the entire manipulator of n kinematic chains can be found by simple addition:

$$\mathbf{K} = \sum_{i=1}^{n} \mathbf{K}_i \tag{2.8}$$

2.2.7 First Natural Frequency

Natural frequencies of a mechanism are an important measure of system performance with respect to mechanism vibratory behaviour which directly influences the mechanism accuracy and precision. In fact, the analysis of the natural frequencies depicts the system dynamic characteristics which cannot be detected by the kinematic analysis, like dynamic singularities, where the system dynamic performance degenerates (Krefft and Hesselbach, 2005). Since natural frequencies are directly related to the resonance phenomenon, so in order to avoid any resonance, natural frequencies of a system are desired to be as large as possible. Accordingly, the first natural frequency of any system is crucial. Hence, one of the design objective can be the maximization of the first natural frequency of the mechanism. Natural frequencies of a PKM can be determined by solving the eigenvalue problem of

the equation of motion of the mechanism, as:

$$\left|\mathbf{K} - \boldsymbol{\omega}^2\mathbf{M}\right| = 0 \tag{2.9}$$

$\mathbf{K}$ and $\mathbf{M}$ being, respectively, the stiffness and the mass matrix of the mechanism. $\boldsymbol{\omega}$ (rad/sec) is the vector of the natural angular frequencies of the mechanism and $|\ .\ |$ denotes the matrix determinant. Assuming that ω_1 is the first natural angular frequency:

$$\omega_1 = \min\left(\boldsymbol{\omega}\right) \tag{2.10}$$

The first linear natural frequency f_{n1} can be defined as:

$$f_{n1} = \omega_1/2\pi \tag{2.11}$$

In general, it is considered that the first natural frequency has to be out of the range of normal use of the machine, and especially for machine tools, greater than 100 Hz (Briot *et al.*, 2009). The first natural frequency depends on the pose of the tool. This criterion is mainly a local index, however, in (Briot *et al.*, 2009), the smallest first natural frequency throughout the workspace of the mechanism is considered as a global index.

2.2.8 Summary of Performance Measures and Indices

Many performance measures and indices exist to characterize a PKM. In the context of design optimization, we can use these indices either as objective functions or constraints. Generally, a global performance index is used as an objective function whereas a local performance measure is used as a constraint, see Table 2.1. In the scope of this study, we

Table 2.1 – *Summary of performance indices/measures*

Performance Index	Used as a Constraint	Used as an Objective
Workspace size		✓
Condition number	✓	
Global condition number		✓
Stiffness	✓	
Natural frequency	✓	
Accuracy	✓	
Sensitivity	✓	
Mechanism mass/inertia		✓

will choose a set of indices to realize the multiobjective design optimization of a mechanism as an illustrative example.

■

2.3 Case Study: Multiobjective Design Optimization of a 3-$\underline{P}RR$ Planar Parallel Manipulator

Planar parallel manipulators (PPMs) are distinguished by the feature that all their components and corresponding motions, including end-effector, generate planar motions. These mechanisms are simple with their simple kinematics and control-loop. Their obvious demerit is their unsuitability to carry out a large payload whose the weight is normal to the plane of motion.

A family of three degrees of freedom planar parallel mechanisms, which has been the research topic of many researchers (Gosselin *et al.*, 1996; Williams II and Joshi, 1999; Kang *et al.*, 2001; Jiang and Gosselin, 2008; Briot *et al.*, 2008) is classified as RRR, RPR, PRR, PPP etc, where R and P stands for revolute and prismatic joints, respectively. Out of this set of mechanism, the subject of this work is the type, PRR. However, a similar approach can also be applied to other mechanisms.

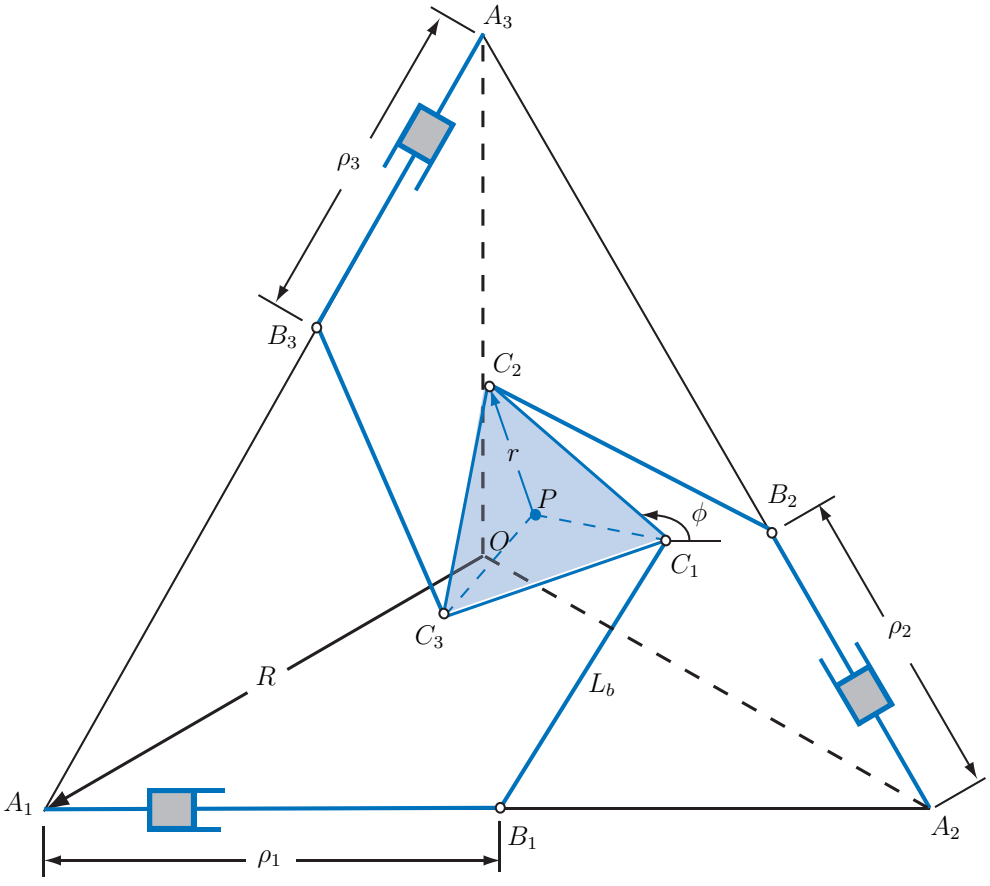

Figure 2.2 – *3–$\underline{P}RR$ architecture*

2.3.1 Architecture of 3-$\underline{P}RR$ PPMs

A three-degree-of freedom PPM with three identical chains is shown in Fig. 2.2. Each kinematic chain is of $\underline{P}RR$–type and consists of one actuated prismatic joint, $\underline{P}$; two revolute joints, R; and two links. This 3-$\underline{P}RR$ manipulator is intended to position and orient the equilateral triangle-shaped platform $C_1C_2C_3$ in the plane i.e., two translational and one rotational dof. The geometric center of the platform $C_1C_2C_3$, denoted by P, is the operation point of the manipulator. Displacements of the three prismatic joints (ρ_1,ρ_2,ρ_3) are the input variables whereas the position (x_p,y_p) of point P and the orientation (ϕ) of the platform are the output variables. The base-platform of the manipulator is also an equilateral triangle with A_1, A_2 and A_3 as triangle summits and point O as the geometric center of the base-triangle, which is also the origin of the reference frame. Prismatic actuators are located at points A_i (i = 1,2,3) with orientation angles α_i of 0°,120° and 240° i.e., aligned with the sides of the base-platform.

Parameters describing the manipulator geometry are:

- R: radius of the circumscribed circle of triangle $A_1A_2A_3$ with center O ($R = OA_i$);
- r: radius of the circumscribed circle of triangle $C_1C_2C_3$ with center P ($r = PC_i$);
- L_b: length of the intermediate bars ($L_b = B_iC_i$).

2.3.2 Kinematic Modeling of 3-$\underline{P}RR$

Knowing the geometric parameters of the mechanism (R, r, L_b), the inverse kinematic model (IKM) provides the relation between the actuators displacements (ρ_i) for a specified position (x_p, y_p) and the orientation (ϕ) of the moving platform, i.e.,

$$\boldsymbol{\rho} = f(\mathbf{x}_p) \tag{2.12}$$

where

$$\boldsymbol{\rho} = \begin{bmatrix} \rho_1 & \rho_2 & \rho_3 \end{bmatrix}^T \qquad \mathbf{x}_p = \begin{bmatrix} x_p & y_p & \phi \end{bmatrix}^T \tag{2.13}$$

A quadratic equation can be developed with the known geometry to describe Eq. 2.12 as given by (Chablat *et al.*, 2002), i.e.,

$$a_i\rho_i^2 + b_i\rho_i + c_i = 0 \tag{2.14}$$

where a_i, b_i and c_i are given by:

$$a_1 = 4 \tag{2.15a}$$

$$b_1 = -\left(4x_p - 4r\cos\phi + 2R\sqrt{3}\right) \tag{2.15b}$$

$$c_1 = \left(2x_p - 2r\cos\phi + R\sqrt{3}\right)^2 + \left(2y_p - 2r\sin\phi + R\right)^2 \tag{2.15c}$$

$$a_2 = 4 \tag{2.15d}$$

$$b_2 = 2x_p + r\left(\cos\phi - \sqrt{3}\sin\phi\right) - R\sqrt{3} + \sqrt{3}\left(2y_p - r\left(\sqrt{3}\cos\phi - \sin\phi\right) + R\right) \tag{2.15e}$$

$$c_2 = \left(2x_p + r\left(\cos\phi + \sqrt{3}\sin\phi\right) - R\sqrt{3}\right)^2 + \left(2y_p - r\left(\sqrt{3}\cos\phi - \sin\phi\right) + R\right)^2 - 4L_b^2 \tag{2.15f}$$

$$a_3 = 4 \tag{2.15g}$$

$$b_3 = \left(2x_p + r\left(\cos\phi - \sqrt{3}\sin\phi\right)\right) + \sqrt{3}\left(2y_p + r\left(\sqrt{3}\cos\phi + \sin\phi\right) - 2R\right) \tag{2.15h}$$

$$c_3 = \left(2x_p + r\left(\cos\phi - \sqrt{3}\sin\phi\right)\right)^2 + \left(2y_p + r\left(\sqrt{3}\cos\phi + \sin\phi\right) - 2R\right)^2 - 4L_b^2 \tag{2.15i}$$

It should be noted that Eq. 2.14 has eight solutions (for $i = 1, 2, 3$) corresponding to the eight working modes of the mechanism (Chablat and Wenger, 1998). The choice of the working mode can also be used as a design parameter of the mechanism as the location of the singular configuration depends on the chosen working mode, as shown in (Chablat *et al.*, 2002).

Similarly, direct kinematic model (DKM) defines the position and orientation (x_p, y_p, ϕ) of the platform as a function of the actuators displacements, ρ_i, i.e.,

$$\mathbf{x}_p = f(\boldsymbol{\rho}) \tag{2.16}$$

DKM of the 3–$\underline{P}RR$ PPM can be obtained by means of the mechanism geometry which gives six assembly modes (Gosselin and Merlet, 1994).

2.3.3 Kinematic Jacobian Matrix of 3-$\underline{P}RR$ PPM

The kinematic Jacobian matrix defines the relationship between the actuators and mobile platform velocity vectors. Let $\mathbf{p} = [x_p \quad y_p]^T$ be the position vector of the center point of the mobile platform P. For the i^{th} kinematic chain, a close loop vector equation can be

written as,

$$\overrightarrow{OP} = \overrightarrow{OA_i} + \overrightarrow{A_iB_i} + \overrightarrow{B_iC_i} + \overrightarrow{C_iP} \tag{2.17}$$

Equation (2.17) can be expressed algebraically as:

$$\mathbf{p} = R\mathbf{r}_{ai} + \rho_i\mathbf{a}_i + L_b\mathbf{b}_i - r\mathbf{e}_i \tag{2.18}$$

where $\mathbf{a}_i$, $\mathbf{b}_i$, $\mathbf{e}_i$ and $\mathbf{r}_{ai}$ are the unit vectors, as depicted in Fig. 2.3. $\mathbf{a}_i$ and $\mathbf{r}_{ai}$ are constant unit vectors whereas $\mathbf{e}_i$ is a function of platform orientation ϕ. Their relations are given in Annex **??**. $\mathbf{b}_i$ can be obtained from Eq. 2.18 as,

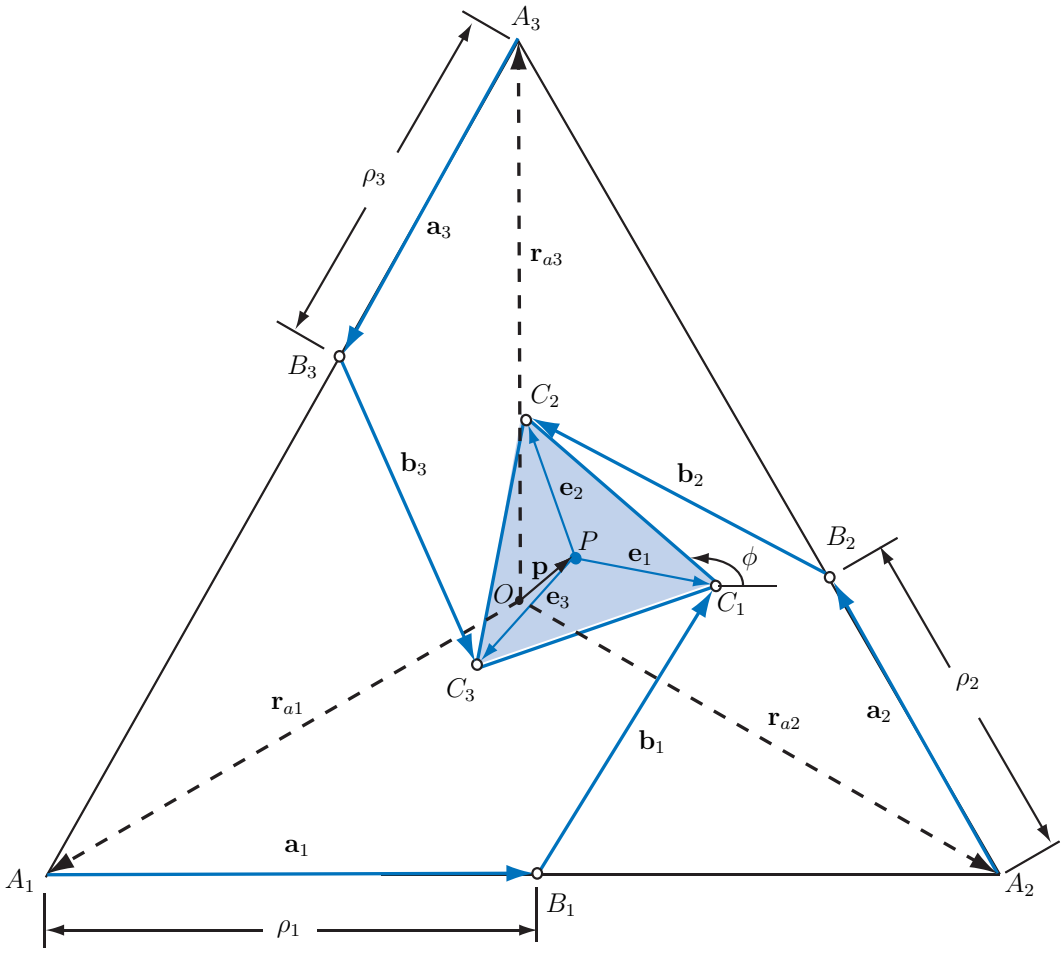

Figure 2.3 – *3–PRR planar parallel manipulator*

$$\mathbf{b}_i = \frac{1}{L_b}\left(\mathbf{p} - R\mathbf{r}_{ai} - \rho_i\mathbf{a}_i + r\mathbf{e}_i\right) \tag{2.19}$$

Upon differentiation of Eq. 2.18 with respect to time we get,

$$\dot{\mathbf{p}} = \dot{\rho}_i\mathbf{a}_i + L_b\dot{\mathbf{b}}_i - r\dot{\mathbf{e}}_i \tag{2.20}$$

■

$\dot{\mathbf{b}}_i$ and $\dot{\mathbf{e}}_i$ can be written as,

$$\dot{\mathbf{b}}_i = \dot{\beta}_i \mathbf{E}\mathbf{b}_i \qquad \dot{\mathbf{e}}_i = \dot{\phi}\mathbf{E}\mathbf{e}_i \tag{2.21}$$

$\dot{\beta}_i$ is the angular velocity of the i^{th} intermediate link and $\mathbf{E}$ is the right angle rotation matrix given by,

$$\mathbf{E} = \begin{bmatrix} 0 & -1 \\ 1 & 0 \end{bmatrix} \tag{2.22}$$

Accordingly, Eq. (2.20) becomes,

$$\dot{\mathbf{p}} = \dot{\rho}_i \mathbf{a}_i + L_b \dot{\beta}_i \mathbf{E}\mathbf{b}_i - r\dot{\phi}\mathbf{E}\mathbf{e}_i \tag{2.23}$$

Upon multiplication of Eq. (2.25) by $\mathbf{b}_i^T$ and using the identity $\mathbf{b}_i^T \mathbf{E}\mathbf{b}_i = 0$, we get:

$$\mathbf{b}_i^T \dot{\mathbf{p}} = \mathbf{b}_i^T \dot{\rho}_i \mathbf{a}_i - r\dot{\phi}\mathbf{b}_i^T \mathbf{E}\mathbf{e}_i \tag{2.24}$$

Rearranging above equation,

$$\mathbf{b}_i^T \dot{\mathbf{p}} + r\mathbf{b}_i^T \mathbf{E}\mathbf{e}_i \dot{\phi} = \mathbf{b}_i^T \mathbf{a}_i \dot{\rho}_i \tag{2.25}$$

$$\begin{bmatrix} \mathbf{b}_1^T & r\mathbf{b}_1^T \mathbf{E}\mathbf{e}_1 \\ \mathbf{b}_2^T & r\mathbf{b}_2^T \mathbf{E}\mathbf{e}_2 \\ \mathbf{b}_3^T & r\mathbf{b}_3^T \mathbf{E}\mathbf{e}_3 \end{bmatrix} \begin{bmatrix} \dot{\mathbf{p}} \\ \dot{\phi} \end{bmatrix} = \begin{bmatrix} \mathbf{b}_1^T \mathbf{a}_1 & 0 & 0 \\ 0 & \mathbf{b}_2^T \mathbf{a}_2 & 0 \\ 0 & 0 & \mathbf{b}_3^T \mathbf{a}_3 \end{bmatrix} \begin{bmatrix} \dot{\rho}_1 \\ \dot{\rho}_2 \\ \dot{\rho}_3 \end{bmatrix} \tag{2.26}$$

$$\mathbf{A}\dot{\mathbf{x}}_p = \mathbf{B}\dot{\boldsymbol{\rho}} \tag{2.27}$$

where

$$\mathbf{A} = \begin{bmatrix} \mathbf{b}_1^T & r\mathbf{b}_1^T \mathbf{E}\mathbf{e}_1 \\ \mathbf{b}_2^T & r\mathbf{b}_2^T \mathbf{E}\mathbf{e}_2 \\ \mathbf{b}_3^T & r\mathbf{b}_3^T \mathbf{E}\mathbf{e}_3 \end{bmatrix} \qquad \mathbf{B} = \begin{bmatrix} \mathbf{b}_1^T \mathbf{a}_1 & 0 & 0 \\ 0 & \mathbf{b}_2^T \mathbf{a}_2 & 0 \\ 0 & 0 & \mathbf{b}_3^T \mathbf{a}_3 \end{bmatrix} \tag{2.28}$$

Therefore, the prismatic joints rates are expressed in terms of the moving platform twist as follows:

$$\dot{\boldsymbol{\rho}} = \mathbf{B}^{-1}\mathbf{A}\dot{\mathbf{x}}_p = \mathbf{J}_p \dot{\mathbf{x}}_p \tag{2.29}$$

$\mathbf{J}_p$ is the kinematic Jacobian matrix of the manipulator.

$$\mathbf{J} = \mathbf{B}^{-1}\mathbf{A} = \frac{1}{\mathbf{a}_i.\mathbf{b}_i}\begin{bmatrix} \mathbf{b}_1 & r\mathbf{k}\,(\mathbf{b}_1 \times \mathbf{e}_1) \\ \mathbf{b}_2 & r\mathbf{k}\,(\mathbf{b}_2 \times \mathbf{e}_2) \\ \mathbf{b}_3 & r\mathbf{k}\,(\mathbf{b}_3 \times \mathbf{e}_3) \end{bmatrix} \tag{2.30}$$

The singular configurations of the 3–$\underline{P}RR$ PPM can be obtained by means of a singularity analysis of $\mathbf{J}$ as explained in Chablat *et al.* (2002).

2.3.4 Dexterity of the 3-$\underline{P}RR$ PPM

The terms of the direct Jacobian matrix of the 3-PRR PPM are not homogeneous as they do not have same units. Accordingly, its condition number is meaningless. Indeed, its singular values cannot be arranged in order as they are of different nature. However, the concept of *characteristic length* was used as used in Chablat *et al.* (2002) to analyze the kinetostatic performance of manipulators with multiple inverse kinematic solutions, and therefore to select their best *working mode*.
Accordingly, for 3–$\underline{P}RR$ PPM, the normalized Jacobian matrix, $\tilde{J}_p$ is given by:

$$\tilde{J}_p = \frac{1}{\mathbf{a}_i.\mathbf{b}_i}\begin{bmatrix} \mathbf{b}_1 & r\mathbf{k}\,(\mathbf{e}_1 \times \mathbf{b}_1)\,/l_{ch} \\ \mathbf{b}_2 & r\mathbf{k}\,(\mathbf{e}_2 \times \mathbf{b}_2)\,/l_{ch} \\ \mathbf{b}_3 & r\mathbf{k}\,(\mathbf{e}_3 \times \mathbf{b}_3)\,/l_{ch} \end{bmatrix} \tag{2.31}$$

$l_{ch} = \sqrt{2}r\sin\gamma$ being the characteristic length of the manipulator (Chablat *et al.*, 2002), used to obtain dimensionally homogeneous Jacobian matrix. r is the moving platform radius and $\gamma = \pi/2$.
When γ is equal to $\pi/2$, *i.e.*, when B_iC_i is perpendicular to C_iP, the manipulator finds itself at a configuration furthest away from the parallel singularities.
Consequently, the condition number of $\mathbf{J}_p$, can be used as a dexterity index of the manipulator.

2.3.5 Stiffness Matrix

The stiffness model of the 3-$\underline{P}RR$ PPM is obtained by means of the refined lumped mass modeling presented in Pashkevich *et al.* (2009b), as discussed in Sec. 2.2.6.
Let us consider a general schematic of the 3-$\underline{P}RR$ PPM that is composed of a mobile platform connected to a fixed base by means of three identical kinematics chains, as shown in Fig. 2.4. Each kinematic chain contains an actuated prismatic joint "$\underline{P}$" and two passive revolute joints "R".
According to the flexible model described in Pashkevich *et al.* (2009b), each kinematic chain of the 3-$\underline{P}RR$ manipulator can be considered as a serial architecture as shown in

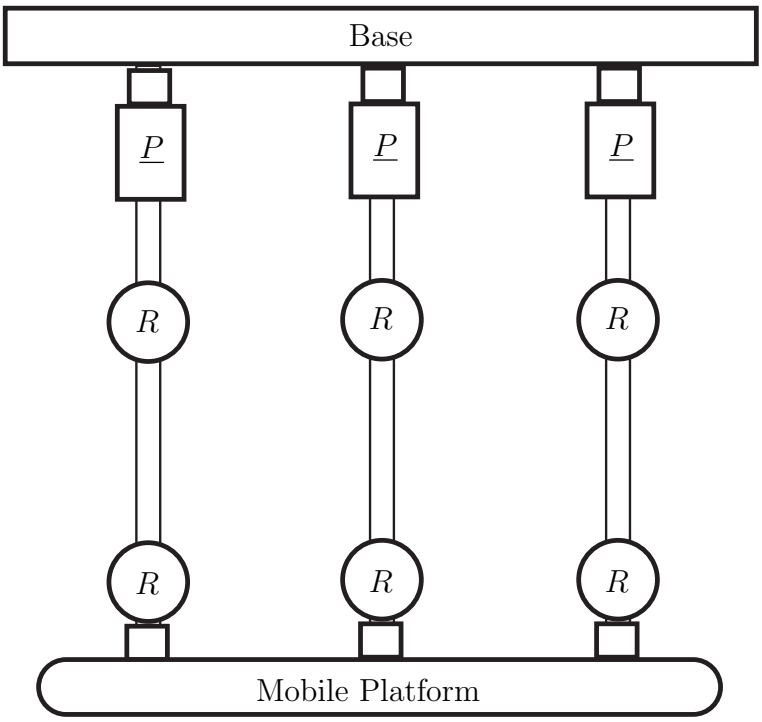

Figure 2.4 – *Schematic diagram of a 3-PRR*

Fig. 2.5 that contains sequentially:

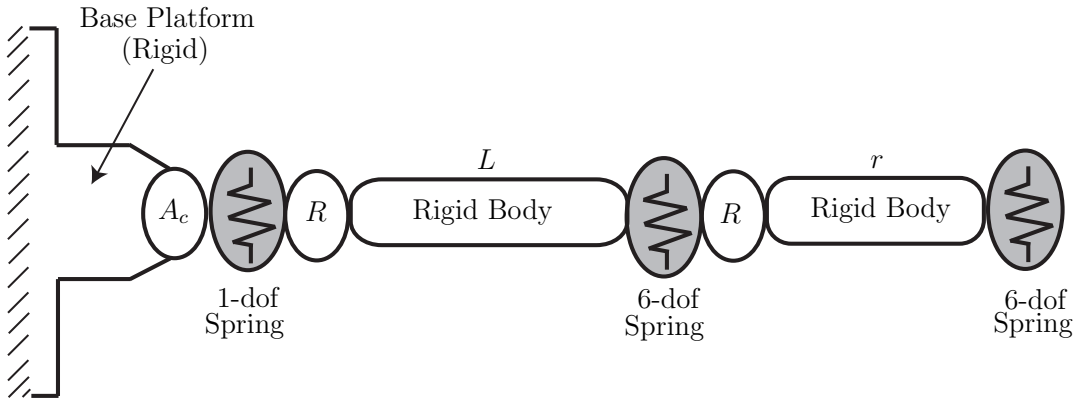

Figure 2.5 – *Flexible model of the single kinematic chains of the 3-PRR PPM, A_c stands for actuating joint and R for revolute joint*

- a rigid link between the manipulator base and the i^{th} actuated joint (part of the base platform) described by the constant homogeneous transformation matrix $\mathbf{T}^i_{Base}$;
- a 1-dof actuated joint, defined by the homogeneous matrix function $\mathbf{V}_a(q^i_0)$ where q^i_0 is the actuated coordinate;
- a 1-dof virtual spring describing the actuator mechanical stiffness, which is defined by the homogeneous matrix function $\mathbf{V}_{s1}(\theta^i_0)$ where θ^i_0 is the virtual spring coordinate corresponding to the translational spring;

- a 1-dof passive R-joint at the beginning of the leg allowing one rotation angle q_2^i , which is described by the homogeneous matrix function $\mathbf{V}_{r1}(q_2^i)$
- a rigid leg of length L linking the foot and the movable platform, which is described by the constant homogeneous transformation matrix $\mathbf{T}_L^i$;
- a 6-dof virtual spring describing the leg stiffness, which is defined by the homogeneous matrix function $\mathbf{V}_{s2}\left(\theta_1^i \cdots \theta_6^i\right)$, with θ_1^i, θ_2^i, θ_3^i and θ_4^i, θ_5^i, θ_6^i being the virtual spring coordinates corresponding to the spring translational and rotational deflections;
- a 1-dof passive R-joint between the leg and the platform, allowing one rotation angle q_3^i, which is described by the homogeneous matrix function $\mathbf{V}_{r2}(q_3^i)$;
- a rigid link of length r from the manipulator leg to the geometric center of the mobile platform, which is described by the constant homogeneous transformation matrix $\mathbf{T}_r^i$;
- a 6-dof virtual spring describing the stiffness of the moving platform, which is defined by the homogeneous matrix function $\mathbf{V}_{s3}\left(\theta_7^i \cdots \theta_{12}^i\right)$, θ_7^i, θ_8^i, θ_9^i and θ_{10}^i, θ_{11}^i, θ_{12}^i being the virtual spring coordinates corresponding to translational and rotational deflections of link C_iP;
- a homogeneous transformation matrix $\mathbf{T}_{End}^i$ characterizes the rotation from the 6-dof spring associated with link C_iP and the manipulator base frame;

The corresponding mathematical expression defining the end-effector location subject to variations in all above defined coordinates of the i^{th} kinematic chain can be written as follows:

$$\mathbf{T}^i = \mathbf{T}_{Base}^i \mathbf{V}_a^i \left(q_0^i\right) \mathbf{V}_{s1}\left(\theta_0^i\right) \mathbf{V}_{r1}\left(q_1^i\right) \mathbf{T}_L^i \mathbf{V}_{s2}\left(\theta_1^i \cdots \theta_6^i\right) \mathbf{V}_{r2}(q_2^i) \mathbf{T}_r^i \mathbf{V}_{s3}\left(\theta_7^i \cdots \theta_{12}^i\right) \mathbf{T}_{Base}^i \tag{2.32}$$

From Pashkevich *et al.* (2009b), the kinetostatic model of the i^{th} leg of the 3-$\underline{P}RR$ PPM can be reduced to a system of two matrix equations, namely,

$$\begin{bmatrix} \mathbf{S}_\theta^i & \mathbf{J}_q^i \\ \mathbf{J}_q^i & \mathbf{0}_{2\times 2} \end{bmatrix} \begin{bmatrix} \mathbf{f}_i \\ \delta \mathbf{q}_i \end{bmatrix} = \begin{bmatrix} \delta \mathbf{t}_i \\ \mathbf{0}_2 \end{bmatrix} \tag{2.33}$$

where the sub-matrix $\mathbf{S}_\theta^i = \mathbf{J}_\theta^i {\mathbf{K}_\theta^i}^{-1} {\mathbf{J}_\theta^i}^T$ describes the spring compliance relative to the geometric center of the moving platform. $\mathbf{J}_\theta^i$ of size 6×13 is the Jacobian matrix related to the virtual springs whereas sub-matrix $\mathbf{J}_q^i$ of size 6×2 takes into account the passive joint influence on the moving platform motions.

${\mathbf{K}_\theta^i}^{-1}$ matrix, of size 13×13, describes the compliance of the virtual springs and takes the

form:

$$\mathbf{K}_{\theta}^{i\,-1} = \begin{bmatrix} \mathbf{K}_{act}^{i\,-1} & \mathbf{0}_{1\times 6} & \mathbf{0}_{1\times 6} \\ \mathbf{0}_{6\times 1} & \mathbf{K}_{leg}^{i\,-1} & \mathbf{0}_{6\times 6} \\ \mathbf{0}_{6\times 1} & \mathbf{0}_{6\times 6} & \mathbf{K}_{pf}^{i\,-1} \end{bmatrix} \tag{2.34}$$

where,

- $\mathbf{K}_{act}^{i}$: 1×1 stiffness matrix of the i^{th} actuator;
- $\mathbf{K}_{leg}^{i}$: 6×6 stiffness matrix of the i^{th} intermediate leg;
- $\mathbf{K}_{pf}^{i}$: 6×6 stiffness matrix of the i^{th} platform.

The compliance matrices of the intermediate legs and the i^{th} link of the moving platform are calculated by means of the stiffness model of a cantilever beam, namely,

$$\mathbf{K}_{i}^{-1} = \begin{bmatrix} \frac{L}{EA} & 0 & 0 & 0 & 0 & 0 \\ 0 & \frac{L^3}{3EI_z} & 0 & 0 & 0 & \frac{L^2}{2EI_z} \\ 0 & 0 & \frac{L^3}{3EI_y} & 0 & -\frac{L^2}{2EI_y} & 0 \\ 0 & 0 & 0 & \frac{L}{GI_x} & 0 & 0 \\ 0 & 0 & -\frac{L^2}{2EI_y} & 0 & \frac{L}{EI_y} & 0 \\ 0 & \frac{L^2}{2EI_z} & 0 & 0 & 0 & \frac{L}{EI_z} \end{bmatrix} \tag{2.35}$$

where,

- L: length of the beam ($L = L_b$ for intermediate legs and $L = r$ for the platform links);
- A: cross-sectional area of the beam ($A_{L_b} = \pi r_j^2$, $A_r = \pi r_p^2$);
- $I_z = I_y$: polar moment of inertia about y and z axis, (for intermediate legs and the moving platform links, their expressions are $\pi r_j^4/4$ and $\pi r_p^4/4$, respectively;
- $I_x = I_z + I_y$: polar moment of inertia about x-axis or longitudinal axis of the beam;
- E: modulus of elasticity of the material;
- G: modulus of rigidity of the material, ($G = E/\left(2 - 2\nu\right)$, ν being the Poisson ratio).

If $\mathbf{f}_i$ is the wrench exerted on the i^{th} leg of the 3-$\underline{P}RR$ PPM at the geometric center of the moving platform and $\delta\mathbf{t}_i$ is the corresponding translational and rotational displacements vector then the motion-to-force mapping is obtained from Eq. 2.33 by using Cartesian stiffness matrix $\mathbf{K}_i$ of the i^{th} leg,

$$\mathbf{f}_i = \mathbf{K}_i\,\delta\mathbf{t}_i \tag{2.36}$$

■

Finally, the Cartesian stiffness matrix $\mathbf{K}$ of the 3-$\underline{P}RR$ PPM is found with a simple addition of $\mathbf{K}_i$ matrices, namely,

$$\mathbf{K} = \sum_{i=1}^{3} \mathbf{K}_i \tag{2.37}$$

2.4 Multiobjective Optimization of PKMs-Problem Formulation

In general, PKMs design process simultaneously deals with two groups of criteria, one related to the kinematic properties while the other relates to the kinetostatic/dynamic properties of the mechanism. Both of these groups include a number of performance measures that essentially vary throughout the workspace but remain within the prescribed bounds. Kinematic aspects are comparatively less complex and are usually based on the concept of critical points whereas kinetostatic aspects work with detailed description of the structure and often requires extensive computing efforts. One of the major design issues of kinetostatic design is the computation of the stiffness matrix (Pashkevich *et al.*, 2009a). Keeping in view these complexities and the fact that the kinematic and kinetostatic properties are usually mutually inclusive, a multiobjective optimization approach is proposed, with simultaneous consideration of performance measures/criteria from both kinematic and kinetostatic domain. The proposed approach, on the one hand, deals with the geometric/kinematic design in order to determine the PKM geometry including the link lengths and the joint limits and on the other hand, it considers the kinetostatic design to determine the size and the mass properties of the links.

Multiobjective optimization is formulated to determine the optimum geometric parameters of a PKM in order to maximize its workspace as well as to minimize the mass of the mechanism in motion. The proposed approach operates with the workspace discretization and the considered performance measures and constrains are evaluated/verified for each of the workspace grid point.

2.4.1 Optimization objectives

The mass in motion of the mechanism is considered to be the first objective of the optimization problem. Mass and inertia are functions of PKM dimensions, i.e., the link lengths, cross-sectional area, thickness. Hence, in general, the total mass of a PKM, m_t, is composed of the mass of the moving platform, m_{pf}, the mass of the n_b intermediate links/joints, m_b, and the moving mass of the n_s actuators/sliders, m_s, i.e.,

$$m_t = m_{pf} + n_b m_b + n_s m_s \tag{2.38}$$

Since the actuators are fixed, their mass is considered to be constant while the mass of the other two components can easily be calculated by using the geometry of the components and the density d of their material.Consequently, the first objective of the optimization problem can be written as:

$$f_1(\mathbf{x}) = m_t \rightarrow \min \tag{2.39}$$

$\mathbf{x}$ being the vector of geometric design parameters of the PKM. Maximization of the regular dextrous workspace is another important aspect of a manipulator design as it defines the size of the operational space. The quality of the workspace that reflects the shape, size, presence of singularities is of prime importance in PKM designs. Workspace based design optimization of PKMs can usually be solved with two different formulations. The first formulation aims to design a manipulator whose workspace contains a prescribed workspace and the second approach aims to design a manipulator, of which the workspace is as large as possible. However, maximizing the workspace may result to poor design with regard to the manipulator dexterity and manipulability (Stamper *et al.*, 1997). This problem can be solved by properly defining the constraints of the optimization problem. Here, multiobjective optimization problem of PKMs is based on the formulation of workspace maximization, i.e, to determine the optimum geometry of PKM in order to maximize a regular-shaped workspace. Workspace size can be defined by its geometric shape parameters like the radius of a circular/spherical workspace or the sides of the cube for a cubic workspace. If W_c represents the size of the PKM workspace then the design objective will be:

$$f_2(\mathbf{x}) = W_c \rightarrow \max \tag{2.40}$$

Other performance measures like the first natural frequency of the manipulator and the actuators forces can be used either as design objectives or constraints (see Table 2.1).

2.4.2 Optimization Constraints

Besides, the geometric and actuators constraints of the PKM, conditioning of the kinematic Jacobian matrix and accuracy obtained from the stiffness characteristics of the mechanism are considered. Constraining the conditioning of the Jacobian matrix guarantees singularity free workspace whereas limits on accuracy consideration ensure sufficient mechanism stiffness.

Throughout the workspace, with all possible orientation of the end-effector, the minimum of the inverse condition number of the kinematic Jacobian matrix is considered to be

higher than a minimum allowable value, κ_{min}^{-1}, i.e.,

$$\kappa^{-1}(\mathbf{J}) \geqslant \kappa_{min}^{-1} \tag{2.41}$$

The position and orientation accuracy is assessed by using the stiffness parameters of the mechanism. Let $(\delta x, \delta y, \delta z)$ and $(\delta\phi_x, \delta\phi_y, \delta\phi_z)$ be the position and orientation errors of the end-effector subjected to external forces (F_x, F_y, F_z) and torques (τ_z, τ_y, τ_z). Then the constraints will be:

$$\begin{array}{lll} \delta x \leqslant \delta x^{max} & \delta y \leqslant \delta y^{max} & \delta z \leqslant \delta z^{max} \\ \delta\phi_x \leqslant \delta\phi_x^{max} & \delta\phi_y \leqslant \delta\phi_y^{max} & \delta\phi_z \leqslant \delta\phi_z^{max} \end{array} \tag{2.42}$$

where $(\delta x^{max}, \delta y^{max}, \delta z^{max})$ and $\left(\delta\phi_x^{max}, \delta\phi_y^{max}, \delta\phi_z^{max}\right)$ are respectively the maximum allowable position and orientation errors of the end-effector. These accuracy constraints can be expressed in terms of the components of the mechanism stiffness matrix.

2.4.3 Problem Statement

Multiobjective Optimization problem for PKMs can be stated as:
Find the optimum design parameters $\mathbf{x}$ *of a PKM, in order to minimize the mass in motion of the mechanism and to maximize its regular shaped workspace subject to some design constraints, i.e., the inverse condition number of the kinematic Jacobian matrix and accuracy are higher than prescribed values, throughout the whole workspace.*
Mathematically, this problem can be written as:

$$\begin{array}{l} minimize\ f_1(\mathbf{x}) = m_t \\ maximize\ f_2(\mathbf{x}) = W_c \\ \text{over:} \quad \mathbf{x} \\ \text{subject to:} \\ \qquad \kappa^{-1}(\mathbf{J}) \geqslant \kappa_{min}^{-1} \\ \qquad \delta x \leqslant \delta x^{max} \qquad \delta y \leqslant \delta y^{max} \qquad \delta z \leqslant \delta z^{max} \\ \qquad \delta\phi_x \leqslant \delta\phi_x^{max} \qquad \delta\phi_y \leqslant \delta\phi_y^{max} \qquad \delta\phi_z \leqslant \delta\phi_z^{max} \end{array} \tag{2.43}$$

$\mathbf{x}$ being the vector of design parameters of the mechanism.

2.5 Multiobjective Optimization Problem Formulation for a 3–$\underline{P}RR$ Planar Parallel Manipulator

Multiobjective optimization is formulated to determine the optimum geometric parameters of the mechanism in order to minimize its mass in motion and maximize its regular

shaped workspace.

2.5.1 Optimization Design Parameters

Along with the above mentioned geometric parameters (R, r, L_b) of the 3-$\underline{P}RR$ PPM, the dimension of the circular-cross-section of the intermediate bars defined with radius r_j and the circular-cross-section of the platform bars defined with r_p are considered as design variables, also called decision variables. The platform is assumed to be made up of three circular bars, each of length r. Hence, the design parameters vector $\mathbf{x}$ is given by:

$$\mathbf{x} = \begin{bmatrix} R & r & L_b & r_j & r_p \end{bmatrix}^T \tag{2.44}$$

2.5.2 Optimization objectives

The multiobjective optimization problem aims to determine the optimum geometric parameters of a PKM in order to maximize its workspace as well as to minimize the mass of the mechanism in motion. Here, the workspace of the mechanism is discretized and the considered performance measures and constraints are evaluated and verified for each point.

2.5.2.1 Mass in motion of the mechanism

The mass in motion of the mechanism is considered to be the first objective function of the optimization problem. Mass and inertia are functions of manipulator dimensions, i.e., link lengths, cross-sectional area, thickness. Hence, in general, the mass in motion m_t of the mechanism is composed of the mass of the platform, m_{pf}, the mass of the three intermediate bars, m_b, and the mass in motion of the three prismatic actuators, m_s:

$$m_t = m_{pf} + 3m_b + 3m_s \tag{2.45}$$

Since the actuators are fixed, their mass is considered to be constant while the mass of the other two components can easily be calculated by using the geometry of the components and the density d of their material, given as,

$$m_{pf} = \pi r_p^2 r d, \qquad m_b = \pi r_j^2 L_b d \tag{2.46}$$

Consequently, the first objective function of the optimization problem is written as:

$$f_1(\mathbf{x}) = m_t \rightarrow \min \tag{2.47}$$

$\mathbf{x}$ being the vector of the geometric design parameters of the mechanism.

2.5.2.2 Regular workspace size

The quality of the workspace that reflects the shape, size, presence of singularities is of prime importance in PKM design. In the scope of this work, a circular workspace defined with its radius R_w is considered. Furthermore, at each point of the workspace, an angular rotation range $\Delta\phi = 20\,^\circ$ of the platform about the Z-axis can be achieved. A 3-dimensional schematic of the regular shaped workspace is shown in Fig. 2.6, where x_c, y_c are the coordinates of the center of the regular dextrous workspace and ϕ_c is the orientation of the platform at its home-posture (see Fig. 2.3).

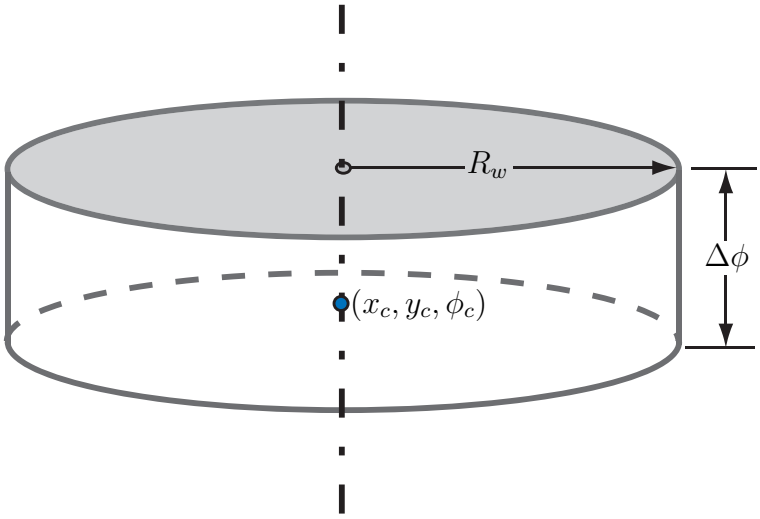

Figure 2.6 – *3-PRR workspace*

Consequently, in order to maximize the manipulator workspace, the second objective of the optimization problem can be written as:

$$f_2(\mathbf{x}) = R_w \to \max \tag{2.48}$$

2.5.3 Optimization constraints

Besides, the geometric and actuators constraints of the PKM, conditioning of the kinematic Jacobian matrix and accuracy obtained from the stiffness characteristics of the mechanism are considered. Constraining the conditioning of the Jacobian matrix guarantees singularity free workspace whereas limits on accuracy consideration ensure sufficient mechanism stiffness.

2.5.3.1 Geometric Constraints

The first constraint is related to the mechanism assembly, namely,

$$L_b + r \geqslant R/2 \tag{2.49}$$

■

In order to avoid prismatic joints intersection, the lower and upper bounds of the prismatic lengths are defined as follows:

$$0 < \rho_i < \sqrt{3}R \tag{2.50}$$

2.5.3.2 Condition number of the kinematic Jacobian matrix

For the design optimization of 3-$\underline{P}RR$ PPM, the minimum of the inverse condition number of the kinematic Jacobian matrix, $\kappa^{-1}(\mathbf{J})$, is supposed to be higher than a prescribed value, say 0.1, throughout the manipulator workspace, for any rotation of its end-effector, i.e.,

$$min\left(\kappa^{-1}(\mathbf{J})\right) \geqslant 0.1 \tag{2.51}$$

2.5.3.3 Accuracy constraints

The position and orientation accuracy is assessed by using the stiffness parameters of the mechanism. Let $(\delta x, \delta y, \delta z)$ and $(\delta\phi_x, \delta\phi_y, \delta\phi_z)$ be the position and orientation errors of the end-effector subjected to external forces (F_x, F_y, F_z) and torques (τ_z, τ_y, τ_z). The constraints related to the accuracy of the manipulator are defined as follows:

$$\begin{array}{lll} \delta x \leqslant \delta x^{max} & \delta y \leqslant \delta y^{max} & \delta z \leqslant \delta z^{max} \\ \delta\phi_x \leqslant \delta\phi_x^{max} & \delta\phi_y \leqslant \delta\phi_y^{max} & \delta\phi_z \leqslant \delta\phi_z^{max} \end{array} \tag{2.52}$$

$(\delta x^{max}, \delta y^{max}, \delta z^{max})$ being the maximum allowable position errors and $\left(\delta\phi_x^{max}, \delta\phi_y^{max}, \delta\phi_z^{max}\right)$ the maximum allowable orientation errors of the end-effector. These accuracy constraints can be expressed in terms of the components of the mechanism stiffness matrix and the wrench applied to the end-effector. Let us assume that the accuracy requirements are:

$$\sqrt{\delta x^2 + \delta y^2} \leqslant 0.0001\,\text{m} \tag{2.53a}$$
$$\delta z \leqslant 0.001\,\text{m} \tag{2.53b}$$
$$\delta\phi_z \leqslant 1\,\text{deg} \tag{2.53c}$$

If the end-effector is subjected to a wrench, whose components are $\|F_{x,y}\| = F_z = 100\,\text{N}$ and $\tau_z = 100\,\text{Nm}$, then the accuracy constraints can be expressed as:

$$k_{xy}^{min} \geqslant \|F_{x,y}\| / \sqrt{\delta x^2 + \delta y^2} = 10^6\ \text{N.m}^{-1} \tag{2.54a}$$
$$k_z^{min} \geqslant F_z/\delta z = 10^5\ \text{N.m}^{-1} \tag{2.54b}$$
$$k_{\phi_z}^{min} \geqslant \tau_z/\delta\phi_z = \frac{10}{\pi/180}\ \text{N.m.rad}^{-1} \tag{2.54c}$$

■

2.5.4 Multiobjective Optimization Problem Statement

Multiobjective optimization problem for a 3–*PRR* PPM can be stated as:
Find the optimum design parameters $\mathbf{x}$ *of a 3–PRR PPM in order to minimize the mass in motion of the mechanism and to maximize its regular shaped workspace subject to some design constraints, i.e., the inverse condition number of the kinematic Jacobian matrix and accuracy are to be higher than prescribed values throughout the manipulator workspace.*
Mathematically, the problem can be written as:

$$\begin{aligned} \text{minimize} \quad & f_1(\mathbf{x}) = m_t \\ \text{maximize} \quad & f_2(\mathbf{x}) = R_w \end{aligned} \tag{2.55}$$

$$\text{over} \quad \mathbf{x} = \begin{bmatrix} R & r & L_b & r_j & r_p \end{bmatrix}^T$$

$$\begin{aligned} \text{subject to :} \quad & g_1 : L_b + r \geqslant \frac{R}{2} \\ & g_2 : 0 < \rho_i < \sqrt{3}R \\ & g_3 : \kappa^{-1}(\mathbf{J}) \geqslant 0.1 \\ & g_4 : k_{xy}^{min} \geqslant \frac{F_{x,y}}{\sqrt{\delta x^2 + \delta y^2}} = 10^6 \\ & g_5 : k_z^{min} \geqslant \frac{F_z}{\delta z} = 10^5 \\ & g_6 : k_{\phi_z}^{min} \geqslant \frac{\tau_z}{\delta \phi_z} = \frac{10}{\pi/180} \\ & \mathbf{x}_{lb} \leqslant \mathbf{x} \leqslant \mathbf{x}_{ub} \end{aligned}$$

where $\mathbf{x}_{lb}$ and $\mathbf{x}_{ub}$ are the lower and upper bounds of $\mathbf{x}$, respectively.

2.5.5 Optimization Results

The multiobjective optimization problem formulated with Eq. (2.55) is solved by means of modeFRONTIER ESTECO (2008) and by using its built-in multiobjective optimization algorithms. MATLAB code is incorporated in order to analyze the system and to get the numerical values for the objective functions and constraints that are analyzed in modeFRONTIER for their optimality and feasibility. A screen-shot of the *modeFRONTIER* model, with five design variables, six constraints and two objective functions, is shown in Fig. 2.7. The lower and upper bounds of the design variables are given in Table 2.2. The manipulator is supposed to be built of steel with a density equal to $d = 7850\,\text{kg/m}^3$ and a Young modulus equal to $E = 210 \times 10^9\,\text{N/m}^2$.
modeFRONTIER is a platform for multi-objective design optimization that integrates

Design Variable	R	r	L_b	r_j	r_p
Lower Bound (lb) [m]	0.05	0.05	0.05	0	0
Upper Bound (ub) [m]	4	4	4	0.1	0.1

Table 2.2 – *Lower and upper bounds of the design variables*

various CAE (Computer Aided Engineering) tools. Using a variety of optimization techniques, the optimization process can be modeled by specifying objectives, constraints and design variables in a graphical user interface environment. The main *modeFRONTIER* blocks are the *External Script* and the *Scheduler* blocks. The *External Script* block is used to solve or analyze the problem by accessing external applications like *MATLAB, CATIA, NASTRAN*, etc. The *Scheduler block*, composed of *DOE* (Design Of Experiments) and *Scheduler* components, is the starting point of the logic flow and is the main governing body of the optimization process. It is used to generate and evaluate different design alternatives. The *DOE* is used to generate a data base of design configurations as the initial population for the optimization algorithms. It gives a preliminary exploration of the design space by means of a variety of *DOE*-algorithms. *Schedulers* take *DOE* data as input and use it as an initial population. These schedulers are basically optimization algorithms based on various optimization techniques, designed to handle both mono-objective and multi-objective problems. The *Logic End* blocks are used to complete the logic flow process and to identify a termination point for the process flow. Several of these blocks can be placed within a project, both to indicate successful and unsuccessful endings.
For each design iteration, workspace coordinates limits are calculated based on the set of design parameters of the mechanism. Then, workspace discretization is performed with respect to its x, y coordinates and with respect to the orientation angle ϕ of the moving platform. The constraints of the problem are evaluated at each grid point of the workspace.

Table 2.3 – modeFRONTIER *algorithm parameters*

Scheduler	MOGA-II
Number of iterations	200
Directional cross-over probability	0.5
Selection probability	0.05
Mutation probability	0.1
DNA string mutation ratio	0.05
DOE algorithm	Sobol
DOE number of designs	30
Total number of iterations	$30 \times 200 = 6000$

A multiobjective genetic algorithm (MOGA) is used to obtain the Pareto frontier based on the mechanism mass and the workspace radius. *modeFRONTIER* scheduler and Design

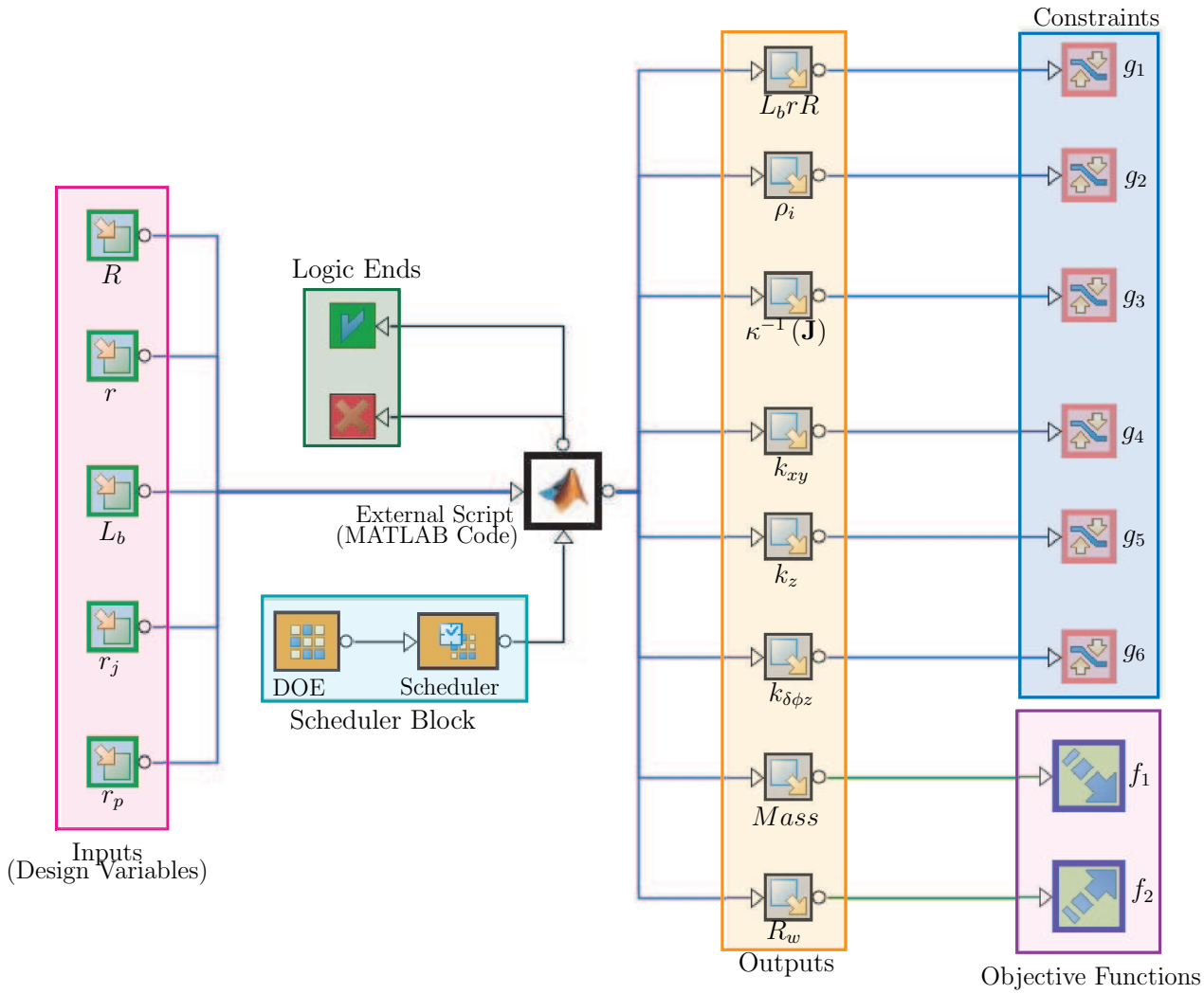

Figure 2.7 – *modeFRONTIER model for 3–PRR PPM Optimization*

Of Experiments (DOE) parameters are given in Table 2.3. MATLAB is used to process and analyze the system for any individual of the current population (generated by the *modeFRONTIER* scheduler). Corresponding to each population set, *MATLAB* returns the output variables that are analyzed by *modeFRONTIER* for the feasible solutions according to the given constraints. At the end, the Pareto-optimal solutions are obtained from the generated feasible solutions.

The Pareto frontier is shown in Fig. 2.8 whereas the design parameters and the corresponding objective functions for two extreme and one intermediate Pareto optimal solutions, as shown in Fig. 2.8, are depicted in Table 2.4.

The designs associated with the three foregoing solutions are shown in Fig. 2.10.

Figure 2.11 illustrates the variational trends as well as the inter-dependency between the objective functions and design variables by means of a scatter matrix. The lower triangular part of the matrix represents the correlation coefficients, ξ, whereas the upper one shows the corresponding scatter plots. The diagonal elements represent the probability density

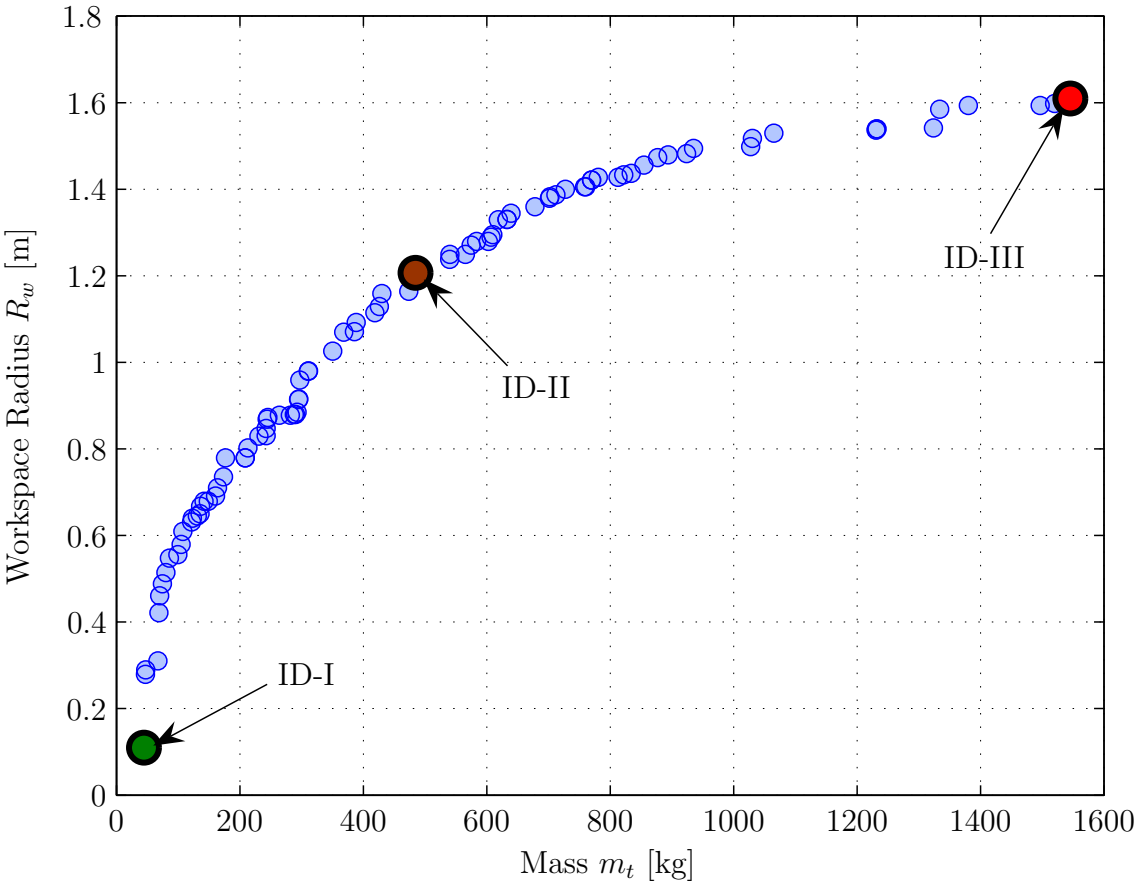

Figure 2.8 – *Pareto frontier for 3-PRR optimization problem*

charts of each variable. The correlation coefficients vary from -1 to 1. Two variables are strongly dependent when their correlation coefficient is close to 1 or -1 and independent when the latter is null.

Figure 2.11 shows that:

- Both objectives functions m_t and R_w are strongly dependent as their correlation coefficient is equal to 0.907;
- Both objectives functions m_t and R_w are strongly dependent of all design variables as all of the corresponding correlation coefficients are greater than 0.7;

Design ID	Design Variables					Objectives	
	R [m]	r [m]	L_b [m]	r_j [m]	r_p [m]	m_t [kg]	R_w [m]
I	1.412	0.319	0.620	0.026	0.023	44.5	0.110
II	3.066	1.283	1.896	0.036	0.056	484.8	1.207
III	3.872	1.947	1.977	0.039	0.096	1545.6	1.609

Table 2.4 – *Three Pareto optimal solutions*

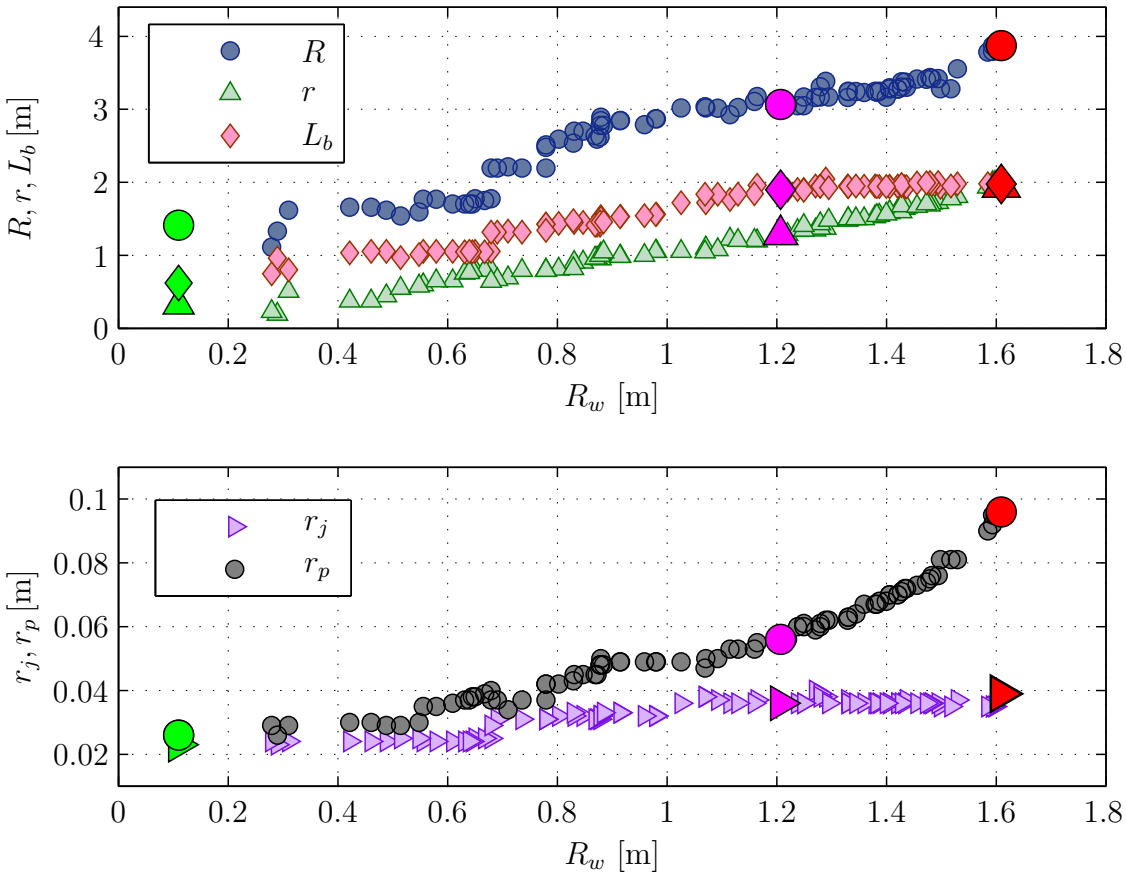

Figure 2.9 – *Design variables as a function of R_w for the Pareto-optimal solutions*

– R_w ($\xi \geqslant 0.830$) is slightly more dependent than m_t ($0.711 \leqslant \xi \leqslant 0.981$) of the design variables;

Figure 2.9 illustrates the design variables R, r, L_b, r_j and r_p as a function of R_w for the Pareto-optimal solutions. It is noteworthy that the higher R_w, the higher the design variables. It is apparent that the variations in variables R, r, L_b and r_j with respect to (w.r.t.) R_w are almost linear whereas the variations in r_p w.r.t. R_w is rather quadratic. As a matter of fact, it should be due to the fact that the higher the size of the mechanism the higher the bending of the moving platform links whereas the intermediate links are mainly subjected to tension and compression. Finally, the three sets of design variables corresponding to the Pareto-optimal solutions depicted in Fig. 2.8 are shown in Fig. 2.9 by means of the green, pink and red symbols.

2.6 Conclusion

In this chapter the problem of dimensional synthesis of parallel kinematics machines was addressed. A multiobjective design optimization problem was formulated in order to deter-

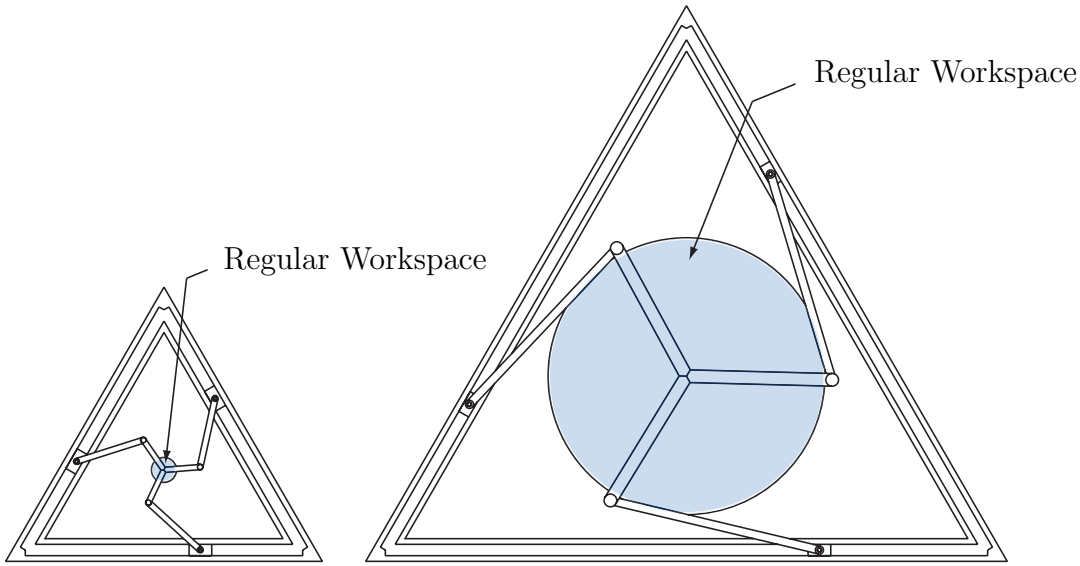

(a) ID–I

(b) ID–II

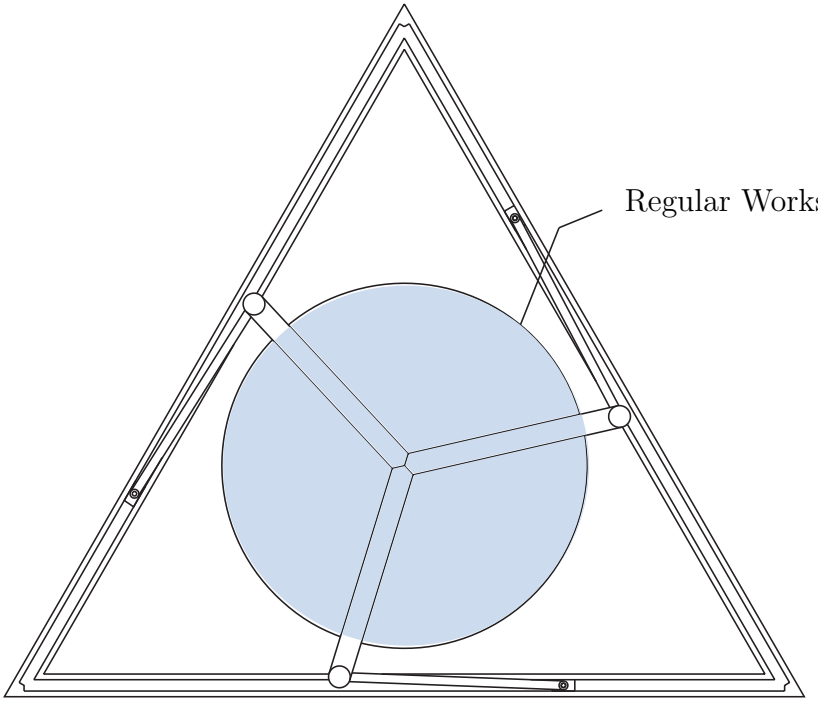

(c) ID–III

Figure 2.10 – *CAD Designs of three Pareto-optimal solutions*

mine optimum structural and geometric parameters of any parallel kinematics machine. The proposed approach is similar to that used in Altuzarra *et al.* (2009) but we took into account the mass and the regular workspace instead of considering the entire volume of the manipulator. The proposed approach was applied to the optimum design of a three-degree-of-freedom planar parallel manipulator with the aim to minimize the mass

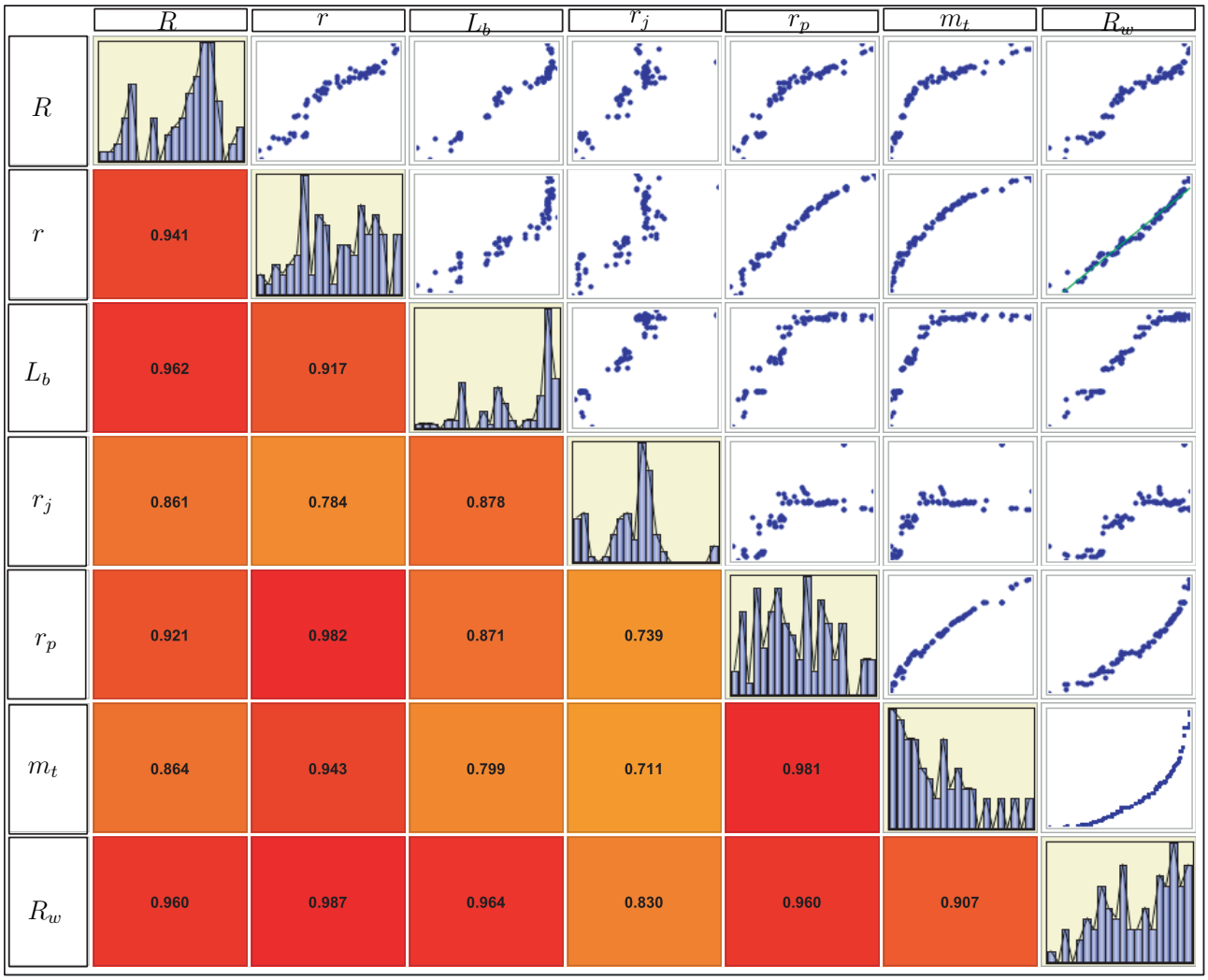

Figure 2.11 – *Scatter matrix illustrating the correlations between the objective functions and the design variables*

in motion of the mechanism and to maximize its regular shaped workspace.

It is apparent that other performance indices can be used as constraints. However, they cannot necessarily be used as objective functions as the latter are usually formulated as a sum of an index over all the manipulator workspace. As an other constraint, we could use the collisions between the legs of the manipulator as illustrated in Lou *et al.* (2008).

In this chapter, actuators are considered to be fixed and their selection has not been considered. Accordingly, the next chapter deals with the actuators selection based on the kinematic and dynamic analysis of the PKMs.

3 Kinematics, Dynamics and Motors Selection of Orthoglide 5-axis

3.1 Orthoglide 5-axis 59

3.2 Trajectory Planning 63

3.2.1 Trajectory-I: Semi-circle 64

3.2.2 Trajectory-II: Circle 65

3.3 Kinematics and Dynamics of the 2-dof Spherical Wrist 66

3.3.1 Spherical Wrist Kinematic Model 67

3.3.2 Spherical Wrist Dynamic Model 72

3.3.3 Results: Kinematic and Dynamic Analysis of Wrist 83

3.3.4 Effect of Machining Forces on Actuators Torque 88

3.3.5 Conclusions 92

3.4 Kinematics and Dynamics of the Orthoglide 3-axis 93

3.4.1 Kinematic Analysis of the Orthoglide 3-axes 93

3.4.2 Dynamics of the Orthoglide 3-axes 97

3.4.3 Motors selection for the Orthoglide 5-axis 98

3.4.4 Effect of the variation of Wrist mass 104

3.5 Conclusion 104

This chapter focuses on the kinematic and dynamic analysis of the Orthoglide 5-axis, a spatial Parallel Kinematics Machine (PKM) developed for high speed operations. The analysis is carried out firstly for the 2-dof spherical wrist of the Orthoglide 5-axis and then for the complete mechanism. Finally, some test trajectories are used to analyze the results and a procedure is proposed for the motors selection.

3.1 Orthoglide 5-axis

The Orthoglide 5-axis, illustrated in Fig. 3.1, is a hybrid PKM composed of a 2-dof spherical wrist mounted on a 3-dof translational parallel manipulator (Chablat and Wenger, 2005). The Orthoglide 3-axis is a Delta-type PKM (Clavel, 1988) dedicated to 3-axis rapid machining applications developed at the Institut de Recherche en Communications et

Figure 3.1 – *Prototype of the Orthoglide-5axis (IRCCyN)*

Cybernétique de Nantes (IRCCyN) (Wenger and Chablat, 2000). This mechanism is composed of three identical legs. Each leg is made up of a prismatic joint, two revolute joints and a parallelogram joint, also called Π joint. Each leg generates two constraint moments, i.e., constrains two rotation of the mobile platform. Therefore, the intersection of three legs constrains its three rotations in order to come up with pure three-dof translational motion. A photograph of the Orthoglide 3-axis is shown in Fig. 3.2.

Orthoglide 3-axis gathers the advantages of both serial and parallel kinematics architectures such as regular dexterous workspace, homogeneous performance, good compactness (Pashkevich *et al.*, 2005), good dynamic performances and high stiffness (Pashkevich *et al.*, 2009b).

The two-dof spherical wrist implemented in Orthoglide 5-axis is derived from the Agile Eye, a three-dof spherical wrist developed by Gosselin and Hamel (1994). This two-dof spherical wrist was designed to be more stiff (Chablat and Wenger, 2007). A CAD model of the Orthodlide 5-axis spherical wrist is shown in Fig. 3.3. It has a closed kinematic chain, composed of five links connected by means of revolute joints. The two revolute joints connected to the base are actuated ones. It is apparent that the revolute joints axes intersect, this common intersection being necessary to obtain a spherical wrist. The dimensions of the Orthoglide 5-axis were determined in order to get a $0.5 \times 0.5 \times 0.5$ m^3 cube within the overall workspace of the prototype. The geometric parameters of the

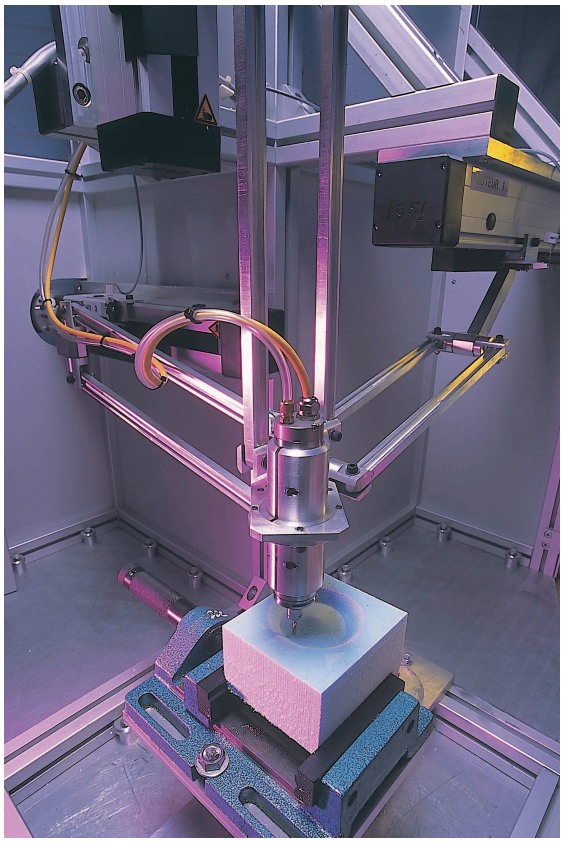

Figure 3.2 – *Orthoglide 3-axis (courtesy: CNRS Photothéque/CARLSON Leif)*

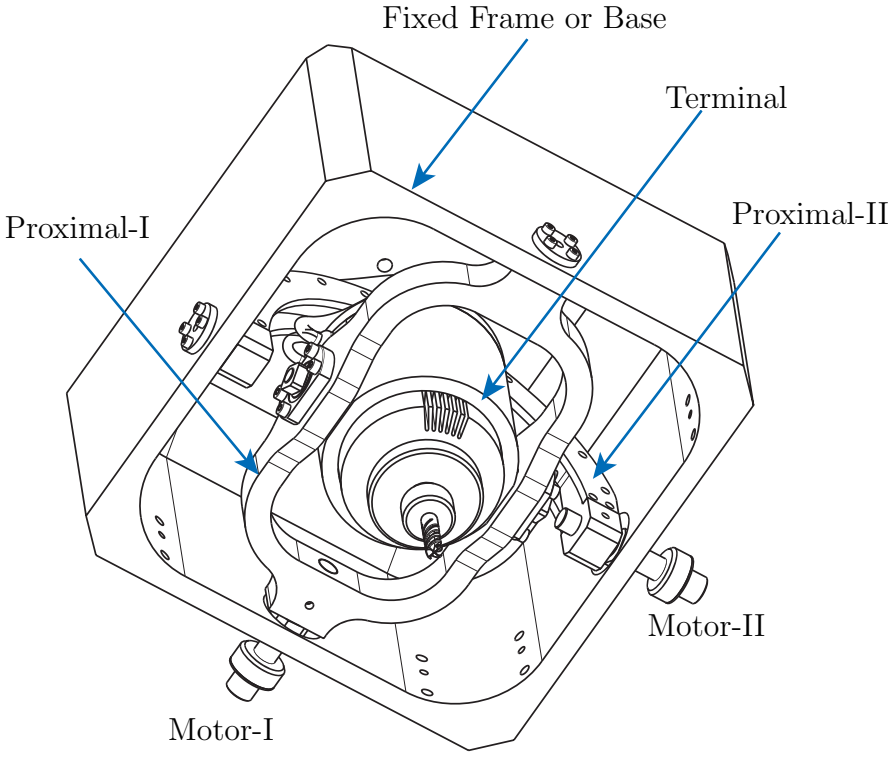

Figure 3.3 – *Spherical wrist of Orthoglide 5-axis*

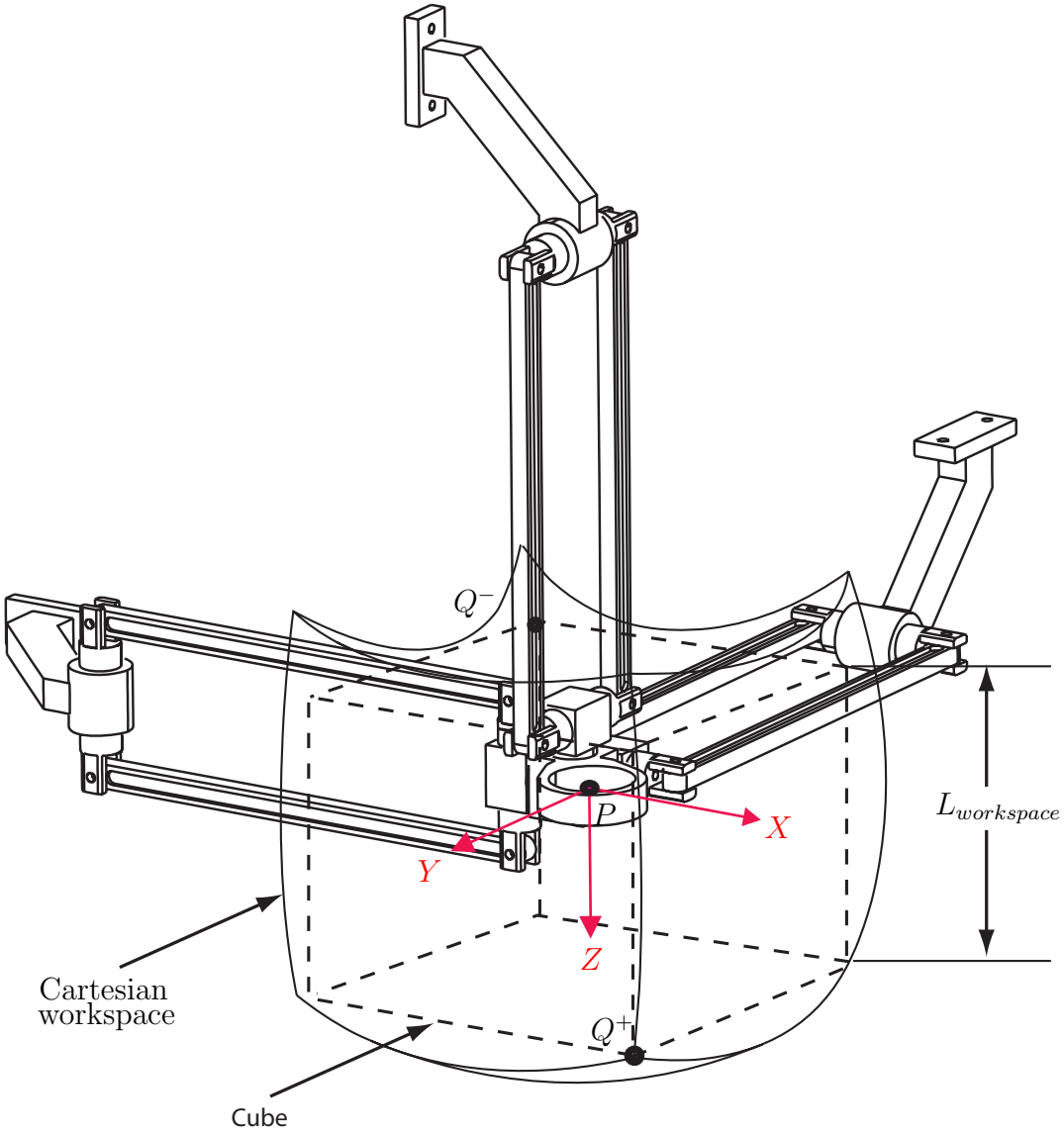

Figure 3.4 – *Orthoglide 5-axis workspace*

manipulator are function of the size of the prescribed cubic Cartesian workspace, namely, its edge length $L_{workspace}$ (Pashkevich *et al.*, 2009b), as shown in Fig. 3.4. The base frame $\mathcal{F}_b$ is defined with the unit vector $\mathbf{e}_i$ in the direction of the i^{th} prismatic joint, namely, X, Y and Z, the origin O being the intersecting point of $\mathbf{e}_i$ (Fig. 3.4). Two points Q^+ and Q^- are defined in such a way that the velocity transmission factor is equal to 1/2 and 2 at these two points, respectively (Chablat and Wenger, 2003). A cube is then constructed, Q^+Q^- being its diagonal. It should be noted that the cubic workspace center, i.e., point C, and the origin O of the reference frame coincide, as shown in Fig. 3.5. In the scope of this study, $L_{workspace}$ is equal to 0.500m. Accordingly, the Cartesian coordinates of points Q^+, Q^- and C for this workspace are given in Table 3.1. Similarly, the prismatic actuator bounds, ρ_{min} and ρ_{max}, can be evaluated (Pashkevich *et al.*, 2009b).

Table 3.1 – *Orthoglide 5-axis workspace parameters*

Workspace size $L_{workspace} = 0.500\,\text{m}$	
Point	Cartesian coordinates [m]
O	$(0, 0, 0)$
C	$(-0.077, -0.077, -0.077)$
Q^+	$(0.183, 0.183, 0.183)$
Q^-	$(-0.317, -0.317, -0.317)$

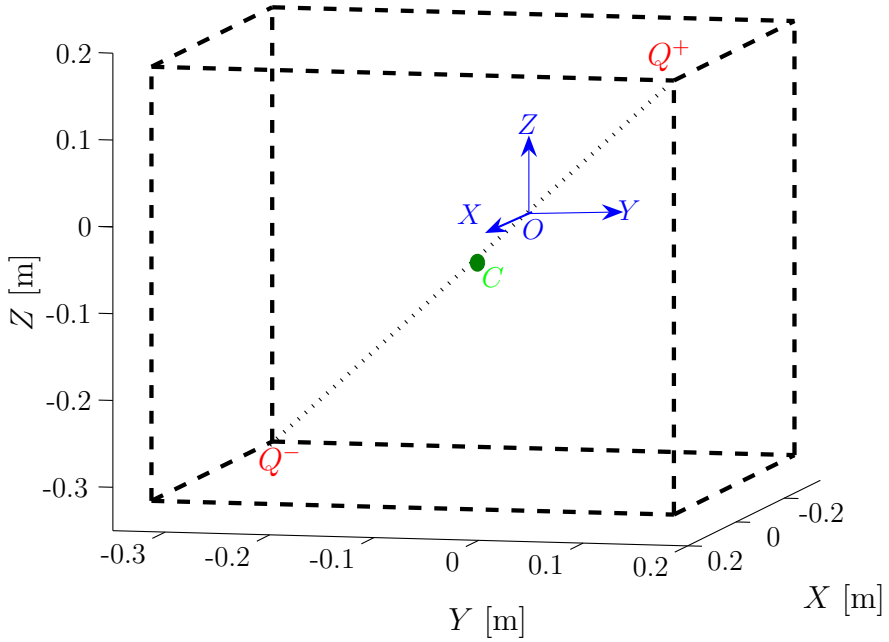

Figure 3.5 – *Orthoglide 5-axis cubic workspace* ($0.5 \times 0.5 \times 0.5\ m^3$)

3.2 Trajectory Planning

In order to analyze the kinematic and dynamic performance of the Orthoglide 5-axis, two test trajectories are proposed. The inverse kinematic and dynamic problems of the manipulator are solved for both the Orthoglide 3-axis and the wrist for these test trajectories. The Orthoglide 5-axis has a quasi-cubic workspace free of singularity and any trajectory can be carried out throughout the workspace. As a remainder, the cubic workspace center, i.e., point I , and the origin O_b of the reference frame do not coincide. The position vector of the cubic workspace center point I is expressed as $\mathbf{dr} = [dx \quad dy \quad dz]^T$. Here, the geometric centre of the path of the test trajectories is supposed to be point I.

The test trajectories are defined as follows:

- Semi-circle of radius R in the vertical plane or in the YZ-plane,
- Circle of radius R in the horizontal plane or in the XY-plane with a constant orientation of vector $\mathbf{v}$ with the Z-axis.

For these two test trajectories, the velocity of the end-effector, *i.e.*, point P, along the

path is constant. Accordingly, for a given test trajectory, the position and velocity of the end-effector can be evaluated as a function of time.

3.2.1 Trajectory-I: Semi-circle of radius R

The semi-circular trajectory-I, in a plane perpendicular to XY-plane, is defined by radius R, trajectory angle ψ with Y-axis, trajectory plane orientation angle ϕ (angle between the trajectory plane and X-axis) and vector $\mathbf{v}$ orientation angle δ, as shown in Fig. 3.6.

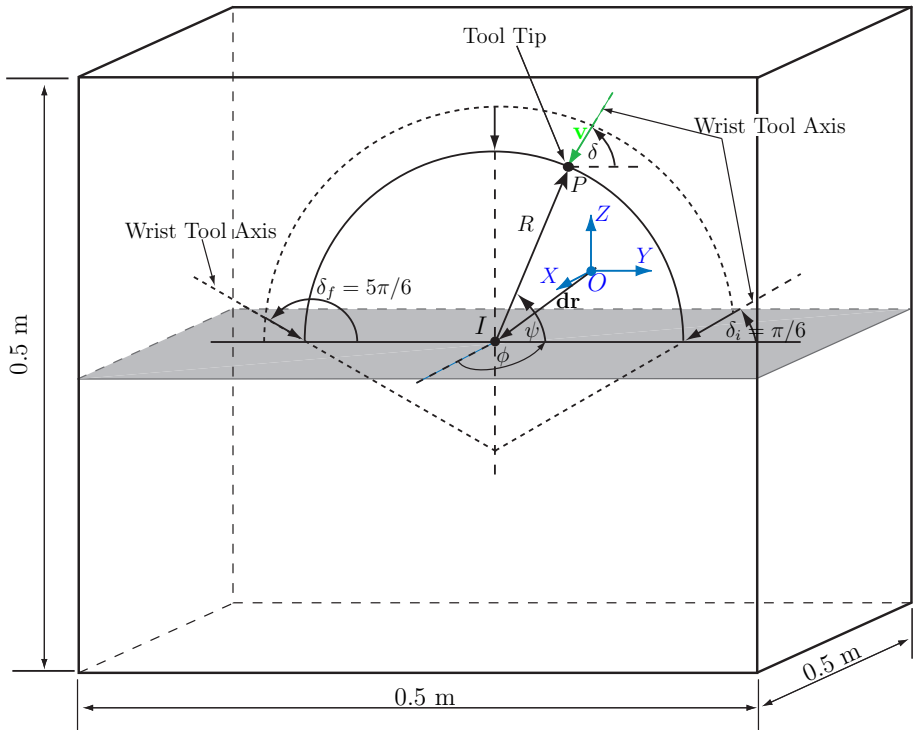

Figure 3.6 – *Orientation of vector* $\mathbf{v}$ *(Traj I)*

Position vector $\mathbf{p}$ and wrist orientation vector $\mathbf{v}$ are given by:

$$\mathbf{p} = \begin{bmatrix} p_x \\ p_y \\ p_z \end{bmatrix} = \begin{bmatrix} dx + R\cos\psi\cos\phi \\ dy + R\cos\psi\sin\phi \\ dz + R\cos\psi \end{bmatrix} \tag{3.1}$$

$$\mathbf{v} = \begin{bmatrix} v_x \\ v_y \\ v_z \end{bmatrix} = \begin{bmatrix} -\cos\delta\cos\phi \\ -\cos\delta\sin\phi \\ -\sin\delta \end{bmatrix} \tag{3.2}$$

where δ varies from $\pi/6$ to $5\pi/6$ while ψ varies from 0 to π.

Trajectory time t is calculated by using the constant velocity V_p of the end-effector and

the length of the trajectory, i.e.

$$t = \frac{R\,(\psi_f - \psi_i)}{V_p} \tag{3.3}$$

ψ_f and ψ_i being the initial and the final values of the trajectory angle (0 and π respectively).

3.2.2 Trajectory-II: Circle of radius R

In this case, the angle of vector $\mathbf{v}$ with the vertical or Z-axis is γ and vector $\mathbf{v}$ goes through a circular trajectory in horizontal plane, defined with radius R and angle ψ, as shown in Fig. 3.7.

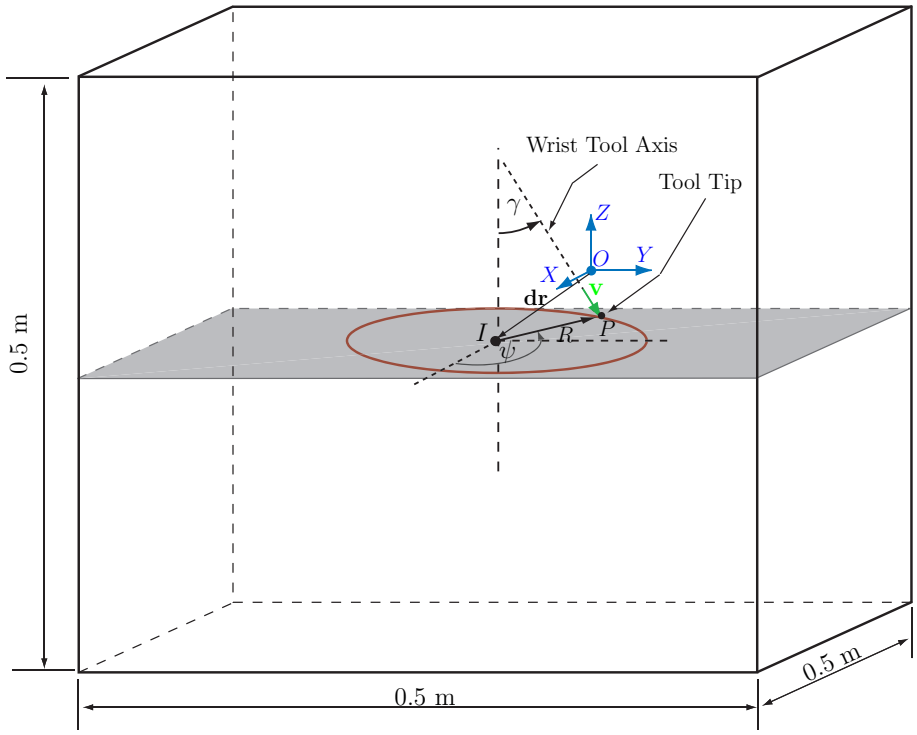

Figure 3.7 – *Orientation of vector* $\mathbf{v}$ *(Traj II)*

Position vector $\mathbf{p}$ and wrist orientation vector $\mathbf{v}$ are given by:

$$\mathbf{p} = \begin{bmatrix} p_x \\ p_y \\ p_z \end{bmatrix} = \begin{bmatrix} dx + R\cos\psi \\ dy + R\cos\psi \\ dz \end{bmatrix} \tag{3.4}$$

$$\mathbf{v} = \begin{bmatrix} v_x \\ v_y \\ v_z \end{bmatrix} = \begin{bmatrix} \sin\gamma\sin\psi \\ \sin\gamma\cos\psi \\ -\cos\gamma \end{bmatrix} \tag{3.5}$$

with ψ varying from 0 to 2π, the trajectory time being $t = \frac{2\pi R}{V_p}$.

3.3 Kinematics and Dynamics of the 2-dof Spherical Wrist of Orthoglide 5-axis

A spherical mechanism can orient or move the end-effector about the center of rotation of the mechanism. A typical 3-dof spherical manipulator provides the three dimensional (3D) rotations like a human hand. However, in most machining applications only 2D rotations are sufficient. Rotation about the axis of symmetry of the end-effector is not necessary and if required, can be provided independently.

Several researchers have worked in the domain of spherical mechanisms mainly for the applications of end-effector orientations. One of the earlier spherical mechanisms is that presented in the work of Asada and Granito (1985) which is a 3-dof spherical wrist with coaxial motors and three kinematics chains. Craver (1989) analyzed a spherical robotic shoulder module. Other major publications to the research and development of the spherical mechanism are the work of Gosselin and Angeles (1988, 1989); Gosselin and Lavoie (1993) where optimum kinematic designs of different types of spherical parallel mechanisms are presented. The Agile Eye, one of the most famous spherical mechanisms designed by Gosselin and Hamel (1994), is a 3-dof parallel mechanism developed to control the orientation of a camera. Several mechanisms have been derived for diverse applications from the Agile Eye. Spherical mechanisms can be implemented in several domains like, in radar applications (Dunlop and Jones, 1999), camera manipulations (Caron, 1997) and surgical applications (Lum *et al.*, 2006). Cavallo and Michelini (2004) introduced a 3-dof spherical parallel mechanism composed of three identical kinematic chains to orient the propeller and duct of a small autonomous underwater vehicle (AUV). Main contributions for the design and analysis of spherical mechanisms are reported in (Asada and Granito, 1985; Gosselin and Angeles, 1988, 1989; Gosselin and Lavoie, 1993; Gosselin and Hamel, 1994; Innocenti and Castelli, 1993; Alizade *et al.*, 1994; Tsai, 1999; Karouia and Hervè, 2002; Merlet, 2006c).

In this section, the kinematic and dynamic analysis of the 2-dof spherical wrist of Orthoglide 5-axis is presented. Here, we focus on the evaluation of the velocities, accelerations and the torques required by the actuators of the spherical wrist. First, the kinematics of the spherical wrist is studied and then its dynamics is analyzed by means of the Newton-Euler approach. The geometric and inertial parameters are determined with a CAD software. The performance of the manipulator is emphasized by means of several test trajectories. Finally, the actuators are selected from the catalogue based on the velocities and torques required by the actuators to carry out the test trajectories.

As already mentioned, the Orthoglide 5-axis wrist is derived from the Agile Eye, hence

it follows identical kinematic and dynamic behaviour as discussed in (Caron, 1997) for a camera manipulator. Therefore, in order to derive the kinematic and dynamic models of the Orthoglide 5-axis wrist, we used a similar approach and nomenclature as presented by Caron (1997). However, subsequent modifications are made, as the architecture of the Orthoglide 5-axis wrist is not the same as that of the said camera manipulator with regard to the distal and the proximal-II geometry and application. Moreover, the influence of the external and/or machining forces on the dynamic performance is also considered.

3.3.1 Spherical Wrist Kinematic Model

3.3.1.1 Notations and symbols for the spherical wrist analysis

Following nomenclature is used exclusively for the kinematic and dynamic analysis of the Orthoglide wrist:

t	:	Terminal
d	:	Distal
p_1	:	Proximal-I
p_2	:	Proximal-II
$\mathbf{e}_i$	:	Unit vector along the i^{th} articulations
a to **h**	:	Forces
A to H	:	Components of forces
m to **r**	:	Moments
M to R	:	Components of moments
$\mathbf{f}_g$	:	Gravitational force
F_g	:	Components of gravitational force
$\mathbf{f}_c$	:	Machining or cutting force
F_c	:	Components of Machining or cutting force
g	:	Vector of gravitational acceleration
m	:	Mass of the components
j	:	Inertial force
J	:	Components of inertial force
a	:	Acceleration vector of center of mass
k	:	Inertial terms
K	:	Components of inertial terms
I	:	Inertia matrix
l_i	:	Distance between the geometric center and center of mass along the i^{th} direction
L_i	:	Distance between the geometric center and the point of application of the force along the i^{th} direction
L_c	:	Distance between the machining tool tip and the wrist geometric center

$\boldsymbol{\omega}, \dot{\boldsymbol{\omega}}$	:	Angular velocity and acceleration
α_i	:	Angle between Z_i and Z_{i+1}
$R_i\,(X_i, Y_i, Z_i)$	:	Reference frame associated with the i^{th} articulation
$\mathbf{v}$	:	Orientation vector of the end-effector

3.3.1.2 Reference frames and Wrist DH–parameters

The spherical wrist of the Orthoglide 5-axis is composed of a closed kinematic chain made up of five components: proximal-I, proximal-II, distal, terminal and the base. These five links are connected by means of revolute joints, of which axes intersect at the center of the mechanism. Besides, only the two revolute joints connected to the base of the wrist are actuated. The distal has an imaginary axis of rotation passing through the intersection point of other joint axis and perpendicular to the plane of proximal-II. A unit vector $\mathbf{e}_i$ and a reference frame R_i are associated to each joint, the Z_i-axis and $\mathbf{e}_i$ being coincident. The angle between $\mathbf{e}_1$ and $\mathbf{e}_2$ is denoted by α_0 and the angle between $\mathbf{e}_i$ and $\mathbf{e}_{i+2}$ is denoted by α_i, for $i = 1 \cdots 4$. Reference frame R_1 is defined in such a way that Z_1-axis coincides with $\mathbf{e}_1$, and $\mathbf{e}_2$ lies in the X_1Z_1-plane. Similarly R_2 has its Z_2-axis in the direction of $\mathbf{e}_2$, and $\mathbf{e}_1$ lies in the X_2Z_2-plane. Reference frame R_i $(i = 3, 4, 5, 6)$ with $Z_i = \mathbf{e}_i$ are defined by the rotation of frame R_{i-2} and following the Denavit-Hartenberg (DH) conventions. DH-conventions for the Orthoglide wrist are summarized as follows:

- Z_i: axis of the i^{th} joint;
- X_i: common perpendicular to Z_{i-2} and Z_i;
- Y_i: respecting the right hand rule;
- a_i: distance between Z_i and Z_{i+2};
- b_i: distance between X_i and X_{i+2};
- α_i: angle between Z_i and Z_{i+2} about X_{i+2};
- θ_i: angle between X_i and X_{i+2} about Z_i.

As all joint axes intersect at a common point, the origin of all frames are the same i.e., $a_i = b_i = 0$. Figure 3.8 shows the orientations of reference frames attached to the Orthoglide wrist according to the DH-convention. The corresponding DH-parameters are given in Table 3.3.

3.3.1.3 Kinematics of the Orthoglide wrist

The kinematic equations of the Orthoglide wrist are developed with the help of the reference frames defined above and the DH-parameters. Vector $\mathbf{v}$ depicts the orientation of the wrist end-effector (cutting tool etc), which is defined in reference frame R_5 by means

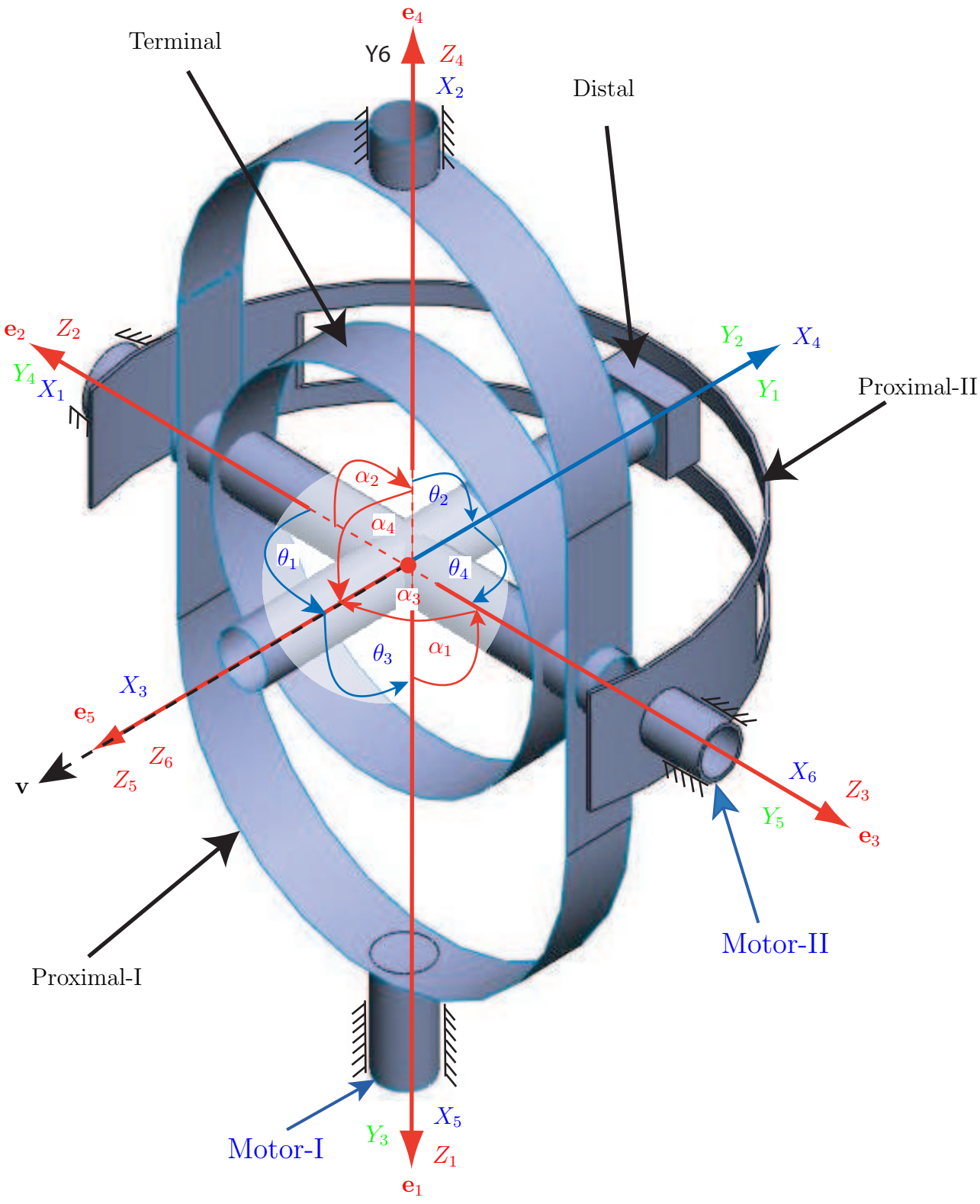

Figure 3.8 – *Orientations of reference frames according to DH-Conventions for the Orthoglide Wrist*

of the three angles β_1, β_2 and γ illustrated in Fig. 3.9-(a):

– β_1 being the angle between $\mathbf{e}_5$ and the projection of $\mathbf{v}$ to $\mathbf{e_3} - \mathbf{e_5}$-plane;

Table 3.3 – *DH-parameters for Orthoglide wrist*

i	a_i	b_i	α_i	θ_i	
				time t	home configuration
0	0	0	$\pi/2$	-	-
1	0	0	$\pi/2$	θ_1	$-\pi/2$
2	0	0	$\pi/2$	θ_2	$\pi/2$
3	0	0	$\pi/2$	θ_3	$\pi/2$
4	0	0	$\pi/2$	θ_4	$-\pi/2$

– β_2 being the angle between $\mathbf{v}$ and $\mathbf{e_3} - \mathbf{e_5}$-plane;

– γ being the angle between $\mathbf{v}$ and $\mathbf{e_3}$.

The expression of $\mathbf{v}$ in R_5 is then defined as,

$$\mathbf{v}_5 = \begin{bmatrix} \sin\beta_2 & \sin\beta_1\cos\beta_2 & \cos\beta_1\cos\beta_2 \end{bmatrix}^T \tag{3.6}$$

Since vectors $\mathbf{v}$ and $\mathbf{e}_5$ coincide (Fig. 3.8), i.e. $\mathbf{v} = \mathbf{e_5}$, $\beta_1 = \beta_2 = 0$ and $\gamma = \pi/2$. The orientation of vector $\mathbf{v}$ is defined in reference frame R_1 by the Pan (ϕ_1) and Tilt (ϕ_2) angles as shown in Fig. 3.9-(b). With the definitions of ϕ_1 and ϕ_2, the components of $\mathbf{v}$ in R_1 are given by:

$$\mathbf{v}_1 = \begin{bmatrix} \cos\phi_1\cos\phi_2 & \sin\phi_1\cos\phi_2 & \sin\phi_2 \end{bmatrix}^T \tag{3.7}$$

with,

$$\phi_1 = \tan^{-1}\frac{v_{y1}}{v_{x1}} \qquad \phi_2 = \tan^{-1}\frac{v_{z1}}{\sqrt{v_{x1}^2 + v_{y1}^2}} \tag{3.8}$$

Finally, the inverse kinematic problem of the wrist can be derived from $\mathbf{v}$, α, β_1, β_2, γ, ϕ_1 and ϕ_2. The relations for the joints variables (θ_1, θ_2, θ_3, θ_4) are summarized in Table 3.4 Caron (1997).

From Table 3.4, θ_1 and θ_2 can have two solutions but while considering the geometry of the mechanism only one of the latter is possible. These relations are given in Table 3.5.

Similarly, analytical relations of joints rates, i.e. joints velocities and acceleration can be obtained with the help of the previous relations of joint displacements and unit vectors $\mathbf{e_i}$. These relations are given in Annex A, however, numerical techniques, like finite difference method can also be used to obtain joint velocities and accelerations.

■

Table 3.4 – *Relations of* θ_1, θ_2, θ_3, θ_4

$\theta_1 = \tan^{-1}\left(\frac{2T}{1-T^2}\right)$	$T = \frac{-B \pm \sqrt{B^2 - 4AC}}{2A}$ $A = v_z c\alpha_1 + v_y s\alpha_1 - c\gamma$ $B = 2v_x s\alpha_1$ $C = v_z c\alpha_1 - v_y c\alpha_1 - c\gamma$
$\theta_3 = \tan^{-1}\left(\frac{a \times e + b \times d}{a \times d - b \times e}\right)$	$a = s\beta_2$ $b = s\alpha_3 c\beta_1 c\beta_2 - c\alpha_3 s\beta_1 c\beta_2$ $d = v_x c\theta_1 + v_y s\theta_1$ $e = -v_x s\theta_1 c\alpha_1 + v_y c\theta_1 c\alpha_1 + v_z c\alpha_1$
$\theta_2 = \tan^{-1}\left(\frac{2T}{1-T_2^2}\right)$	$u_x = s\theta_1 s\alpha_1 c\alpha_3 + s\theta_1 c\theta_3 c\alpha_1 s\alpha_3 + c\theta_1 s\theta_3 s\alpha_3$ $u_y = -c\theta_1 s\alpha_1 c\alpha_3 - c\theta_1 c\theta_3 c\alpha_1 s\alpha_3 + s\theta_1 s\theta_3 s\alpha_3$ $u_z = c\alpha_1 c\alpha_3 - c\theta_3 c\alpha_1 c\alpha_3$ $A_2 = u_x s\alpha_0 c\alpha_2 + u_y s\alpha_2 + u_z c\alpha_0 c\alpha_2 - c\alpha_4$ $B_2 = 2\left(u_x c\alpha_0 s\alpha_2 - u_z s\alpha_0 s\alpha_2\right)$ $C_2 = u_x s\alpha_0 c\alpha_2 - u_y s\alpha_2 + u_z c\alpha_0 c\alpha_2 - c\alpha_4$ $T_2 = \frac{-B_2 \pm \sqrt{B_2^2 - 4A_2C_2}}{2A_2}$
$\theta_4 = \tan^{-1}\left(\frac{s_4}{c_4}\right)$	$s_4 = \frac{u_x c\theta_2 c\alpha_0 + u_y s\theta_2 - u_z c\theta_2 s\alpha_0}{s\alpha_4}$ $c_4 = \frac{a_4 + b_4 + d_4}{s\alpha_4}$
NB:- c and s stands for *cosine* and *sine* functions respectively	

Table 3.5 – *Summary of* θ_1, θ_2, θ_3, θ_4 *relations*

θ_i	Functional relation	Possible solutions	Feasible solution	Home config.
θ_1	$\theta_1 = f\left(v_x, v_y, v_z, \alpha_1, \gamma\right)$	2 $(\theta_{11}, \theta_{12})$	θ_{11} with $T = \frac{-B + \sqrt{B^2 - 4AC}}{2A}$	$-\pi/2$
θ_2	$\theta_2 = f\left(\theta_1, \theta_2, \alpha_i\right)\ i = 0 \cdots 4$	2 $(\theta_{21}, \theta_{22})$	θ_{22} with $T = \frac{-B - \sqrt{B^2 - 4AC}}{2A}$	$\pi/2$
θ_3	$\theta_3 = f\left(v_x, v_y, v_z, \theta_1, \alpha_1, \alpha_3, \beta_1, \beta_2\right)$	1 (θ_3)	θ_3	$\pi/2$
θ_4	$\theta_4 = f\left(\theta_1, \theta_2, \theta_3, \alpha_i\right)\ i = 0 \cdots 4$	1 (θ_4)	θ_4	$-\pi/2$

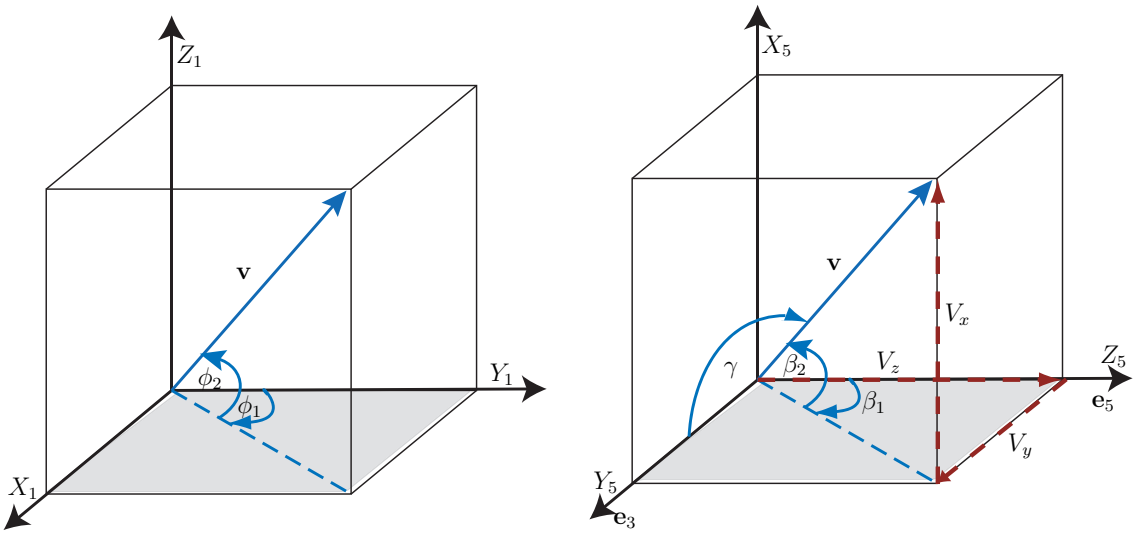

(a) $\mathbf{v}$ in R_1 (b) $\mathbf{v}$ in R_5

Figure 3.9 – *Definition of* $\mathbf{v}$ *in frames* R_1 *and* R_5

3.3.2 Spherical Wrist Dynamic Model

Dynamic analysis is of primary importance to investigate the forces and moments applied to the actuators to carry out a desired task or motion by the manipulator.

As a first step, the wrist joints displacements are calculated from the kinematic model as discussed in the previous section. Velocities and accelerations of each component are obtained with the help of kinematic modeling. Similarly, the first and second derivatives of the unit vectors $\mathbf{e_1}$, $\mathbf{e_2}$, $\mathbf{e_3}$, $\mathbf{e_4}$ and $\mathbf{e_5}$ are calculated. Detailed relations of these calculations are obtained from Caron (1997) and given in Annex A. Finally, a system of equilibrium equations, obtained from the free body diagrams of each wrist component, is used to get the relations of actuators torques. A flow chart of the torques calculations methodology is given in Fig. 3.10. In the following sections, the simplified equilibrium equations for the Orthoglide wrist are developed by means of the Newton-Euler approach.

3.3.2.1 Equilibrium Equations

In order to draw the Free Body Diagrams (FBD) and consequently to write the equilibrium equations for terminal, distal, proximal-I and proximal-II, Newton-Euler approach is used with the following assumptions:

- friction forces are neglected;
- a spherical joint is assumed between the distal and the terminal link to obtain an isostatic mechanism;
- a planar joint between the distal and the proximal -2 is considered.

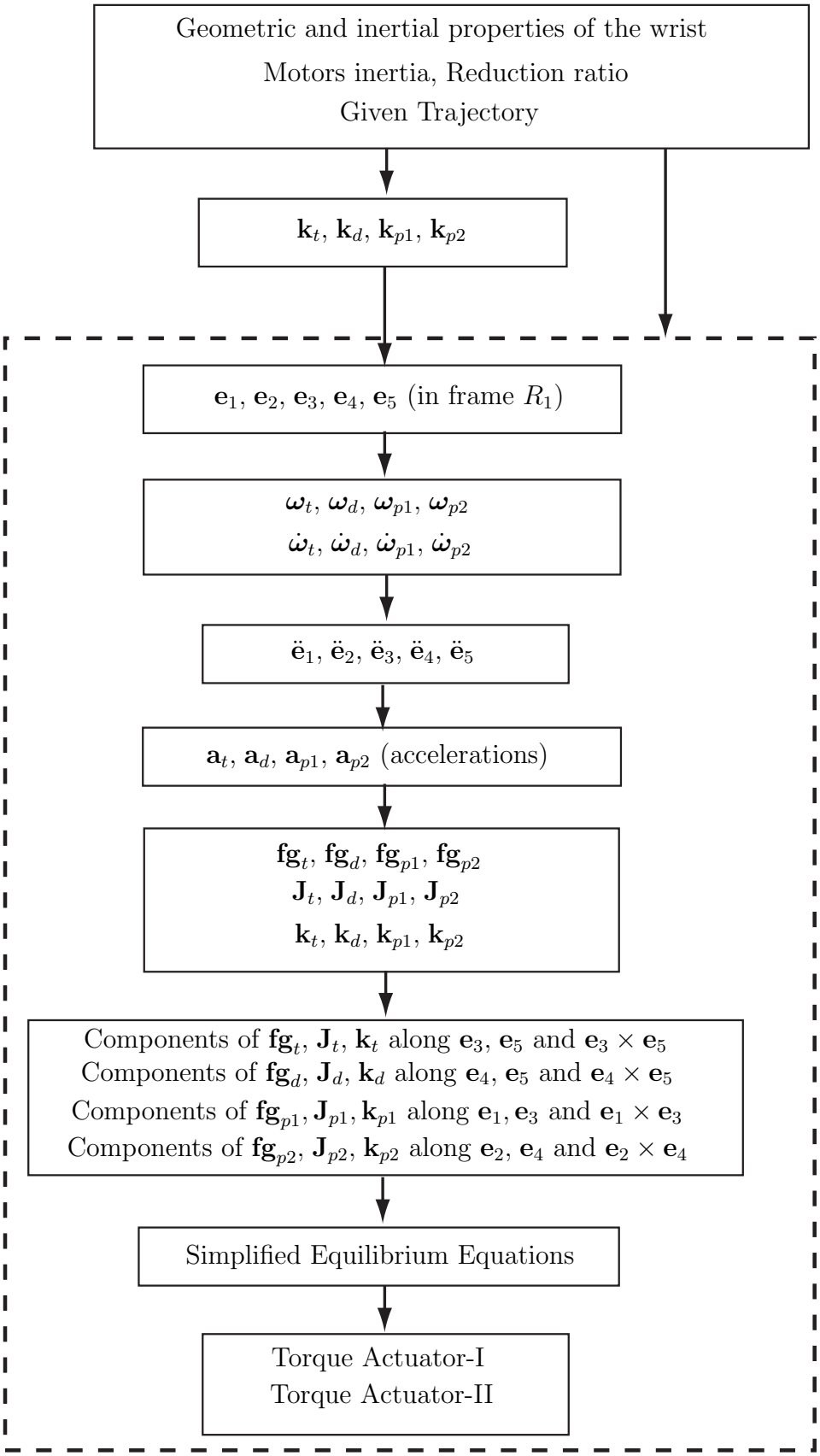

Figure 3.10 – *Flow chart of wrist dynamic model*

With these assumptions, the FBD of terminal, distal, proximal-1 and proximal-2 are drawn, as shown in Figs. 3.11 to 3.14. The forces and moments exerted on the four moving wrist components are summarized below:

- two forces **a** and **b** and one moment **m** are exerted on the terminal;
- two forces **c** and **c** are exerted on the distal link;
- two forces **g** and **h** and two moments **n** and **p** are exerted on the proximal-1;
- two forces **e** and **f** and a moment **r** are exerted on the proximal-2.

These forces and moments are resolved into orthogonal components with respect to the attached unit vectors. A set of 24 equilibrium equations is written for the moving components of the wrist.

3.3.2.2 Terminal-Equilibrium Equations

There are two forces **a** and **b** and one moment **m** acting on the terminal. The components of these forces and moments are shown in the terminal FBD in Fig. 3.11. The equilibrium equations corresponding to the FBD of terminal are given by:

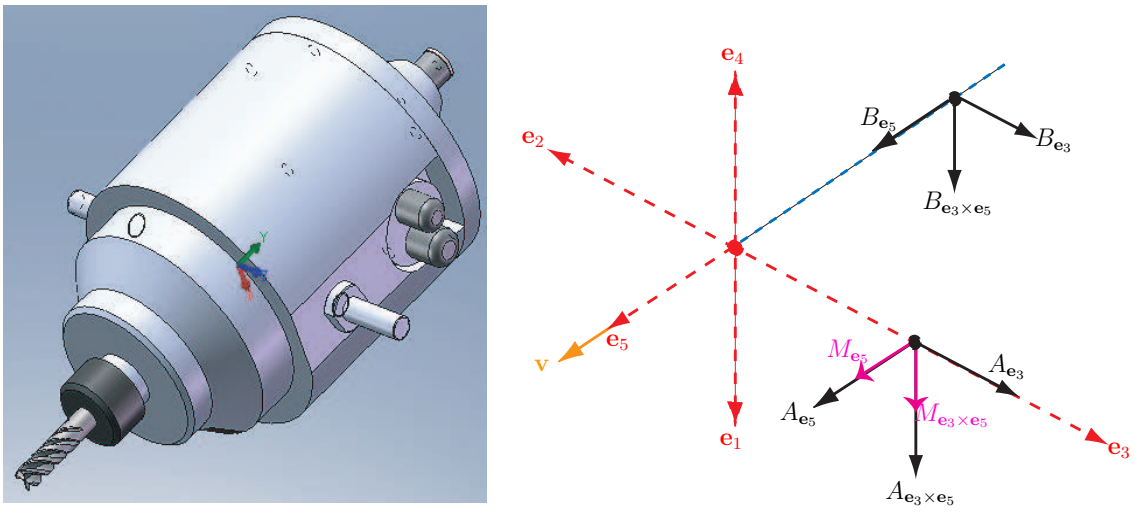

(a) CAD model (b) FBD

Figure 3.11 – *CAD model and FBD of terminal*

$$\sum F_{\mathbf{e}_3} = A_{\mathbf{e}_3} + B_{\mathbf{e}_3} + F^t_{g\mathbf{e}_3} = J^t_{\mathbf{e}_3} \tag{3.9a}$$

$$\sum F_{\mathbf{e}_5} = A_{\mathbf{e}_5} + B_{\mathbf{e}_5} + F^t_{g\mathbf{e}_5} = J^t_{\mathbf{e}_5} \tag{3.9b}$$

$$\sum F_{\mathbf{e}_3\times\mathbf{e}_5} = A_{\mathbf{e}_3\times\mathbf{e}_5} + B_{\mathbf{e}_3\times\mathbf{e}_5} + F^t_{g\mathbf{e}_3\times\mathbf{e}_5} = J^t_{\mathbf{e}_3\times\mathbf{e}_5} \tag{3.9c}$$

$$\sum M_{\mathbf{e}_3} = -L^t_{\mathbf{e}_5} B_{\mathbf{e}_3\times\mathbf{e}_5} - l^t_{\mathbf{e}_3\times\mathbf{e}_5} F^t_{g\mathbf{e}_5} + l^t_{\mathbf{e}_5} F^t_{g\mathbf{e}_3\times\mathbf{e}_5} = K^t_{\mathbf{e}_3} \tag{3.9d}$$

$$\sum M_{\mathbf{e}_5} = M_{\mathbf{e}_5} - L^t_{\mathbf{e}_3} A_{\mathbf{e}_3\times\mathbf{e}_5} - l^t_{\mathbf{e}_3} F^t_{g\mathbf{e}_3\times\mathbf{e}_5} + l^t_{\mathbf{e}_3\times\mathbf{e}_5} F^t_{g\mathbf{e}_3} = K^t_{\mathbf{e}_5} \tag{3.9e}$$

$$\sum M_{\mathbf{e}_3\times\mathbf{e}_5} = M_{\mathbf{e}_3\times\mathbf{e}_5} + L^t_{\mathbf{e}_5} B_{\mathbf{e}_3} + L^t_{\mathbf{e}_3} A_{\mathbf{e}_5} + l^t_{\mathbf{e}_3} F^t_{g\mathbf{e}_5} - l^t_{\mathbf{e}_5} F^t_{g\mathbf{e}_3} = K^t_{\mathbf{e}_3\times\mathbf{e}_5} \tag{3.9f}$$

where $F^t_{g\mathbf{e}_3}$, $F^t_{g\mathbf{e}_5}$, $F^t_{g\mathbf{e}_3\times\mathbf{e}_5}$ are the gravity terms, $K^t_{g\mathbf{e}_3}$, $K^t_{g\mathbf{e}_5}$, $K^t_{g\mathbf{e}_3\times\mathbf{e}_5}$ are the inertial terms (function of angular velocity, acceleration and inertia matrix) and $J^t_{g\mathbf{e}_3}$, $J^t_{g\mathbf{e}_5}$, $J^t_{g\mathbf{e}_3\times\mathbf{e}_5}$ are the inertial forces (function of linear acceleration and mass) on the terminal along $\mathbf{e}_3$, $\mathbf{e}_5$ and $\mathbf{e}_3 \times \mathbf{e}_5$ directions, respectively. Other variables used in these equations are defined in the next section.

3.3.2.3 Distal-Equilibrium Equations

Only two forces **c** and **d** act on the distal. Components of these two forces are shown in FBD of distal in Fig. 3.12. Equilibrium equations corresponding to this FBD are given by:

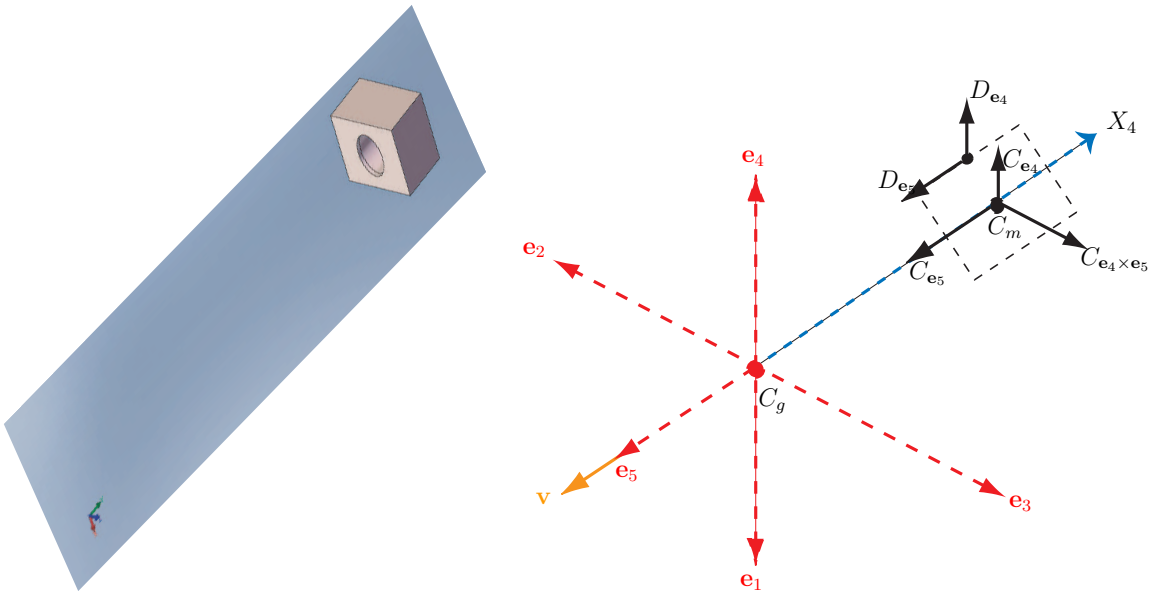

(a) CAD model (b) FBD

Figure 3.12 – *CAD model and FBD of Distal*

$$\sum F_{\mathbf{e}_4} = C_{\mathbf{e}_4} + D_{\mathbf{e}_4} + F^d_{g\mathbf{e}_4} = J^d_{\mathbf{e}_4} \tag{3.10a}$$

$$\sum F_{\mathbf{e}_5} = C_{\mathbf{e}_5} + D_{\mathbf{e}_5} + F^d_{g\mathbf{e}_5} = J^d_{\mathbf{e}_5} \tag{3.10b}$$

$$\sum F_{\mathbf{e}_4\times\mathbf{e}_5} = C_{\mathbf{e}_4\times\mathbf{e}_5} + F^d_{g\mathbf{e}_4\times\mathbf{e}_5} = J^d_{\mathbf{e}_4\times\mathbf{e}_5} \tag{3.10c}$$

$$\sum M_{\mathbf{e}_4} = -L^d_{\mathbf{e}_5} C_{\mathbf{e}_4\times\mathbf{e}_5} + l^d_{\mathbf{e}_5} F^d_{g\mathbf{e}_4\times\mathbf{e}_5} - l^d_{\mathbf{e}_4\times\mathbf{e}_5} F^d_{g\mathbf{e}_5} = K^d_{\mathbf{e}_4} \tag{3.10d}$$

$$\sum M_{\mathbf{e}_5} = -l^d_{\mathbf{e}_4} F^d_{g\mathbf{e}_4\times\mathbf{e}_5} + l^d_{\mathbf{e}_4\times\mathbf{e}_5} F^d_{g\mathbf{e}_4} = K^d_{\mathbf{e}_5} \tag{3.10e}$$

$$\sum M_{\mathbf{e}_4\times\mathbf{e}_5} = L^d_{\mathbf{e}_5} C_{\mathbf{e}_4} + L^d_{\mathbf{e}_4} D_{\mathbf{e}_5} + L^d_{\mathbf{e}_5} D_{\mathbf{e}_4} + l^d_{\mathbf{e}_4} F^d_{g\mathbf{e}_5} - l^d_{\mathbf{e}_5} F^d_{g\mathbf{e}_4} = K^d_{\mathbf{e}_4\times\mathbf{e}_5} \tag{3.10f}$$

where $F^d_{g\mathbf{e}_4}$, $F^d_{g\mathbf{e}_5}$, $F^d_{g\mathbf{e}_4\times\mathbf{e}_5}$ are the gravity terms, $K^d_{g\mathbf{e}_4}$, $K^d_{g\mathbf{e}_5}$, $K^d_{g\mathbf{e}_4\times\mathbf{e}_5}$ are the inertial terms and $J^d_{g\mathbf{e}_4}$, $J^d_{g\mathbf{e}_5}$, $J^d_{g\mathbf{e}_4\times\mathbf{e}_5}$ are the inertial forces on the distal along $\mathbf{e}_4$, $\mathbf{e}_5$ and $\mathbf{e}_4\times\mathbf{e}_5$ directions, respectively.

3.3.2.4 Proximal–I-Equilibrium Equations

There are two forces **g** and **h** and two moments **n** and **p** acting on the proximal-I. Fig. 3.13 shows the FBD of proximal-I with the components of these forces and moments. Equilibrium equations corresponding to the FBD are given by:

$$\sum F_{\mathbf{e}_1} = G_{\mathbf{e}_1} + H_{\mathbf{e}_1} + F^{p1}_{g\mathbf{e}_1} = J^{p1}_{\mathbf{e}_4} \tag{3.11a}$$

$$\sum F_{\mathbf{e}_3} = G_{\mathbf{e}_3} + H_{\mathbf{e}_3} + F^{p1}_{g\mathbf{e}_3} = J^{p1}_{\mathbf{e}_3} \tag{3.11b}$$

$$\sum F_{\mathbf{e}_1\times\mathbf{e}_3} = G_{\mathbf{e}_1\times\mathbf{e}_3} + H_{\mathbf{e}_1\times\mathbf{e}_3} + F^{p1}_{g\mathbf{e}_1\times\mathbf{e}_3} = J^{p1}_{\mathbf{e}_1\times\mathbf{e}_3} \tag{3.11c}$$

$$\sum M_{\mathbf{e}_1} = N_{\mathbf{e}_1} + P_{\mathbf{e}_1} + L^{p1}_{\mathbf{e}_3} G_{\mathbf{e}_1\times\mathbf{e}_3} + l^{p1}_{\mathbf{e}_3} F^{p1}_{g\mathbf{e}_1\times\mathbf{e}_3} - l^{p1}_{\mathbf{e}_1\times\mathbf{e}_3} F^{p1}_{g\mathbf{e}_3} = K^{p1}_{\mathbf{e}_1} \tag{3.11d}$$

$$\sum M_{\mathbf{e}_3} = P_{\mathbf{e}_3} - L^{p1}_{\mathbf{e}_1} H_{\mathbf{e}_1\times\mathbf{e}_3} - l^{p1}_{\mathbf{e}_1} F^{p1}_{g\mathbf{e}_1\times\mathbf{e}_3} + l^{p1}_{\mathbf{e}_1\times\mathbf{e}_3} F^{p1}_{g\mathbf{e}_1} = K^{p1}_{\mathbf{e}_3} \tag{3.11e}$$

$$\sum M_{\mathbf{e}_1\times\mathbf{e}_3} = N_{\mathbf{e}_1\times\mathbf{e}_3} + P_{\mathbf{e}_1\times\mathbf{e}_3} + L^{p1}_{\mathbf{e}_1} H_{\mathbf{e}_3} + L^{p1}_{\mathbf{e}_3} G_{\mathbf{e}_1} - l^{p1}_{\mathbf{e}_3} F^{p1}_{g\mathbf{e}_1} + l^{p1}_{\mathbf{e}_1} F^{p1}_{g\mathbf{e}_3} = K^{p1}_{\mathbf{e}_1\times\mathbf{e}_2} \tag{3.11f}$$

where $F^{p1}_{g\mathbf{e}_1}$, $F^{p1}_{g\mathbf{e}_3}$, $F^{p1}_{g\mathbf{e}_1\times\mathbf{e}_3}$ are the gravity terms, $K^{p1}_{g\mathbf{e}_1}$, $K^{p1}_{g\mathbf{e}_3}$, $K^{p1}_{g\mathbf{e}_1\times\mathbf{e}_3}$ are the inertial terms and $J^{p1}_{g\mathbf{e}_1}$, $J^{p1}_{g\mathbf{e}_3}$, $J^{p1}_{g\mathbf{e}_1\times\mathbf{e}_3}$ are the inertial forces on the proximal–I along $\mathbf{e}_1$, $\mathbf{e}_3$ and $\mathbf{e}_1 \times \mathbf{e}_3$ directions, respectively.

3.3.2.5 Proximal–II-Equilibrium Equations

Two forces **e** and **f** and a moment **r** act on the proximal-II. Components of these forces and moment are shown in the FBD of proximal–II in Fig. 3.14. Equilibrium equations

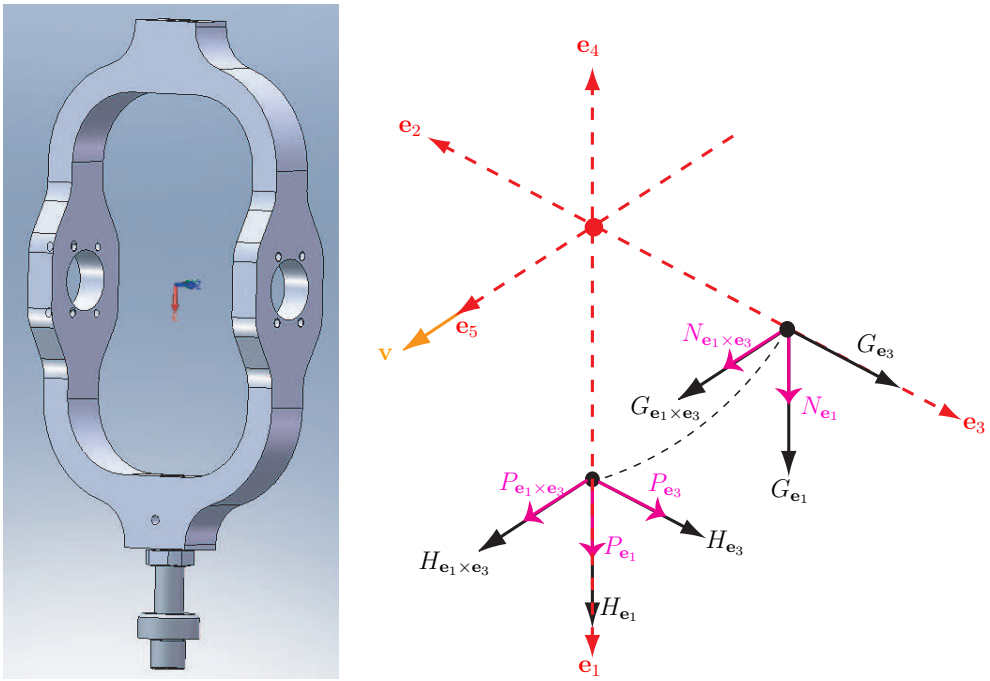

(a) CAD model (b) FBD

Figure 3.13 – *CAD model and FBD of Proximal-1*

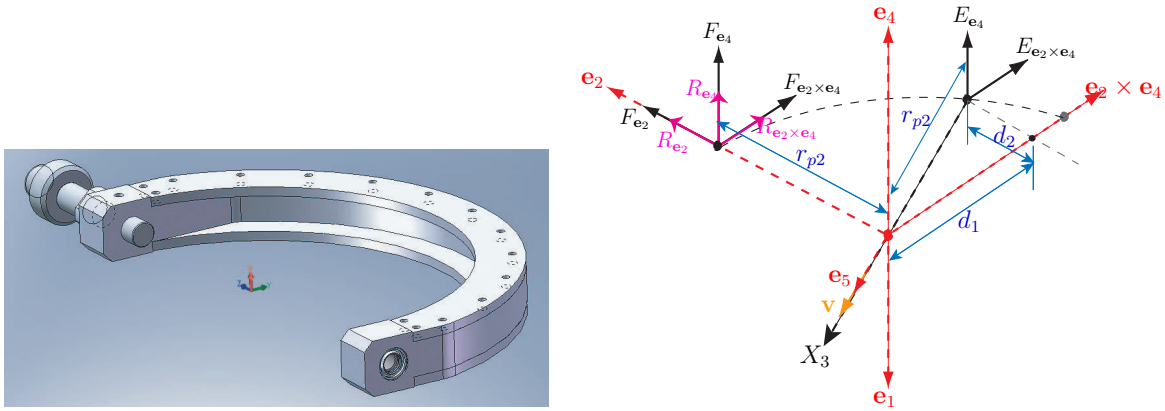

(a) CAD model (b) FBD

Figure 3.14 – *CAD model and FBD of Proximal-2*

corresponding to the FBD are given by:

$$\sum F_{\mathbf{e}_2} = F_{\mathbf{e}_2} + F^{p2}_{g\mathbf{e}_2} = J^{p2}_{\mathbf{e}_2} \tag{3.12a}$$

$$\sum F_{\mathbf{e}_4} = F_{\mathbf{e}_4} + E_{\mathbf{e}_4} + F^{p2}_{g\mathbf{e}_4} = J^{p2}_{\mathbf{e}_4} \tag{3.12b}$$

$$\sum F_{\mathbf{e}_2\times\mathbf{e}_4} = F_{\mathbf{e}_2\times\mathbf{e}_4} + E_{\mathbf{e}_2\times\mathbf{e}_4} + F^{p2}_{g\mathbf{e}_2\times\mathbf{e}_4} = J^{p2}_{\mathbf{e}_2\times\mathbf{e}_4} \tag{3.12c}$$

$$\sum M_{\mathbf{e}_2} = R_{\mathbf{e}_2} - L^{p2}_{\mathbf{e}_2\times\mathbf{e}_4}E_{\mathbf{e}_4} - l^{p2}_{\mathbf{e}_2\times\mathbf{e}_4}F^{p2}_{g\mathbf{e}_4} + l^{p2}_{\mathbf{e}_4}F^{p2}_{g\mathbf{e}_2\times\mathbf{e}_4} = K^{p2}_{\mathbf{e}_2} \tag{3.12d}$$

$$\sum M_{\mathbf{e}_4} = R_{\mathbf{e}_4} - L^{p2}_{\mathbf{e}_2}F_{\mathbf{e}_2\times\mathbf{e}_4} - d_3E_{\mathbf{e}_4} + l^{p2}_{\mathbf{e}_2}F^{p2}_{g\mathbf{e}_4} - l^{p2}_{\mathbf{e}_4}F^{p2}_{g\mathbf{e}_2\times\mathbf{e}_4} = K^{p2}_{\mathbf{e}_4} \tag{3.12e}$$

$$\sum M_{\mathbf{e}_2\times\mathbf{e}_4} = R_{\mathbf{e}_2\times\mathbf{e}_4} + L^{p2}_{\mathbf{e}_2}F_{\mathbf{e}_4} + d_3E_{\mathbf{e}_4} + l^{p2}_{\mathbf{e}_2}F^{p2}_{g\mathbf{e}_4} - l^{p2}_{\mathbf{e}_4}F^{p2}_{g\mathbf{e}_4} = K^{p2}_{\mathbf{e}_2\times\mathbf{e}_4} \tag{3.12f}$$

where,

$d_1 = r_{p2}\cos(-\theta_1 - \pi/2)$ $\quad$ $d_2 = r_{p2}\sin(-\theta_1 - \pi/2)$

r_{p2} being the radius of proximal-II. $F^{p2}_{g\mathbf{e}_2}$, $F^{p2}_{g\mathbf{e}_4}$, $F^{p2}_{g\mathbf{e}_2\times\mathbf{e}_4}$ are the gravity terms, $K^{p2}_{g\mathbf{e}_2}$, $K^{p2}_{g\mathbf{e}_4}$, $K^{p2}_{g\mathbf{e}_2\times\mathbf{e}_4}$ are the inertial terms and $J^{p2}_{g\mathbf{e}_2}$, $J^{p2}_{g\mathbf{e}_4}$, $J^{p2}_{g\mathbf{e}_2\times\mathbf{e}_4}$ are the inertial forces on the proximal–II along $\mathbf{e}_2$, $\mathbf{e}_4$ and $\mathbf{e}_2 \times \mathbf{e}_4$ directions, respectively.

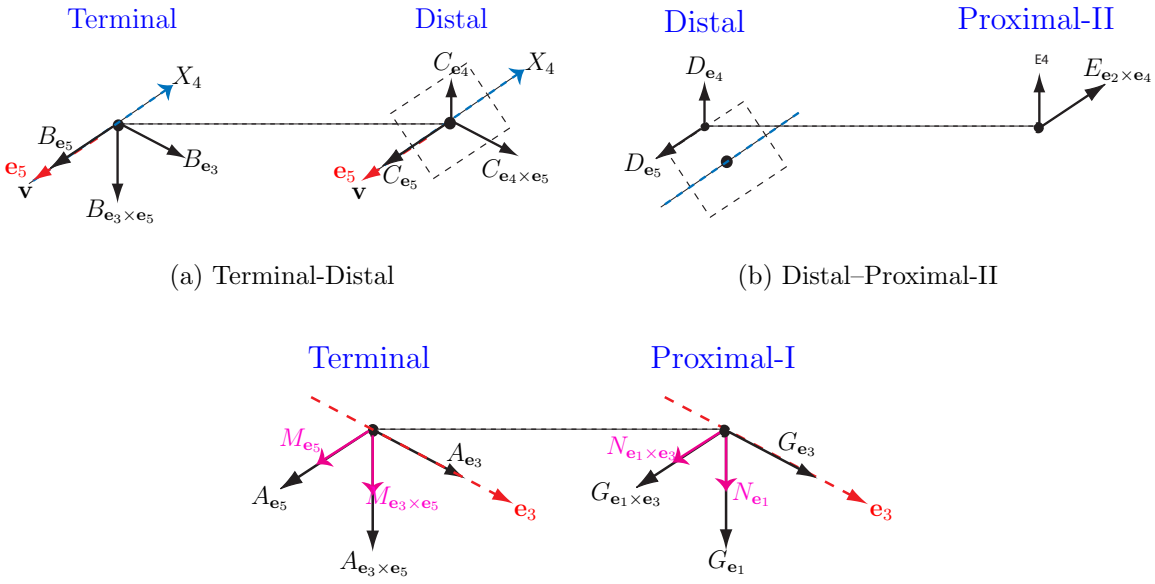

(a) Terminal-Distal

(b) Distal–Proximal-II

(c) Terminal–Proximal-I

Figure 3.15 – *Compatibility Free body diagrams*

3.3.2.6 Equations of Compatibility

Along with equilibrium equations, compatibility equations, i.e., action-reaction equilibrium equations at terminal–distal, terminal–proximal-I and distal–proximal-II interac-

tion points, as shown in Fig. 3.15, are also written.

$$B_{\mathbf{e}_3} = -C_{\mathbf{e}_4}\left(\mathbf{e}_4 \cdot \mathbf{e}_3\right) - C_{\mathbf{e}_4\times\mathbf{e}_5}\left[\left(\mathbf{e}_4 \times \mathbf{e}_5\right) \cdot \mathbf{e}_3\right] - C_{\mathbf{e}_5}\left(\mathbf{e}_5 \cdot \mathbf{e}_3\right) \tag{3.13a}$$

$$B_{\mathbf{e}_5} = -C_{\mathbf{e}_5} \tag{3.13b}$$

$$B_{\mathbf{e}_3\times\mathbf{e}_5} = -C_{\mathbf{e}_4}\left[\mathbf{e}_4 \cdot \left(\mathbf{e}_3 \times \mathbf{e}_5\right)\right] - C_{\mathbf{e}_4\times\mathbf{e}_5}\left[\left(\mathbf{e}_4 \times \mathbf{e}_5\right) \cdot \left(\mathbf{e}_3 \times \mathbf{e}_5\right)\right] \tag{3.13c}$$

$$G_{\mathbf{e}_1} = -A_{\mathbf{e}_5}\left(\mathbf{e}_5 \cdot \mathbf{e}_1\right) - A_{\mathbf{e}_3\times\mathbf{e}_5}\left[\left(\mathbf{e}_3 \times \mathbf{e}_5\right) \cdot \mathbf{e}_1\right] - A_{\mathbf{e}_3}\left(\mathbf{e}_3 \cdot \mathbf{e}_1\right) \tag{3.13d}$$

$$G_{\mathbf{e}_3} = -A_{\mathbf{e}_3} \tag{3.13e}$$

$$G_{\mathbf{e}_1\times\mathbf{e}_3} = -A_{\mathbf{e}_5}\left[\mathbf{e}_5 \cdot \left(\mathbf{e}_1 \times \mathbf{e}_3\right)\right] - A_{\mathbf{e}_3\times\mathbf{e}_5}\left[\left(\mathbf{e}_3 \times \mathbf{e}_5\right) \cdot \left(\mathbf{e}_1 \times \mathbf{e}_3\right)\right] \tag{3.13f}$$

$$N_{\mathbf{e}_1} = -M_{\mathbf{e}_5}\left(\mathbf{e}_5 \cdot \mathbf{e}_1\right) - M_{\mathbf{e}_3\times\mathbf{e}_5}\left[\left(\mathbf{e}_3 \times \mathbf{e}_5\right) \cdot \mathbf{e}_1\right] \tag{3.13g}$$

$$N_{\mathbf{e}_1\times\mathbf{e}_3} = -M_{\mathbf{e}_5}\left[\mathbf{e}_5 \cdot \left(\mathbf{e}_1 \times \mathbf{e}_3\right)\right] - M_{\mathbf{e}_3\times\mathbf{e}_5}\left[\left(\mathbf{e}_3 \times \mathbf{e}_5\right) \cdot \left(\mathbf{e}_1 \times \mathbf{e}_3\right)\right] \tag{3.13h}$$

$$E_{\mathbf{e}_4} = -D_{\mathbf{e}_4} \tag{3.13i}$$

$$E_{\mathbf{e}_2\times\mathbf{e}_4} = -D_{\mathbf{e}_5}\left[\mathbf{e}_5 \cdot \left(\mathbf{e}_2 \times \mathbf{e}_4\right)\right] \tag{3.13j}$$

3.3.2.7 Actuators Torques Calculations

The system of equations so obtained can be solved to calculate the torques experienced by the wrist actuators i.e. P_{e1} and R_{e2}. A list of necessary calculations or simplified equilibrium equations are given below.

$$B_{\mathbf{e}_3\times\mathbf{e}_5} = \left(-K^t_{\mathbf{e}_3} - l^t_{\mathbf{e}_3\times\mathbf{e}_5}F^t_{g\mathbf{e}_5} + l^t_{\mathbf{e}_5}F^t_{g\mathbf{e}_3\times\mathbf{e}_5}\right)/L^t_{\mathbf{e}_5} \tag{3.14a}$$

$$C_{\mathbf{e}_4\times\mathbf{e}_5} = \left(-K^d_{\mathbf{e}_4} + l^d_{\mathbf{e}_5}F^d_{g\mathbf{e}_4\times\mathbf{e}_5} - l^d_{\mathbf{e}_4\times\mathbf{e}_5}F^d_{g\mathbf{e}_5}\right)/L^d_{\mathbf{e}_5} \tag{3.14b}$$

$$C_{\mathbf{e}_4} = \left(-B_{\mathbf{e}_3\times\mathbf{e}_5} - C_{\mathbf{e}_4\times\mathbf{e}_5}\left[\left(\mathbf{e}_4 \times \mathbf{e}_5\right) \cdot \left(\mathbf{e}_3 \times \mathbf{e}_5\right)\right]\right) / \left[\mathbf{e}_4 \cdot \left(\mathbf{e}_3 \times \mathbf{e}_5\right)\right] \tag{3.14c}$$

$$B_{\mathbf{e}_3} = -C_{\mathbf{e}_4}\left(\mathbf{e}_4 \cdot \mathbf{e}_3\right) - C_{\mathbf{e}_4\times\mathbf{e}_5}\left[\left(\mathbf{e}_4 \times \mathbf{e}_5\right) \cdot \mathbf{e}_3\right] - C_{\mathbf{e}_5}\left(\mathbf{e}_5 \cdot \mathbf{e}_3\right) \tag{3.14d}$$

$$D_{\mathbf{e}_4} = J^d_{\mathbf{e}_4} - C_{\mathbf{e}_4} - F^d_{g\mathbf{e}_4} \tag{3.14e}$$

$$D_{\mathbf{e}_5} = \left(K^d_{\mathbf{e}_4\times\mathbf{e}_5} - L^d_{\mathbf{e}_5}C_{\mathbf{e}_4} - L^d_{\mathbf{e}_5}D_{\mathbf{e}_4} - l^d_{\mathbf{e}_4}F^d_{g\mathbf{e}_5} + l^d_{\mathbf{e}_5}F^d_{g\mathbf{e}_4}\right)/L^d_{\mathbf{e}_4} \tag{3.14f}$$

■

$$C_{\mathbf{e}_5} = J^d_{\mathbf{e}_5} - D_{\mathbf{e}_5} - F^d_{g\mathbf{e}_5} \tag{3.14g}$$

$$B_{\mathbf{e}_5} = -C_{\mathbf{e}_5} \tag{3.14h}$$

$$A_{\mathbf{e}_3} = J^t_{\mathbf{e}_3} - B_{\mathbf{e}_3} - F^t_{g\mathbf{e}_3} \tag{3.14i}$$

$$A_{\mathbf{e}_5} = J^t_{\mathbf{e}_5} - B_{\mathbf{e}_5} - F^t_{g\mathbf{e}_5} \tag{3.14j}$$

$$A_{\mathbf{e}_3\times\mathbf{e}_5} = J^t_{\mathbf{e}_3\times\mathbf{e}_5} - B_{\mathbf{e}_3\times\mathbf{e}_5} - F^t_{g\mathbf{e}_3\times\mathbf{e}_5} \tag{3.14k}$$

$$M_{\mathbf{e}_5} = K^t_{\mathbf{e}_5} + L^t_{\mathbf{e}_3} A_{\mathbf{e}_3\times\mathbf{e}_5} + l^t_{\mathbf{e}_3} F^t_{g\mathbf{e}_3\times\mathbf{e}_5} - l^t_{\mathbf{e}_3\times\mathbf{e}_5} F^t_{g\mathbf{e}_3} \tag{3.14l}$$

$$M_{\mathbf{e}_3\times\mathbf{e}_5} = K^t_{\mathbf{e}_3\times\mathbf{e}_5} - L^t_{\mathbf{e}_5} B_{\mathbf{e}_3} - L^t_{\mathbf{e}_3} A_{\mathbf{e}_5} - l^t_{\mathbf{e}_3} F^t_{g\mathbf{e}_5} + l^t_{\mathbf{e}_5} F^t_{g\mathbf{e}_3} \tag{3.14m}$$

$$N_{\mathbf{e}_1} = -M_{\mathbf{e}_5} (\mathbf{e}_5 \cdot \mathbf{e}_1) - M_{\mathbf{e}_3\times\mathbf{e}_5} [(\mathbf{e}_3 \times \mathbf{e}_5) \cdot \mathbf{e}_1] \tag{3.14n}$$

$$E_{\mathbf{e}_4} = -D_{\mathbf{e}_4} \tag{3.14o}$$

$$G_{\mathbf{e}_1\times\mathbf{e}_3} = -A_{\mathbf{e}_5} [\mathbf{e}_5 \cdot (\mathbf{e}_1 \times \mathbf{e}_3)] - A_{\mathbf{e}_3\times\mathbf{e}_5} [(\mathbf{e}_3 \times \mathbf{e}_5) \cdot (\mathbf{e}_1 \times \mathbf{e}_3)] \tag{3.14p}$$

$$P_{\mathbf{e}_1} = K^{m1}_{\mathbf{e}_1}\eta_1^2 + K^{p1}_{\mathbf{e}_1} - N_{\mathbf{e}_1} - L^{p1}_{\mathbf{e}_3} G_{\mathbf{e}_1\times\mathbf{e}_3} - l^{p1}_{\mathbf{e}_3} F^{p1}_{g\mathbf{e}_1\times\mathbf{e}_3} + l^{p1}_{\mathbf{e}_1\times\mathbf{e}_3} F^{p1}_{g\mathbf{e}_3} \tag{3.14q}$$

$$R_{\mathbf{e}_2} = K^{m1}_{\mathbf{e}_1}\eta_1^2 + K^{p2}_{\mathbf{e}_2} + L^{p2}_{\mathbf{e}_2\times\mathbf{e}_4} E_{\mathbf{e}_4} + l^{p2}_{\mathbf{e}_2\times\mathbf{e}_4} F^{p2}_{g\mathbf{e}_4} - l^{p2}_{\mathbf{e}_4} F^{p2}_{g\mathbf{e}_2\times\mathbf{e}_4} \tag{3.14r}$$

where $K^{m1}_{\mathbf{e}_1}$, $K^{m2}_{\mathbf{e}_2}$ are the inertia and η_1, η_2 are the reduction ratios of actuator-I and II, respectively.

3.3.2.8 Wrist Dynamic Parameters

The input parameters of the dynamic model of the Orthoglide wrist are:

- mass of each component (m^t, m^d, m^{p1}, m^{p2});
- distance between wrist geometric center and center of mass of each component (l);
- distance between wrist geometric center and the point of application of force (L);
- inertia matrices of wrist component (I^t, I^d, I^{p1}, I^{p2});
- inertia of actuators (K^{m1}, K^{m2});
- reduction ratios of actuators (μ_{m1},μ_{m2}).

The mass and inertial parameters are determined by means of a CAD software. The geometric parameters (l or L) along the corresponding unit vectors are determined from the drawings or CAD models of wrist components, as shown in Fig. 3.16. Numerical values of these wrist parameters are given in Table 3.6

3.3.2.9 Wrist Motors Parameters

In the preliminary design stage, FFA 20-80 harmonic drive motors are selected for both actuators. Motors specifications, taken from the motor catalogue, are given in Table 3.7. Subsequently their inertia is incorporated in the dynamic equations.

■

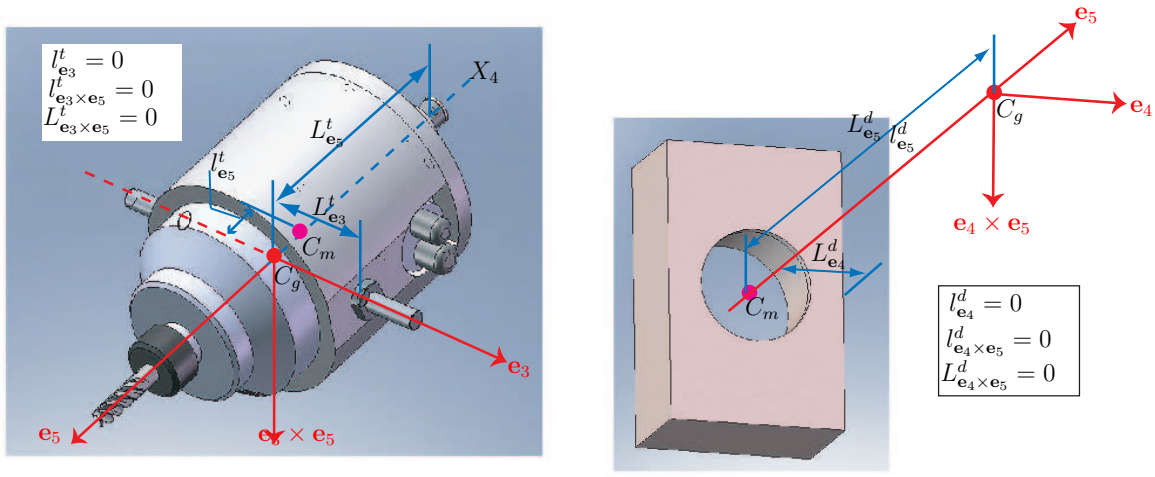

(a) Terminal

(b) Distal

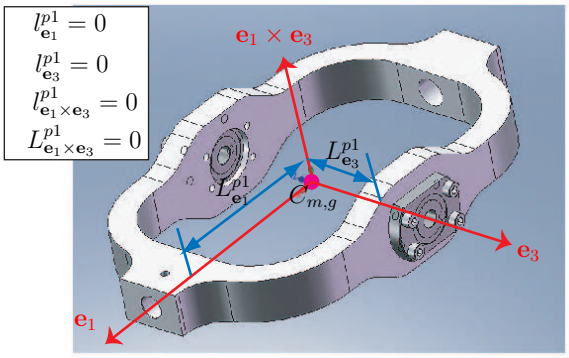

(c) Proximal-I

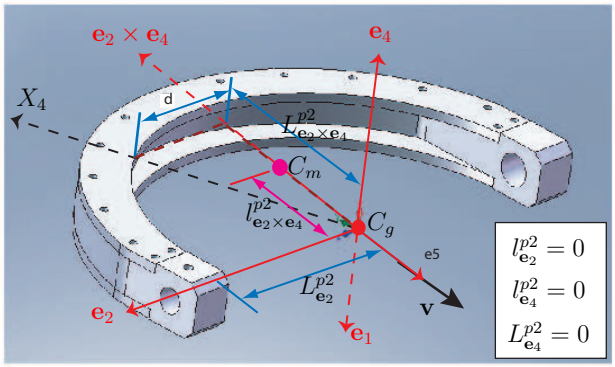

(d) Proximal-II

Figure 3.16 – *Orthoglide Wrist Parameters*

Table 3.6 – *Orthoglide wrist parameters*

Terminal			
Mass m^t	4.026 kg		
$l^t_{\mathbf{e}_3}$	0 m	$L^t_{\mathbf{e}_3}$	0.060 m
$l^t_{\mathbf{e}_5}$	-0.015 m	$L^t_{\mathbf{e}_5}$	0.120 m
$l^t_{\mathbf{e}_3\times\mathbf{e}_5}$	0 m	$L^t_{\mathbf{e}_3\times\mathbf{e}_5}$	0 m
$I^t =$	$\begin{bmatrix} 11877753.77 & -13179.19 & 4277.05 \\ -13179.19 & 6250584.07 & 16030.45 \\ 4277.05 & 16030.45 & 11891806.12 \end{bmatrix}$		10^{-3} kg.m^2
Proximal–I			
Mass m^{p1}	1.178 kg		
$l^{p1}_{\mathbf{e}_1}$	0 m	$L^{p1}_{\mathbf{e}_1}$	0.100 m
$l^{p1}_{\mathbf{e}_3}$	-0.015 m	$L^{p1}_{\mathbf{e}_3}$	0.060 m
$l^{p1}_{\mathbf{e}_1\times\mathbf{e}_3}$	0 m	$L^{p1}_{\mathbf{e}_1\times\mathbf{e}_3}$	0 m
$I^{p1} =$	$\begin{bmatrix} 6520212.98 & -0.01 & 0.01 \\ -0.01 & 10613268.62 & 0 \\ 0.01 & 0 & 4359403.54 \end{bmatrix}$		10^{-3} kg.m^2
Proximal–II			
Mass m^{p2}	1.7159 kg		
$l^{p2}_{\mathbf{e}_2}$	0 m	$L^{p2}_{\mathbf{e}_2}$	0.130 m
$l^{p4}_{\mathbf{e}_2}$	0 m	$L^{p2}_{\mathbf{e}_4}$	0 m
$l^{p2}_{\mathbf{e}_2\times\mathbf{e}_2}$	0.072 m	d	$r_{p2}\sin(-\theta_1-\pi/2)$
		$L^{p2}_{\mathbf{e}_2\times\mathbf{e}_4}$	$r_{p2}\cos(-\theta_1-\pi/2)$
$I^{p2} =$	$\begin{bmatrix} 13018906.53 & 2.01 & -0.37 \\ 2.01 & 16870339.12 & -6371.34 \\ -0.37 & -6371.34 & 29589152.59 \end{bmatrix}$		10^{-3} kg.m^2
Distal			
Mass m^d	0.04094 kg		
$l^d_{\mathbf{e}_4}$	0 m	$L^d_{\mathbf{e}_4}$	0.010 m
$l^d_{\mathbf{e}_5}$	-0.120 m	$L^d_{\mathbf{e}_5}$	0.120 m
$l^d_{\mathbf{e}_4\times\mathbf{e}_5}$	0 m	$L^d_{\mathbf{e}_4\times\mathbf{e}_5}$	0 m
$I^d =$	$\begin{bmatrix} 600144.89 & 0 & 0 \\ 0 & 5550.32 & 0 \\ 0 & 0 & 602694.90 \end{bmatrix}$		10^{-3} kg.m^2

Table 3.7 – *Motors parameters of the Orthoglide Wrist*

FFA 20-80 Harmonic Drive	
Nominal speed	2500 rpm
Maximum speed	6500 rpm
Maximum torque at output shaft	74 Nm
Continuous torque	23 Nm
Moment of inertia	0.00262 kg.m^4
Rated power	800 W

3.3.3 Results: Kinematic and Dynamic Analysis of Wrist

The kinematics of the Orthoglide wrist is analyzed for the test trajectories presented in Sec. 3.2. The velocity of the end-effector i.e. point P (on the tip of the wrist tool), throughout the trajectory, is taken as constant i.e. $V_p = 1$ m/s.

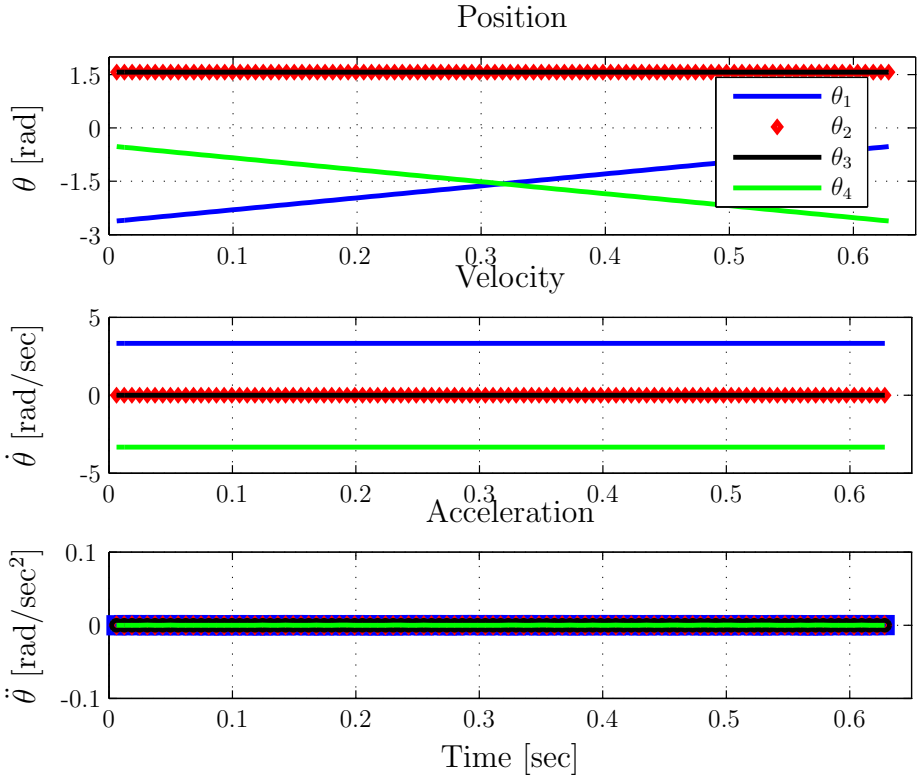

Figure 3.17 – *Joints positions, velocities and accelerations (Traj-I, R=0.200 m, $\phi = 90°$)*

Figures 3.17 and 3.18 display the plots of position, velocity and acceleration of the wrist joints for the test trajectory-I for $\phi = 90°$ and $\phi = 45°$, respectively, with $R = 0.250$ m. Similarly, Fig. 3.19 shows the joints angles, rates and accelerations for trajectory-II with $R = 0.200$ m and $\gamma = 45°$.

Figure 3.17 is the case where wrist end-effector moves in the YZ-plane ($\phi = 90°$) so only one of the wrist actuator with joint displacement (θ_1) works, while Figs. 3.18 and 3.19 represent the cases where both of actuators work. Compared to Traj-I, both wrist

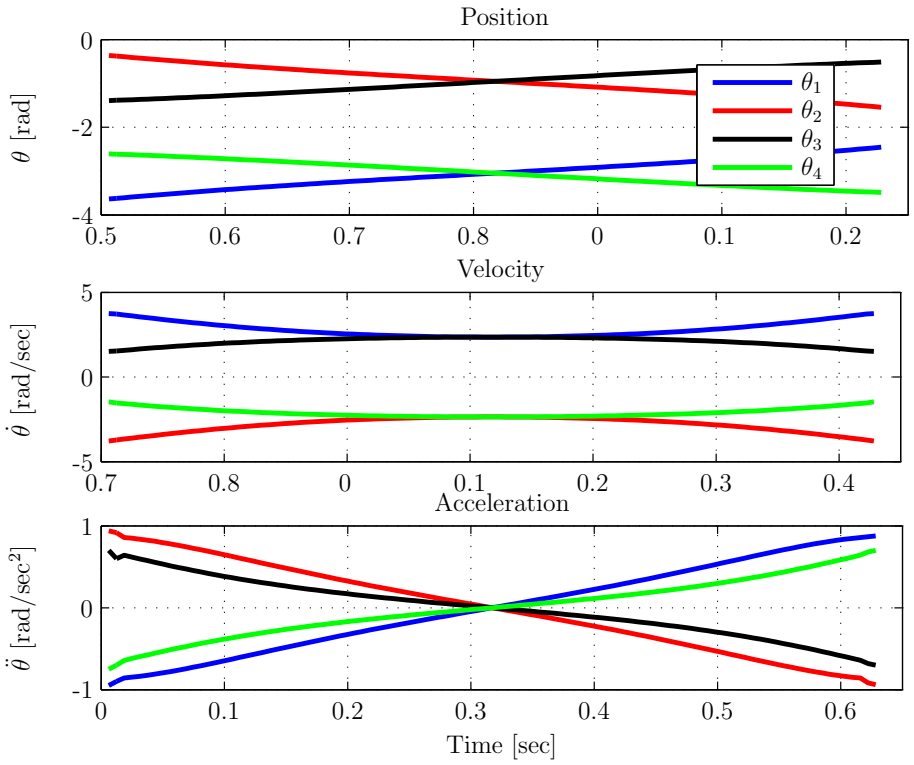

Figure 3.18 – *Joints positions, velocities and accelerations (Traj-I, R=0.200 m, $\phi = 45°$)*

actuators experience greater velocities and accelerations for Traj-II (max velocity=5 m/s and max acceleration=22 m/s^2). This can be explained by the higher order variations of rotation angles in Traj-II than to linear variations of rotation angles in Traj-I.

For the same test trajectories, the dynamic model is used to calculate the actuators torques, as shown in Fig. 3.20.

Table 3.8 – *Kinematics and dynamics peak values for Traj.-II (without external forces)*

γ [deg]	Radius [m]	Max Velocity [rad/s]				Max Acceleration] [rad/s^2]				Max Torque [Nm]		Max Power [W]	
		$\dot{\theta}_1$	$\dot{\theta}_2$	$\dot{\theta}_3$	$\dot{\theta}_4$	$\ddot{\theta}_1$	$\ddot{\theta}_2$	$\ddot{\theta}_3$	$\ddot{\theta}_4$	τ_1	τ_2	P_1	P_2
30	0.250	2.31	2.31	2.00	2.00	7.29	7.29	9.21	9.21	0.68	1.22	0.64	1.20
	0.150	3.84	3.84	3.33	3.33	20.24	20.24	25.59	25.59	0.90	1.67	1.58	2.77
	0.100	5.77	5.77	5.00	5.00	45.54	45.54	57.58	57.59	1.35	2.55	3.89	6.43
	0.050	11.53	11.53	10.00	10.00	182.15	182.15	230.30	230.35	3.75	7.29	24.33	37.46
45	0.250	3.99	3.99	2.83	2.83	13.96	13.96	15.92	15.92	0.94	1.73	1.26	2.43
	0.150	6.65	6.65	4.71	4.71	38.78	38.78	44.22	44.22	1.23	2.37	3.86	5.97
	0.100	9.98	9.98	7.07	7.07	87.26	87.26	99.48	99.48	1.79	3.62	11.14	14.69
	0.050	19.96	19.96	14.14	14.14	349.03	349.03	397.94	397.94	5.58	10.38	80.14	92.25
60	0.250	6.90	6.90	3.46	3.46	34.05	34.05	27.36	27.36	1.11	2.16	3.17	5.22
	0.150	11.49	11.49	5.77	5.77	94.59	94.59	75.99	75.99	1.54	3.03	13.47	15.78
	0.100	17.24	17.24	8.66	8.66	212.82	212.82	170.98	170.98	3.31	4.72	44.17	45.04
	0.050	34.48	34.48	17.32	17.32	851.30	851.30	683.92	683.92	12.94	13.84	347.23	320.89

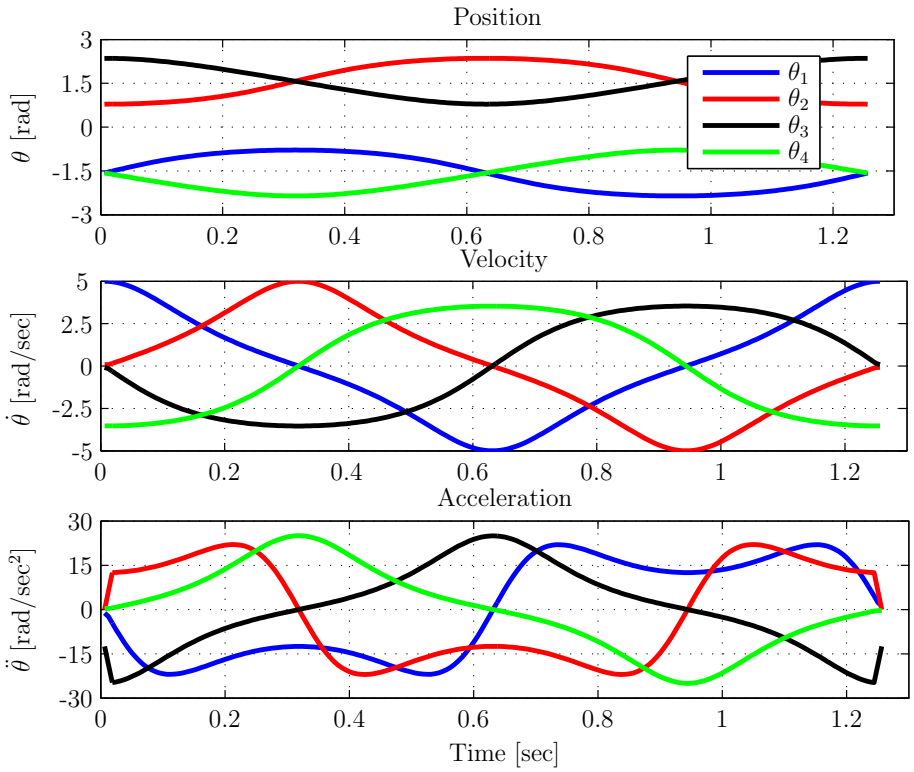

Figure 3.19 – *Position, velocity and acceleration of articulations (Traj-II, R=0.200 m, $\gamma = 45°$)*

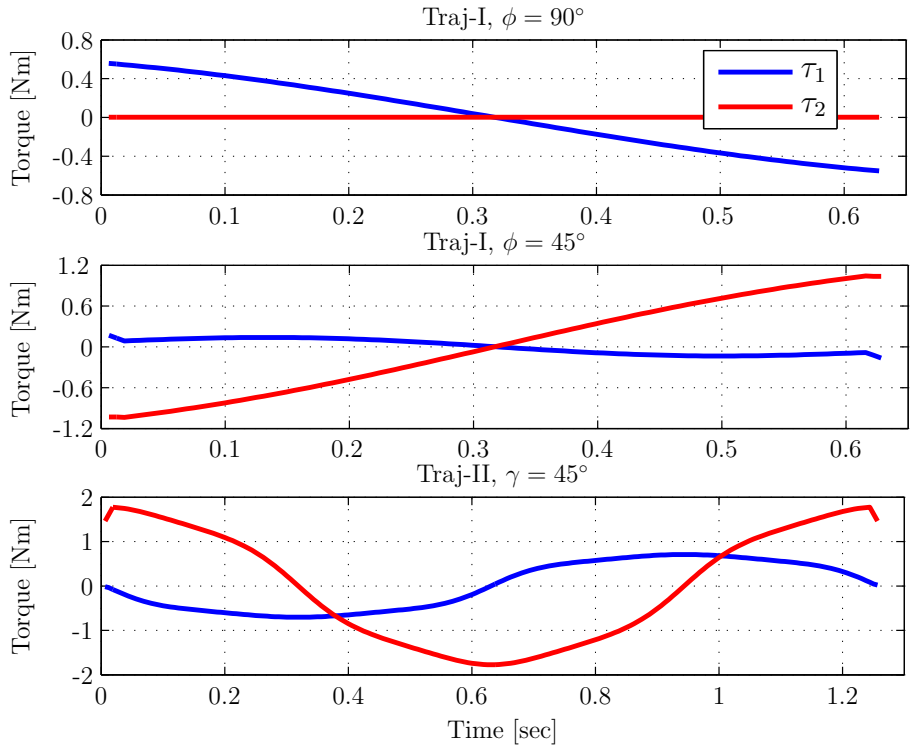

Figure 3.20 – *Actuators torques vs time (Traj-I and II, R=0.200 m)*

Trajectory-II is analyzed for different radii ($R = 0.050, 0.100, 0.150, 0.250$ m) and for $\gamma = 30, 45, 60$ degrees. For each case, maximum values of actuators velocity, acceleration

and torques are calculated, as summarized in Table 3.8, where τ_1 and P_1 (resp. τ_2 and P_2) is the torque and the power requirement of actuators 1 (resp. 2). Bar charts of peak torques and powers versus trajectory radii and orientation γ are shown in Fig. 3.21. Similarly, Fig. 3.22 shows the actuators torques for different values of γ with $R = 0.250$ m. From Table 3.8, it is apparent that the lower R and the higher γ, the higher the required actuators torque and power. Accordingly, a trajectory with a radius R equal to 0.050 m and an orientation γ equal to 60° is more critical than the other test trajectories; it requires higher maximum velocities, accelerations and torques. Furthermore, the peak values of velocities and accelerations of both actuators are the same for all test trajectories.

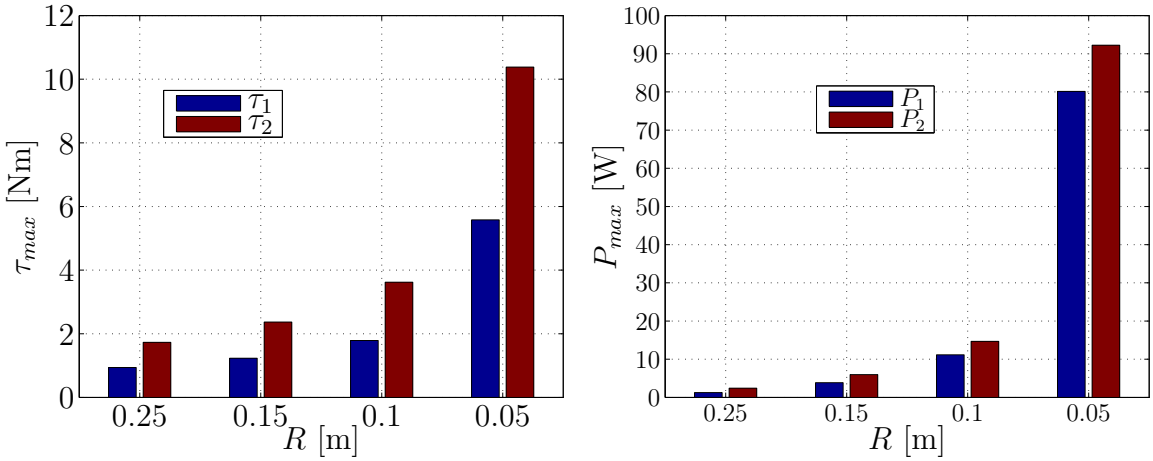

(a) τ_{max} vs R ($\gamma =$ 45°)

(b) P_{max} vs R ($\gamma =$ 45°)

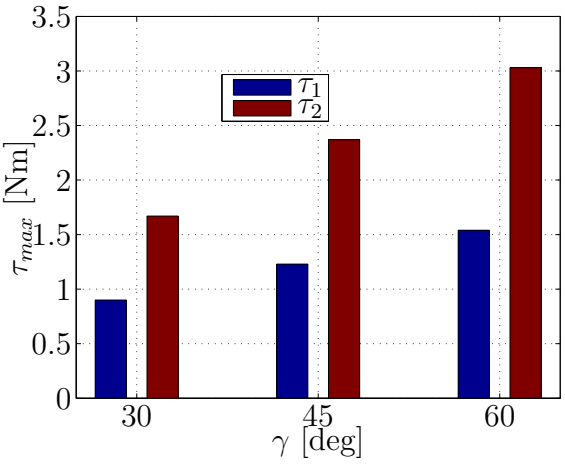

(c) τ_{max} vs γ ($R = 0.15$ m)

Figure 3.21 – *Actuators maximum torques and powers vs trajectory radii and γ (Traj. II)*

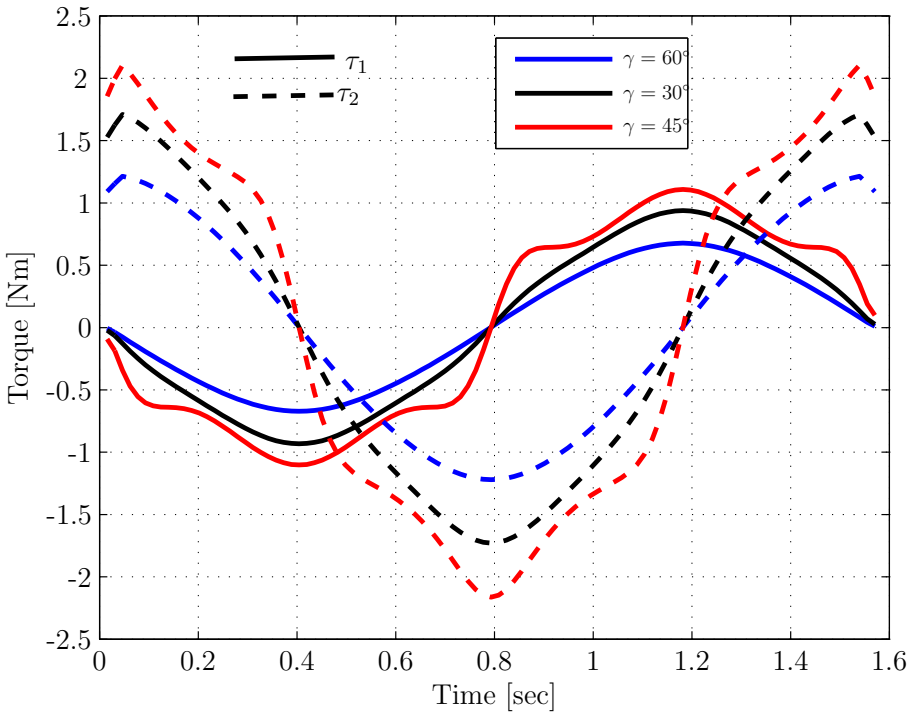

Figure 3.22 – *Actuators torques with different values of* γ *(*$R = 0.250$ *m, Traj-II)*

3.3.3.1 Results Verification–Virtual Work Approach

In order to verify the results obtained with the Newton-Euler approach, the principle of virtual work is used. As a matter of fact, variations in kinetic and potential energies, i.e., ΔKE and ΔPE are evaluated during a time interval Δt. The total energy variation ΔE over Δt is defined as $\Delta E = \Delta KE + \Delta PE$. The total virtual work W is calculated as the product of the mean torques and the corresponding angular displacement during each time interval Δt, i.e.,

$$W = \bar{\tau}_1 \Delta\theta_1 + \bar{\tau}_2 \Delta\theta_2 \tag{3.15}$$

$\bar{\tau}_1$ and $\bar{\tau}_2$ being the mean torques of actuators 1 and 2, respectively, during time Δt.

In the light of principal of virtual work, the difference between the global virtual work W and ΔE should be null due to the energy conservation. Accordingly, we computed the difference between W and ΔE and checked the dynamic model of the wrist, i.e., $\Delta W = \Delta E - W$. This difference is highlighted in Fig. 3.23 for the above considered test trajectories. It turns out that ΔW is null in all cases. Consequently, the dynamic model of the wrist makes sense. The relations to calculate the kinematic and potential energies of the wrist components are given in Annex A.

■

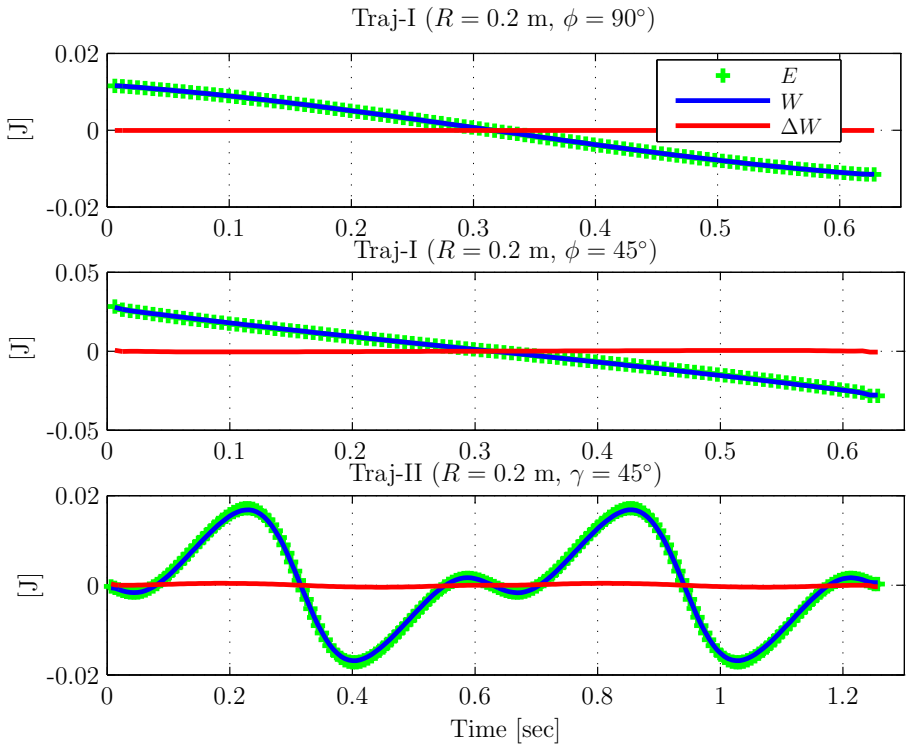

Figure 3.23 – *Energy balance for wrist dynamics (Traj-I and II)*

3.3.4 Effect of Machining Forces on Actuators Torque

So far we have not taken into account the effect of the machining or cutting forces on the wrist dynamics. To cater for these forces we redraw the free body diagram of the terminal as shown in Fig. 3.24. The distance between the tool tip and geometric center of wrist is taken as L_c and cutting force, $\mathbf{f}_c$, is resolved in its three orthogonal components, i.e.,

$$\mathbf{f_c} = \begin{bmatrix} F_{ce3} & F_{ce5} & F_{ce3\times e5} \end{bmatrix}^{\mathbf{T}} \tag{3.16}$$

For the FBD shown in Fig. 3.24, rewriting the fore-mentioned equilibrium equations for terminal (Eqs. 3.9), we get,

$$\sum F_{\mathbf{e}_3} = A_{\mathbf{e}_3} + B_{\mathbf{e}_3} + F^t_{g\mathbf{e}_3} + F_{c\mathbf{e}_3} = J^t_{\mathbf{e}_3} \tag{3.17a}$$

$$\sum F_{\mathbf{e}_5} = A_{\mathbf{e}_5} + B_{\mathbf{e}_5} + F^t_{g\mathbf{e}_5} + F_{c\mathbf{e}_5} = J^t_{\mathbf{e}_5} \tag{3.17b}$$

$$\sum F_{\mathbf{e}_3\times\mathbf{e}_5} = A_{\mathbf{e}_3\times\mathbf{e}_5} + B_{\mathbf{e}_3\times\mathbf{e}_5} + F^t_{g\mathbf{e}_3\times\mathbf{e}_5} + F_{c\mathbf{e}_3\times\mathbf{e}_5} = J^t_{\mathbf{e}_3\times\mathbf{e}_5} \tag{3.17c}$$

$$\sum M_{\mathbf{e}_3} = -L^t_{\mathbf{e}_5} B_{\mathbf{e}_3\times\mathbf{e}_5} - l^t_{\mathbf{e}_3\times\mathbf{e}_5} F^t_{g\mathbf{e}_5} + l^t_{\mathbf{e}_5} F^t_{g\mathbf{e}_3\times\mathbf{e}_5} + L_c F_{c\mathbf{e}_3\times\mathbf{e}_5} = K^t_{\mathbf{e}_3} \tag{3.17d}$$

$$\sum M_{\mathbf{e}_5} = M_{\mathbf{e}_5} - L^t_{\mathbf{e}_3} A_{\mathbf{e}_3\times\mathbf{e}_5} - l^t_{\mathbf{e}_3} F^t_{g\mathbf{e}_3\times\mathbf{e}_5} + l^t_{\mathbf{e}_3\times\mathbf{e}_5} F^t_{g\mathbf{e}_3} = K^t_{\mathbf{e}_5} \tag{3.17e}$$

$$\sum M_{\mathbf{e}_3\times\mathbf{e}_5} = M_{\mathbf{e}_3\times\mathbf{e}_5} + L^t_{\mathbf{e}_5} B_{\mathbf{e}_3} + L^t_{\mathbf{e}_3} A_{\mathbf{e}_5} + l^t_{\mathbf{e}_3} F^t_{g\mathbf{e}_5} - l^t_{\mathbf{e}_5} F^t_{g\mathbf{e}_3} - L_c F_{c\mathbf{e}_3} = K^t_{\mathbf{e}_3\times\mathbf{e}_5} \tag{3.17f}$$

■

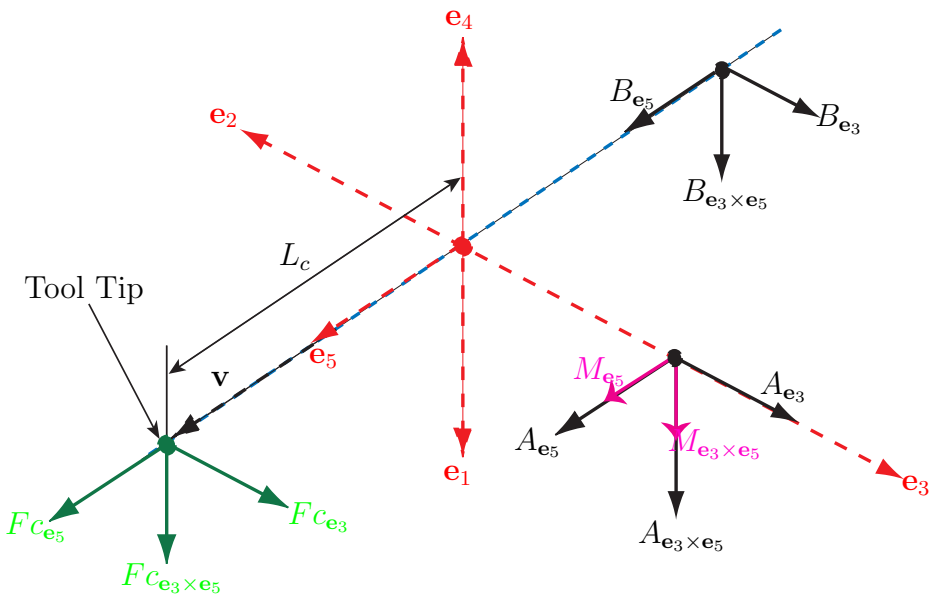

Figure 3.24 – *Terminal FBD with machining forces*

With these new set of equilibrium equations, some of the actuators equations, presented earlier (Eqs. 3.14), containing the terms of the terminal, will change accordingly. Modified set of actuators equations is:

$$B_{\mathbf{e}_3\times\mathbf{e}_5} = \left(-K^t_{\mathbf{e}_3} - l^t_{\mathbf{e}_3\times\mathbf{e}_5}F^t_{g\mathbf{e}_5} + l^t_{\mathbf{e}_5}F^t_{g\mathbf{e}_3\times\mathbf{e}_5} + L_cF_{c\mathbf{e}_3\times\mathbf{e}_5}\right)/L^t_{\mathbf{e}_5} \tag{3.18a}$$

$$C_{\mathbf{e}_4\times\mathbf{e}_5} = \left(-K^d_{\mathbf{e}_4} + l^d_{\mathbf{e}_5}F^d_{g\mathbf{e}_4\times\mathbf{e}_5} - l^d_{\mathbf{e}_4\times\mathbf{e}_5}F^d_{g\mathbf{e}_5}\right)/L^d_{\mathbf{e}_5} \tag{3.18b}$$

$$C_{\mathbf{e}_4} = \left(-B_{\mathbf{e}_3\times\mathbf{e}_5} - C_{\mathbf{e}_4\times\mathbf{e}_5}\left[(\mathbf{e}_4\times\mathbf{e}_5)\cdot(\mathbf{e}_3\times\mathbf{e}_5)\right]\right)/\left[\mathbf{e}_4\cdot(\mathbf{e}_3\times\mathbf{e}_5)\right] \tag{3.18c}$$

$$B_{\mathbf{e}_3} = -C_{\mathbf{e}_4}(\mathbf{e}_4\cdot\mathbf{e}_3) - C_{\mathbf{e}_4\times\mathbf{e}_5}\left[(\mathbf{e}_4\times\mathbf{e}_5)\cdot\mathbf{e}_3\right] - C_{\mathbf{e}_5}(\mathbf{e}_5\cdot\mathbf{e}_3) \tag{3.18d}$$

$$D_{\mathbf{e}_4} = J^d_{\mathbf{e}_4} - C_{\mathbf{e}_4} - F^d_{g\mathbf{e}_4} \tag{3.18e}$$

$$D_{\mathbf{e}_5} = \left(K^d_{\mathbf{e}_4\times\mathbf{e}_5} - L^d_{\mathbf{e}_5}C_{\mathbf{e}_4} - L^d_{\mathbf{e}_5}D_{\mathbf{e}_4} - l^d_{\mathbf{e}_4}F^d_{g\mathbf{e}_5} + l^d_{\mathbf{e}_5}F^d_{g\mathbf{e}_4}\right)/L^d_{\mathbf{e}_4} \tag{3.18f}$$

$$C_{\mathbf{e}_5} = J^d_{\mathbf{e}_5} - D_{\mathbf{e}_5} - F^d_{g\mathbf{e}_5} \tag{3.18g}$$

$$B_{\mathbf{e}_5} = -C_{\mathbf{e}_5} \tag{3.18h}$$

$$A_{\mathbf{e}_3} = J^t_{\mathbf{e}_3} - B_{\mathbf{e}_3} - F^t_{g\mathbf{e}_3} - F_{c\mathbf{e}_3} \tag{3.18i}$$

$$A_{\mathbf{e}_5} = J^t_{\mathbf{e}_5} - B_{\mathbf{e}_5} - F^t_{g\mathbf{e}_5} - F_{c\mathbf{e}_5} \tag{3.18j}$$

$$A_{\mathbf{e}_3\times\mathbf{e}_5} = J^t_{\mathbf{e}_3\times\mathbf{e}_5} - B_{\mathbf{e}_3\times\mathbf{e}_5} - F^t_{g\mathbf{e}_3\times\mathbf{e}_5} - F_{c\mathbf{e}_3\times\mathbf{e}_5} \tag{3.18k}$$

$$M_{\mathbf{e}_5} = K^t_{\mathbf{e}_5} + L^t_{\mathbf{e}_3}A_{\mathbf{e}_3\times\mathbf{e}_5} + l^t_{\mathbf{e}_3}F^t_{g\mathbf{e}_3\times\mathbf{e}_5} - l^t_{\mathbf{e}_3\times\mathbf{e}_5}F^t_{g\mathbf{e}_3} \tag{3.18l}$$

$$M_{\mathbf{e}_3\times\mathbf{e}_5} = K^t_{\mathbf{e}_3\times\mathbf{e}_5} - L^t_{\mathbf{e}_5}B_{\mathbf{e}_3} - L^t_{\mathbf{e}_3}A_{\mathbf{e}_5} - l^t_{\mathbf{e}_3}F^t_{g\mathbf{e}_5} + l^t_{\mathbf{e}_5}F^t_{g\mathbf{e}_3} + L_cF_{c\mathbf{e}_3} \tag{3.18m}$$

$$N_{\mathbf{e}_1} = -M_{\mathbf{e}_5}(\mathbf{e}_5\cdot\mathbf{e}_1) - M_{\mathbf{e}_3\times\mathbf{e}_5}\left[(\mathbf{e}_3\times\mathbf{e}_5)\cdot\mathbf{e}_1\right] \tag{3.18n}$$

$$E_{\mathbf{e}_4} = -D_{\mathbf{e}_4} \tag{3.18o}$$

$$G_{\mathbf{e}_1\times\mathbf{e}_3} = -A_{\mathbf{e}_5}\left[\mathbf{e}_5\cdot(\mathbf{e}_1\times\mathbf{e}_3)\right] - A_{\mathbf{e}_3\times\mathbf{e}_5}\left[(\mathbf{e}_3\times\mathbf{e}_5)\cdot(\mathbf{e}_1\times\mathbf{e}_3)\right] \tag{3.18p}$$

■

$$P_{\mathbf{e}_1} = K^{m1}_{\mathbf{e}_1}\eta_1^2 + K^{p1}_{\mathbf{e}_1} - N_{\mathbf{e}_1} - L^{p1}_{\mathbf{e}_3}G_{\mathbf{e}_1\times\mathbf{e}_3} - l^{p1}_{\mathbf{e}_3}F^{p1}_{g\mathbf{e}_1\times\mathbf{e}_3} + l^{p1}_{\mathbf{e}_1\times\mathbf{e}_3}F^{p1}_{g\mathbf{e}_3} \tag{3.18q}$$

$$R_{\mathbf{e}_2} = K^{m2}_{\mathbf{e}_1}\eta_2^2 + K^{p2}_{\mathbf{e}_2} + L^{p2}_{\mathbf{e}_2\times\mathbf{e}_4}E_{\mathbf{e}_4} + l^{p2}_{\mathbf{e}_2\times\mathbf{e}_4}F^{p2}_{g\mathbf{e}_4} - l^{p2}_{\mathbf{e}_4}F^{p2}_{g\mathbf{e}_2\times\mathbf{e}_4} \tag{3.18r}$$

In order to analyze the effects of machining or cutting forces, three equal components of $\mathbf{f}_c$ are assumed to simplify the problem, i.e.,

$$F_{c\mathbf{e}_3} = F_{c\mathbf{e}_5} = F_{c\mathbf{e}_3\times\mathbf{e}_5} = F_c$$

Actuators torques are calculated while considering the machining forces of different magnitudes and for trajectory radius of 0.150 m with $\gamma = 45°$ and $L_c = 0.060$ m. Results are presented in Fig. 3.25.

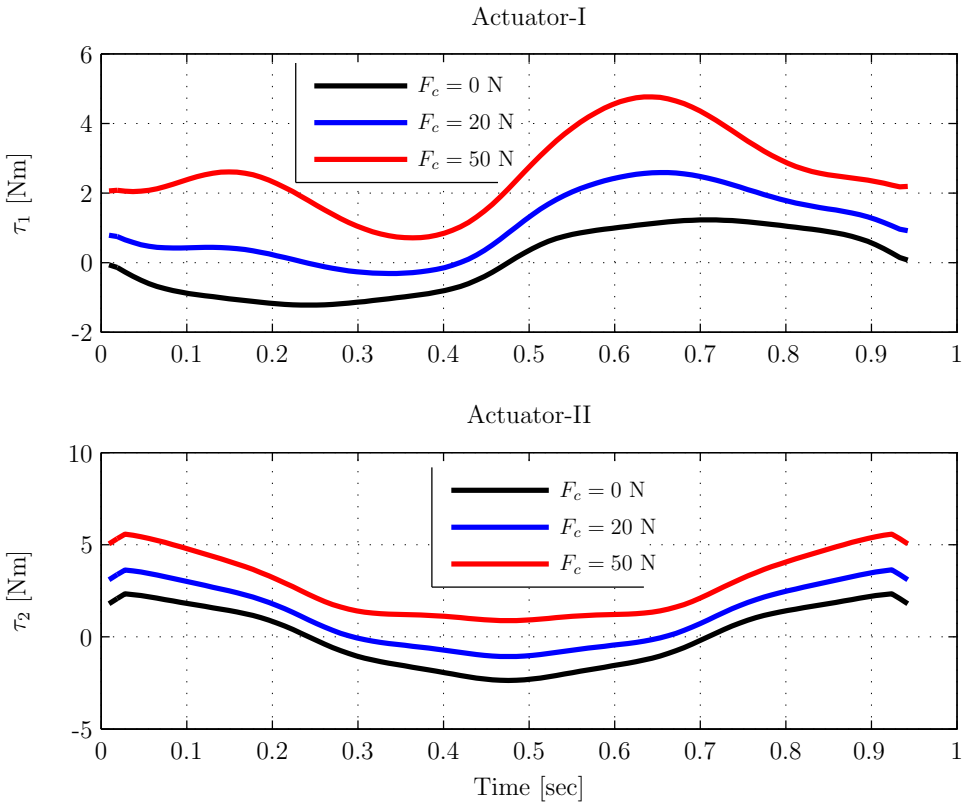

Figure 3.25 – *Actuators torques vs Time with machining forces ($\gamma = 45°$ $R = 0.150$ m, Traj-II)*

Similarly, three values of moment arm of machining forces L_c are taken, i.e., L_c= 0.06, 0.110 and 0.15 m and maximum actuators torques and powers are calculated for different values of F_c. Results are presented in Table 3.9 and are shown in Fig. 3.26.

Figure 3.26-(c) shows that for the machining forces of 125 N and 150 N, actuators torques exceed the motors continuous torque (23 Nm) but still they remain well below the maximum motors torque (74 Nm). Hence, for the given test trajectories, considered motors can work for a range of machining forces. These results also represent the considerable influence of the length of the moment arm L_c of the machining forces (or the tool length)

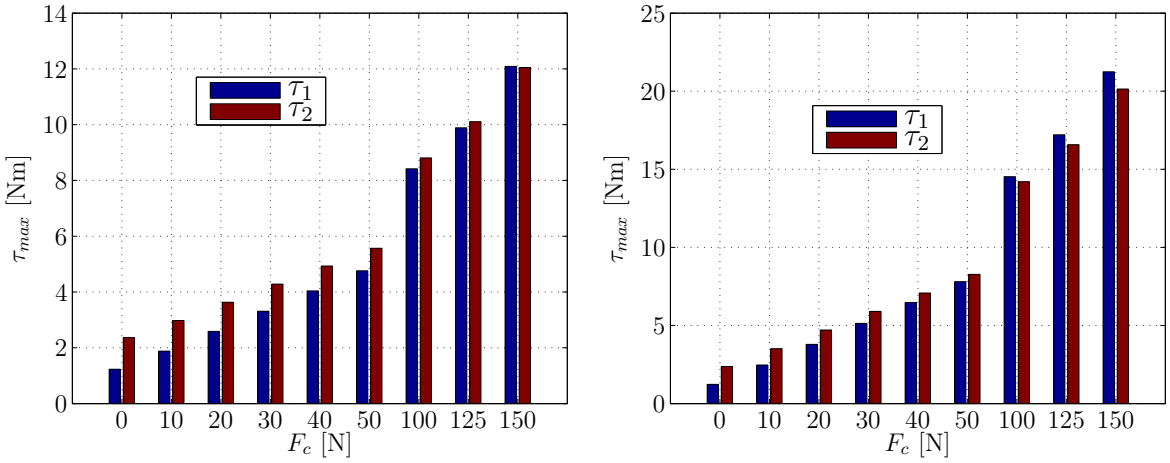

(a) L_c= 0.060 m (b) L_c= 0.110 m

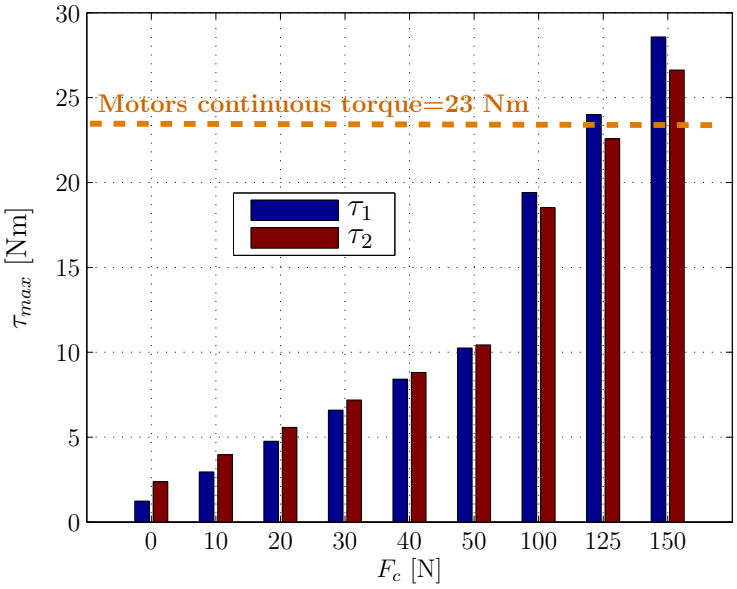

(c) L_c= 0.150 m

Figure 3.26 – *Actuators maximum torques with respect to machining forces (Traj-II, R=0.150 m)*

Table 3.9 – *Maximum actuators torques and powers with machining forces ($\gamma = 45°$, $R = 0.150$ m, Traj-II)*

F_c [N]	$L_c = 0.060$ m				$L_c = 0.110$ m				$L_c = 0.150$ m			
	Max Torque [Nm]		Max Power [W]		Max Torque [Nm]		Max Power [W]		Max Torque [Nm]		Max Power [W]	
0	1.23	2.37	3.86	5.97	1.23	2.37	3.86	5.97	1.23	2.37	3.86	5.97
10	1.88	2.98	6.86	8.46	2.47	3.52	9.38	10.59	2.95	3.96	11.42	12.36
20	2.59	3.63	9.89	11.03	3.79	4.71	14.99	15.48	4.76	5.57	19.08	19.16
30	3.31	4.28	12.95	13.70	5.13	5.90	20.61	20.55	6.59	7.19	26.78	26.17
40	4.04	4.93	16.02	16.38	6.47	7.08	26.27	25.69	8.42	8.81	34.53	33.36
50	4.76	5.57	19.08	19.16	7.81	8.27	31.95	30.96	10.25	10.43	42.29	40.63
100	8.42	8.81	34.53	33.36	14.53	14.21	60.38	57.86	19.41	18.52	81.05	77.89
125	9.89	10.11	40.74	39.16	17.21	16.58	71.75	68.86	23.99	22.57	100.4	96.71
150	12.09	12.05	50.04	48.02	21.24	20.14	88.80	85.42	28.57	26.62	119.8	115.59

on the actuators torques. It should be kept in mind that, in these results, F_c is not the total machining force but is the constant component of $\mathbf{f_c}$. Magnitude of total machining force will be equal to $\sqrt{F_c^2 + F_c^2 + F_c^2} = \sqrt{3}F_c$.

3.3.5 Conclusions

In this section, we dealt with the kinematics and dynamics of the spherical wrist of Orthoglide 5-axis. The kinematic and dynamic performance of the wrist were analyzed and its actuators primarily selection was proposed by means of several test trajectories. A methodology was introduced to evaluate the velocities, accelerations and torques required by the actuators. The influence of the machining forces as well as the tool length on the wrist actuators torques and powers were also studied. It turns out that the primarily selected motors with a continuous torque of 23 Nm and of power equal to 800 W are suitable for the wrist of the Orthoglide 5-axis prototype. Finally, the following points should be considered for further analysis:

- the friction between the links;
- the planar joint between distal and proximal-II should be analyzed more precisely;
- the weight of the machining tool;
- more complex, sharp and random trajectories should be analyzed;
- real machining forces instead of constant machining force components.

3.4 Kinematics and Dynamics of the Orthoglide 3-axis

The Orthoglide 5-axis mechanism is composed of a 3-dof translating manipulator and a 2-dof spherical wrist. In the previous sections, we carried out the kinematic and dynamic analysis of the spherical wrist. In this section, the kinematic and dynamic of the 3-dof translating manipulator, Orthoglide 3-axis, is analyzed, thanks to the thesis research work of Guégan (2003). Eventually, a preliminary selection of the motor is proposed based on the analysis.

3.4.1 Kinematic Analysis of the Orthoglide 3-axes

The geometric parameters of the Orthoglide 3-axis are defined as a function of the size of a prescribed cubic Cartesian workspace that is free of singularities and internal collision. The kinematic architecture of the Orthoglide-3axis is shown in Fig. 3.27 where A_1B_1, A_2B_2 and A_3B_3 represent the prismatic joints and P is the end-effector. Due to its Delta-linear architecture, the Orthoglide 3-axis is a translating parallel manipulator with 3-dof.
A simplified model of the Orthoglide 3-axis is illustrated in Fig. 3.28 (Pashkevich *et al.*, 2006) in which three links of length L are connected by means of a spherical joint to end-effector P at one end and to the corresponding prismatic joints A_i at the other end. θ_x, θ_y and θ_z are the angles between the links and the corresponding prismatic joints axes. The input position vector of the prismatic joint variables is represented by $\rho = (\rho_x, \quad \rho_y, \quad \rho_z)$ and the output position vector of the end-effector by $\mathbf{p} = (p_x, \quad p_y, \quad p_z)$.
Using these notations, the inverse kinematic relations for a spherical singularity free workspace can be written as (Pashkevich *et al.*, 2005).

$$\begin{aligned} \rho_x &= p_x + \sqrt{L^2 - p_y^2 - p_z^2} \\ \rho_y &= p_y + \sqrt{L^2 - p_x^2 - p_z^2} \\ \rho_z &= p_z + \sqrt{L^2 - p_x^2 - p_y^2} \end{aligned} \tag{3.19}$$

Due to the Orthoglide geometry and manufacturing technology, the displacement of its prismatic joints is bounded (Pashkevich *et al.*, 2005), namely,

$$0 \leqslant \rho_{x,y,z} \leqslant 2L \tag{3.20}$$

The kinematic performance of the Orthoglide 3-axis is analyzed by means of the foregoing test trajectories with constant velocity of the end-effector i.e. $V_p = 1$ m/s. Accordingly the actuated prismatic joints positions, rates and accelerations are plotted in Figs. 3.29 to 3.31, for both test trajectories with trajectory radius of 0.2 m.
Figure 3.29 shows the kinematic performance required by the prismatic actuators when

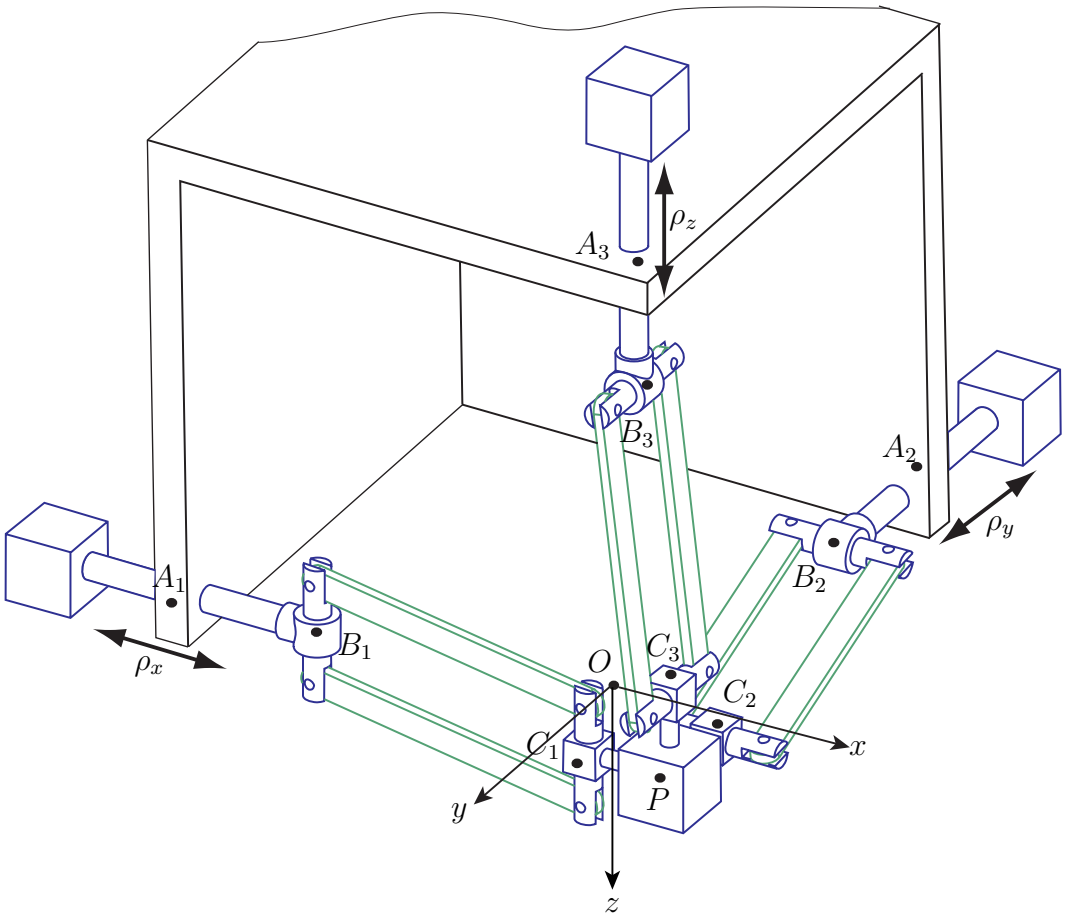

Figure 3.27 – *Schematic of the Orthoglide 3-axis*

end-effector P moves in YZ-plane. Even if P does not move along X-axis, the displacement of the prismatic actuator mounted along X-axis is not null. Figures 3.30 and 3.31 display the required kinematic performance of the motors when P follows Traj.-I ($\phi = 45°$) and Traj.-II ($\gamma = 45°$), respectively, for $R = 0.200\,\text{m}$. The maximum velocities and accelerations of the prismatic actuators required for the three test trajectories are summarized in Table 3.10. It can be noticed that the maximum prismatic joint velocity is equal to 1.07 m/s whereas maximum acceleration is equal to 6.33 m/s^2 for the considered trajectories.

Table 3.10 – *Maximum prismatic joints rates and accelerations for test trajectories ($R = 0.200\,m$)*

Test Trajectory	Max Absolute Velocity [m/s]			Max Absolute Acceleration [m/s^2]		
Traj-I, $\phi = 90°$	0.12	1.01	1.06	0.62	6.32	6.32
Traj-I, $\phi = 45°$	0.77	0.77	1.07	4.51	4.51	6.33
Traj-II, $\gamma = 45°$	0.77	0.77	1.07	4.51	4.51	6.33

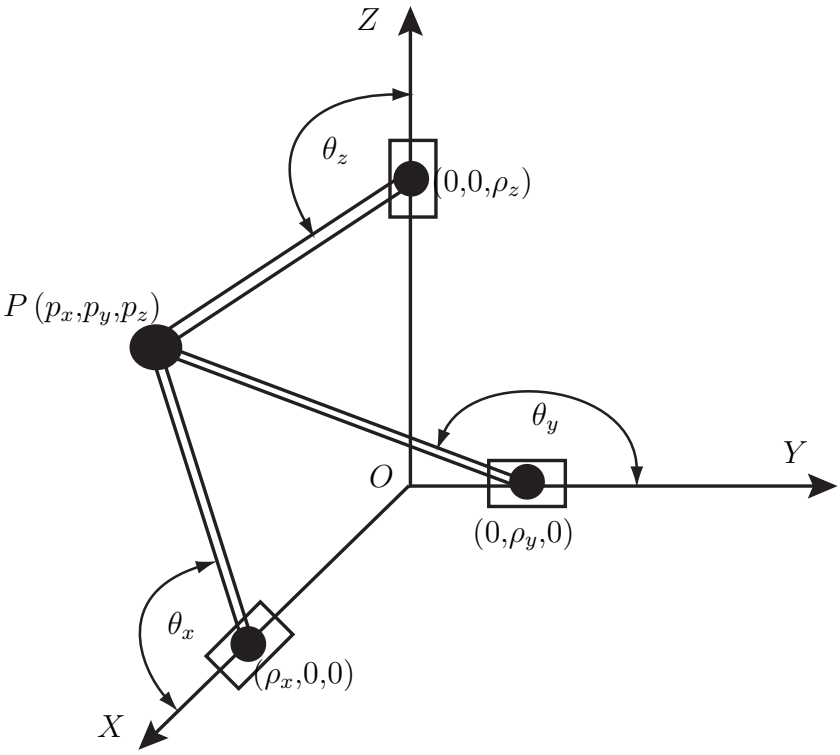

Figure 3.28 – *Simplified model of the Orthoglide 3-axis (Pashkevich et al., 2006)*

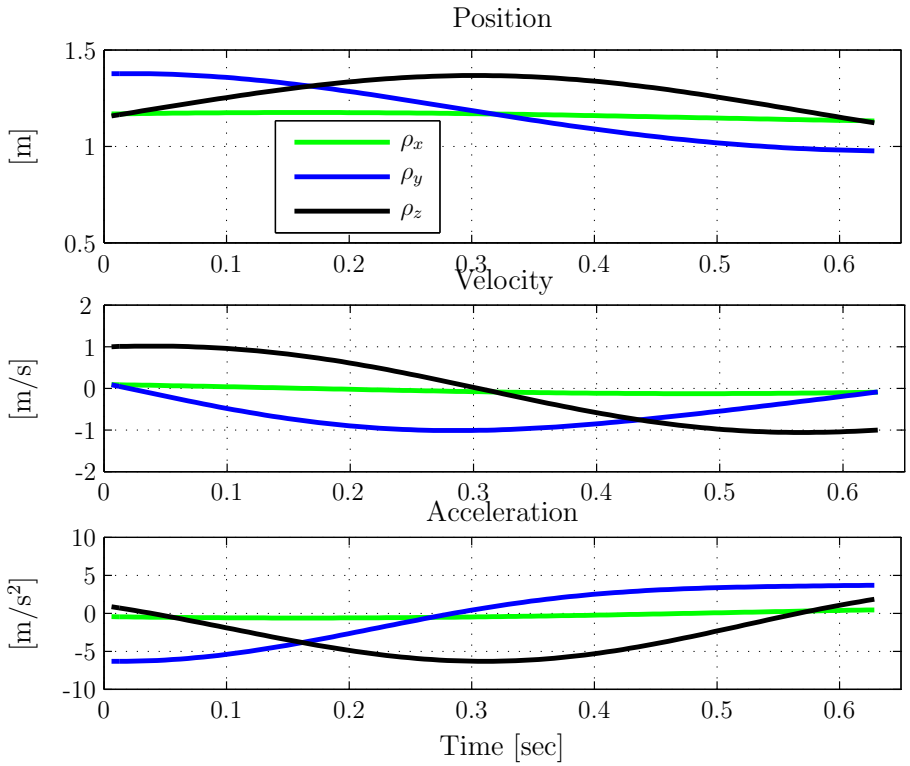

Figure 3.29 – *Actuated prismatic joints position and rates of the Orthoglide 3-axis for Traj-I with* $R = 0.200\,m$ *and* $\phi = 90°$

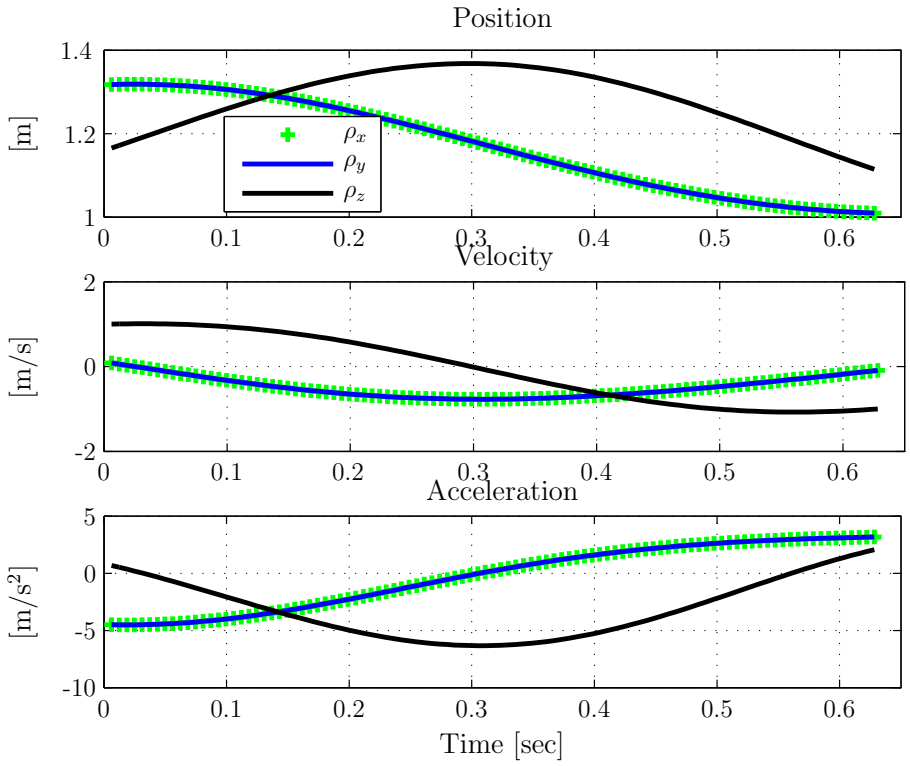

Figure 3.30 – *Actuated prismatic joints position and rates of the Orthoglide 3-axis for Traj-I with* $R = 0.200\,m$ *and* $\phi = 45°$

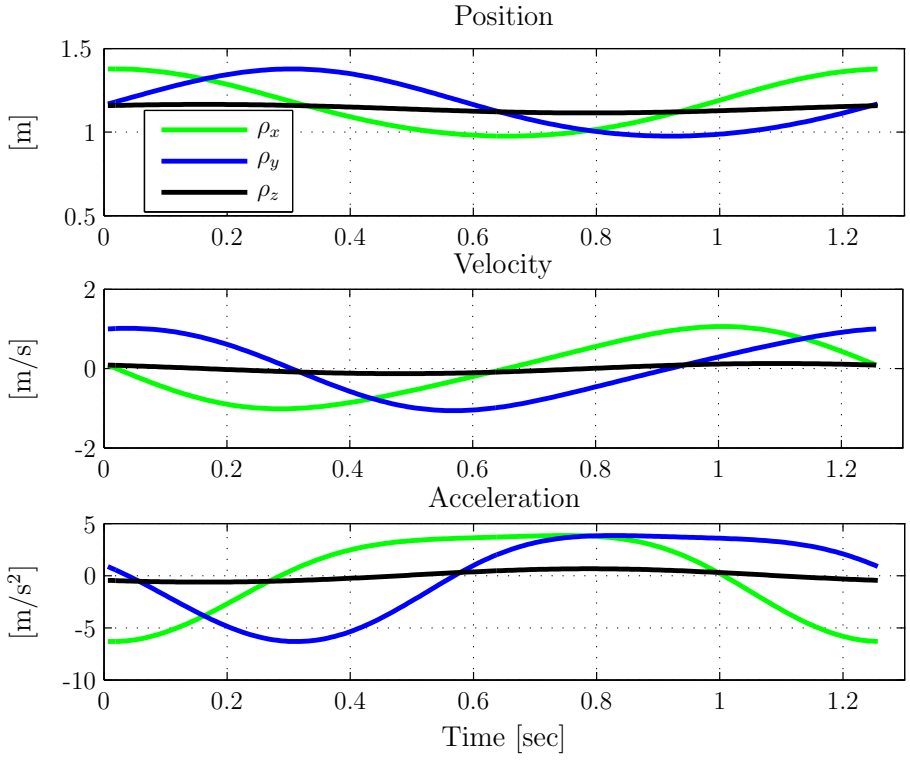

Figure 3.31 – *Actuated prismatic joints position and rates of the Orthoglide 3-axis for Traj-II with* $R = 0.200\,m$ *and* $\gamma = 45°$

3.4.2 Dynamics of the Orthoglide 3-axes

The dynamic analysis of the Orthoglide 3-axis is performed in order to evaluate the torques required by the three actuated prismatic joints. Here, we take advantage of the dynamic model developed by Guégan (2003). The geometric and dynamic parameters used in the analysis are defined in (Guégan, 2003) which are obtained from SYMORO+ (SYmbolic MOdeling of Robots), a software for the automatic generation of symbolic model of robots (Wisama and Denis, 1997). Figure 3.32 illustrates a leg of the Orthoglide with the definition of the parameters and the frames attached to all its components (Guégan, 2003). Parameters of the arm used in the dynamic model are the masses of different components,

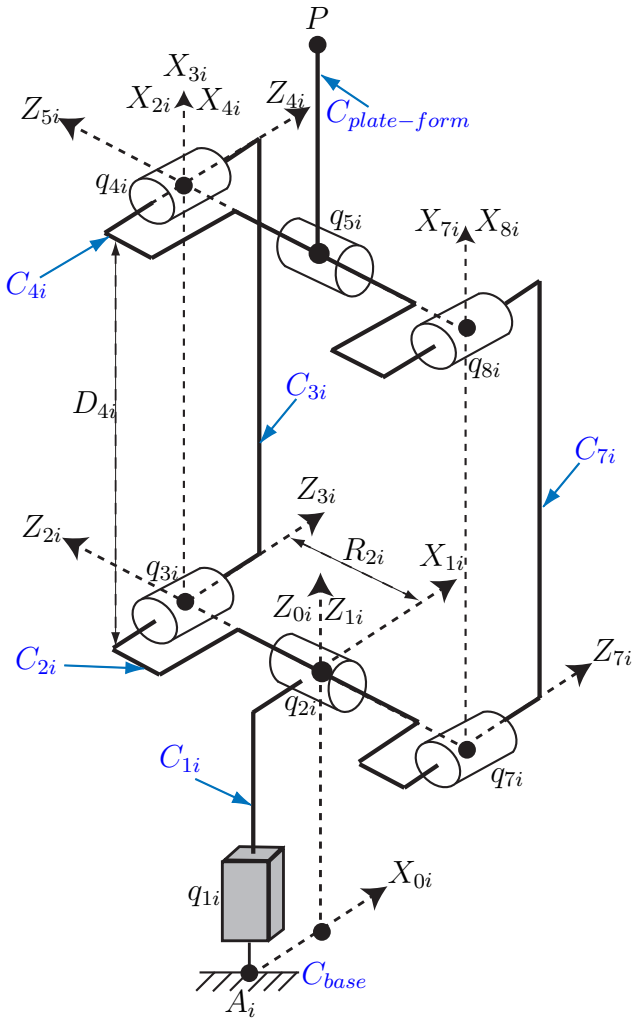

Figure 3.32 – *Orthoglide leg parameterization for the dynamic analysis*

dimensions of parallelogram (D_{4i}, R_{2i}), and the radius of gyration of component C_2. These parameters for Orthoglide 5-axis, obtained by means of SolidWorks CAD software and from the geometry of the mechanism, are given in Table 3.11. The dynamic performance of the Orthoglide 3-axis is then evaluated for different test trajectories. The actuators forces required to follow the above discussed test trajectories are shown in Fig. 3.33.

■

Table 3.11 – *Parameters of the Orthoglide 5-axis arm*

Parameters	Symbol	Value	Units	Source
Mass of the platform (wrist)	M_p	22.86	kg	SolidWorks
Mass of the member C_{1i}	M_{1i}	6	kg	SolidWorks
Mass of the members C_{2i} and C_{4i}	M_{2i}, M_{4i}	2.4	kg	SolidWorks
Mass of the members C_{3i} and C_{7i}	M_{3i}, M_{7i}	1.8	kg	SolidWorks
Length of the parallelograms	D_{4i}	0.7765	m	Geometry
Width of the parallelograms	R_{2i}	0.200	m	Geometry
Radius of gyration of member C_2	ρ_{gyr}	0.0705	m	SolidWorks

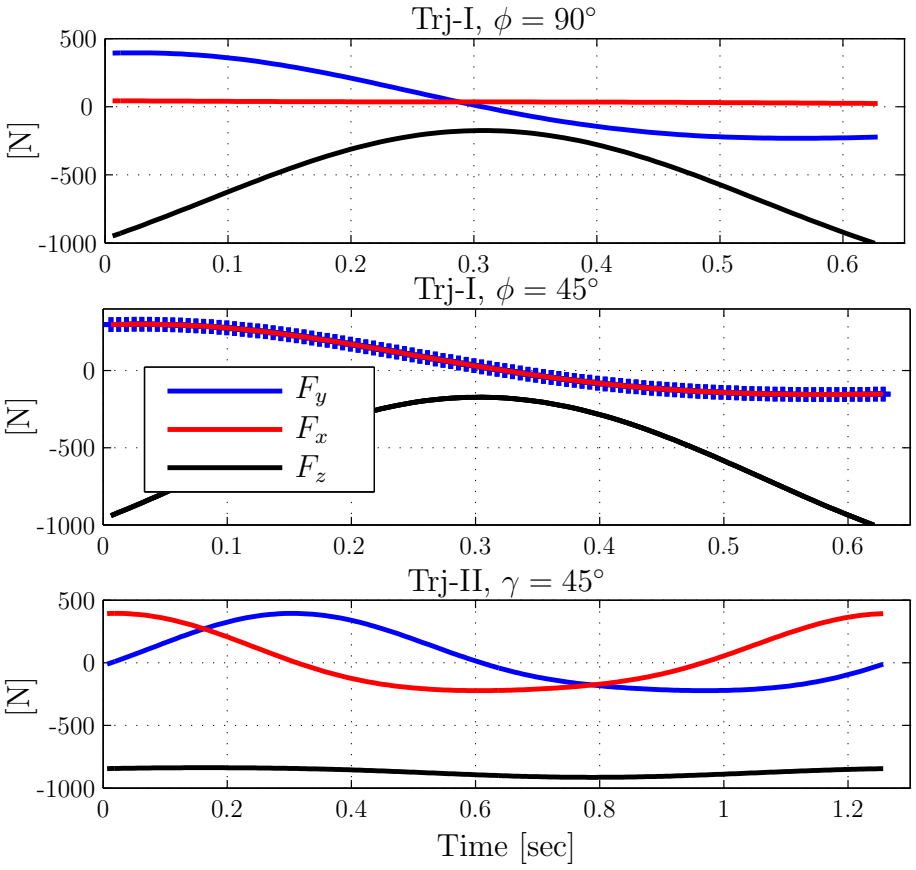

Figure 3.33 – *Orthoglide 3-axis actuators forces for Traj-I and II (R=0.2 m)*

3.4.3 Motors selection for the Orthoglide 5-axis

Based on the kinematic and dynamic models of the Orthoglide 3-axis, a methodology is adopted for the primarily selections of the Orthoglide 5-axis motors. The hit and trial approach is used to consider several motors from the catalogues. These motors are then tested for the Orthoglide prismatic actuators for various test trajectories while taking into account the motors and the mechanism parameters. The kinematic and dynamic performance of the mechanism are analyzed for each motor and based on these results, a

primary selection is proposed for the prismatic actuators of the Orthoglide 5-axis. In the following sections, we will consider, one by one, different steps or aspects of the procedure.

3.4.3.1 Ball Screw Parameters

The selected ball screw for the prismatic joints of the Orthoglide 5-axis is of a diameter of 0.025 m, length of 0.800 m, pitch of 0.025 m and is made up of steel. It has a friction moment of 0.5 Nm and its efficiency is equal to 85%. Therefore, the moment of inertia I_{bs} and the friction force F_f of the ball screw can be computed, as summarized in Table 3.12.

Table 3.12 – *Ball screw calculation for Orthoglide 5-axis*

Material density	d_{bs}	7870 kg.m−3
Length	l_{bs}	0.800 m
Radius	r_{bs}	0.0125 m
Pitch	p_{bs}	0.025
Friction Moment/Torque	M_f	0.5 Nm
Efficiency	e_{bs}	85%
Mass	m_{bs}	$m_{bs} = (\pi r_{bs}^2 l_{bs})\, d_{bs}$ kg
Inertia	I_{bs}	$I_{bs} = 0.5 m_{bs} r_{bs}^2 = 2.4145 \times 10^{-4}$ kg.m^2
Friction force	F_f	$F_f = 2\pi e_{bs} M_f / p_{bs} = 106.8$ N

3.4.3.2 Motors Selection from Catalogues

Four motors with different characteristics have been tested, as shown in Table 3.13. These are MaxPlusPlus (MPP) Series Servo motors and are taken from the catalogue of Parker Hannifin Corporation.

Table 3.13 – *Motors Parameters from Catalogue*

No.	Motor Model	Speed [rpm]	Power [W]	Continuous Torque [Nm]	Maximum Torque [Nm]	Rotor Inertia [kg.m^2]	Voltage [V]
M1	MPP0921C	5000	600	1.6	5.0	4.41x10^{-5}	230
M2	MPP0922C	4200	1100	2.9	9.3	7.80x10^{-5}	230
M3	MPP0923D	5000	1600	4.0	12.8	1.13x10^{-4}	230
M4	MPP1002D	4900	1600	4.6	14.5	2.599x10^{-4}	230

3.4.3.3 Actuators Inertia

So far we know the inertia of the lead screw and motor. A timing belt is used between motor and lead screw with a reduction factor equal to two ($\eta = 2$). The coupling inertia

is supposed to be null, i.e., $I_{coupling} = 0$. Hence, the inertia reflected to the motor I_{mr} is equal to:

$$I_{mr} = I_{rotor} + I_{coupling} + I_{bs}/\eta^2 \tag{3.21}$$

The inertia of the actuators of the Orthoglide 5-axis is,

$$M_{ai} = \upsilon^2 I_{mr} \tag{3.22}$$

$\upsilon = 2\pi/p_{bs}$ being the transmission factor of the ball screw.

3.4.3.4 Preliminary Motors Tests

An important consideration about the motors selection is the comparison of the motor inertia with that of the lead screw inertia or inertia reflected to the motor. A standard practice is to compare the motor inertia with the reflected inertia of the ball screw:

$$1.5\, I_m \geqslant \frac{I_{bs}}{\eta^2} \tag{3.23}$$

Direct comparison can also be performed to have a rough idea of motor size compared to the lead screw, i.e.,

$$1.5\, I_m \geqslant I_{bs} \tag{3.24}$$

The results of the comparison for the four considered motors are given in Table 3.14. Maximum linear output speed of the lead screw is also given for two reduction factors, which is calculated from the relation,

$$V_{out} = \frac{V_m p_{bs}}{60\eta} \tag{3.25}$$

It can be seen from Table 3.14 that the inertia of motors M1, M2 and M3 is too small

Table 3.14 – *Preliminary Motors Tests*

No.	Motor Model	Motor Speed [rpm]	Power [W]	Rotor Inertia [kg.m^2]	Output Speed, V_{out} [m/s]			$1.5I_m \geqslant I_{bs}$	$1.5I_m \geqslant I_{bs}/\eta^2$	
					$\eta = 1$	$\eta = 2$	$\eta = 4/3$		$\eta = 2$	$\eta = 4/3$
M1	MPP0921C	5000	600	4.410E-05	2.08	1.04	1.56	X	✓	X
M2	MPP0922C	4200	1100	7.800E-05	1.75	**0.875**	1.31	X	✓	X
M3	MPP0923D	5000	1600	1.130E-04	2.08	1.04	1.56	X	✓	✓
M4	MPP1002D	4900	1600	2.599E-04	2.04	1.02	1.53	✓	✓	✓

to satisfy the direct motor inertia comparison tests while with a reduction factor of 2, all motors satisfy the reflected inertia test. It should also be noted that motor M2 is not

■

capable of providing required velocity of 1 m/s at the output with a reduction factor of 2. The other three motors marginally satisfy the required velocity condition for $\eta = 2$ and safely satisfy the latter for $\eta = 4/3$.

3.4.3.5 Orthoglide Arm Dynamic

Although the preliminary motors selection suggests to eliminate motor M2, to go further inside, the results of the dynamic model are obtained for all of four motors. Table 3.15 and Fig. 3.34 shows the maximum values of the forces experienced by the actuators and corresponding required power of the motors, for both trajectories (for $\eta = 2$). These results show that motor M1 do not have sufficient power required by the mechanism for the considered trajectories. Motor M2 satisfies power requirements but is not able to provide required velocity, as discussed above. Motors M3 and M4 satisfy both velocity and power constrains, as shown in . So, for further analysis we will only consider motors M3 and M4.

Table 3.15 – *Power requirements with different motors ($\eta = 2$)*

Motor	Traj Radius [m]	Trajectory I						Trajectory II					
		Max Actuator Force [N]			Max Actuator Power [W]			Max Actuator Force [N]			Max Actuator Power [W]		
		F_1	F_2	F_3	P_1	P_2	P_3	F_1	F_2	F_3	P_1	P_2	P_3
M1 (600 W)	20	329	136	652	220	20	650	327	327	632	220	210	80
	0.100	624	146	658	340	20	660	625	625	633	380	340	80
	0.050	1155	161	782	580	20	680	1162	1159	646	670	580	80
	0.025	2187	188	1945	1040	20	1000	2206	2195	669	1250	1040	80
M2 (1100 W)	0.200	342	135	676	220	20	680	340	340	656	230	220	80
	0.100	648	144	681	350	20	680	650	649	649	390	350	80
	0.050	1201	157	852	600	20	690	1208	1204	657	700	600	80
	0.025	2276	181	2101	1080	20	1070	2294	2284	669	1300	1090	80
M3 (1600 W)	0.200	356	134	702	230	20	700	354	354	680	230	220	80
	0.100	673	142	705	360	20	710	675	674	675	400	370	80
	0.050	1248	153	924	620	20	710	1255	1251	673	720	630	80
	0.025	2367	173	2262	1130	20	1150	2385	2375	671	1350	1130	80
M4 (1600 W)	0.200	414	135	809	250	20	810	413	413	784	260	250	90
	0.100	778	137	804	420	20	810	780	779	789	460	420	90
	0.050	1446	138	1229	720	20	790	1453	1450	810	820	720	90
	0.025	2751	141	2937	1320	20	1470	2769	2760	854	1540	1320	90

Although with $\eta = 2$, M3 and M4 motors are able to provide required velocity but the difference between the required velocity and the available velocity at the output is very small (about 0.02 m/s), this may cause some problems in the vicinity of singular configurations. For safety reason, the reduction factor was reduced to $\eta = 4/3$ and results obtained for M3 and M4 are shown in Table 3.16 and in Fig. 3.35. By decreasing reduction factor, although we have gained extra output velocity but at the expense of increased inertia, the power requirement for the same trajectories increased. Furthermore, motor M4 is out of power for sharp trajectories of radius 0.025 m while motor M3 satisfies all the trajectories. So, this implies the selection of motor M3. The comparisons and results

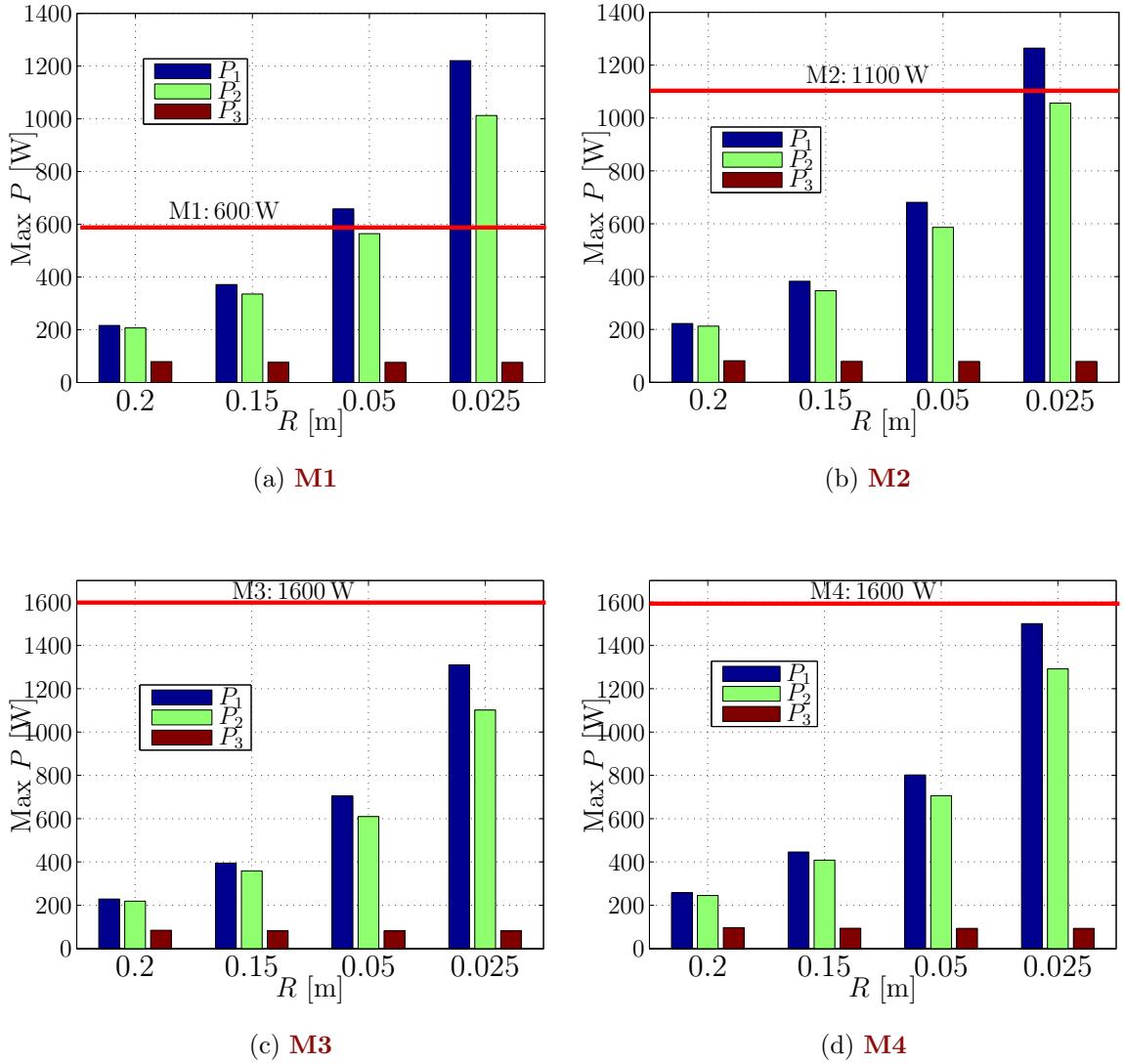

(a) **M1** (b) **M2**

(c) **M3** (d) **M4**

Figure 3.34 – *Max power requirement with four motors (Traj-II, $\eta = 2$)*

Table 3.16 – *Power requirements for M3 and M4 motors ($\eta = 4/3$)*

Motor	Traj Radius [m]	Trajectory I						Trajectory II					
		Max Actuators Forces [N]			Max Actuator Power [W]			Max Actuator Force [N]			Max Actuator Power [W]		
		F_1	F_2	F_3	P_1	P_2	P_3	F_1	F_2	F_3	P_1	P_2	P_3
M3 (1600 W)	0.200	386	134	757	240	20	760	384	384	733	250	240	90
	0.100	727	138	756	390	20	760	729	728	734	430	390	90
	0.050	1350	145	1081	670	20	750	1356	1353	743	770	670	90
	0.025	2565	156	2609	1230	20	1310	2582	2573	765	1450	1230	90
M4 (1600 W)	0.200	444	138	864	270	20	860	443	443	837	280	260	100
	0.100	832	138	855	440	20	850	834	833	848	480	440	100
	0.050	1547	141	1386	770	20	830	1555	1551	880	870	770	100
	0.025	2949	147	3285	1420	20	1640	2966	2957	948	1640	1420	100

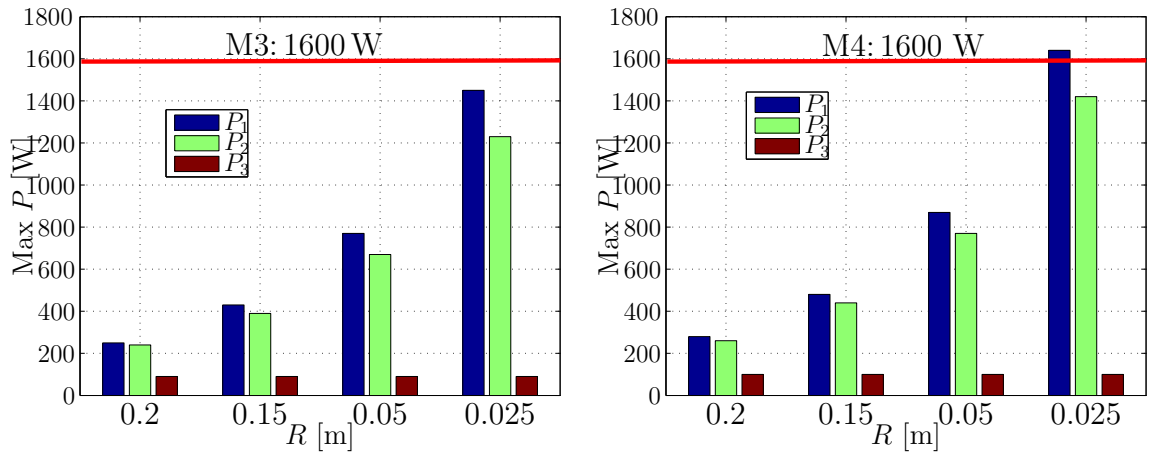

(a) **M3** (b) **M4**

Figure 3.35 – *Max Power Requirement for M3 and M4 motors (Traj-II, $\eta = 4/3$)*

presented so far suggest the selection of motor M3, which is able to provide the required power and velocity. A reduction factor equal to 4/3 is safer to get the required actuators velocities for the considered test trajectories.

Table 3.17 – *Effect of the variation of wrist mass for M3 ($\eta = 2$)*

Motor	Traj Radius [m]	Mass Change [kg]	Trajectory I						Trajectory II					
			Max Power [W]			Average Rate of Change of Power [W/kg]			Max Power [W]			Average Rate of Change of Power [W/kg]		
	R	dm	P_1	P_2	P_3	$\frac{\partial P_1}{\partial m}$	$\frac{\partial P_2}{\partial m}$	$\frac{\partial P_3}{\partial m}$	P_1	P_2	P_3	$\frac{\partial P_1}{\partial m}$	$\frac{\partial P_3}{\partial m}$	$\frac{\partial P_3}{\partial m}$
M3	0.2	0	228	17	702	2.33	0.10	10.15	233	224	85	2.18	2.20	1.26
		5	240	18	753				244	235	91			
		10	251	18	804				255	246	97			
		15	263	19	854				266	257	104			
	0.100	0	366	17	705	5.02	0.12	10.65	404	367	82	5.83	5.01	1.22
		5	391	18	758				434	392	88			
		10	416	18	811				463	417	94			
		15	441	19	865				492	442	101			
	0.050	0	624	17	707	9.53	0.17	11.51	724	625	82	12.14	9.50	1.21
		5	671	18	764				784	672	88			
		10	719	19	822				845	720	94			
		15	767	20	879				906	767	100			
	0.025	0	1130	18	1150	18.14	0.30	16.36	**1349**	1131	82	**24.20**	18.18	1.23
		5	1221	19	1232				1470	1222	88			
		10	1312	21	1313				1591	1312	94			
		15	1403	23	1395				**1712**	1403	100			

3.4.4 Effect of the variation of Wrist mass

In the previous analysis, the wrist mass is the sum of the mass of the wrist components evaluated with Solidworks and the mass of the spindle, which is about 23 kg. In order to analyze the effects of the variations in the wrist mass, dm, or extra loads, power requirements for different test trajectories was determined with various wrist masses. The results obtained for motors M3 and M4 are given in Tables 3.17 and 3.18, respectively.

Table 3.18 – *Effect of the variation of wrist mass for M4 ($\eta = 2$)*

Motor	Traj Radius [m]	Mass Change [kg]	Trajectory I						Trajectory II					
			Max Power [W]			Average Rate of Change of Power [W/kg]			Max Power [W]			Average Rate of Change of Power [W/kg]		
	R	dm	P_1	P_2	P_3	$\frac{\partial P_1}{\partial m}$	$\frac{\partial P_2}{\partial m}$	$\frac{\partial P_3}{\partial m}$	P_1	P_2	P_3	$d\frac{\partial P_1}{\partial m}$	$\frac{\partial P_3}{\partial m}$	$\frac{\partial P_3}{\partial m}$
M4	0.200	0	254	17	809	2.33	0.10	10.15	262	250	96	2.17	2.20	1.26
		5	266	18	860				273	261	103			
		10	277	18	911				283	272	109			
		15	289	18	961				294	283	115			
	0.100	0	416	17	804	5.02	0.11	10.65	456	417	94	5.83	5.01	1.22
		5	441	17	857				485	442	100			
		10	467	18	910				514	467	106			
		15	492	19	964				543	492	112			
	0.050	0	721	17	789	9.53	0.14	11.51	821	721	93	12.14	9.54	1.2
		5	768	18	847				882	769	99			
		10	816	18	905				943	816	105			
		15	863	19	962				1003	864	111			
	0.025	0	1320	17	1471	18.14	0.24	16.26	1539	1321	93	24.20	18.16	1.16
		5	1411	18	1552				**1660**	1411	99			
		10	1502	19	1634				**1781**	1502	105			
		15	1593	20	**1716**				**1902**	1593	111			

From these results, it can be seen that the effect of variations in the wrist mass is maximum for sharper trajectories ($R = 0.025$ m), with maximum effect of 24.2 W/kg. Since with motor M3, we need a maximum power of 1349 W for 0.025 m radius trajectories (for $dm = 0$), it has a power margin of 1600-1349= 251 W, which implies that motor M3 can bear an extra load of up to 251/24.2=10.4 kg for 0.025 m radius trajectories. Motor M4, being already at power margin for 0.025 m trajectories, can not accommodate any increase of wrist mass, while for less sharp trajectories it can work with a mass increment of up to 15 to 20 kg, but of course with less power margin compared to M3.

3.5 Conclusion

This chapter dealt with the kinematic and dynamic analysis of the Orthoglide 5-axis, a five-degree-of-freedom manipulator. First, it turned out that kinematic and dynamic ana-

lysis of the translating part and the spherical wrist of the manipulators can be decoupled. The geometric and inertial parameters of the manipulator were determined by means of a CAD software. We came up with the dynamic model of the spherical wrist by means of a Newton-Euler approach. Besides, this model checked with the principle of virtual work. Then, the required motors performance were evaluated for some test trajectories. Various simulations results showed that the FFA 20–80 harmonic drive motors of 800 W and the MPP0923D servo motors of 1600 W, primarily selected for the wrist and Orthoglide 3-axis, respectively, are suitable for the prototype of the Orthoglide 5-axis. In future works, friction forces as well as payload need to be considered in the dynamic analysis with more complex test trajectories.

In the next chapter, we will discuss the the path placement optimization problem in order to optimize or improve the performance of a given PKM by means of better placement of the tasks in its workspace.

4 Single and Multiobjective Path Placement Optimization

4.1 Introduction 108

4.2 Path Placement Optimization 110

4.2.1 Design Variables: Path Location Parameters 110

4.2.2 Optimization Objectives 112

4.2.3 Optimization Constraints 116

4.2.4 Problem Statement and Solution 116

4.3 Case Study: Application to the Orthoglide 3-axis 120

4.3.1 Objective Functions Formulation for the Orthoglide 3-axis 122

4.3.2 Test Path and External Forces 125

4.4 Results and Discussions 128

4.4.1 Results: Mono-Objective Path Placement Optimization 129

4.4.2 Results: Multi-objective Path Placement Optimization 134

4.5 Conclusions 139

This chapter deals with the single and multi-objective path placement optimization for Parallel Kinematics Machines (PKMs) based on energy consumption, actuators torques and shaking forces. It proposes a methodology to determine the optimal location of a given test path within the workspace of a PKM in order to minimize the electric energy used by the actuators, their maximal torque and the shaking forces subject to the geometric, kinematic and dynamic constraints. The proposed methodology is applied to the Orthoglide 3-axis, a three-degree-of-freedom translational PKM, as an illustrative example. The optimization problem is formulated firstly as single-objective and then as multiobjective. The electric energy consumption is taken as the sole optimization objective function for single-objective optimization whereas electric energy consumption, actuators torques and shaking forces are considered for multiobjective formulation.

4.1 Introduction

Optimal trajectory planning of manipulators has been a relevant area for roboticists for many years. Indeed, several authors have worked on trajectory planning based on different optimization objectives. A review of trajectory planning techniques is given in (Ata, 2007). Trajectory planning deals with the determination of the path and velocity/acceleration profiles (or the time history of the robot's joints), the start and end points of the trajectory being predefined and fixed in the workspace. As a matter of fact, this approach is suitable for most of practical robotic applications. A path is a continuous curve in the configuration space connecting the initial configuration of the manipulator to its final configuration (Rajan, 1985). Trajectory planning usually aims at minimizing the travel distance (Tian and Collins, 2003), travel time (Chan and Zalzala, 1993; Cao *et al.*, 1994; Pledel, 1995) and/or the energy consumed (Shugen, 1995; Field, 1995; Hirakawa and Kawamura, 1997; Khoukhi *et al.*, 2007), while satisfying the geometric, kinematic and dynamic constraints of the mechanism.

Another less explored aspect of trajectory planning is the placement of a given path within the workspace. It aims at determining the optimum location of a predefined path to be followed by the end-effector of the manipulator within its workspace with respect to one or many given objective(s) and constraint(s). This path can be the shape of a component to be machined, a welded profile or an artistic/decorative profile etc. In such situations, the trajectory planner cannot alter the shape of the path but he/she can only play with the location of that path within the workspace of the manipulator in order to optimize one or several criterion(a). Such an approach can be very interesting in many robotic applications. For example, in machining, a workpiece can be better located within the workspace of the robot to perform a given operation more efficiently with respect to the energy consumed.

The path placement problem has not been extensively studied in the past. Nevertheless, some researchers proposed to solve it with respect to various optimization objectives. Several performance criteria for path placement problems can be considered simultaneously (multiobjective) or individually, such as travel time, different kinetostatic performance indices (such as, manipulability or the conditioning number of the normalized kinematic Jacobian matrix), kinematic performance (velocity, acceleration), accessibility, collisions, wear and vibration reduction, energy consumption and so on.

Nelson and Donath (1990) proposed an algorithm for the optimum location of an assembly task in the manipulator workspace while taking the manipulability measure as the optimization criterion. They considered that the location of the assembly task within the workspace that results in the highest manipulability is a locally optimal position for performing the assembly. However, Aspragathos (1996); Aspragathos and Foussias (2002) mentioned that the manipulability index and the dexterity, usually quantified by the

condition number of the normalized Jacobian matrix of the manipulator, can characterize the motion ability of the manipulator, but these criteria cannot depict the ability of a manipulator to move in a given direction. Hence they introduced a criterion to characterize the best velocity performance of the robot end-effector with the path location. They used the concept of the orientation of the manipulability ellipsoid relative to the desired path and used genetic algorithm to come up with an optimal solution.

Fardanesh and Rastegar (1988) proposed an approach for optimal positioning of a prescribed task in the workspace of a $2R$-manipulator. The optimal location of the task is considered to be the location that yields the minimum cycle time. In another study, Feddema (1996) formulated and solved a problem of robot base placement for a minimum joint motion time within a work cell. The proposed algorithm considered the kinematics and the maximum acceleration of each joint in order to obtain a 25% cycle time improvement for a typical example.

Hemmerle and Prinz (1991) presented an algorithm for optimum path placement of a redundant manipulator by defining a cost function related to robot joints motion and limits. The proposed approach did not consider the path as a whole but discrete points of that path, hence cost function considers the performance only at the node points and not the path in-between the nodes.

Chou and Sadler (1993) developed an optimization technique for the optimum placement of a robotic manipulator based on the actuators torque requirements. Pamanes and Zeghloul (1991) considered multiple kinematic indices to find the optimal placement of a manipulator by specifying the path with a number of points and then assigning an optimization criterion to each point. The objective was to find the path location in order to have optimal values of all the criteria assigned to the path points. In (Pamanes *et al.*, 1991), the problem of optimal placement with joint-limits and obstacle avoidance is addressed. Lately, a general formulation was presented to determine the optimal location of a path for a redundant manipulator while dealing with mono- and multiobjective optimization problems (Pamanes *et al.*, 2008).

With a general literature survey, it comes out that although several performance indices are introduced or considered, there is no emphasis on the dynamic aspects reflecting the energy consumption by the PKM actuators. Another less explored but important criterion of optimal path placement can be the minimization of the shaking forces and moments experienced by the base of the PKM. Shaking forces and moments can affect the performance of a PKM in terms of excessive loads, accuracy, wear, fatigue, etc. Accordingly, we introduce two indices characterizing the variations and the maximum value of the shaking forces. The maximum actuators torque is also considered as another objective of optimum path placement. Hence, in this chapter, we propose an approach to optimize the location of a given path to be followed by the end-effector of a PKM within its workspace, in order to minimize the electric energy consumed by its actuators, minimize the shaking forces

and/or moments and minimize the maximum actuators torques. The proposed approach is applied to the Orthoglide 3-axis for some test paths and the results are presented while formulating either a mono-objective or a multi-objective optimization problem.

4.2 Path Placement Optimization

The problem aims at determining the optimal location of a predefined path in order to optimize some objective functions. The entire path is supposed to be known within the framework of this research work. The path location can be defined in a similar way as to define the location of a workpiece with respect to a manipulator reference point. The path location optimization problem is composed of three sets, namely, the set of design variables, the set of objective functions and the set of design constraints. Accordingly, the optimization problem aims at determining the design variables characterizing the path location, in order to minimize or maximize the objective functions subjected to the design constraints.

4.2.1 Design Variables: Path Location Parameters

In order to formulate and describe the problem, two reference frames are defined: i) the path frame $\mathcal{F}_p$ and ii) the base frame $\mathcal{F}_b$, as shown in Fig. 4.1(a). The path frame $\mathcal{F}_p$, is attached to the given/required path at a suitable point such as the geometric center of the path. As $\mathcal{F}_p$ is attached to the path, the end-effector trajectory parameters remain constant in this reference frame, no matter where it is located. In other words, the path is fully defined and constant in $\mathcal{F}_p$. It can also be named workpiece frame as it characterizes the position and the orientation of the workpiece within the manipulator workspace. The base frame $\mathcal{F}_b$ can also be called global or manipulator frame. It is attached to the manipulator base and is used to locate a workpiece (or $\mathcal{F}_p$) with respect to the manipulator coordinate system. The location and orientation of $\mathcal{F}_p$ with respect to $\mathcal{F}_b$ can be defined in such a way that the whole path lies within the workspace. The position of $\mathcal{F}_p$ with respect to $\mathcal{F}_b$ is defined with the Cartesian coordinates of the origin of $\mathcal{F}_p$. The relative orientation of the two frames is characterized by means of Euler angles. However, keeping in view the constraints of the manipulator wrist, Euler angles are uniquely defined in the context of milling operation with the parameterization given in Fig. 4.1(b). It allows to avoid the singularity of Euler parameters. As a matter of fact, any trajectory defined in $\mathcal{F}_p$ can be expressed/transformed in the base frame $\mathcal{F}_b$ by means of a transformation matrix. For instance, point P, of Cartesian coordinates $x_{P_p}, y_{P_p}, z_{P_p}$ in $\mathcal{F}_p$ can be expressed in $\mathcal{F}_b$ as follows:

$$\left[\begin{array}{c} \mathbf{p} \end{array} \right]_{\mathcal{F}_b} = {}^{b}\mathbf{T}_p \left[\begin{array}{c} \mathbf{p} \end{array} \right]_{\mathcal{F}_p} \tag{4.1}$$

■

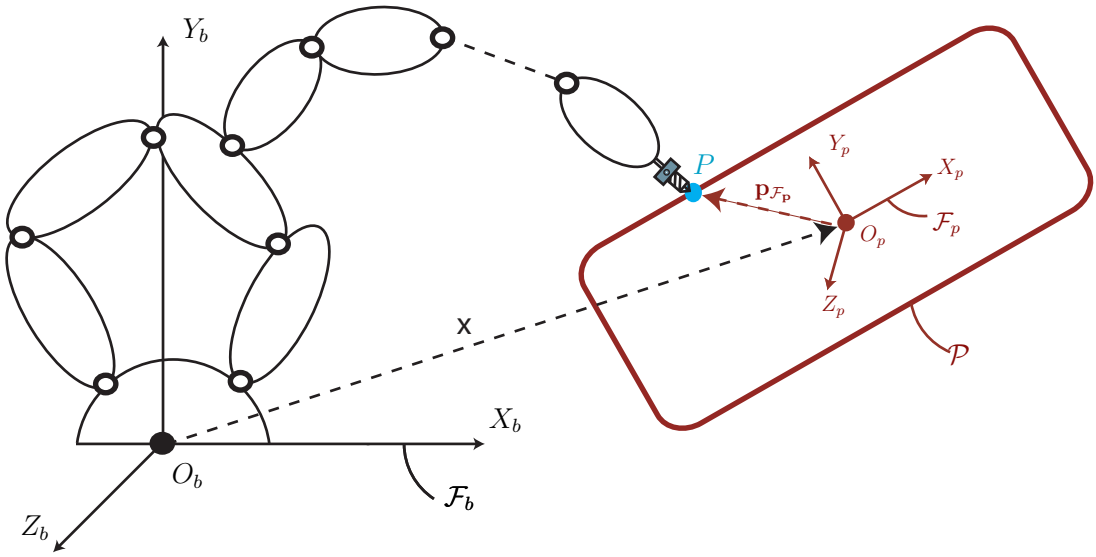

(a) Path $\mathcal{P}$ to be followed by the end-effector P of a manipulator

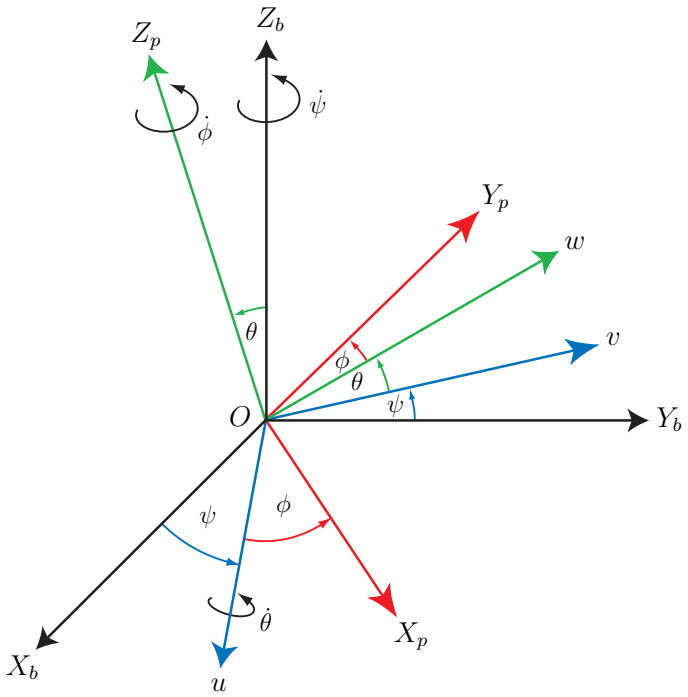

(b) Euler angles

Figure 4.1 – *Path placement characterization, $\mathcal{F}_b$ and $\mathcal{F}_p$ being the base and path frames*

namely,

$$\begin{bmatrix} x_{P_b} \\ y_{P_b} \\ z_{P_b} \\ 1 \end{bmatrix}_{\mathcal{F}_b} = {}^b\mathbf{T}_p \begin{bmatrix} x_{P_p} \\ y_{P_p} \\ z_{P_p} \\ 1 \end{bmatrix}_{\mathcal{F}_p} \tag{4.2}$$

■

${}^b\mathbf{T}_p$ being the transformation matrix from $\mathcal{F}_p$ to $\mathcal{F}_b$. Let $O_p\left(x_{O_p}, y_{O_p}, z_{O_p}\right)$ be the origin of the path frame with respect to $\mathcal{F}_b$ and let (ϕ, θ, ψ) be the Euler angles characterizing the orientation of frame $\mathcal{F}_p$ with respect to frame $\mathcal{F}_b$, as shown in Fig. 4.1(b). Then, the transformation matrix ${}^b\mathbf{T}_p$ is expressed as:

$$
{}^b\mathbf{T}_p = \begin{bmatrix}
\cos\phi\cos\theta & \cos\phi\sin\theta\sin\psi - \sin\phi\cos\psi & \cos\phi\sin\theta\cos\psi + \sin\phi\sin\psi & x_{O_p} \\
\sin\phi\cos\theta & \sin\phi\sin\theta\sin\psi + \cos\phi\cos\psi & \sin\phi\sin\theta\cos\psi - \cos\phi\sin\psi & y_{O_p} \\
-\sin\theta & \cos\theta\sin\psi & \cos\theta\cos\psi & z_{O_p} \\
0 & 0 & 0 & 1
\end{bmatrix} \tag{4.3}
$$

The path placement is specified with ${}^b\mathbf{T}_p$. Let $\mathbf{x} = [x_{O_p} \quad y_{O_p} \quad z_{O_p} \quad \phi \quad \theta \quad \psi]^T$ define the path placement within the workspace of the manipulator in the reference frame $\mathcal{F}_b$. The components of $\mathbf{x}$ are then the design variables of the optimization problem at hand.
In the context of a general machining process like milling operation, the feature to be machined in the workpiece is defined with respect to its frame, namely $\mathcal{F}_p$. Likewise, the machining operation conditions such as machining velocity and acceleration are fully defined in $\mathcal{F}_p$. Finally, the part to be machined is defined by the designer and located in $\mathcal{F}_b$ whereas the machining operation conditions and robot trajectory planning depend on the machining process and are defined in $\mathcal{F}_p$. In the scope of this paper, we introduce a methodology to help the production engineer well locate the workpiece, namely $\mathcal{F}_p$, within the robot base frame $\mathcal{F}_b$ in order to minimize the actuators electric energy consumption, actuators peak torques and the effects of the shaking forces to the manipulator base.

4.2.2 Optimization Objectives

The path placement optimization is performed with the aim of minimizing four objective functions, namely,

1. The electric energy consumption;
2. variations in the shaking forces;
3. the maximum shaking forces;
4. maximum actuators torques.

In the following sections, the mathematical formulations of these objective functions are given.

4.2.2.1 Electric Energy Consumption

The energy used by the motors depends on their corresponding velocities and torques. As a matter of fact, the electric current in the motors varies with motors velocities and torques.

■

Accordingly, the motor self-inductance phenomenon appears. The current I drawn by the motors and the motor electromotive potential V_e can be calculated as a function of the required torque τ and the angular velocity ω of the actuators, namely,

$$I = \frac{\tau}{K_t} \tag{4.4}$$

$$V_e = K_e \omega \tag{4.5}$$

K_t being the torque sensitivity factor or motor constant expressed in [Nm/A] and K_e the back electromotive force constant expressed in [V.(rad/sec)$^{-1}$].
The total electric power P_T is composed of (Lacroux, 1994):

- The resistive power loss (Joule effect):

$$P_J = RI^2 \tag{4.6}$$

- the inductive power loss:

$$P_L = LI\frac{dI}{dt} \tag{4.7}$$

- the power used to produce the electromotive force:

$$P_{EM} = V_e I \tag{4.8}$$

Accordingly, the total electric power P_T can be expressed as follows:

$$P_T = P_J + P_L + P_{EM} \tag{4.9}$$

R being the motor winding resistance expressed in Ohm [Ω] and L the motor inductance coefficient expressed in Henry [H].
Finally, the energy E consumed by a motor can be evaluated by integrating P_T over the total trajectory time T, namely,

$$E = \int_0^T P_T dt \tag{4.10}$$

P_T being the instantaneous electric power at instantaneous time t, defined in Eq. (4.9).
It should be noted that Eq. (4.4) allows us to consider the energy used by the actuators while they do not move but still produce a torque to keep the manipulator at a certain stationary configuration (with respect to that particular direction or actuator), like resisting the gravity. Finally, the total energy E_t consumed by n actuators can be written as:

■

$$E_t = \sum_{i=1}^{n} E_i \tag{4.11}$$

E_i being the total electric energy required by the i^{th} actuator, given by the Eq. (4.10). Consequently, the first objective of the path placement optimization problem can be written as:

$$f_1(\mathbf{x}) = E_t \rightarrow \min \tag{4.12}$$

It is noteworthy that energy calculation model presented in this section is suitable for the brushless motors, which are generally used for PKMs. However, depending on the motors/derives in application, energy calculation model can be developed accordingly.

4.2.2.2 Shaking Forces

Shaking or dynamic forces and moments are the inertial forces and moments exerted on the base of a machine/manipulator due to the uneven mass distribution. These forces/moments may deteriorate system performance by introducing excessive vibration, noise and wear. Furthermore required input torques and forces may also increase to cater for these shaking effects. Fatigue life of the manipulator components is also an aspect that can suffer from shaking forces and moments. Hence, in order to overcome these drawbacks and to improve system performance in terms of accuracy, precision, fatigue life, vibration reduction, motion planning and control, the study of the shaking forces and moments is of prime importance.

A mechanism is said to be force balanced if, for any motion of the mechanism, no reaction force other than gravity is transmitted to its base. Likewise, a mechanism is force and moment balanced if neither reaction force nor moment is transmitted to the base, for any arbitrary motion of the mechanism (Wu and Gosselin, 2004; Moore *et al.*, 2009).

Dynamic balancing of robotic manipulators has been an area of research for some decades and several authors have contributed to this domain by formulating and analyzing the problems for either some particular applications or for more general prospects (Wu and Gosselin, 2004; Moore *et al.*, 2009; Chiou and Chang, 1998). Usually, these research works aim at helping the designer to come up with manipulators that are dynamically balanced. Here, we will use this concept in order to optimize the path location within the workspace of the manipulator so that the shaking forces be as low as possible. For the purpose of simplicity, dynamic forces are exclusively considered in the framework of this research work while dynamic moments are left for future works.

In order to assess the effect of shaking forces, two indices are proposed, namely,

1. Shaking force variation index: $I_{\delta f}$

   Shaking force variation index, $I_{\delta f}$, considers the maximum variation in the shaking

forces along the trajectory, i.e.,

$$I_{\delta f} = \max\left(dF_{sh}\right) \tag{4.13}$$

where $dF_{sh} = \sum_{i=1}^{n} dF_{sh}^{i}$ is the sum of the variations in the n shaking forces, n being the number of limbs or kinematic chains. The variation in the shaking forces for the i^{th} actuator is given by,

$$dF_{sh}^{i} = \sqrt{\left[\max(\mathbf{F}_{x}^{i}) - \min(\mathbf{F}_{x}^{i})\right]^{2} + \left[\max(\mathbf{F}_{y}^{i}) - \min(\mathbf{F}_{y}^{i})\right]^{2} + \left[\max(\mathbf{F}_{z}^{i}) - \min(\mathbf{F}_{z}^{i})\right]^{2}} \tag{4.14}$$

where $\mathbf{F}_{x}^{i}$, $\mathbf{F}_{y}^{i}$ and $\mathbf{F}_{z}^{i}$ are the matrices of dimensions $1\times N_t$, representing the respective force profile along trajectory, N_t being the number of time steps.

The variations in the shaking forces will have a strong influence on the base platform vibrations. Hence, the second objective function of the path optimization problem can be written as,

$$f_2\left(\mathbf{x}\right) = I_{\delta f} \rightarrow \min \tag{4.15}$$

2. Maximum shaking force index: I_f
   Maximum shaking force index, I_f, characterizes the magnitude of the maximum shaking forces experienced by the base platform along the trajectory, i.e.

$$I_f = \max\left(\mathbf{F}_{sh}\right) \tag{4.16}$$

   where $\mathbf{F}_{sh} = \sum_{i=1}^{n} \mathbf{F}_{sh}^{i}$ is $1\times N_t$ dimensional vector representing the sum of the shaking forces experienced by the n actuators with N_t time steps.
   The magnitude of the maximum shaking forces gives an idea of the maximum extra loads experienced by the actuators resulting from the shaking forces, for a particular trajectory. Hence the knowledge of the maximum shaking forces can help the designer in actuators selection to cater for these excessive loads on the system. Accordingly, the third objective function of the path optimization problem can be written as,

$$f_3\left(\mathbf{x}\right) = I_f \rightarrow \min \tag{4.17}$$

4.2.2.3 Maximum Torque

In order to reduce the actuators loads, the magnitude of the maximum torque τ_{max} experienced by the manipulators actuators is considered. The maximum torque τ_{max} expe-

rienced by the actuators is defined as,

$$\tau_{max} = \max\left(\tau_{1_{max}}, \ldots, \tau_{n_{max}}\right) \tag{4.18}$$

$\tau_{i_{max}}$ being the magnitude of the maximum torque experienced by the i^{th} actuator along the trajectory. Consequently, the fourth objective function of the path optimization problem can be written as,

$$f_4\left(\mathbf{x}\right) = \tau_{max} \rightarrow \min \tag{4.19}$$

4.2.3 Optimization Constraints

The path placement optimization problem is subjected to geometric, kinematic and dynamics constraints. Geometric constraints include joint limits and the boundaries of the workspace. Kinematic constraints deal with the maximum actuators velocities whereas dynamic constraints are related to actuators wrenches, namely,

$$\begin{aligned} &q_{il} \leqslant q_i \leqslant q_{iu} \\ &|\dot{q}_i| \leqslant \dot{q}_{iu} \\ &|\tau_i| \leqslant \tau_{iu} \end{aligned} \tag{4.20}$$

q_i is the i^{th} actuator displacement (q_{il} and q_{iu} are their corresponding lower and upper bounds). $\dot{q}_i$ is the i^{th} actuator rate ($\dot{q}_{iu}$ is the upper bound or maximum acceptable actuator velocity) and τ_i is the i^{th} actuator torque with τ_{iu} being the upper bound or maximum actuator torque.

For a given path placement vector $\mathbf{x}$, these constraints can be evaluated by means of the PKM kinematic, velocity and dynamic models. It is noteworthy that geometric constraints guarantee that the whole path lies within the prescribed workspace. Similarly, the bounds on actuators rates and torques ($\dot{q}_{iu}$ and τ_{iu} respectively) ensure that the PKM does not meet any singular configuration while following the path.

4.2.4 Problem Statement and Solution

The goal of this research work is to help the path planner find the best location of the path to be followed by the end-effector of a PKM or robot in order to minimize the four objective functions defined in the foregoing subsections. In this vein, a mono-objective and a multiobjective optimization problems are formulated.

4.2.4.1 Mono-Objective: Minimization of the Energy Path Placement

The goal of mono-objective optimum path placement problem is set to find the best location of a given path in order to minimize the energy consumed by the PKM actuators. It can be formulated as:

"*For a predefined path in $\mathcal{F}_p$, find the optimum location and orientation of $\mathcal{F}_p$ with respect to $\mathcal{F}_b$, defined by the decision variables* $\mathbf{x}$*, in order to minimize the electric energy used by the manipulator actuators to generate that path, while respecting the geometric, kinematic and dynamic constraints of the manipulator.*"

It can also be formulated mathematically as follows:

$$\min_{\mathbf{x}} E_t = \sum_{i=1}^{n} E_i(\mathbf{x}) \qquad \text{subject to:} \begin{cases} q_{il} \leqslant q_i \leqslant q_{iu} \\ |\dot{q}_i| \leqslant \dot{q}_{iu} \\ |\tau_i| \leqslant \tau_{iu} \end{cases} \qquad (i = 1 \ \cdots \ n) \tag{4.21}$$

4.2.4.2 Problem Resolution– Mono-objective

To solve the problem, a general optimization approach is proposed. As illustrated in Fig. 4.2, the approach can be summarized in three constituent elements or phases, namely, preparation phase, evaluation phase and optimization phase. Detail process can be listed as:

1. Manipulator geometric, dynamic and electric parameters are used as the known input data of the optimization problem;
2. definition of the base reference frame $\mathcal{F}_b$;
3. definition of the path reference frame $\mathcal{F}_p$ at a suitable reference point of the path;
4. complete description of the given path in $\mathcal{F}_p$. At this stage, displacement, velocity and acceleration profiles of end-effector are defined in $\mathcal{F}_p$;
5. with an initial guess of design variables $\mathbf{x}_0 = \begin{bmatrix} x_{O_{p0}} & y_{O_{p0}} & z_{O_{p0}} & \phi_0 & \theta_0 & \psi_0 \end{bmatrix}^T$, $\mathcal{F}_p$ is located with respect to $\mathcal{F}_b$;
6. the transformation matrix ${}^b\mathbf{T}_p$ is calculated from $\mathbf{x}$;
7. using ${}^b\mathbf{T}_p$, trajectory parameters are calculated in $\mathcal{F}_b$, i.e., calculation of the Cartesian velocities and accelerations of the end-effector;
8. the actuated variables q_i are calculated by means of the Inverse Kinematic Model (IKM) of the manipulator;
9. the actuators velocity $\dot{q}_i$ and acceleration $\ddot{q}_i$ profiles are derived from the Inverse Velocity Model (IVM) of the manipulator;
10. the actuators torques τ_i are derived from the Inverse Dynamic model (IDM) of the manipulator;

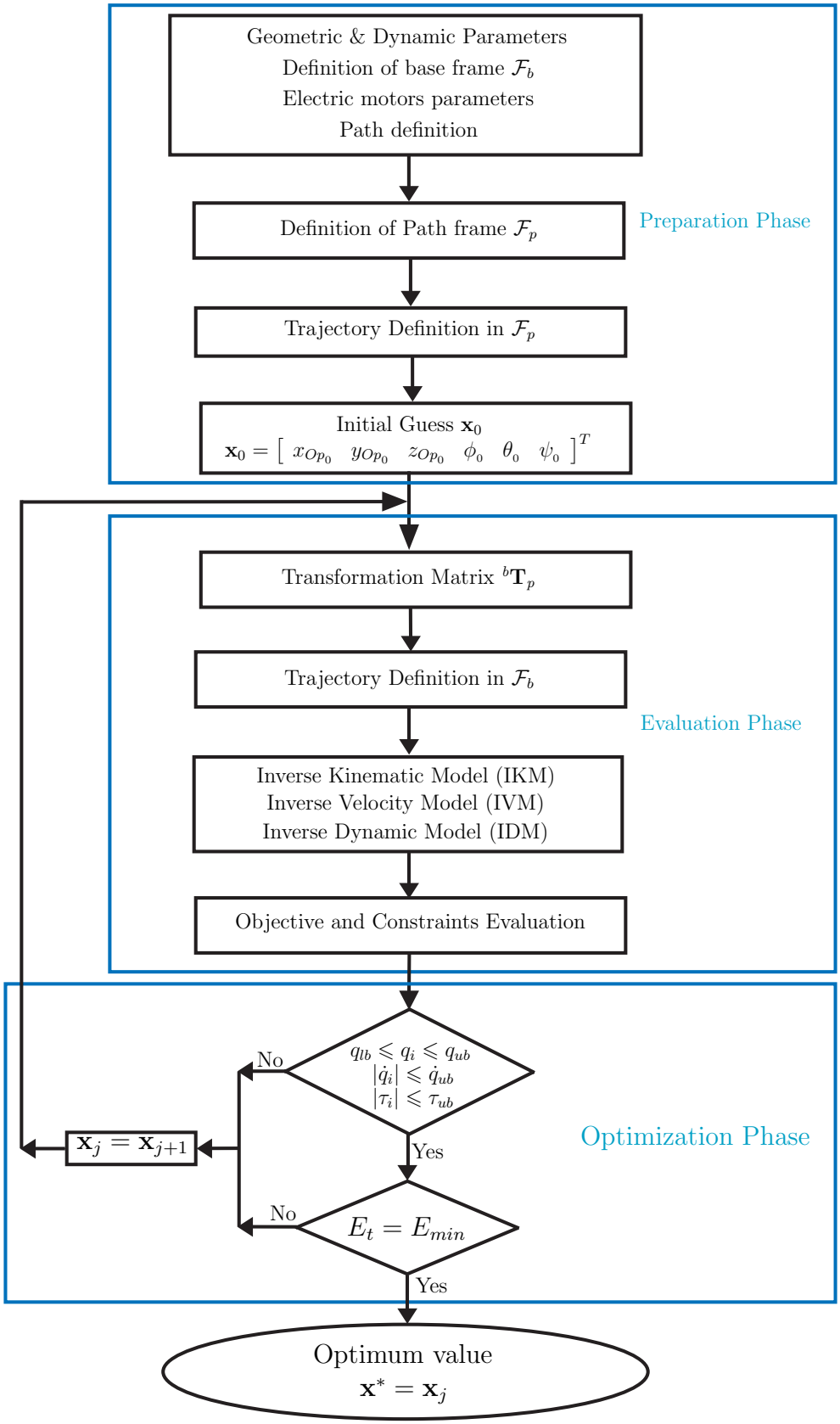

Figure 4.2 – *Flowchart of mono-objective path placement optimization process*

11. the current I and voltage V_e required by each actuator are calculated by using the actuators torques, velocities, the motors torque sensitivity factor K_t and the back electromotive force constant K_e, as defined in Eqs.(4.4) and (4.5);
12. the electric power P_{T_i} consumed by the i^{th} actuator is obtained from the current, voltage and actuators electric constants, as defined in Eq. (4.9);
13. the electric energy E_i consumed by the i^{th} actuator is then calculated by integrating the consumed power P_{Ti} over total trajectory time T, as given by Eq. (4.10). Subsequently, the total electric energy E_t used by the manipulator is obtained by adding up the energy consumed by all actuators;
14. the constraints and the convergence criteria are verified at each iteration j. The convergence criteria are up to the user. It can be the constraints or objective function tolerances, the number of iterations and so on;
15. the optimization algorithm (iterative process) is used to find out the optimum design variables, namely, $\mathbf{x}^*=[x^*_{O_p} \quad y^*_{O_p} \quad z^*_{O_p} \quad \phi^* \quad \theta^* \quad \psi^*]^T$ in order to minimize E_t.

Finally, the optimum path placement is obtained by means of the position of point O_p and the orientation of $\mathcal{F}_p$ with respect to $\mathcal{F}_b$, defined by $(x^*_{O_p}, y^*_{O_p}, z^*_{O_p})$ and $(\phi^*, \theta^*, \psi^*)$, respectively.

4.2.4.3 Multiobjective Path Placement Optimization

Multiobjective path placement optimization problem with the aforementioned optimization objectives can be stated as:
"*For a predefined path in $\mathcal{F}_p$, find the optimum location and orientation of $\mathcal{F}_p$ with respect to $\mathcal{F}_b$, defined by the decision variables* $\mathbf{x}$*, in order to minimize the objective functions f_1, f_2, f_3 and f_4 while respecting the kinematic, velocity and dynamic constraints of the manipulator*"
Mathematically, for k objective functions, the problem can be formulated as follows:

$$\min_{\mathbf{x}} \left(f_1(\mathbf{x}), \ldots, f_k(\mathbf{x})\right) \qquad \text{subject to:} \begin{cases} q_{il} \leqslant q_i \leqslant q_{iu} \\ |\dot{q}_i| \leqslant \dot{q}_{iu} \\ |\tau_i| \leqslant \tau_{iu} \end{cases} \qquad (i = 1 \ \cdots \ n) \qquad (4.22)$$

4.2.4.4 Problem Resolution–Multiobjective

To solve the problem, a general optimization approach based on Multi-Objective Genetic Algorithm (MOGA) is proposed as illustrated in Fig. 4.3. This approach can be broken down into four constituent elements or phases:

1. Preparation Phase: Manipulator geometric, dynamic and electric parameters along with the definition of the required path are used as the known input data of the

optimization problem. The base frame $\mathcal{F}_b$ is defined. The path to be followed by the end-effector of the robot is defined in the path frame $\mathcal{F}_p$. The terms of the transformation matrix from $\mathcal{F}_p$ to $\mathcal{F}_b$ are the decision variables of the optimization problem.

2. Evaluation Phase: At this stage, the inverse kinematic model (IKM), the inverse velocity model (IVM) and the inverse dynamic model (IDM) of the manipulator are determined for each set of design parameters obtained from the generated population of the genetic algorithm. Accordingly, the objective functions and the constraints of the optimization problem are evaluated.
3. Optimization Phase: A Multi-Objective Genetic Algorithm (MOGA) is used to generate the initial populations, evaluate the objective functions and constraints in order to generate new populations by carrying out the reproduction, cross over and mutation operations. Finally, after a certain number of generations, the MOGA gives a population of feasible solutions.
4. Solutions Phase: The Pareto optimal solutions are obtained from the final feasible population.

4.3 Case Study: Application to the Orthoglide 3-axis

The proposed path placement optimization approach is applied to the Orthoglide 3-axis as a case study. The Orthoglide 3-axis has a quasi-cubic workspace and a trajectory can be carried out within the boundaries of the workspace. However, changing the location of the workpiece or path in the workspace can affect various performance indices of the manipulator. The energy used by the three prismatic actuators can also vary for the same path carried out at different locations within the prescribed cubic workspace. Here, we expect to find the best location of a given path or trajectory profile in order to minimize the total electric energy used by the actuators. In this vein, various test paths are considered and an optimization algorithm is used to come up with the optimal location of the paths within the manipulator workspace.

As discussed in Sec. 3.1, the Orthoglide 3-axis geometric parameters are function of the size of the prescribed cubic Cartesian workspace, defined by its edged length, $L_{workspace}$. Pashkevich *et al.* (2009b).

In the scope of this study, $L_{workspace}$ is equal to 0.200 m. Accordingly, the coordinates of points Q^+, Q^- and C for this workspace are given in Table 4.1. Similarly, the prismatic actuator bounds, ρ_{min} and ρ_{max}, can be calculated Pashkevich *et al.* (2009b). Table 4.2 shows the lower and the upper bounds of the prismatic joints displacements and their maximum allowable velocity and torque for the Orthoglide 3-axis.

■

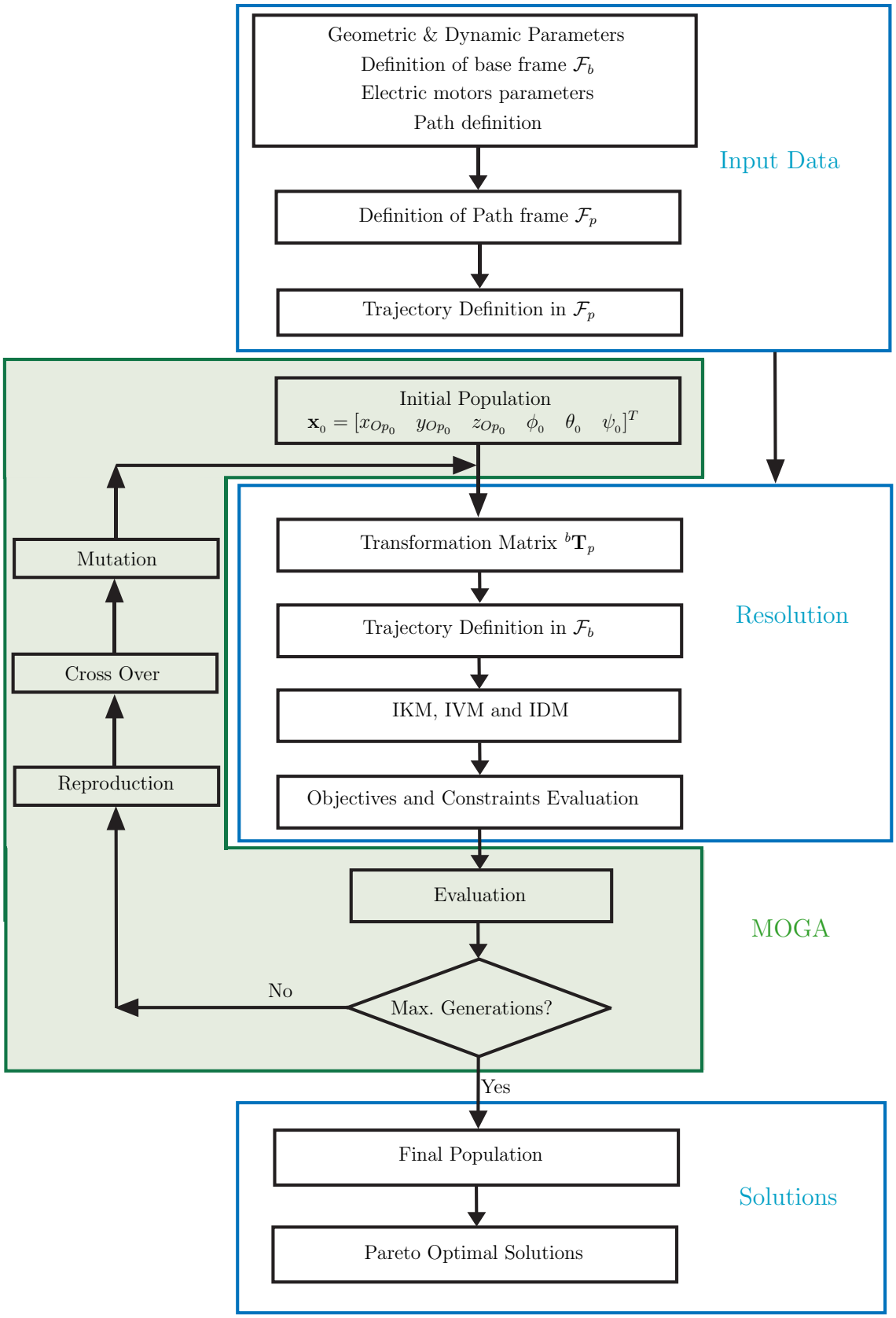

Figure 4.3 – *Flowchart of multiobjective path placement optimization process*

Table 4.1 – *Orthoglide 3-axis workspace parameters*

Workspace size $L_{workspace} = 0.2$ m	
Point	Cartesian coordinates in $\mathcal{F}_b$ [m]
O_b	(0, 0, 0)
C	$(-0.027, -0.027, -0.027)$
Q^+	(0.73, 0.73, 0.73)
Q^-	$(-0.127, -0.127, -0.127)$

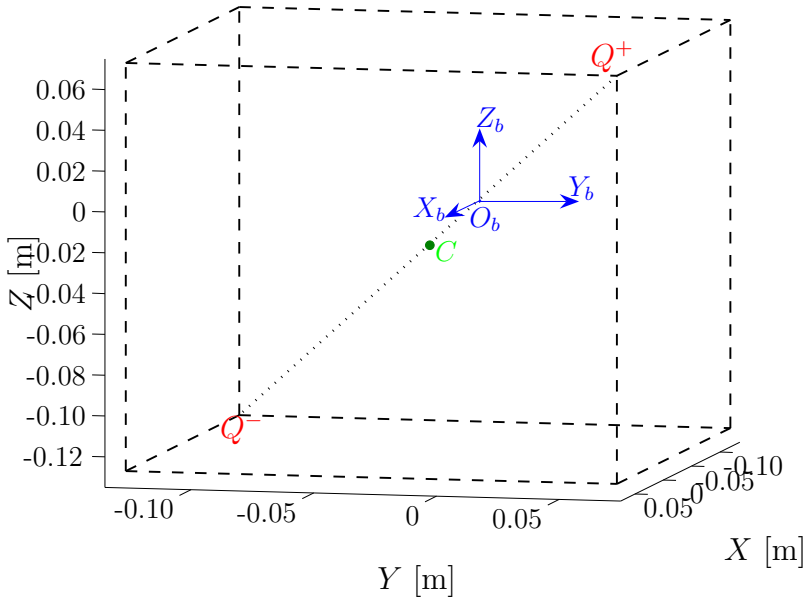

Figure 4.4 – *Orthoglide 3-axis cubic workspace* ($0.2 \times 0.2 \times 0.2$ m^3)

4.3.1 Objective Functions Formulation for the Orthoglide 3-axis

4.3.1.1 Electric Energy

The electric energy E_i used by each actuator is calculated by means of Eqs. (4.4) to (4.10). As the Orthoglide 3-axis has three *3-phase Sanyo Denki* synchronous servo motors ($reference$: $P30B0604D$), Eq. (4.9) is multiplied by 3 to cater for the power consumed by the each phase of the motor in order to calculate the electric power P_{Ti} used by each actuator, i.e.,

$$P_{T_i} = 3(RI^2 + LI\frac{dI}{dt} + V_eI) \tag{4.23}$$

Table 4.2 – *Orthoglide 3-axis actuators parameters* ($i = x,y,z$)

$\rho_{i_{min}}$	0.126 m
$\rho_{i_{max}}$	0.383 m
$v_{i_{max}}$	1.00 m.s^{-1}
$\tau_{i_{max}}$	1.274 Nm

4.3.1.2 Shaking forces

Shaking forces $\mathbf{f}_{sh}$ at the base platform of a manipulator depend on the mass and the acceleration of the center of mass of each moving element. For a system of w masses $\mathbf{f}_{sh}$ can be expressed as:

$$\mathbf{f}_{sh} = \sum_{j=1}^{w} m_j \ddot{c}_j \tag{4.24}$$

where m_j is the mass and $\ddot{c}_j$ is the acceleration of the center of mass of the j^{th} element. In order to calculate the shaking forces at the Orthoglide 3-axis base-frame, three reference frames, corresponding to each leg, are defined at points A_1, A_2 and A_3, as shown in Fig. 4.5. The shaking forces for each leg are calculated independently in the respective

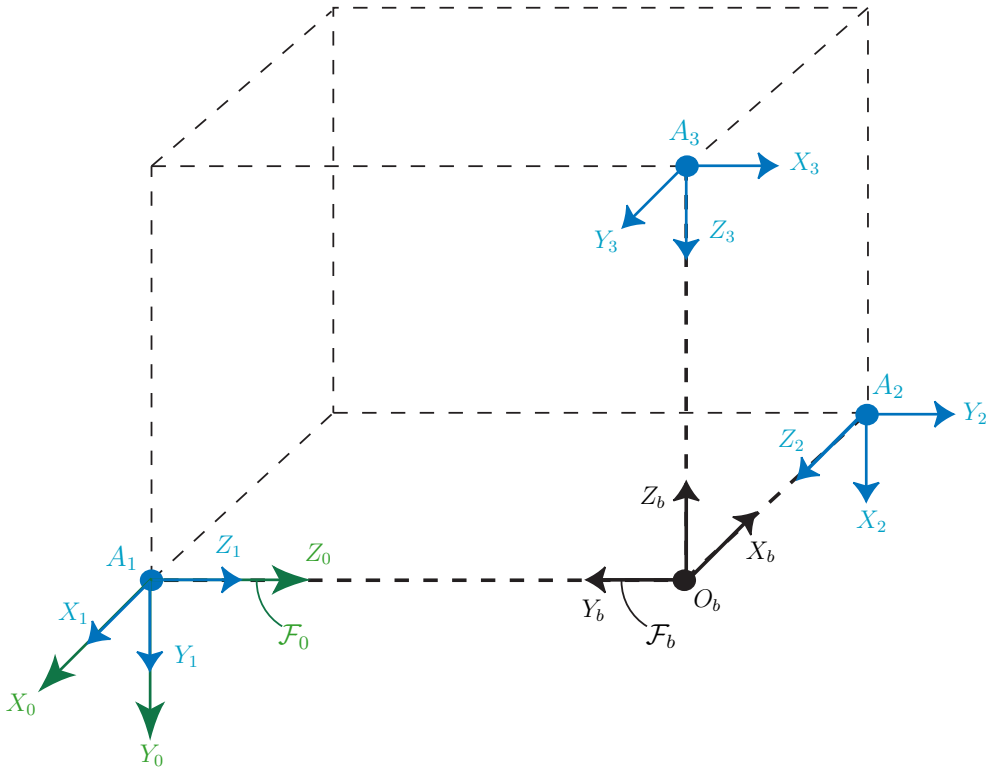

Figure 4.5 – *Definition of the reference frames*

reference frame. Each leg is supposed to be composed of six components, namely,
M_1: foot of length L_f,
M_2: the small side of the parallelogram joint attached to the foot. Its length is equal to d,
M_3,M_4: the longer sides of the parallelogram joint. Their length is equal to L_b,
M_5: the small side of the parallelogram joint attached to the end-effector,
M_6: the link between M_5 and the end-effector of length e.
Besides these leg elements, there are two other moving masses: the mass of the moving part of the prismatic actuator, M_a and the one of the end-effector M_p. The mass of each

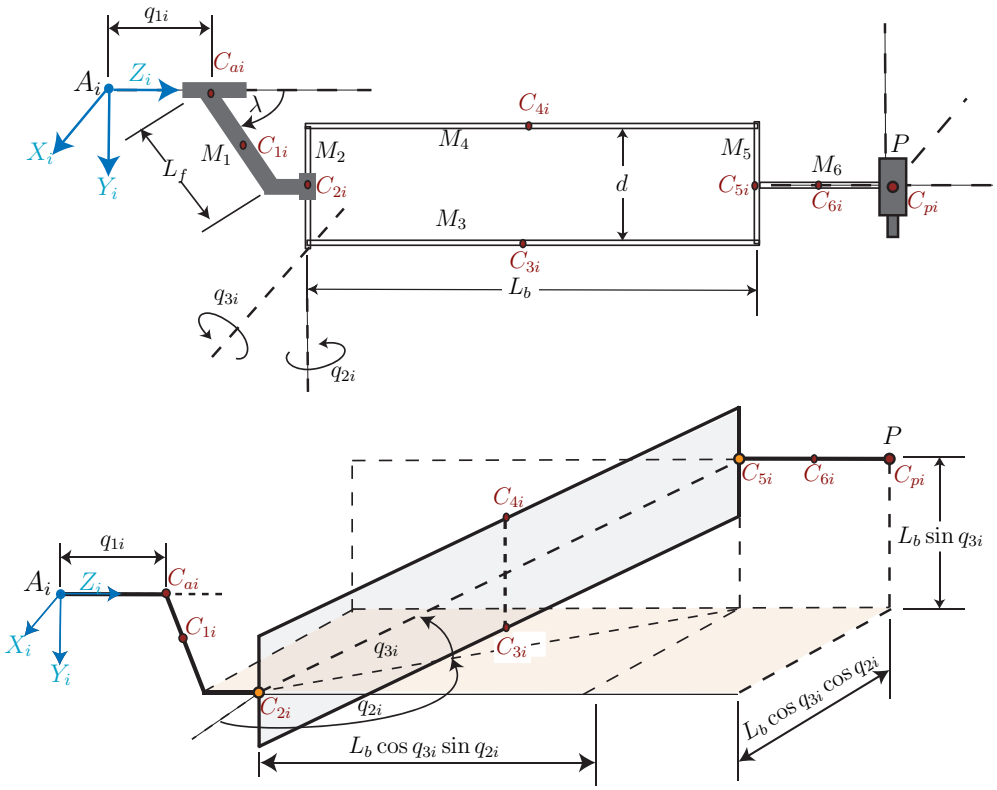

Figure 4.6 – *Orthoglide 3-axis i^{th} leg*

member M_j is denoted by m_j and the center of mass with respect to the point A_i ($i = 1,2,3$) of each element is denoted by C_{ji}, ($j = 1 \ldots 6,a,p$), as shown in Fig. 4.6. Mass of each element and geometric parameters of the Orthoglide 3-axis are presented in Table 4.3. Assuming the material of the leg components is homogeneous with center of mass at their geometric center, vectors $\mathbf{c}_{ji}$ of the j^{th} element of the i^{th} leg can be expressed in terms of the geometric (L_b, L_f, d, e, λ) and the configuration (q_{1i}, q_{2i}, q_{3i}) parameters of the Orthoglide, as shown in Fig. 4.6. Subsequently, acceleration $\ddot{\mathbf{c}}_{ji}$ of each element can be calculated. These relations are given in the Annex B. Knowing the mass and acceleration

Table 4.3 – *Parameters of the Orthoglide 3-axis Leg*

Parameter	Value	Parameter	Value
m_a	0.300 kg	L_b	0.310 m
m_1	0.248 kg	d	0.080 m
m_2, m_5	0.095 kg	L_f	0.150 m
m_3, m_4	0.117 kg	e	0.031 m
m_6	0.010 kg	λ	45 °
m_p	0.932 kg		

of each element of the i^{th} leg, the shaking forces at the base point of the leg (point A_i)

can be calculated by using Eq. (4.24), i.e,

$$\mathbf{f}_{sh}^{i} = (m_1 + m_a)\,\ddot{\mathbf{c}}_{1i} + m_2\ddot{\mathbf{c}}_{2i} + m_3\ddot{\mathbf{c}}_{3i} + m_4\ddot{\mathbf{c}}_{4i} + m_5\ddot{\mathbf{c}}_{5i} + m_6\ddot{\mathbf{c}}_{6i} + m_p\ddot{\mathbf{c}}_{pi} \tag{4.25}$$

The total shaking force at the base frame of the Orthoglide 3-axis can be obtained by summing up the forces experienced at points A_1, A_2 and A_3. With the definitions of reference frames at points A_i, the total shaking force in the reference frame $\mathcal{F}_0$, of origin point A_1, as shown in Fig. 4.5, can be written as:

$$\mathbf{f}_{sh}^{0} = \begin{bmatrix} F_x^1 + F_z^2 + F_y^3 \\ F_y^1 + F_x^2 + F_z^3 \\ F_z^1 + F_y^2 + F_x^3 \end{bmatrix} \tag{4.26}$$

The magnitude of the shaking force experienced by the i^{th} actuator at point A_i, can be written as:

$$F_{sh}^{i} = \sqrt{(F_x^i)^2 + \left(F_y^i\right)^2 + (F_z^i)^2} \tag{4.27}$$

Accordingly, two shaking force indices, defined in Sec. 4.2.2.2, can be calculated for the given discrete time steps.

4.3.1.3 Maximum Torque

The magnitude of the maximum torque τ_{max} experienced by the Orthoglide actuators can be written as:

$$\tau_{max} = \max\left(\tau_{1_{max}}, \tau_{2_{max}}, \tau_{3_{max}}\right) \tag{4.28}$$

with $\tau_{i_{max}} = \max(\tau_i)$, τ_i being the $1\times N_t$ dimensional vector of the i^{th} actuator for N_t trajectory points.

4.3.2 Test Path and External Forces

In order to apply the methodology proposed for path placement optimization, a rectangular test path is proposed. The test path is defined by the length L and the width W of the rectangle, as shown in Fig. 4.7(a). Path reference frame $\mathcal{F}_p$ is located at the geometric center of the rectangle. This type of path can be the example of the generation of a rectangular pocket like that of Fig. 4.7(b)). The position of $\mathcal{F}_p$ in the base frame $\mathcal{F}_b$ is defined with the Cartesian coordinates of the origin of $\mathcal{F}_p$, $O_p(x_{O_p}, y_{O_p}, z_{O_p})$ and the orientation of $\mathcal{F}_p$ with respect to $\mathcal{F}_b$ is given by Euler's angles, as depicted in Fig. 4.1(b). For the sake of simplicity, only one of the three rotation angles is considered, i.e., rotation about Z_b-axis

while X_bY_b and X_pY_p planes are considered to be always parallel. Accordingly, there are four path placement variables, i.e., x_{O_p}, y_{O_p}, z_{O_p} and ϕ, as illustrated in Fig. 4.7(a).

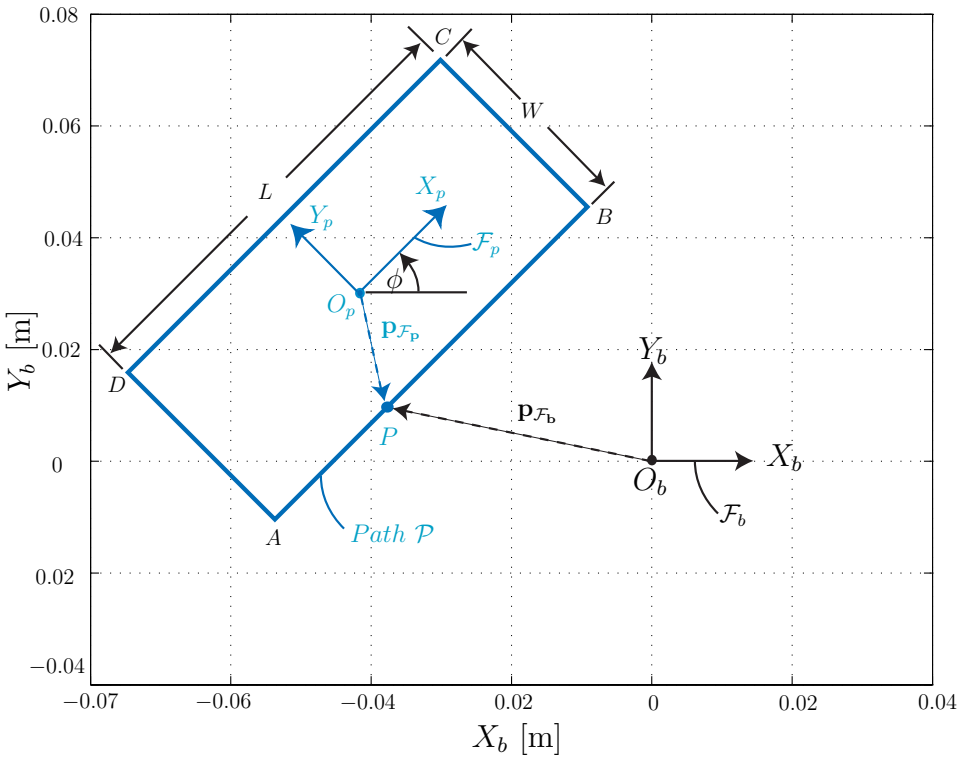

(a) Rectangular test path

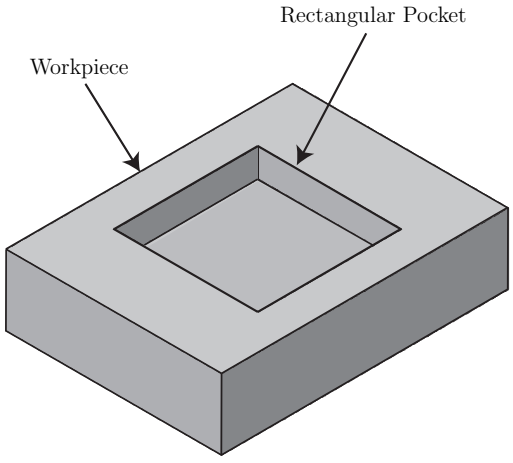

(b) Rectangular pocket

Figure 4.7 – *Test path characterization*

The magnitude of the end-effector velocity is supposed to be constant along the path. Hence, for given path dimensions, position vector $\mathbf{p}_{\mathcal{F}_\mathbf{p}} = [x_{Pp} \quad y_{Pp} \quad z_{Pp}]^T$ and velocity

vector $\mathbf{v}_{\mathcal{F}_\mathbf{p}} = [\dot{x}_{Pp} \quad \dot{y}_{Pp} \quad \dot{z}_{Pp}]^T$ in the path frame can be evaluated as a function of time. Figure 4.8 shows the position and velocity profiles in $\mathcal{F}_p$ for a $0.05\,\mathrm{m}\times 0.10\,\mathrm{m}$ rectangular path and for a constant end-effector velocity of $1.0\,\mathrm{m.s}^{-1}$. Position and velocity vectors defined in $\mathcal{F}_p$ can be expressed in $\mathcal{F}_b$ by means of the transformation matrix defined in Eq. (4.3), namely,

$$\begin{bmatrix} x_{P_b} \\ y_{P_b} \\ z_{P_b} \\ 1 \end{bmatrix} = \begin{bmatrix} \cos\phi & -\sin\phi & 0 & x_{Op} \\ \sin\phi & \cos\phi & 0 & y_{Op} \\ 0 & 0 & 1 & z_{Op} \\ 0 & 0 & 0 & 1 \end{bmatrix} \begin{bmatrix} x_{P_p} \\ y_{P_p} \\ z_{P_p} \\ 1 \end{bmatrix}$$

$$\begin{bmatrix} \dot{x}_{P_b} \\ \dot{y}_{P_b} \\ \dot{z}_{P_b} \\ 1 \end{bmatrix} = \begin{bmatrix} \cos\phi & -\sin\phi & 0 & 0 \\ \sin\phi & \cos\phi & 0 & 0 \\ 0 & 0 & 1 & 0 \\ 0 & 0 & 0 & 1 \end{bmatrix} \begin{bmatrix} \dot{x}_{P_p} \\ \dot{y}_{P_p} \\ \dot{z}_{P_p} \\ 1 \end{bmatrix}$$

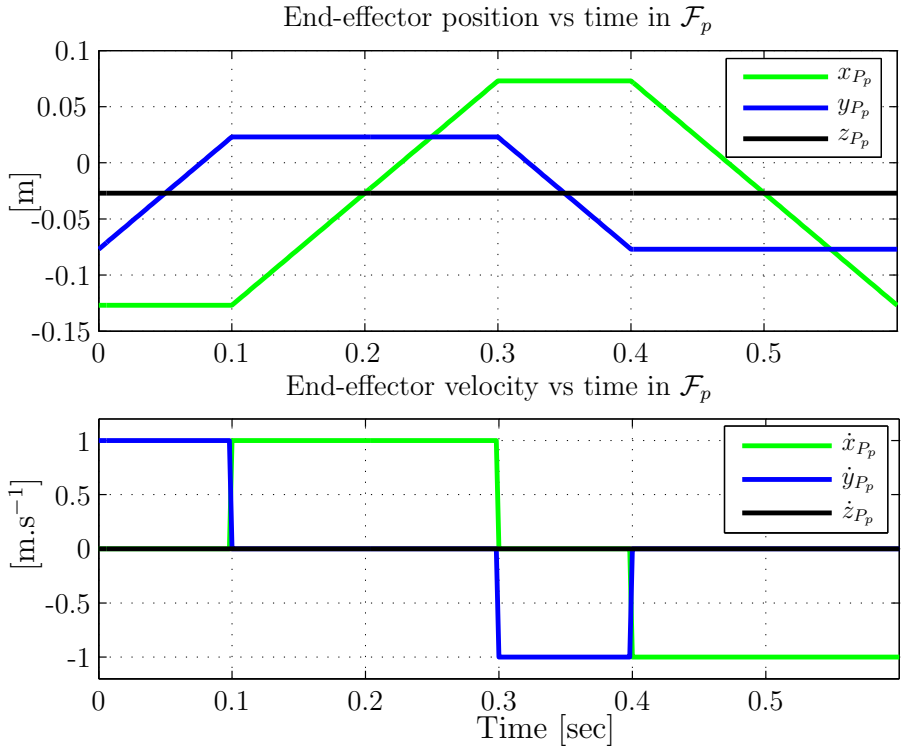

Figure 4.8 – *Test trajectory for a rectangular path of size* $0.05 \times 0.10\,m^2$

with $\mathbf{x} = [x_{O_p} \quad y_{O_p} \quad z_{O_p} \quad \phi]^T$ being the decision variables vector of the optimization problem. For a matter of simplicity and not to deal with tangent and curvature discontinuities, we consider that the path is composed of four independent line segments. Therefore, we do not pay attention to the discontinuities between the segments.

In order to analyze the effect of external cutting/machining forces in the generation of a given path, a groove milling operation is considered as shown in Fig. 4.9. With constant

feed rate or end-effector velocity v_p of magnitude $0.66\,\mathrm{m.s^{-1}}$, i.e., $40\,\mathrm{m.min^{-1}}$, the following components of cutting forces are considered, (Majou *et al.*, 2007):

F_f: component in the feed direction = 10 N

F_a: component along the axis of cutting tool = 25 N

F_r: component perpendicular to F_f and F_a= 215 N

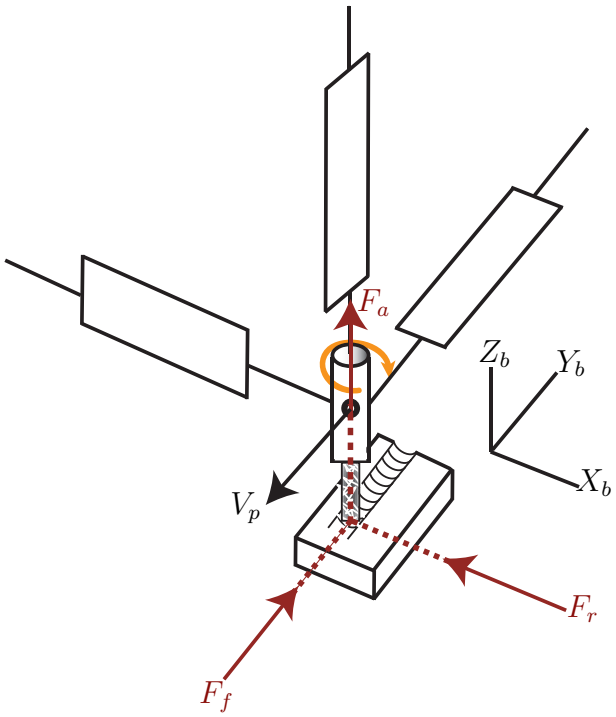

Figure 4.9 – *Cutting forces (Majou et al., 2007)*

4.4 Results and Discussions

The optimal path placement process introduced in this chapter is highlighted for Orthoglide 3-axis by means of the rectangular test paths presented in the previous section. The path placement optimization problem for the Orthoglide 3-axis is formulated and solved, separately, both for mono-objective and multi-objective formulations. The kinematic, velocity and dynamic models of the manipulator are used to evaluate the required actuator displacements, velocities and torques. It should be noted that within the prescribed workspace, the Orthoglide 3-axis is free of internal collisions and that there is not any limit on the passive joints. Therefore, the geometric constraints for the path placement problem are the upper and lower limits of the prismatic joints variables. The kinematic constraints are the maximum velocities that the prismatic actuators can produce whereas the dynamic constraints are the limits of the torque/force that the actuators can produce. The kinematic and dynamic constraints are obtained from the catalogue, as given in Table 4.2.

■

As already mentioned, the decision variables are the Cartesian coordinates of the origin of $\mathcal{F}_p$ and the orientation angle of $\mathcal{F}_p$ with respect to $\mathcal{F}_b$.

4.4.1 Results: Mono-Objective Path Placement Optimization for Orthoglide 3-axis

Mono-objective path placement optimization problem, presented in Eq. 4.21, is formulated for Orthoglide 3-axis as follows,

$$\min_{\mathbf{x}} E_t = \sum_{i=1}^{n} E_i(\mathbf{x}) \qquad \text{subject to: } \begin{cases} \rho_{min} \leqslant \rho_{x,y,z} \leqslant \rho_{max} \\ |v_{x,y,z}| \leqslant v_{max} \\ |\tau_{x,y,z}| \leqslant \tau_{max} \end{cases} \tag{4.29}$$

where $\mathbf{x} = \begin{bmatrix} x_{Op} & y_{Op} & z_{Op} & \phi \end{bmatrix}^T$. The subscripts x, y and z are used for three prismatic actuators or three Cartesian directions. ρ_{min} and ρ_{max} are respectively the minimum and maximum displacements of the prismatic joints as presented in Table 4.1.

The optimization problem is solved by using the MATLAB *fmincon* function, which is a general constrained optimization solver using the derivative-based search algorithms. The optimization process was performed with different starting points and it turned out that MATLAB *fmincon* function always converges to the same solution no matter the starting point. Furthermore, to study the variation pattern of energy requirements at different points within the workspace, a workspace discretisation is carried out with respect to the path placement variables and the energy is calculated for each of the discrete point for a given path while verifying the constraints.

The optimization process is performed for different rectangular test paths with constant aspect ratio of 2, i.e., $L/W = 2$. With the help of the optimization algorithm, the location of the path corresponding to minimum and maximum energy consumption is obtained, i.e., the best and the worst path locations with respect to the electric energy consumption. Figures 4.10 and 4.11 show the location of different rectangular paths with the minimum and maximum energy consumption in the Orthoglide 3-axis cubic workspace. The magnitude of the energy used for both the best and the worst cases and the corresponding gain of energy is given in Table 4.4 and is illustrated in Fig. 4.12. In Fig. 4.12, % saving is the percent energy saving between the best(minimum) and the worst(maximum) energy consumption.

It can be seen from Figs. 4.10 and 4.11 that the energy consumption is a minimum when the path is located in the vicinity of the isotropic configuration with $\phi = 0\,^\circ$ and is a maximum when the path is located in the vicinity of point Q^- with $\phi = 45\,^\circ$. From Fig. 4.12, it can be noticed that the smaller the path, the higher the energy saving. This higher gain for the smaller path is due to the higher range of displacement of the path

Table 4.4 – *Minimum and maximum energy used for a given rectangular path*

Rectangular path dimensions [m]		E_{min} [J]	E_{max} [J]	% gain
Width (W)	Length (L)			
0.02	0.04	15.26	44.46	65.68
0.03	0.06	22.88	61.35	62.71
0.04	0.08	30.41	76.31	60.15
0.05	0.10	38.55	89.80	57.07
0.06	0.12	46.83	102.11	54.13
0.07	0.14	56.82	113.46	49.92
0.08	0.16	65.94	121.17	46.89

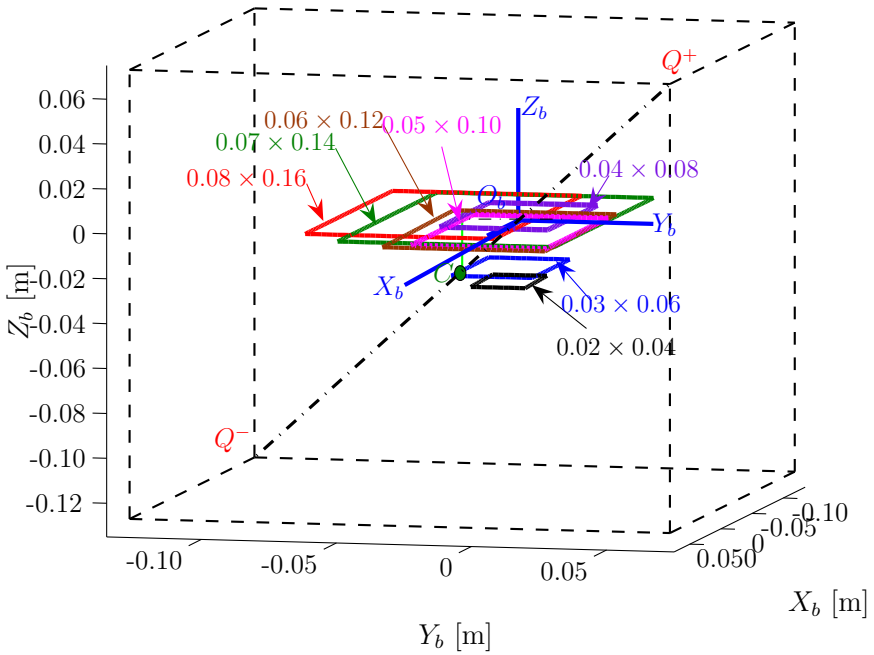

Figure 4.10 – *Locations of rectangular path of different sizes (W m × Lm) that yield a minimum energy consumption*

within the manipulator workspace.

In order to view the energy variation trends in the workspace, a test path of size 30 m × 60 m is taken and the energy required for the generation of this test path is evaluated for several positions and orientations. Figure 4.13 shows the variations in the energy used with respect to x_{Op} and z_{Op} for a constant orientation ϕ of 0 ° and for three different values of y_{Op}. Figure 4.14 illustrates the isocontours of the energy required by the motors with respect to x_{Op} and y_{Op} for given values of z_{Op} and ϕ, namely, $z_{Op} = 0$ and $\phi = 0\,°$. From Fig. 4.13, it is apparent that the energy required is not sensitive to variations in z_{Op}. The reason being that the path lies in the X_bY_b-plane and the actuators displacements along Z_b-axis is not significant. Figures 4.13 and 4.14 also show that the energy required by the motors is a minimum when the path is located in the neighbourhood of the isotropic configuration

■

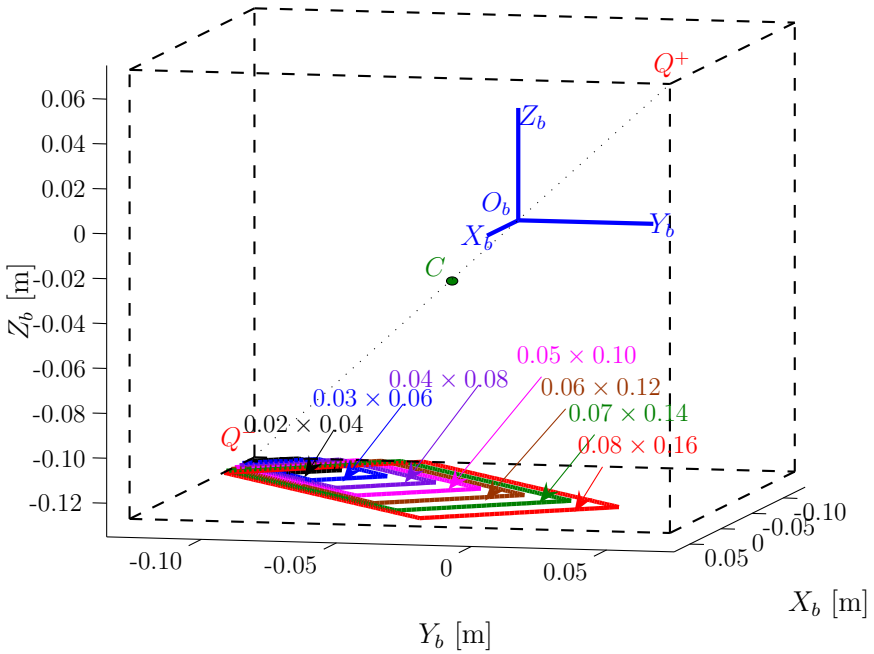

Figure 4.11 – *Locations of rectangular path of different sizes ($W\,m \times L\,m$) that yield a maximum energy consumption*

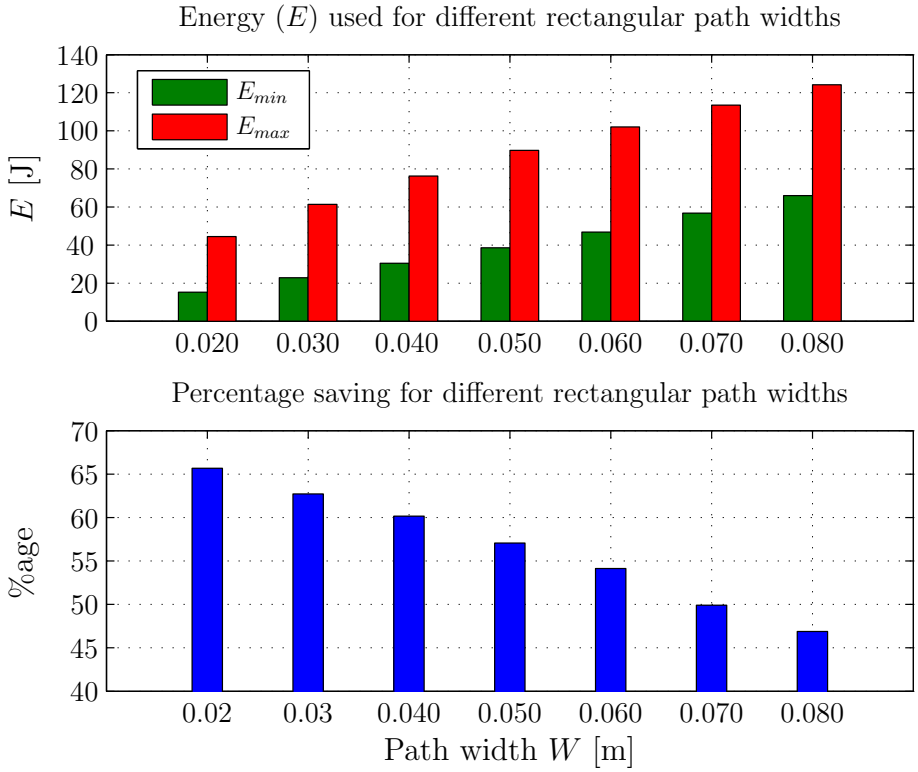

Figure 4.12 – *E_{min} and E_{max} and percentage saving as a function of the rectangular path width ($L = 2W$)*

and is a maximum when the latter is located in the neighbourhood of singularities.

Figures 4.15 and 4.16 show the variations in the energy used with the path orientation in different areas of the cubic workspace. It can be seen that the energy used is usually maximum when $\phi = 45\,°$. However, for some path locations, the energy consumption is

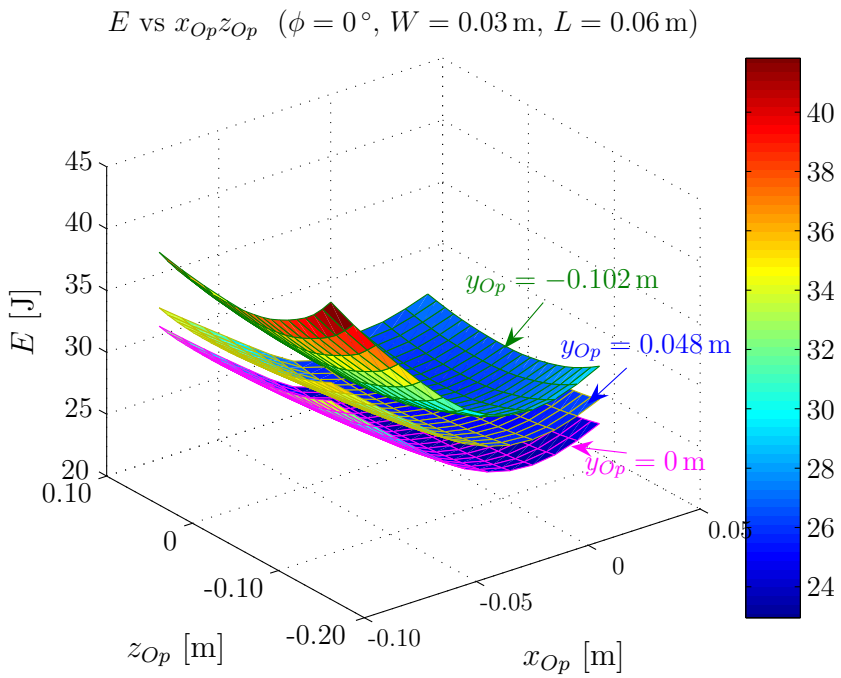

Figure 4.13 – *Energy as a function of x_{Op} and z_{Op} for a 30 m×60 m rectangular path*

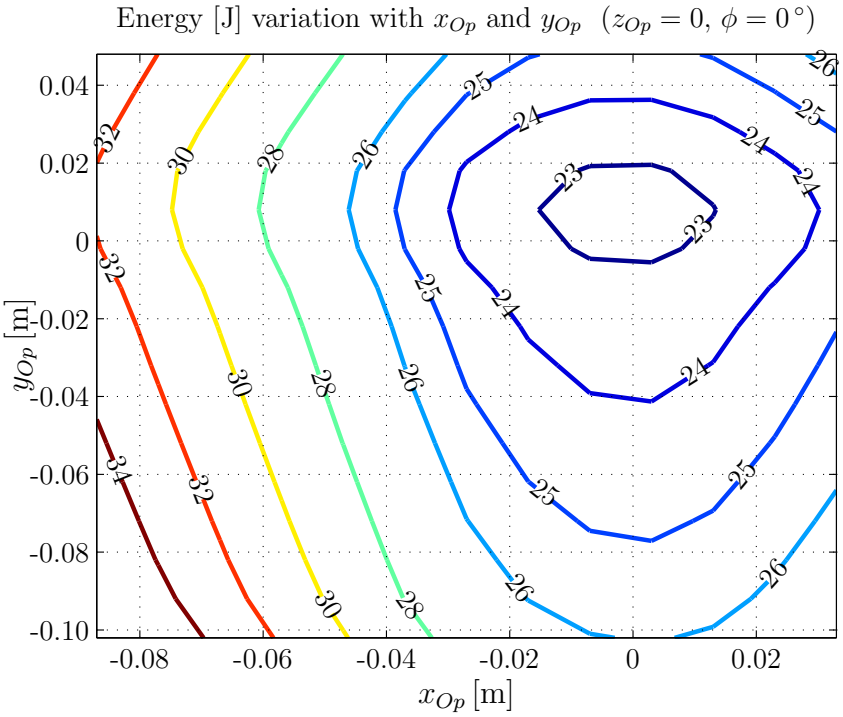

Figure 4.14 – *Energy vs x_{Op} and y_{Op} for 30 m × 60 m rectangular path*

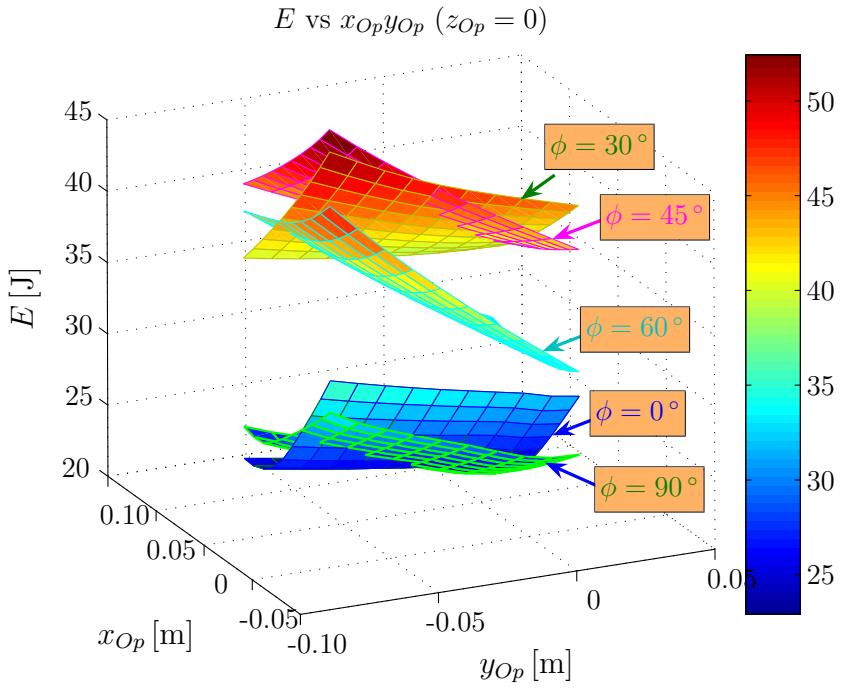

Figure 4.15 – *Energy as a function of x_{Op} and y_{Op} for different orientations ($z_{Op} = 0$)*

maximum for a path orientation other than 45 °. For example, the energy required at the upper right corner of the workspace is higher for $\phi = 30\,°$ than $\phi = 45\,°$.

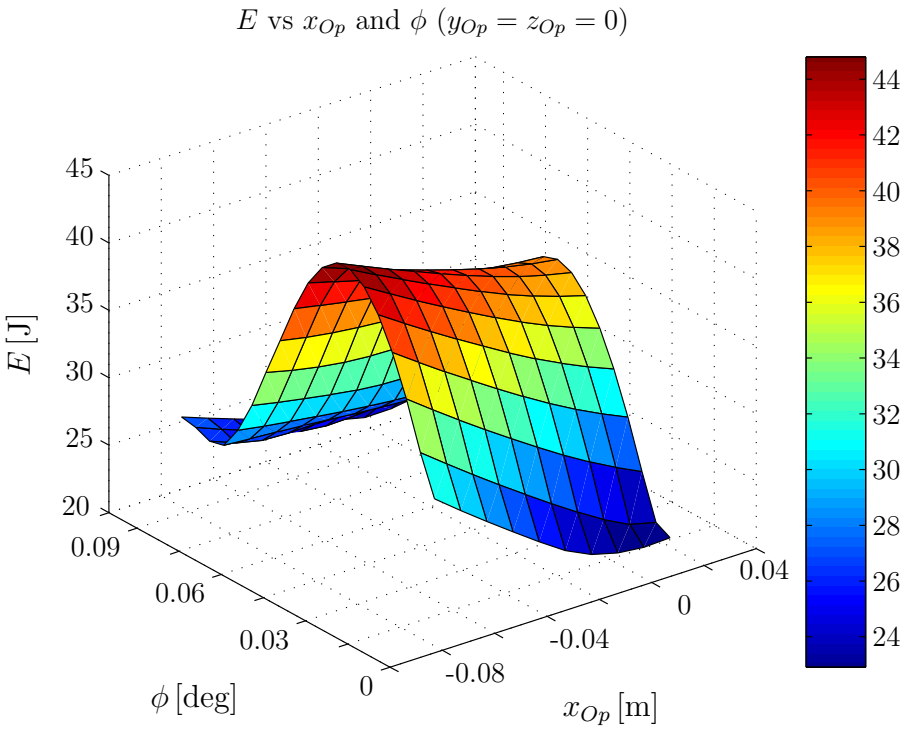

Figure 4.16 – *Energy as a function of x_{Op} and ϕ for $y_{Op} = z_{Op} = 0$*

Figure 4.17 shows the comparison of trajectory parameters of 0.03 m × 0.06 m test path for minimum and maximum energy locations. It makes sense that when $E = E_{max}$ the range of actuators displacement is larger than when $E = E_{min}$. Similarly actuators experience

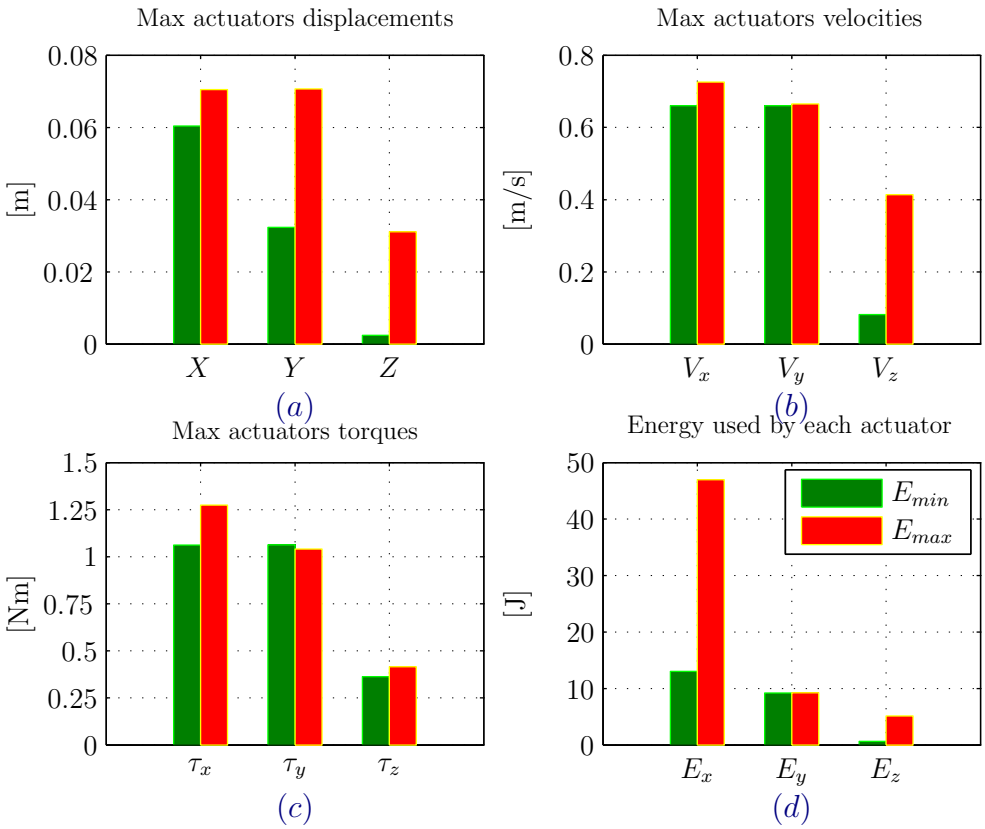

Figure 4.17 – *Comparison of* $0.03\,m \times 0.06\,m$ *trajectory parameters for* E_{min} *and* E_{max} *locations*

higher values of maximum velocities and torques when $E = E_{max}$ as shown in Fig. 4.17(b-c), which results in higher energy consumption for each actuator, as shown in Fig. 4.17(d). These results mean that the actuators may reach their performance limits due to an inappropriate location of the path in the workspace.

4.4.2 Results: Multi-objective Path Placement Optimization for Orthoglide 3-axis

Multi-objective optimum path placement problem, presented in Eq. 4.22, is formulated for Orthoglide 3-axis as follows,

$$\min_{\mathbf{x}} \left(f_1 : \; E_t, f_2 : I_{\delta f}, f_3 : I_f, f_4 : \tau_{max}\right) \qquad \text{subject to:} \begin{cases} \rho_{min} \leqslant \rho_{x,y,z} \leqslant \rho_{max} \\ |v_{x,y,z}| \leqslant v_{max} \\ |\tau_{x,y,z}| \leqslant \tau_{max} \end{cases} \tag{4.30}$$

The problem can be modeled in any multiobjective optimization environment. Over here, *MATLAB* along with *modeFRONTIER* softwares are used to implement and demonstrate the proposed methodology for Orthoglide 3-axis. A screen-shot of the *modeFRONTIER* model, with four design variables, four constraints and four objective functions, is shown in Fig. 4.18.

A multiobjective genetic algorithm (MOGA) is used to obtain the Pareto frontiers

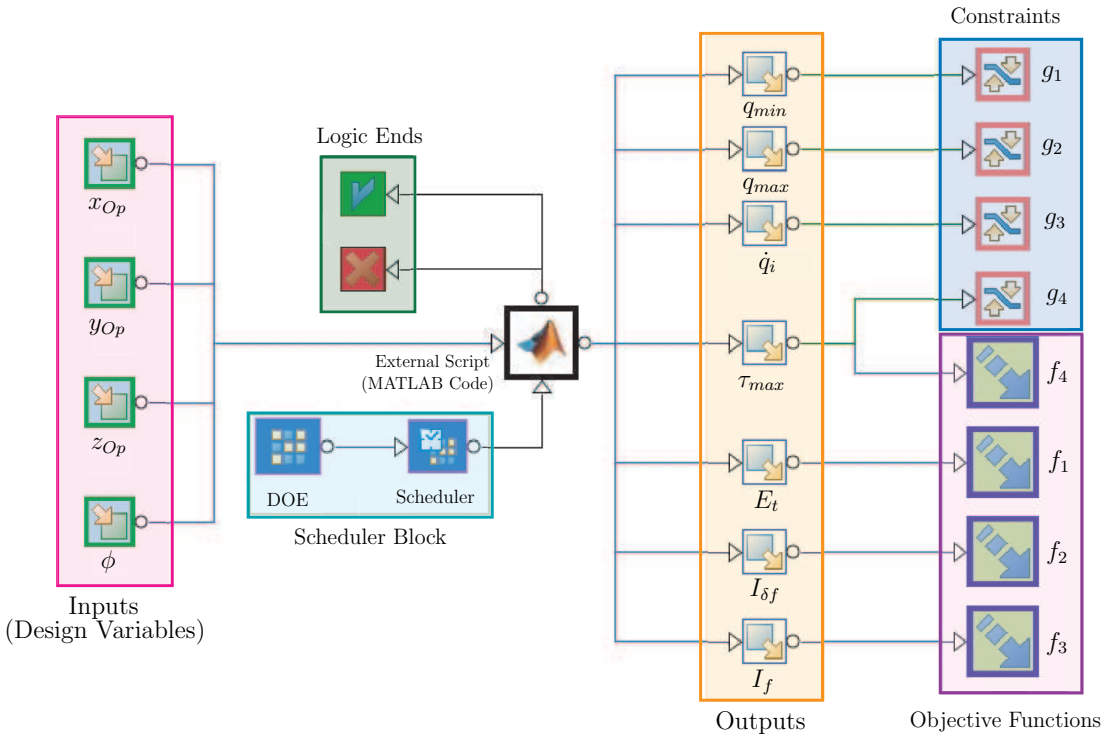

Figure 4.18 – *modeFRONTIER model*

Table 4.5 – modeFRONTIER *algorithm parameters*

Scheduler	MOGA-II
Number of iterations	100
Directional cross-over probability	0.5
Selection probability	0.05
Mutation probability	0.1
DNA string mutation ratio	0.05
DOE algorithm	Sobol
DOE number of designs	40
Total number of iterations	$40 \times 100 = 4000$

for a rectangular test path of dimensions 0.03 m ×0.06 m with an end-effector velocity V_p=0.66 m.s^{-1}. *modeFRONTIER* scheduler and DOE parameters are given in Table 4.5. MATLAB is used to process and analyze the system for any individual of the current population (generated by the *modeFRONTIER* scheduler). Corresponding to each population set, *MATLAB* returns the output variables that are analyzed by *modeFRONTIER* for the feasible solutions according to the given constraints. At the end, the Pareto-optimal solutions are obtained from the generated feasible solutions.

The Pareto frontiers obtained are shown in Fig. 4.19. Maximum and minimum (optimum) values of each objective, corresponding design parameters and percentage variation (%Δ) are given in Table 4.6. Path locations in the Orthoglide 3-axis workspace for maximum and minimum objective functions are shown in Fig. 4.20.

Table 4.6 shows that the variation in the shaking forces ($I_{\delta f}$) can be significantly reduced

Table 4.6 – *Design parameters that correspond to the Pareto solutions for which the objective functions are either a minimum or a maximum*

Objective		x_p [m]	y_p [m]	z_p [m]	ϕ [deg]	Value	Δ	%Δ
E_t [J]	E_{max}	−0.0276	−0.0348	−0.0789	37.2	56.49	33.54	59.38
	E_{min}	0.0141	−0.0044	0.0097	1.44	22.94		
$I_{\delta f}$ [N]	$I_{\delta fmax}$	−0.0204	−0.0693	−0.0019	0.63	2.445	2.41	98.60
	$I_{\delta fmin}$	0.0009	−0.0011	−0.0164	45.0	0.034		
I_f [N]	I_{fmax}	0.0389	−0.0801	−0.1114	40.1	2.620	0.456	17.39
	I_{fmin}	0.0009	−0.0011	−0.0164	45.0	2.164		
τ_{max} [Nm]	τ_{max}	0.0381	−0.0056	0.0714	24.0	1.135	0.287	25.24
	τ_{min}	0.0053	0.0069	−0.1166	42.0	0.849		

(almost to zero) with an appropriate path placement. As a matter of fact, up to 60% of the energy consumption can be saved with a proper path placement. Maximum shaking forces I_f and maximum actutators torque τ_{max} can be reduced to 17% and 25%, respectively.

Figure 4.21 shows the shaking forces experienced by three prismatic actuators of Orthoglide 3-axis for minimum energy consumption and minimum $I_{\delta f}$ path locations. It can be seen that although the maximum values of the shaking forces for both Pareto-points are almost the same, their variations can be reduced considerably with proper path location. The smoother the shaking force variations, the lower the vibrations in the mechanism. From Table 4.6 and Fig. 4.20-(a) it can be noted that optimum points with respect to E_t, $I_{\delta f}$ and I_f lie in the neighbourhood of the isotropic configuration of the manipulator ($x_p = y_p = z_p \approx 0$) whereas for τ_{max}, z_p attain their minimum value, i.e., at the base of the workspace. Similarly with respect to orientation, ϕ, E_t is minimum for $\phi \approx 0\,^\circ$ and the other three objectives are minimum for $\phi \approx 45\,^\circ$.

Figure 4.22 summarizes the variational trends as well as the inter-dependency between the objective functions and design variables by means of a scatter matrix. The lower triangular part of the matrix represents the correlation coefficients whereas the upper one shows the corresponding scatter plots. Diagonal elements represents the probability density charts of each variable. The correlation coefficients vary from -1 to 1. Two variables are strongly dependent when their correlation coefficient is close to -1 or 1 and independent when the latter is null. From Fig. 4.22,

– E_t, $I_{\delta f}$ and τ_{max} strongly dependent as the correlation coefficients between E_t and $I_{\delta f}$, E_t and τ_{max} and $I_{\delta f}$ and τ_{max} are equal to -0.822, -0.785 and 0.819, respectively.

■

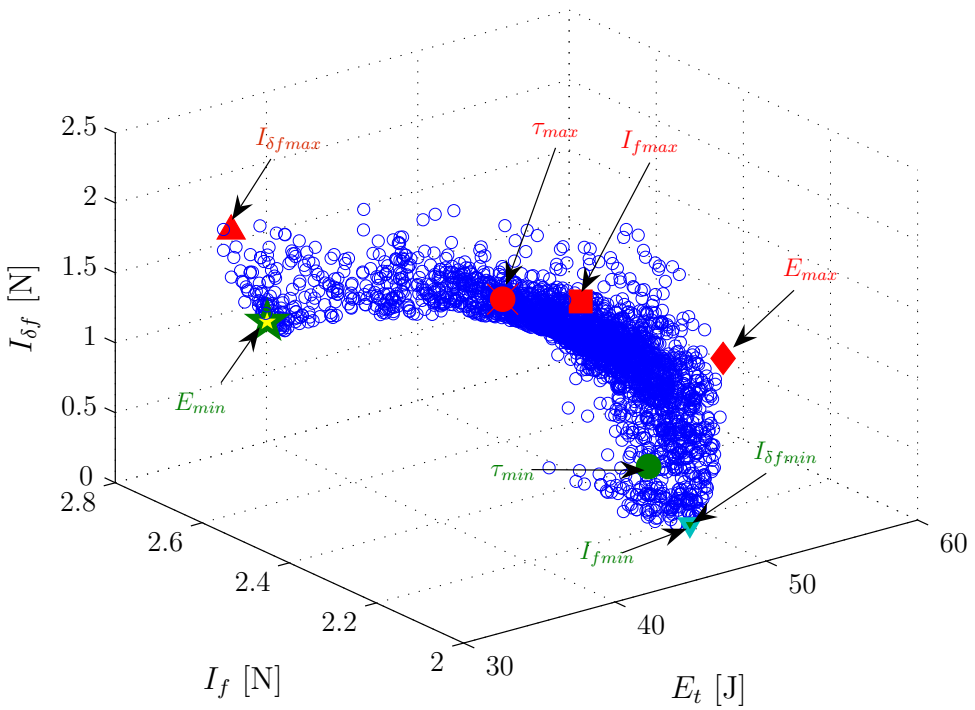

(a) E_t Vs I_f Vs $I_{\delta f}$

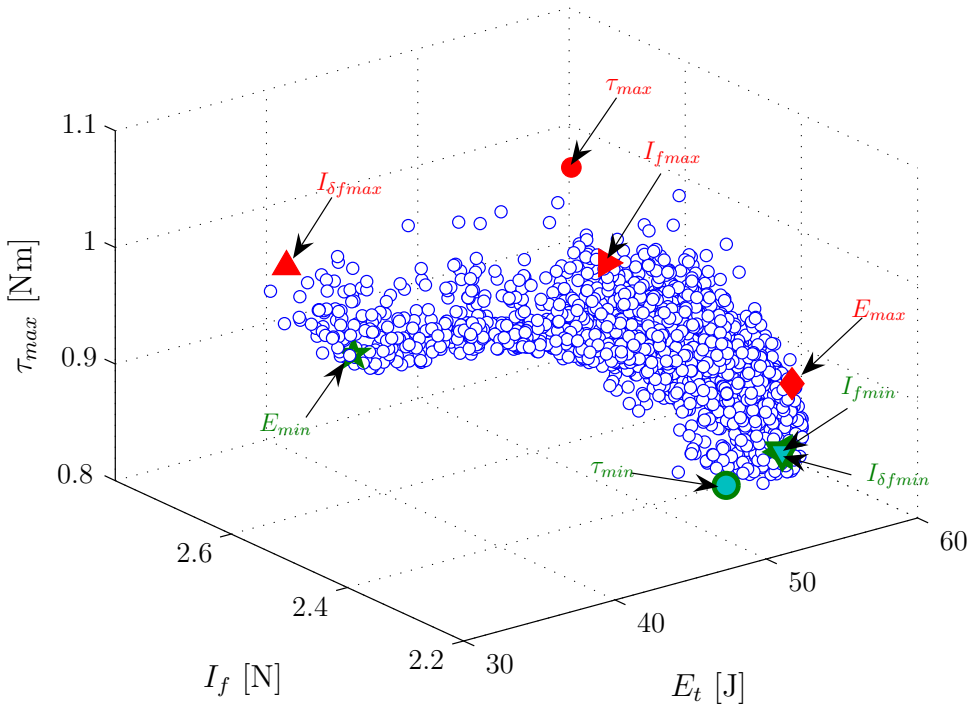

(b) E_t Vs I_f Vs τ_{max}

Figure 4.19 – *Pareto frontier for the Orthoglide 3-axis path placement problem*

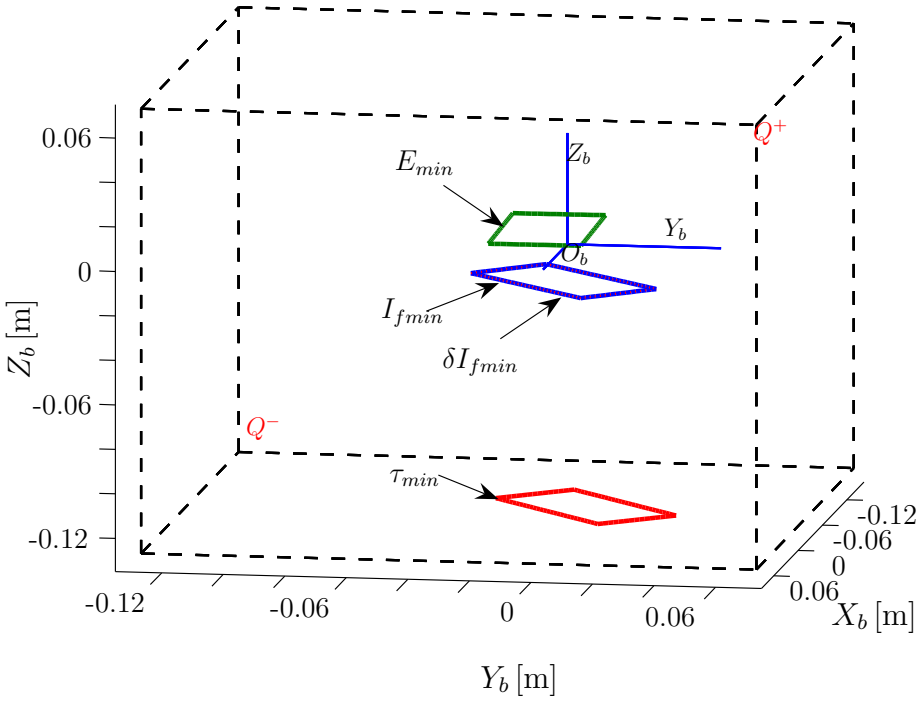

(a) Minimum objectives locations

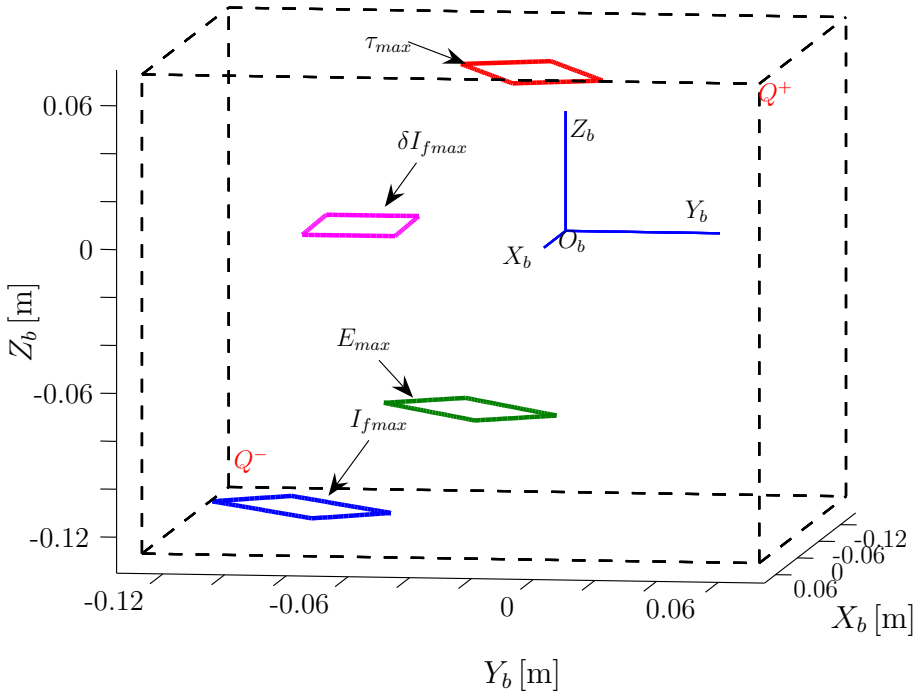

(b) Maximum objectives locations

Figure 4.20 – *Path locations in the Orthoglide 3-axis workspace for minimum and maximum objective functions*

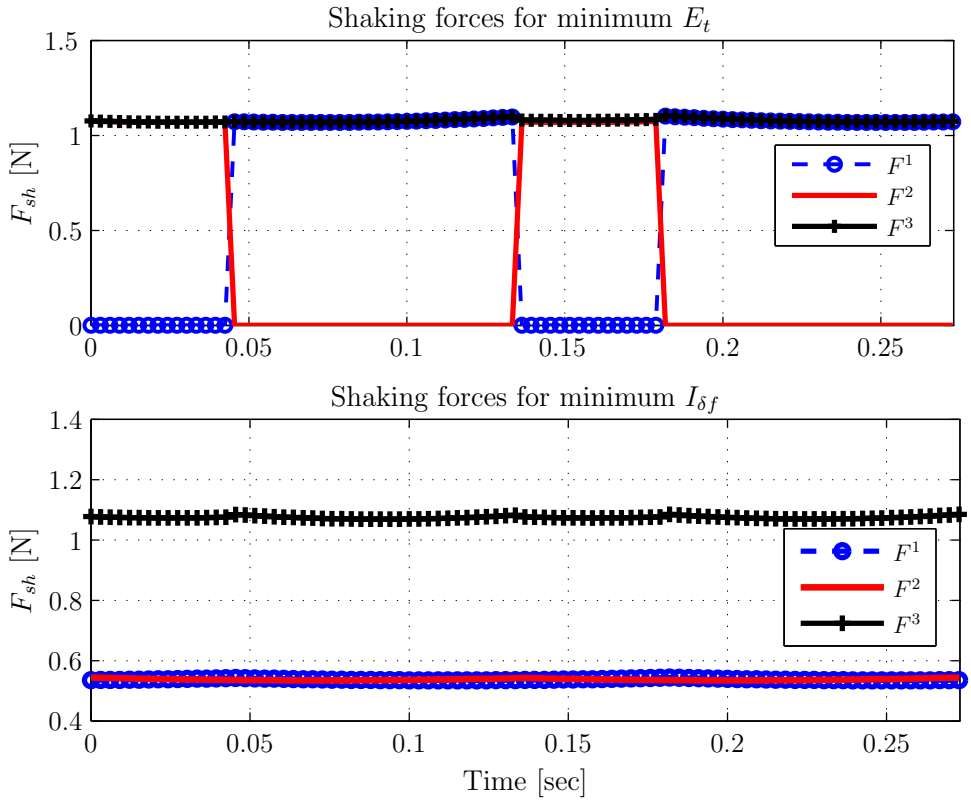

Figure 4.21 – *Shaking forces experienced by three actuators for E_{min} and $I_{\delta f min}$*

However, the lower E_t, the higher τ_{max} and $I_{\delta f}$.

- the correlation of I_f with E_t, $I_{\delta f}$ and τ_{max} is very low as the corresponding correlation coefficients are equal to -0.113, 0.185 and -0.065, respectively.
- ϕ has strong and direct correlation with E_t (0.907) whereas it has strong and inverse correlation with $I_{\delta f}$ and τ_{max} (-0.966, -0.828, respectively);
- x_p, y_p, z_p have very week or unpredictable relations with respect to all objectives and parameters.

As $I_{\delta f}$ and τ_{max} are linearly related, the lower $I_{\delta f}$, the lower τ_{max}, no matter the scale of variation of both functions. E_t and $\tau_m ax$ are antagonistic. Likewise, E_t and $I_{\delta f}$ are antagonistic. Regarding the design variables, the path orientation ϕ is the most influential for the considered test path. Finally, the foregoing results are only valid for the Ortho-glide 3-axis manipulator and the given test path. However, the methodology illustrated in this section is appropriate for any manipulator and test path.

4.5 Conclusions

An approach to optimally locate a given trajectory profile, path or task within the workspace of a manipulator presented. The electric energy consumed by the actuators to carry

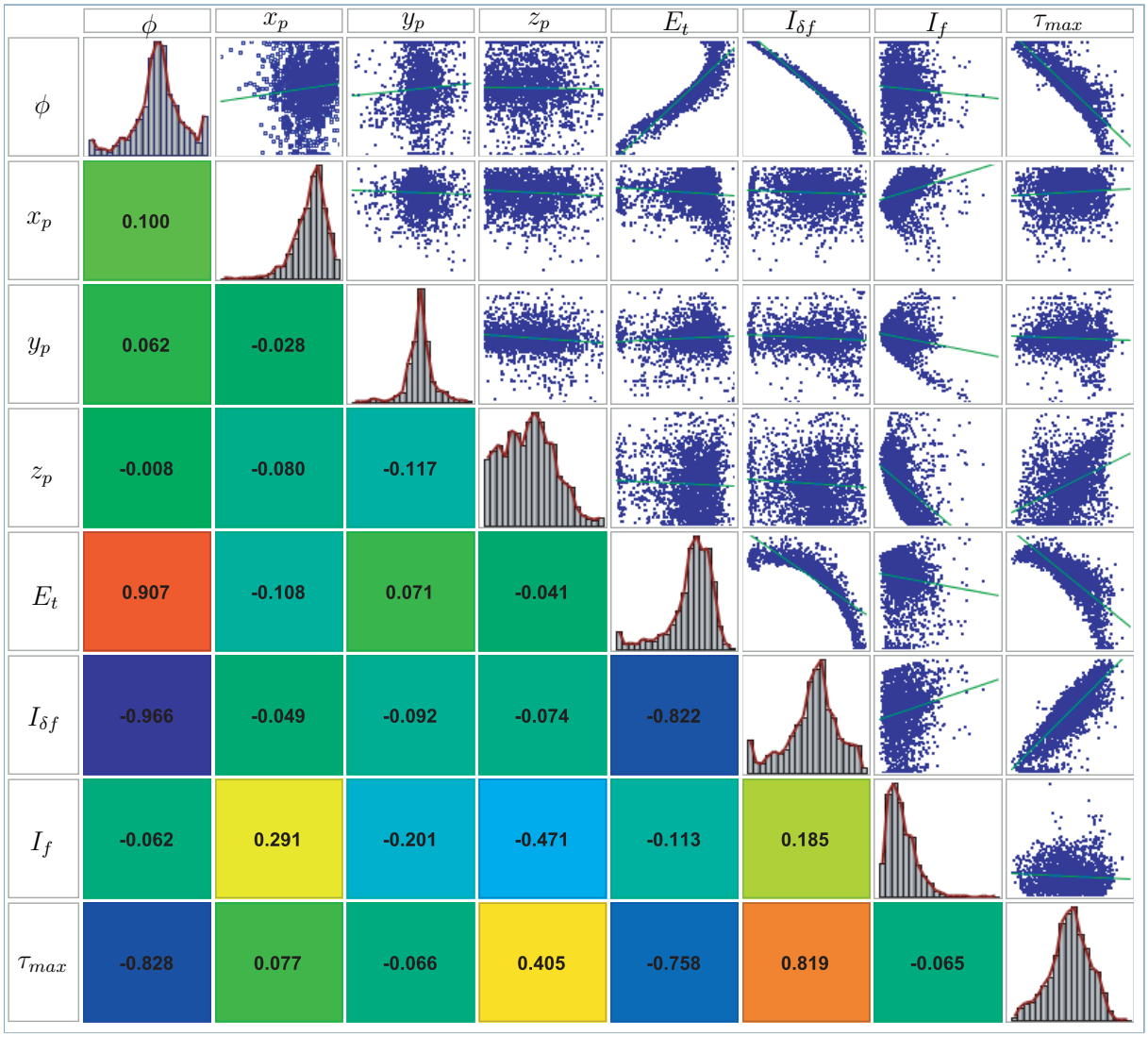

Figure 4.22 – *Scatter matrix for objective functions and design variables*

out that given path is considered as the primary optimization criterion. The minimization of the effects of the shaking forces and minimization of the actuators peak torques are considered as other optimum path placement criteria, hence obtaining a multiobjective optimization problem. The electric energy requirement is calculated with the help of the required actuators torques and velocities along with motors electric parameters. Kinematic, velocity and dynamic modelings are used to evaluate the actuators velocities, accelerations and torques to realize the given path at a certain location in the workspace. To guarantee the feasibility of the solution, actuators performance limits such as their joint limits, maximum velocities and torque capabilities are used as the constraints of the optimization problem.

The proposed methodology is applied to a single and a multiobjective optimization problems for the Orthoglide 3-axis, a 3-dof translating parallel manipulator having a regular cubic workspace. Rectangular shaped test paths are considered as illustrative examples.

Such paths are similar to that used to realize a pocketing operation.
The use of the electric energy instead of mechanical energy as an optimization criterion is pertinent. Although actuator electric energy consumption depends on the mechanical energy requirements, the electric energy evaluation is more comprehensive than its mechanical counterpart. The general approach used to calculate the mechanical energy with the help of manipulator velocity and dynamic models, i.e., by using actuators torques and velocities, may lead to an under estimation of the energy requirements in the case where actuators are experiencing torques whereas they do not move. Besides, usual mechanical energy calculations do not consider the resistive energy loss in the motors windings neither the energy loss due to the variations in the actuators velocities. Those variations affect the current requirements and hence induce electromotive forces in the actuators. Accordingly, the electric energy formulation takes into account all these energy losses.
The energy required to perform a given task depends on the position and the orientation of the task within the workspace of the manipulator. Accordingly, some electric energy can be saved by properly selecting the position and the orientation of the task. Indeed, a misplaced task can cause excessive energy consumption and can force the actuators to go over their performance limits.
For the Orthoglide 3-axis, the optimum path location is found to be in the neighbourhood of the isotropic configuration but there is no general rule to predict the exact optimal position and orientation of a task particularly for a complicated three dimensional task or for an irregular workspace. However, a detailed analysis of the energy variation within the workspace for a given task can lead to the optimal position/orientation of that particular task. Numerical optimization algorithms are useful for such a comprehensive analysis in which all the problem constraints and performance measures can be considered simultaneously.
Variations in the shaking forces experienced by the base platform of a manipulator are also path location dependent. However, the lower the effects of the shaking forces, the higher the energy consumption. Magnitude of the maximum shaking forces can also be reduced with path location but to a lower extent compared to the reduction of variations in shaking forces. Similarly, the magnitude of the maximum actuators torques can be reduced with an appropriate path location. However, the lower the shaking forces effects and the higher the maximum actuators torques, the higher the energy consumption. Hence, the user has to make a compromise.
In future works, other objective functions have to be considered such as the stiffness and the manipulability of the manipulator for the realization of more complex tasks and in case of irregular workspaces. Furthermore, to have a complete picture of shaking effects, along with shaking forces, shaking moments should also be considered. Finally, the optimal path placements obtained should be checked experimentally.

Conclusions

Parallel manipulators, also known as parallel kinematics machines (PKMs), have attracted attention for their high speed, better accuracy, low mass/inertia properties and high structural stiffness. These are attractive features for the innovative machine-tool architectures; however practical utilization for the potential benefits requires an extensive and efficient analysis of their structure, kinematics and dynamics.

PKMs design, like any other product design, goes through many phases and requires, as a prerequisite, a designer's knowledge as well as years long experience for a design to be appreciable. A designer is faced with a great amount of variables and parameters, each one needed to be analyzed carefully. While some are more important than others, to know how important they are with respect to each other can be an exhaustive task. Still, there are times when less important variables play the most important role in the failure of an engineering structure. It is only natural that while dealing with a very complex design of enormous proportions, it is not possible for a designer to take into account all the variables simultaneously. An optimization process, however, does not require such an experience and it is faster than conventional design processes. Design optimization based on numerical algorithms and techniques can be applied to various engineering systems to help a designer come out with a proposal that is more efficient, light weight, reliable, safe, cost effective and that satisfies the user too. This requires not only the final product to be optimized but also the optimization of manufacturing process as well as the optimum use/application of the product. This requires not only the final product to be optimized but also the optimization of manufacturing process as well as the optimum use/application of the product.

PKMs design, like any other product design, goes through many phases and requires, as a prerequisite, a designer's knowledge as well as years long experience for a design to be appreciable. A designer is faced with a great amount of variables and parameters, each one needed to be analyzed carefully. While some are more important than others, to know how important they are with respect to each other can be an exhaustive task. Still,

there are times when less important variables play the most important role in the failure of an engineering structure. It is only natural that while dealing with a very complex design of enormous proportions, it is not possible for a designer to take into account all the variables simultaneously. An optimization process, however, does not require such an experience and it is faster than conventional design processes. Design optimization based on numerical algorithms and techniques can be applied to various engineering systems to help a designer come out with a proposal that is more efficient, light weight, reliable, safe, cost effective and that satisfies the user too. This requires not only the final product to be optimized but also the optimization of manufacturing process as well as the optimum use/application of the product.

In the third chapter, we dealt with the kinematic and dynamic analyses of the Orthoglide 5-axis, a five-degree-of-freedom manipulator. First, it turned out that kinematic and dynamic analysis of the translating part and the spherical wrist of the manipulators can be decoupled. The geometric and inertial parameters of the manipulator were determined by means of a CAD software. We came up with the dynamic model of the spherical wrist by means of a Newton-Euler approach. Besides, this model has been checked with the principle of virtual work. Then, the required motors performance were evaluated for some test trajectories. Various simulations results showed that the FFA 20-80 harmonic drive motors of 800 W and the MPP0923D servo motors of 1600 W, primarily selected for the wrist and Orthoglide 3-axis respectively, are suitable for the Orthoglide 5-axis. In future works, friction forces as well as payload will be considered in the dynamic analysis and further test trajectories will be performed.

In the fourth chapter, an approach to optimally locate a given trajectory profile, path or task within the workspace of a PKM is presented. The electric energy consumed by the actuators to carry out that given path is considered as the primary optimization criterion. The shaking forces effects as well as the the actuators peak torques are considered as other optimum path placement criteria, hence obtaining a multiobjective optimization problem. The electric energy requirement is calculated with the help of the required actuators torques and velocities along with motors electric parameters. Kinematic, velocity and dynamic modeling is used to come up with the trajectory parameters like actuators velocities, accelerations and torques to realize the given path at a certain location in the workspace. To guarantee the feasibility of the solution, actuators performance limits such as their joint limits, maximum velocities and torque capabilities are used as the constraints of the optimization problem.

The use of the electric energy instead of mechanical energy as an optimization criterion is pertinent. Although actuator electric energy consumption depends on the mechanical energy requirements, the electric energy evaluation is more comprehensive than its mechanical counterpart. The general approach used to calculate the mechanical energy with the help of manipulator velocity and dynamic models, i.e., by using actuators torques and

velocities, may lead to an under estimation of the energy requirements in the case where actuators are experiencing torques with a null velocity. Besides, usual mechanical energy calculations do not consider the resistive energy loss in the motors windings as well as the energy loss due to the variations in the actuators velocities. Those variations affect the current requirements and hence induce electromotive forces in the actuators. Accordingly, the electric energy formulation takes into account all these energy losses.

Variations in the shaking forces experienced by the base platform of a manipulator also vary with the path locations. However, the lower the effects of the shaking forces, the higher the energy consumption. Magnitude of the maximum shaking forces can also be reduced with path location but to a lower extend compared to the reduction of the variation of shaking forces. Similarly, the magnitude of the maximum actuators torques can be reduced with appropriate path location. However, the energy consumption may increase with the minimization of the shaking forces effects and maximum torque. Hence, a trade-off has to made by the designer.

Futures works:

In the framework of this thesis, some optimization issues were tackled like design optimization, actuators selection for a given application and path placement optimization. Here is a list of tasks that should be done following the foregoing results:

- Multi-objective design optimization of several PKMs by using other different design criteria than the ones proposed in Chapter II, such as their first natural frequency. The cross-section type parameters could be used as decision variables to find the optimal components shapes.
- The multi-objective design optimization results should be validated experimentally by means of some prototypes realizations.
- In the design optimization of the 3-PRR planar parallel manipulator presented in Chapter II, only one working mode of the manipulator was considered. Later on, the manipulator working mode will be used as a discrete decision variable of the optimization problem in order to come up with more general results. The joints stiffness will be considered as well as decision variables of the design optimization problem.
- A Graphical User Interface (GUI) will be developed to help the designer distinguish between the Pareto optimal solutions obtained from the foregoing multi-objective design optimization problem.
- In order to get a more realistic dynamic modelling of Orthoglide 5-axis, the friction forces as well as the payload have to be considered. It will be done later on in order to test more complex trajectories.

– As far as the multi-objective path placement problem is concerned, other objective functions have to be considered such as the stiffness and the manipulability of the manipulator for the realization of more complex tasks and in case of irregular workspaces. Furthermore, to have a complete picture of shaking effects, along with shaking forces, shaking moments should also be considered. Finally, the optimal path placements obtained will be checked experimentally.

Publications

Journal Papers

[1]. **R. Ur-Rehman**, S. Caro, D. Chablat and P. Wenger, "Path Placement Optimization of Manipulators Based on Energy Consumption - Application to the Orthoglide 3-axis," *Transaction of Canadian Society for Mechanical Engineering*, Vol. 33(3), 2009.

[2]. **R. Ur-Rehman**, S. Caro, D. Chablat and P. Wenger, "Multiobjective Path Placement Optimization of Parallel Kinematics Machines Based on Energy Consumption, Shaking Forces and Maximum Actuators Torques - Application to the Orthoglide," *Mechanism and Machine Theory*, (to appear in 2010).

Conference Papers

[1]. **R. Ur-Rehman**, S. Caro, D. Chablat and P. Wenger, "Kinematic and Dynamic Analyses of the Orthoglide 5-axis," *Congress on Mechatronics*, Le Grand-Bornand, France, (May 21-23, 2008).

[2]. **R. Ur-Rehman**, S. Caro, D. Chablat and P. Wenger, "Kinematic and Dynamic Analysis of the 2-DOF Spherical Wrist of Orthoglide 5-axis," *Third International Congress Design and Modelling of Mechanical Systems (CMSM'2009)*, Hammamet, Tunis, (March 16-18, 2009).

[3]. **R. Ur-Rehman**, S. Caro, D. Chablat and P. Wenger, "Multiobjective Design Optimization of 3-PRR Planar Parallel Manipulators," *CIRP Design 2010*, Nantes, France, (April 19-21, 2010).

[4]. S. Caro, **R. Ur-Rehman**, D. Chablat and P. Wenger, "Comparison of Planar Parallel Manipulator Architectures based on a Multi-objective Design Optimization Approach," *ASME 2010 International Design Engineering Technical Conferences (IDETC)*, Montréal, Canada, (August 15-18, 2010).

References

Abdel-Malek, K. and Yeh, H. J., 1997, "Analytical boundary of the workspace for general 3-dof mechanisms," *International Journal of Robotics Research* 16, no. 2, pp. 198–213, ISSN 0278-3649.

Abraham, A., Jain, L., and Goldberg, R., 2005, *Evolutionary Multiobjective Optimization. Theoretical Advances and Applications*, Springer-Verlag.

Alba-Gomez, O., Wenger, P., and Pamanes, A., 2005, "Consistent kinetostatic indices for planar 3-dof parallel manipulators, application to the optimal kinematic inversion," *ASME Design Engineering Technical Conferences*, Long Beach, U.S.A, pp. 24–28.

Alciatore, D. and Ng, C., 1994, "Determining manipulator workspace boundaries using the Monte Carlo Method and Least Squares Segmentation," *ASME Robotics: Kinematics, Dynamics, and Controls* 72, pp. 141–146.

Alizade, R. I., Tagiyev, N. R., and Duffy, J., 1994, "A forward and reverse displacement analysis of an in-parallel spherical manipulator," *Mechanism and Machine Theory* 29(1), pp. 125–137.

Altuzarra, O., Salgado, O., Hernandez, A., *et al.*, 2009, "Multiobjective optimum design of a symmetric parallel Schönflies-Motion generator," *ASME Journal of Mechanical Design* 131, no. 3, pp. 031002–1–031002–11.

Andersson, J., 2001, "Survey of MO optimization in engineering design," Tech. rep., Linköping University, Sweden.

Angeles, J., 2002, *Fundamentals of Robotic Mechanical Systems: Theory Methods and Algorithms*, Springer-Verlag, New York.

Angeles, J. and Rojas, A. A., 1987, "Manipulator inverse kinematics via condition number minimization and continuation," *The International Journal of Robotics and Automation* 2, no. 2, pp. 61–69.

Arora, J., 1989, *Introduction to Optimum Design*, McGraw-Hill, New York.

Asada, H. and Granito, C., 1985, "Kinematic and static characterization of wrist

joints and their optimal design," *Proceedings of the IEEE Conference on Robotics and Automation*, Saint Louis, USA, pp. 244–250.

Aspragathos, N. A., 1996, "Optimal location of path following tasks in the workspace of a manipulator using genetic algorithm," *ARK'96, Published in Recent Advances in Robot Kinematics*, Kluwer Academic Publishers, Portroz, Slovinia, pp. 179–188.

Aspragathos, N. A. and Foussias, S., 2002, "Optimal location of a robot path when considering velocity performance," *Robotica* 20, no. 2, pp. 139–147, ISSN 0263-5747.

Ata, A. A., 2007, "Optimal trajectory planning of manipulators," *Journal of Engineering Science and Technology* 2, no. 1, pp. 32–54.

Bai, S. and Caro, S., 2009, "Design and analysis of a 3-PPR planar robot with U-shape base," *Proceedings of the 14th International Conference on Advanced Robotics*, Munich, Germany.

Baret, M., 1978, "Six degrees of freedom large motion system for flight simulators, piloted aircraft environment simulation techniques," *In AGARD Conference Proceedings n° 244 , Piloted aircraft environment simulation techniques*, Brussels, Belgium, pp. 22–1/22–7.

Binaud, N., Caro, S., and Wenger, P., 2008, "Sensitivity analysis of degenerate and non-degenerate planar parallel manipulators," *EUCOMES-European Conference on Mechanism Science*, Cassino, Italy.

Bouyer, E., Caro, S., Chablat, D., *et al.*, 2007, "The multiobjective optimization of a prismatic drive," *Proceedings of ASME Design Engineering Technical Conferences*, Las Vegas, Nevada, USA.

Briot, S. and Bonev, I. A., 2008, "Accuracy analysis of 3-dof planar parallel robots," *Mechanism and Machine Theory* 43, no. 4, pp. 445–458.

Briot, S., Bonev, I. A., Chablat, D. Wenger, P., *et al.*, 2008, "Self-motions of general 3-RPR planar parallel robots," *The International Journal of Robotics Research* 27, no. 7, pp. 855–866.

Briot, S., Pashkevich, A., and Chablat, D., 2009, "On the optimal design of parallel robots taking into account their deformations and natural frequencies," *ASME Design Engineering Technical Conferences*, San Diego, USA.

Brogårdh, T., 2007, "Present and future robot control development–An industrial perspective," *Annual Reviews in Control* 31, no. 1, pp. 69–79, ISSN 1367-5788.

Bruzzone, L. E., Molfino, R., and Razzoli, R. P., 2002, "Modelling and design of a parallel robot for laser-cutting applications," *IASTED International Conference on. Modelling, Identification and Control*, Innsbruck, Austria, pp. 518–522.

Cao, B., Doods, G., and Irwin, G., 1994, "Time optimal and smooth constrained path

planning for robot manipulators," *Proceedings of the IEEE International Conference on Robotics and Automation*, vol. 43, Minneapolis, pp. 1853–1858.

Caro, S.and Binaud, N. and Wenger, P., 2008, "Sensitivity analysis of planar parallel manipulators," *ASME Proceedings of International Design Engineering Technical Conferences*, New York City.

Caro, S., 2003, *Conception robust de mechanisms*, Ph.D. Thesis, Ecole Centrale de Nantes, Nantes, France.

Caro, S., Bennis, F., and Wenger, P., 2005, "Tolerance synthesis of mechanisms: A robust design approach," *ASME Journal of Mechanical Design* 127, no. 1, pp. 86–94.

Caro, S., Binaud, N., and Wenger, P., 2009, "Sensitivity analysis of 3-RPR planar parallel manipulators," *ASME Journal of Mechanical Design* to appear.

Caro, S., Chablat, D., and Bouyer, E., 2007, "The optimization of a novel prismatic drive," *IFToMM International Journal Problems of Mechanics* 26, no. 1, pp. 32–42.

Caro, S., Wenger, P., Bennis, F., *et al.*, 2006, "Sensitivity analysis of the Orthoglide, a 3-dof translational parallel kinematic machine," *ASME Journal of Mechanical Design* 128, pp. 392–402.

Caron, F., 1997, *Analyse et conception d'un manipulateur parallèle sphérique à deux degrés de liberté pour l'orientation d'une caméra*, M.Eng. Thesis, Laval University, Quebec, Canada.

Cavallo, E. and Michelini, R., 2004, "A robotic equipment for the guidance of a vectored thruster AUV," *Proceedings of 35th International Symposium on Robotics ISR2004*, vol. 1, Paris, pp. 1–6.

Ceccarelli, M., Carbone, G., and Ottaviano, E., 2005, "Multi criteria optimum design of manipulators," *Bulletin of the Polish Academy of Sciences Technical Sciences*, vol. 53.

Chablat, D. and Wenger, P., 1998, "Working modes and aspects in fully parallel manipulators," *Proceedings of the IEEE International Conference on Robotics and Automation*, pp. 1964–1969.

Chablat, D. and Wenger, P., 2003, "Architecture optimization of a 3-dof parallel mechanism for machining applications, The Orthoglide," *IEEE Transactions On Robotics and Automation* 19, no. 3, pp. 403–410.

Chablat, D. and Wenger, P., 2005, "Device for the movement and orientation of an object in space and use thereof in rapid machining," *CNRS/Ecole Centrale de Nantes. European patent EP1597017 (23 November 2005), US patent: US 20070062321 (22 march 2007).*

Chablat, D. and Wenger, P., 2007, "A six degree-of-freedom Haptic device based on

the Orthoglide and a hybrid Agile Eye," *CoRR* abs/0707.3550.

Chablat, D., Wenger, P., Caro, S., *et al.*, 2002, "The isoconditioning loci of planar 3-dof parallel manipulator," *Proceedings of DETC'2002, ASME Design Engineering Technical Conference*, Montreal, Quebec, Canada.

Chablat, D., Wenger, P., Majou, F., *et al.*, 2004, "An interval analysis based study for the design and the comparison of three-degrees-of-freedom parallel kinematic machines," *The International Journal of Robotics Research* 23, no. 6, pp. 615–624.

Chan, K. K. and Zalzala, A., 1993, "Genetic-based minimum time trajectory planning of articulated manipulators with torque constraints," *IEEE Colloquium on Genetic Algorithms for Control Systems Engineering*, London, pp. 4/1–4/3.

Chanal, H., Duc, E., and Ray, P., 2006, "A study of the impact of machine tool structure on machining processes," *International Journal of Machine Tools and Manufacture* 46, no. 2, pp. 98 –106, ISSN 0890-6955.

Chiou, S.T.and Bai, G. and Chang, W. K., 1998, "Optimum balancing design of the drag-link drive of mechanical presses for precision cutting," *International Journal of Machine Tools and Manufacture* 38, no. 3, pp. 131–141.

Chou, H. and Sadler, J., 1993, "Optimal location of robot trajectories for minimization of actuator torque," *Mechanism and Machine Theory* 28, no. 2, pp. 145–158.

Clavel, R., 1988, "Delta, a fast robot with parallel geometry," *Proceedings of the 18th International Symposium on Industrial Robots*, pp. 91–100.

Cleary, K. and Arai, T., 1991, "A prototype parallel manipulator: Kinematics, construction, software, workspace results and singularity analysis," *Proceedings of International Conference on Robotics and Automation*, Sacramento, California, pp. 566–571.

Company, O., 2000, *Machines-outils rapides à structure parallèle. Méthodologie de conception, applications et nouveaux concepts*, Ph.D. Thesis, Université de Montpelleir–II, France.

Company, O., 2006, "Survey of existing parallel kinematics mechanisms," Tech. rep., Université de Montpelleir–II, France, LIRMM internal report.

Craver, W. M., 1989, *Structural analysis and design of a three-degree-of-freedom robotic shoulder module*, M.Eng. Thesis, The University of Texas at Austin, Department of Mechanical Engineering.

Dasgupta, B. and Choudhury, P., 1999, "A general strategy based on the Newton-Euler approach for the dynamic formulation of parallel manipulators," *Mechanism and Machine Theory* 34, no. 6, pp. 801–824.

Duffy, J., 1996, *Statics and Kinematics with Applications to Robotics*, Cambridge

University Press, New York.

Dunlop, G. and Jones, T., 1999, "Position analysis of a two dof parallel mechanism-the Canterbury tracker," *Mechanism and Machine Theory* 34, no. 4, pp. 599–614.

Erdman, A. G., 1993, *Modern Kinematics–Developments in the Last Forty Years*, John Wiley & Sons, New York.

ESTECO, 2008, "modeFRONTIER, Version 4.0.3," URL http://www.esteco.it.

Fan, K.-C., Wang, H., Zhao, J.-W., *et al.*, 2003, "Sensitivity analysis of the 3-PRS parallel kinematic spindle platform of a serial-parallel machine tool," *International Journal of Machine Tools & Manufacture* 43, no. 15, pp. 1561–1569.

Fardanesh, B. and Rastegar, J., 1988, "Minimum cycle time location of a task in the workspace of a robot arm," *Proceedings of the 27th Conference on Decision Control*, Austin, Texas, pp. 2280–2283.

Feddema, J. T., 1996, "Kinematically optimal robot placement for minimum time coordinated motion," *Proceedings of the IEEE 13th International Conference on Robotics and Automation*, Part 4, pp. 22–28.

Ferraresi, C., Montacchini, G., and Sorli, M., 1995, "Workspace and dexterity evaluation of 6-dof spatial mechanisms," *Proceedings of the 9th World Congress on the theory of Machines and Mechanism*, Milan, pp. 51–61.

Fichter, E., 1986, "A Stewart platform- based manipulator: general theory and practical construction," *The International Journal of Robotics Research* 5, no. 2, pp. 157–182.

Field, G., 1995, "Iterative dynamic programming, an approach to minimum energy trajectory planning for robotic manipulators," *Proceedings of the IEEE International Conference on Robotics and Automation*, vol. 3, Minneapolis, pp. 2755–2760.

French, C. W., Schultz, A. E., *et al.*, 2004, "Multi-axial subassemblage testing (Mast) system: description and capabilities," *13th World Conference on Earthquake Engineering*, Vancouver, Canada.

Gallardo-Alvarado, J., 2005, "Kinematics of a hybrid manipulator by means of screw theory," *Multibody System Dynamics* 14, no. 3, pp. 345–366.

Gallardo-Alvarado, J., Rico, J. M., and Frisoli, A., 2003, "Dynamics of parallel manipulators by means of screw theory," *Mechanism and Machine Theory* 38, no. 11, pp. 1113–1131.

Gogu, G., 2006, "Fully-isotropic hexapods," *In: Lenarc(ic(J, Roth B (Eds) Advances in Robot Kinematics: Mechanisms and Motion*, Springer, Dordrecht, pp. 323–330, ISBN 1-4020-3481-4.

Gosselin, C., 1992, "The optimum design of robotic manipulators using dexterity

indices," *Robotics and Autonomous Systems* 9, no. 4, pp. 213–226.

Gosselin, C. M., 1990a, "Determination of the workspace of 6-dof parallel manipulators," *ASME Journal of Mechanical Design* 112, no. 3, pp. 331–336.

Gosselin, C. M. and Angeles, J., 1988, "The optimum kinematic design of a planar three-degree-of-freedom parallel manipulator," *ASME Journal of Mechanisms, Transmission and Automation in Design* 110, pp. 35–41.

Gosselin, C. M. and Angeles, J., 1989, "The optimum kinematic design of a spherical three-degree-of-freedom parallel manipulator," *Journal of Mechanisms, Transmissions and Automation in Design* 111, no. 2, pp. 202–207.

Gosselin, C. M. and Angeles, J., 1991, "A global performance index for the kinematic optimization of robotic manipulators," *ASME Journal of Mechanical Design* 113, no. 3, pp. 220–226.

Gosselin, C. M. and Hamel, J., 1994, "The agile eye: a high performance three-dof camera-orienting device," *IEEE International conference on Robotics and Automation*, San Diego, pp. 781–787.

Gosselin, C. M. and Lavoie, E., 1993, "On the kinematic design of spherical three-degree-of-freedom parallel manipulators," *The International Journal of Robotics Research* 12, no. 4, pp. 394–402.

Gosselin, C. M., Lemieux, S., and Merlet, J. P., 1996, "A new architecture of planar three-degree-of-freedom parallel Manipulator," *Proceedings of the IEEE International Conference on Robotics and Automation*, Minneapolis, Minnesota, pp. 3738–3743.

Gosselin, C. M. and Merlet, J. P., 1994, "The direct kinematics of planar parallel manipulators: special architectures and number of solutions," *Mechanism and Machine Theory* 29, no. 8, pp. 1088–1097.

Gosselin, C. M. and Sefrioui, J., 1991, "Polynomial solutions for the direct kinematic problem of planar three-degree-of-freedom parallel manipulator," *International Conference on Advanced Robotics*, Pisa, Italy.

Gosselin, C. M.and Angeles, J., 1990b, "Singularity analysis of closed-loop kinematic chains," *IEEE Transaction on Robotics and Automation* 6, no. 3, pp. 281–290.

Gough, V. E. and Whitehall, S. G., 1962, "Universal tyre testing machine," *Proceedings of the 9^{th} International Technical Congress*, F.I.S.I.T.A, Institution of Mechanical Engineers, London.

Guégan, S., 2003, *Contribution à la modélisation et l'identification dynamique des robots parallèles*, Ph.D. Thesis, Ecole Centrale de Nantes, Nantes, France.

Gupta, K. G. and Roth, B., 1982, "Design considerations for manipulator works-

pace," *ASME Journal of Mechanical Design* 104, no. 4, pp. 704–711.

Han, C., Kim, J., Kim, J., *et al.*, 2002, "Kinematic sensitivity analysis of the 3-UPU parallel mechanism," *Mechanism and Machine Theory* 37, pp. 787–798.

Hao, F. and Merlet, J.-P., 2005, "Multi-criteria optimal design of parallel manipulators based on interval analysis," *Mechanism and Machine Theory* 40, no. 2, pp. 157–171.

Hay, A. M. and Snyman, J. A., 2004, "Methodologies for the optimal design of parallel manipulators," *International Journal for Numerical Methods in Engineering* 59, no. 11, pp. 131–152.

Hemmerle, J. S. and Prinz, F., 1991, "Optimal path placement for kinematically redundant manipulators," *Proceedings of the IEEE International Conference on Robotics and Automation*, vol. 2, pp. 1234–1244.

Hervé, J.-M. and Sparacino, F., 1992, "Star. A new concept in robotics," *Proceedings of the 3rd International Workshop on Advances in Robot Kinematics*, Ferrara, Italy, pp. 176–183.

Hirakawa, A. and Kawamura, A., 1997, "Trajectory planning of redundant manipulators for minimum energy consumption without matrix inversion," *Proceedings of the IEEE International Conference on Robotics and Automation*, New Mexico, pp. 2415–2420.

Hunt, K. H., 1978, *Kinematic Geometry of Mechanisms*, Oxford, Cambridge.

Husty, M. L., 1996, "An algorithm for solving the direct kinematics of general Stewart-Gough platforms," *Mechanism and Machine Theory* 31, no. 4, pp. 365–380.

Ibrahim, O., 2006, *Contribution à la modélisation dynamique des robots parallèles et des robots hybrides*, Ph.D. Thesis, Ecole Centrale/Université de Nantes.

Innocenti, C. and Castelli, V. P., 1993, "Echelon form solution of direct kinematics for the general fully-parallel spherical wrist," *Mechanism and Machine Theory* 28, no. 4, pp. 553–561.

Jiang, Q. and Gosselin, C. M., 2008, "Geometric optimization of planar 3-RPR parallel mechanisms," *Transactions of the Canadian Society for Mechanical Engineering* 31, no. 4, pp. 457–468.

Jilla, C., 2002, *A multiobjective, multidisciplinary design optimization methodology for the conceptual design of distributed satellite systems*, Ph.D. Thesis, Massachusetts Institute of Technology.

Kang, B., Chu, J., and Mills, K., 2001, "Design of high speed planar parallel manipulator and multiple simultaneous specification control," *Proceedings of the IEEE International Conference on Robotics and Automation*, Seoul, Korea.

Karouia, M. and Hervè, J. M., 2002, "A family of novel orientational 3-dof parallel robots," *Proceedings of the 14th CISM-IFToMM RoManSy Symposium*, vol. 14, Udine, Italy, pp. 359–368.

Katz, R., Li, Z., and Pierrot, F., 2001, "Conceptual design of a high speed drilling machine (HSDM) based on PKM module," Technical report no. 37, ERC/RMS, College of Engineering, The University of Michigan.

Khoukhi, A., Baron, L., and Balazinski, M., 2007, "A projected gradient augmented Lagrangian approach to multi-objective trajectory planning of redundant robots," *Transactions of the Canadian Society for Mechanical Engineering* 31, no. 4, pp. 391–405.

Kohli, D. and Spanos, J., 1985, "Workspace analysis of mechanical manipulators using polynomial discriminants," *Journal of Mechanisms,Transmission and Automation in Design* 107, pp. 209–215.

Kong, X. and Gosselin, C. M., 2002, "Type synthesis of 3-dof spherical parallel manipulators based on screw theory," *Proceedings of DETC'02 ASME 2002 Design Engineering Technical Conferences and Computer and Information in Engineering Conference*, Montreal, Canada.

Kong, X. and Gosselin, C. M., 2004, "Type synthesis of 3-dof translational parallel manipulators based on screw theory," *ASME Journal of Mechanical Design* 126, pp. 83–92.

Kosinska, A., Galicki, M., and Kedzior, K., 2003, "Determination of parameters of 3-dof spatial orientation manipulators for a specified workspace," *Robotica* 21, no. 2, pp. 179–183, ISSN 0263-5747.

Krefft, M. and Hesselbach, J., 2005, "Elastodynamic optimization of parallel kinematics," *Proceedings of the IEEE International Conference on Automation Science and Engineering*, Edmonton, Canada.

Krut, S., 2003, *Contribution à l'étude des robots parallèles l'égers, 3T-1R et 3T-2R, à forts débattements angulaires*, Ph.D. Thesis, University of Montpellier-II, France.

Kucuka, S. and Bingulb, Z., 2006, "Comparative study of performance indices for fundamental robot manipulators," *Robotics and Autonomous Systems* 54, no. 7, pp. 567–573.

Kuen, Y., 2002, *Geometry, dynamics and control of parallel manipulators*, Ph.D. Thesis, The Hong Kong University of Science and Technology.

Kumar, A. and Waldron, K. J., 1981, "The workspace of mechanical manipulators," *ASME Journal of Mechanical Design* 103, pp. 665–672.

Lacroux, G., 1994, *Les actionneurs électriques pour la robotique et les asservisse-*

ments, 2nd ed., Technique et Documentation Lavoisier, Paris.

Lee, K. M. and Shah, D. K., 1988, "Dynamic analysis of a three-degrees-of-freedom in parallel actuated manipulator," *IEEE Journal of Robotics and Automation* 4, no. 3, pp. 361–368.

Lee, T. W. and Cwiakala, M., 1985, "Generation and evaluation of a manipulator workspace based on optimum path search," *Journal of Mechanisms,Transmission and Automation in Design* 107, pp. 245–255.

Lee, T. W. and Yang, D. C. H., 1983, "On the evaluation of manipulator workspace," *Journal of Mechanisms, Transmission and Automation in Design* 105, pp. 70–77.

Li, H., Yang, Z., and Huang, T., 2009, "Dynamics and elasto-dynamics optimization of a 2-dof planar parallel pick and place robot with flexible links," *Journal of Structural and Multidisciplinary Optimization* 38, no. 2, pp. 195–204.

Liu, X. J., Tang, X., and Wang, J., 2005, "HANA: a novel spatial parallel manipulator with one rotational and two translational degrees of freedom," *Robotica* 23, no. 2, pp. 257–270.

Liu, X. J., Wang, J., Oh, K. K., *et al.*, 2004, "A new approach to the design of a Delta robot with a desired workspace," *Journal of Intelligent and Robotic Systems* 39, no. 2, pp. 209–225.

Lou, Y., Liu, G., Chen, N., *et al.*, 2005, "Optimal design of parallel manipulators for maximum effective regular workspace," *Proceedings of the IEEE/RSJ International Conference on Intelligent Robots and Systems*, Alberta, pp. 795–800.

Lou, Y., Liu, G., and Li, Z., 2008, "Randomized optimal design of parallel manipulators," *IEEE Transactions on Automation Science and Engineering* 5, no. 2, pp. 223–233.

Lum, M. J. H., Rosen, J., Sinanan, M. N., *et al.*, 2006, "Kinematic optimization of serial and parallel spherical mechanism for a minimally invasive surgical robot," *IEEE Transactions on Biomedical Engineering*, vol. 53.

Ma, O. and Angeles, J., 1991a, "Architecture singularities of platform manipulators," *Proceedings of the IEEE International Conference on Robotics and Automation*, pp. 1542–1547.

Ma, O. and Angeles, J., 1991b, "Optimum architecture design of platform manipulators," *Proceedings of the 5^{th} International Conference on Advanced Robotics*, Pisa, Italy, pp. 1130–1135.

Majou, F.and Gosselin, C., Wenger, P., and Chablat, D., 2007, "Parametric stiffness analysis of the Orthoglide," *Mechanism and Machine Theory* 42, no. 3, pp. 296–311.

Majou, F., Wenger, P., and Chablat, D., 2001, "The design of parallel kinematic

machine tools using kinetostatic performance criteria," *3rd International Conference on Metal Cutting and High Speed Machining*, Metz, France.

Majou, F.and Wenger, P. and Chablat, D., 2007, "A Novel method for the design of 2-dof Parallel mechanisms for machining applications," *CoRR* abs/0705.1280.

Marler, R. T. and Arora, J. S., 2004, "Survey of multi-objective optimization methods for engineering," *Structural and Multidisciplinary Optimization* 26, no. 6, pp. 369–395.

Menon, C., Vertechy, R., Markot, M., *et al.*, 2009, "Geometrical optimization of parallel mechanisms based on natural frequency evaluation: application to a spherical mechanism for future space applications," *IEEE Transactions on Robotics* 25, no. 1, pp. 12–24.

Merlet, J. P.and Gosselin, C. M. and Mouly, N., 1998, "Workspaces of planar parallel manipulators," *Mechanism and Machine Theory* 33, no. 1, pp. 7–20.

Merlet, J. P., 1989, "Singular configurations of parallel manipulators and Grassmann geometry," *The International Journal of Robotics Research* 8, no. 5, pp. 45–56.

Merlet, J. P., 1995, "Determination of the orientation workspace of parallel manipulators," *Journal of Intelligent and Robotic Systems* 13, no. 2, pp. 143–160.

Merlet, J.-P., 2006a, "Computing the worst case accuracy of a PKM over a workspace or a trajectory," *The 5th Parallel Kinematics Seminar*, Chemnitz, Germany, pp. 83–96.

Merlet, J. P., 2006b, "Jacobian, manipulability, condition Number and Accuracy of parallel robots," *Journal of Mechanical Design* 128, pp. 199–206.

Merlet, J. P., 2006c, *Parallel Robots*, Kluwer Academic Publishers, Norwell, MA, USA, ISBN 0792363086.

Miller, K., 2004, "Optimal design and modeling of spatial parallel manipulators," *The International Journal of Robotics Research* 23, no. 2, pp. 127–140.

Miller, K. and Clavel, R., 1992, "The Lagrange-based model of Delta-4 robot dynamics," *Robotersysteme* 8, no. 1, pp. 49–54.

Mohammadi Daniali, H. R., Zsombor-Murray, P. J., and Angeles, J., 1995, "Singularity analysis of a general class of planar parallel manipulators," *Proceedings of the IEEE International Conference on Robotics and Automation*, Nagoya, Japan, pp. 1547–1552.

Moore, B., Schicho, J., and Gosselin, C. M., 2009, "Determination of the complete set of shaking force and shaking moment balanced planar four-bar linkages," *Mechanism and Machine Theory* 44, no. 7, pp. 1338–1347.

Nelson, B. and Donath, M., 1990, "Optimizing the location of assembly tasks in a

manipulator's workspace," *Journal of Robotic System* 7, no. 6, pp. 791–811.

Nielsen, J.and Roth, B., 1999, "On the kinematic analysis of robotic mechanisms," *The International Journal of Robotics Research* 18, no. 12, pp. 1147–1160.

Ottaviano, E. and Ceccarelli, M., 2000, "Workspace and optimal design of a pure translation parallel manipulator-Tsai manipulator," *Meccanica* 35, no. 3, pp. 203–214.

Ottaviano, E. and Ceccarelli, M., 2001, "Optimal design of CAPAMAN (Cassino Parallel Manipulator) with prescribed workspace," *2nd Workshop on Computational Kinematics KC2001*, Seoul, South Korea, pp. 35–43.

Pamanes, G. J. A., Cuan-Duron, E., and Zeghloul, S., 2008, "Single and multiobjective optimization of path placement for redundant robotic manipulators," *Ingeniería Investigación y Tecnología* 9, no. 3, pp. 211–237.

Pamanes, G. J. A. and Zeghloul, S., 1991, "Optimal placement of robotic manipulators using multiple kinematic criteria," *Proceedings of the IEEE International Conference on Robotics and Automation*, vol. 1, pp. 933–938.

Pamanes, G. J. A., Zeghloul, S., and Lallemand, J., 1991, "On the optimal placement and task compatibility of manipulators," *Proceedings of the IEEE International Conference on Advanced Robotics-'91 ICAR*, vol. 2, pp. 1694–1697.

Park, F. C. and Kim, J. W., 1999, "Singularity analysis of closed kinematic chains," *ASME Journal of Mechanical Design* 121, no. 1, pp. 32–38.

Pashkevich, A., Chablat, D., and Wenger, P., 2006, "Kinematics and workspace analysis of a three-axis parallel manipulator: the Orthoglide," *Robotica* 24, no. 1, pp. 39–49, ISSN 0263-5747.

Pashkevich, A., Chablat, D., and Wenger, P., 2009a, "Design optimization of parallel manipulators for high-speed precision machining application," *13th IFAC Symposium on Information Control Problems in Manufacturing*, Moscow, Russia.

Pashkevich, A., Chablat, D., and Wenger, P., 2009b, "Stiffness analysis of overconstrained parallel manipulators," *Mechanism and Machine Theory* 44, no. 5, pp. 966 – 982.

Pashkevich, A., Wenger, P., and Chablat, D., 2005, "Design strategies for the geometric synthesis of Orthoglide-type mechanisms," *Mechanism and Machine Theory* 40, no. 8, pp. 907–930.

Pham, H. H. and Chen, I.-M., 2003, "Optimal synthesis for workspace and manipulability of parallel flexure mechanism," *Proceeding of the 11th World Congress in Mechanism and Machine Science*, Tianjin, China, pp. 2069–2073.

Pisla, D., Vaida, C., and Plitea, N., 2008, "Modeling and simulation of a new parallel

robot used in minimally invasive surgery," *ICINCO 2008, 5th International Conference on Informatics in Control, Automation and Robotics*, vol. RA-2, Funchal, Madeira, Portugal, pp. 194–201.

Pittens, K. H. and Podhorodeski, R. P., 1993, "A family of Stewart platforms with optimal dexterity," *Journal of Robotic Systems* 10, no. 4, pp. 463–479.

Pledel, P., 1995, "Actuator constraints in point to point motion planning of manipulators," *Proceeding of the 34th IEEE Conference on Decision and Control*, vol. 2, pp. 1009–1010.

Rajan, V. T., 1985, "Minimum time trajectory planning," *Proceedings of the IEEE Conference on Robotics and Automation*, vol. 2, St. Louis, MI, pp. 759–764.

Rao, A., Rao, P., and Saha, S., 2003, "Workspace and dexterity analyses of Hexaslide machine-tool," *Proceedings of the IEEE International Conference on Robotics and Automation*, Taipei, pp. 4104–4109.

Rastegar, J.and Perel, D., 1990, "Generation of manipulator workspace boundary geometry using the Monte Carlo Method and Interactive Computer Graphics," *ASME Journal of Mechanical Design* 112, no. 3, pp. 452–454.

Reboulet, C. and Berthomieu, T., 1991, "Dynamic model of a six degree of freedom parallel manipulator," *Proceedings of 5th International Conference on Advanced Robotics*, Pisa, Italy, pp. 1153–1157.

Rojeski, P. J., 1972, *A system analysis approach to landing gear design*, Ph.D. Thesis, Cornell University, USA.

Salisbury, J. K. and Craig, J. J., 1982, "Articulated hands: force control and kinematic issues," *International Journal of Robotics Research* 1, no. 1, pp. 4–17.

Shan, S. and Wang, G. G., 2005, "An efficient Pareto set identification approach for multi-objective optimization on black-box functions," *ASME Journal of Mechanical Design* 127, no. 5, pp. 866–874.

Shugen, M., 1995, "Real-time algorithm for quasi-minimum energy control of robotic manipulators," *Proceeding of the IEEE International Conference on Industrial Electronics, Control and Instrumentation*, vol. 2, Orlando, USA, pp. 1324–1329.

Sklar, M. and Tesar, D., 1998, "Dynamic analysis of hybrid serial manipulator systems containing parallel modules," *ASME Journal of Mechanisms, Transmissions and Automation in Design* 110, pp. 109–115.

Stamper, R. E., Tsai, L.-W., and Walsh, G. C., 1997, "Optimization of a three-dof translational platform for well-conditioned workspace," *Proceedings of the IEEE International Conference on Robotics and Automation*, New Mexico, pp. 3250–3255.

Stewart, D., 1965, "A platform with six degrees of freedom," *Proceedings of the*

Institution of Mechanical Engineers, vol. 180, Part 1, pp. 371–386.

Stock, M. and Miller, K., 2003, "Optimal kinematic design of spatial parallel manipulators: Application of linear delta robot," *Transactions of the ASME, Journal of Mechanical Design* 125, no. 2, pp. 292–301.

Strang, G., 1976, *Linear Algebra and its Applications*, Academic Press, New York.

Su, Y. X., Duan, B. Y., Peng, B., *et al.*, 2003, "Singularity analysis of fine-tuning Stewart platform for large radio telescope using genetic algorithm," *Mechatronics* 13, no. 5, pp. 413–425.

Sugimoto, K., 1989, "Computational scheme for dynamic analysis of parallel manipulators," *ASME Journal of Mechanisms, Transmissions and Automation in Design* 111, pp. 29–33.

Taguchi, G., 1993, *On Robust Technology Development, Bringing Quality Engineering Upstream*, 0-7918-0028-8, ASME Press.

Thompson, C. and Campbell, P., 1997, "Tendon suspended platform robot," *Robotics and Computer-Integrated Manufacturing* 13, no. 4, pp. 363–363.

Tian, L. and Collins, C., 2003, "Motion planning for redundant manipulators using a floating point genetic algorithm," *Journal of Intelligent and Robotic Systems, Theory and Applications* 38, no. 3–4, pp. 297–312, ISSN 0921-0296.

Tlusty, J., Ziegert, J., and Ridgeway, S., 1999, "Fundamental comparison of the use of serial and parallel kinematics for machines tools," *CIRP Annals–Manufacturing Technology* 48, no. 1, pp. 351–356, ISSN 0007-8506.

Tsai, L. W., 1996, "Kinematics of a three-dof platform with three extensible limbs," *Recent Advances in Robot Kinematics (J. Lenarcic and V. Parenti-Castelli, eds.)*, Kluwer Academic Publishers, pp. 401–410.

Tsai, L.-W., 1999, *Robot Analysis: The Mechanics of Serial and Parallel Manipulators*, John Wiley & Sons, Inc., New York, USA, ISBN 0471325937.

Tsai, L. W., 2000, "Solving the inverse dynamics of a Stewart-Gough manipulator by the principle of virtual work," *ASME Journal of Mechanical Design* 122, no. 1, pp. 3–9.

Tsai, Y. and Soni, A., 1981, "Accessible region and synthesis of robot arm," *ASME Journal of Mechanical Design* 103, pp. 803–811.

Valasek, M. and Sika, Z., 2003, "Pareto set determination and manipulation from multiobjective optimizatio," *Proceedings of the Advanced Engineering Design Conference AED 03,CTUin*, Prague, pp. 185, CD–ROM.

Valasek, M., Sika, Z., Bauma, V., *et al.*, 2005, "Tractable treatment of design by multiobjective optimization –parallel kinematics case study," *Multibody System Dy-*

namics 13, pp. 143–174.

Wang, J. and Masory, O., 1993, "On the accuracy of a Stewart platform - Part I, The effect of manufacturing tolerances," *Proceedings of the IEEE International Conference on Robotics Automation, ICRA*, Atlanta, USA, pp. 114–120.

Weck, M. and Staimer, D., 2002, "Parallel kinematic machine tools-current state and future potentials," *CIRP Annals–Manufacturing Technology* 51, no. 2, pp. 671–683, ISSN 0007-8506.

Wenger, P. and Chablat, D., 2000, "Kinematic analysis of a new parallel machine tool: The Orthoglide," *Proceedings of the 7th International Symposium on Advances in Robot Kinematics*, Portoroz, Slovenia.

Wenger, P., Gosselin, C., and Maille, B., 1999, "A comparative study of serial and parallel mechanism topologies for machine tools," *Proceedings of PKM-99*, Milan, Italy, pp. 23–32.

Williams II, R. L. and Joshi, A. R., 1999, "Planar parallel 3-RPR manipulator," *Proceedings of the* 6th *Conference on Applied Mechanisms and Robotics*, Cincinnati OH.

Wisama, K. and Denis, C., 1997, "SYMORO+: A system for the symbolic modelling of robots," *Robotica* 15, no. 2, pp. 153–161, ISSN 0263-5747.

Wu, Y. and Gosselin, C., 2004, "Synthesis of reactionless spatial 3-dof and 6-dof mechanisms without separate counter-rotations," *The International Journal of Robotics Research* 23, no. 6, pp. 625–642.

Yoshikawa, T., 1985, "Manipulability of robotic mechanisms," *The International Journal of Robotics Research* 4, no. 2, pp. 3–9.

Zentner, J., 2005, *Zur optimalen Gestaltung von Parallelkinematikmaschinen mit Planarantrieben*, Ph.D. Thesis, Faculty of Mechanical Engineering, Technical University of Ilmenau, Germany.

Zlatanov, D., Fenton, R., and Benhabib, B., 1994, "Analysis of the instantaneous kinematics and singular configurations of hybrid-chain manipulators," *Proceedings of the ASME 23rd Biennial Mechanisms Conference*, vol. 72, Minneapolis, MN, USA, pp. 467–476.

Zlatanov, D., Fenton, R. G., and Benhabib, B., 1995, "A unifying framework for classification and interpretation of mechanism singularities," *ASME Journal of Mechanical Design* 117, no. 4, pp. 566–572.

A Orthoglide Wrist Kinematics and Dynamics Relations

This annex presents the mathematical relations used for the kinematic and dynamic calculations of the Orthoglide wrist. The nomenclature and methodology is taken from (Caron, 1997) and is described in Chapter 3. The sequence of relations are given by:

$$\mathbf{g} = \begin{bmatrix} 0 & -9.81 & 0 \end{bmatrix}^T \tag{A.1}$$

$$\mathbf{Q}_0 = \begin{bmatrix} \cos\alpha_0 & 0 & \sin\alpha_0 \\ 0 & 1 & 0 \\ -\sin\alpha_0 & 0 & \cos\alpha_0 \end{bmatrix} \tag{A.2}$$

$$\dot{\boldsymbol{\phi}} = \begin{bmatrix} \dot{\phi}_1 & \dot{\phi}_2 \end{bmatrix}^T \tag{A.3}$$

$$\ddot{\boldsymbol{\phi}} = \begin{bmatrix} \ddot{\phi}_1 & \ddot{\phi}_2 \end{bmatrix}^T \tag{A.4}$$

$$\mathbf{S} = \begin{bmatrix} 0 & -\sin\phi_1 \\ 0 & -\cos\phi_1 \\ 1 & 0 \end{bmatrix} \tag{A.5}$$

$$\dot{\mathbf{S}} = \begin{bmatrix} 0 & -\cos\phi_1 \\ 0 & -\sin\phi_1 \\ 0 & 0 \end{bmatrix} \dot{\boldsymbol{\phi}}_1 \tag{A.6}$$

$$\boldsymbol{\omega} = \mathbf{S}\dot{\boldsymbol{\phi}} \tag{A.7}$$

$$\dot{\boldsymbol{\omega}} = \mathbf{S} \times \ddot{\boldsymbol{\phi}} + \dot{\mathbf{S}} \times \dot{\boldsymbol{\phi}} \tag{A.8}$$

The relations of $\mathbf{e}_1$, $\mathbf{e}_2$, $\mathbf{e}_3$, $\mathbf{e}_4$ and $\mathbf{e}_5$ in frame R_1 are:

$$[\mathbf{e}_1]_1 = \begin{bmatrix} 0 & 0 & 1 \end{bmatrix}^T \tag{A.9}$$

$$[\mathbf{e}_2]_1 = \mathbf{Q}_0 [\mathbf{e}_1]_1 \tag{A.10}$$

$$[\mathbf{e}_3]_1 = \begin{bmatrix} \sin\theta_1 \sin\alpha_1 & -\cos\theta_1 \sin\alpha_1 & \cos\alpha_1 \end{bmatrix}^T \tag{A.11}$$

$$[\mathbf{e}_4]_1 = \begin{bmatrix} \sin\alpha_0\cos\alpha_2 + \sin\theta_0\cos\alpha_0\sin\alpha_2 \\ -\cos\theta_2\sin\alpha_0 \\ \cos\alpha_0\cos\alpha_2 - \sin\theta_2\sin\alpha_0\sin\alpha_2 \end{bmatrix} \tag{A.12}$$

$$[\mathbf{e}_5]_1 = \begin{bmatrix} \sin\alpha_1\cos\alpha_3\sin\theta_1 + \cos\alpha_1\sin\alpha_3\sin\theta_1\sin\theta_3 + \sin\alpha_3\cos\theta_1\sin\theta_3 \\ \sin\alpha_1\cos\alpha_3\sin\theta_1 - \cos\alpha_1\sin\alpha_3\sin\theta_1\sin\theta_3 + \sin\alpha_3\cos\theta_1\sin\theta_3 \\ \cos\alpha_1\cos\alpha_3 - \sin\alpha_1\sin\alpha_3\cos\theta_3 \end{bmatrix} \tag{A.13}$$

Time derivatives relations of different vectors

$$\boldsymbol{\omega}_t = \dot{\theta}_1\mathbf{e}_1 + \dot{\theta}_3\mathbf{e}_3 \tag{A.14}$$

$$\boldsymbol{\omega}_d = \dot{\theta}_2\mathbf{e}_2 + \dot{\theta}_4\mathbf{e}_4 \tag{A.15}$$

$$\boldsymbol{\omega}_{p1} = \dot{\theta}_1\mathbf{e}_1 \tag{A.16}$$

$$\boldsymbol{\omega}_{p2} = \dot{\theta}_2\mathbf{e}_2 \tag{A.17}$$

$$\dot{\mathbf{e}}_1 = \begin{bmatrix} 0 & 0 & 0 \end{bmatrix}^T \tag{A.18}$$

$$\dot{\mathbf{e}}_2 = \begin{bmatrix} 0 & 0 & 0 \end{bmatrix}^T \tag{A.19}$$

$$\dot{\mathbf{e}}_3 = \dot{\theta}_1\left(\mathbf{e}_1 \times \mathbf{e}_3\right) \tag{A.20}$$

$$\dot{\mathbf{e}}_4 = \dot{\theta}_2\left(\mathbf{e}_2 \times \mathbf{e}_4\right) \tag{A.21}$$

$$\dot{\mathbf{e}}_5 = \boldsymbol{\omega} \times \mathbf{e}_4 \tag{A.22}$$

Accelerations and Inertias of the Wrist Components

Terminal:

$$\mathbf{a}^t = l^t_{e3}\ddot{\mathbf{e}}_3 + l^t_{e5}\ddot{\mathbf{e}}_5 + l^t_{e3\times e5}\left(\ddot{\mathbf{e}}_3 \times \mathbf{e}_5\right) + 2\left(\dot{\mathbf{e}}_3 \times \dot{\mathbf{e}}_5\right) + \left(\mathbf{e}_3 \times \ddot{\mathbf{e}}_5\right) \tag{A.23}$$

$$\mathbf{f}^t_g = m^t\mathbf{g} \qquad \mathbf{j}^t_g = m^t\mathbf{a}^t \qquad \mathbf{k}^t = \mathbf{I}^t\dot{\boldsymbol{\omega}}^t + \left(\boldsymbol{\omega}^t \times \mathbf{I}^t\boldsymbol{\omega}^t\right) \tag{A.24}$$

Components of $\mathbf{f}^t_g$, $\mathbf{j}^t$ and $\mathbf{k}^t$ are:

$$F^t_{ge3} = \mathbf{f}^t_g.\mathbf{e}_3 \qquad F^t_{ge5} = \mathbf{f}^t_g.\mathbf{e}_5 \qquad F^t_{ge3\times e5} = \mathbf{f}^t_g.\left(\mathbf{e}_3 \times \mathbf{e}_5\right) \tag{A.25}$$

$$J^t_{e3} = \mathbf{j}^t.\mathbf{e}_3 \qquad J^t_{e5} = \mathbf{j}^t.\mathbf{e}_5 \qquad J^t_{e3\times e5} = \mathbf{j}^t.\left(\mathbf{e}_3 \times \mathbf{e}_5\right) \tag{A.26}$$

$$K^t_{e3} = \mathbf{k}^t.\mathbf{e}_3 \qquad K^t_{e5} = \mathbf{k}^t.\mathbf{e}_5 \qquad K^t_{e3\times e5} = \mathbf{k}^t.\left(\mathbf{e}_3 \times \mathbf{e}_5\right) \tag{A.27}$$

Distal:

$$\mathbf{a}^d = l^d_{e4}\ddot{\mathbf{e}}_4 + l^d_{e5}\ddot{\mathbf{e}}_5 + l^d_{e4\times e5}\left(\ddot{\mathbf{e}}_4 \times \mathbf{e}_5\right) + 2\left(\dot{\mathbf{e}}_4 \times \dot{\mathbf{e}}_5\right) + \left(\mathbf{e}_4 \times \ddot{\mathbf{e}}_5\right) \tag{A.28}$$

$$\mathbf{f}^d_g = m^d\mathbf{g} \qquad \mathbf{j}^d_g = m^d\mathbf{a}^d \qquad \mathbf{k}^d = \mathbf{I}^d\dot{\boldsymbol{\omega}}^d + \left(\boldsymbol{\omega}^d \times \mathbf{I}_d\boldsymbol{\omega}_d\right) \tag{A.29}$$

Components of $\mathbf{f}_g^d$, $\mathbf{j}^d$ and $\mathbf{k}^d$ are:

$$F_{ge4}^d = \mathbf{f}_g^d.\mathbf{e}_4 \qquad F_{ge5}^d = \mathbf{f}_g^d.\mathbf{e}_5 \qquad F_{ge4\times e5}^d = \mathbf{f}_g^d.(\mathbf{e}_4 \times \mathbf{e}_5) \tag{A.30}$$

$$J_{e4}^d = \mathbf{j}^d.\mathbf{e}_4 \qquad J_{e5}^d = \mathbf{j}^d.\mathbf{e}_5 \qquad J_{e4\times e5}^d = \mathbf{j}^d.(\mathbf{e}_4 \times \mathbf{e}_5) \tag{A.31}$$

$$K_{e4}^d = \mathbf{k}^d.\mathbf{e}_4 \qquad K_{e5}^d = \mathbf{k}^d.\mathbf{e}_5 \qquad K_{e4\times e5}^d = \mathbf{k}^d.(\mathbf{e}_4 \times \mathbf{e}_5) \tag{A.32}$$

Proximal–I:

$$\mathbf{a}^{p1} = l_{e1}^{p1}\ddot{\mathbf{e}}_1 + l_{e3}^{p1}\ddot{\mathbf{e}}_3 + l_{e1\times e3}^{p1}(\ddot{\mathbf{e}}_1 \times \mathbf{e}_3) + 2(\dot{\mathbf{e}}_1 \times \dot{\mathbf{e}}_3) + (\mathbf{e}_1 \times \ddot{\mathbf{e}}_3) \tag{A.33}$$

$$\mathbf{f}_g^{p1} = m^{p1}\mathbf{g} \qquad \mathbf{j}_g^{p1} = m^{p1}\mathbf{a}^{p1} \qquad \mathbf{k}^{p1} = \mathbf{I}^{p1}\dot{\boldsymbol{\omega}}^{p1} + \left(\boldsymbol{\omega}^{p1} \times \mathbf{I}^{p1}\boldsymbol{\omega}^{p1}\right) \tag{A.34}$$

Components of $\mathbf{f}^{p1}$, $\mathbf{j}^{p1}$ and $\mathbf{k}^{p1}$ are:

$$F_{ge1}^{p1} = \mathbf{f}_g^{p1}.\mathbf{e}_1 \qquad F_{ge3}^{p1} = \mathbf{f}_g^{p1}.\mathbf{e}_3 \qquad F_{ge1\times e3}^{p1} = \mathbf{f}_g^{p1}.(\mathbf{e}_1 \times \mathbf{e}_3) \tag{A.35}$$

$$J_{e1}^{p1} = \mathbf{j}^{p1}.\mathbf{e}_1 \qquad J_{e3}^{p1} = \mathbf{j}^{p1}.\mathbf{e}_3 \qquad J_{e1\times e3}^{p1} = \mathbf{j}^{p1}.(\mathbf{e}_1 \times \mathbf{e}_3) \tag{A.36}$$

$$K_{e1}^{p1} = \mathbf{k}^{p1}.\mathbf{e}_1 \qquad K_{e3}^{p1} = \mathbf{k}^{p1}.\mathbf{e}_3 \qquad K_{e1\times e3}^{p1} = \mathbf{k}^{p1}.(\mathbf{e}_1 \times \mathbf{e}_3) \tag{A.37}$$

Proximal–II:

$$\mathbf{a}^{p2} = l_{e2}^{p2}\ddot{\mathbf{e}}_2 + l_{e4}^{p2}\ddot{\mathbf{e}}_4 + l_{e2\times e4}^{p2}(\ddot{\mathbf{e}}_2 \times \mathbf{e}_4) + 2(\dot{\mathbf{e}}_2 \times \dot{\mathbf{e}}_4) + (\mathbf{e}_2 \times \ddot{\mathbf{e}}_4) \tag{A.38}$$

$$\mathbf{f}_g^{p2} = m^{p2}\mathbf{g} \qquad \mathbf{j}_g^{p2} = m^{p2}\mathbf{a}^{p2} \qquad \mathbf{k}^{p2} = \mathbf{I}^{p2}\dot{\boldsymbol{\omega}}^{p2} + \left(\boldsymbol{\omega}^{p2} \times \mathbf{I}^{p2}\boldsymbol{\omega}^{p2}\right) \tag{A.39}$$

Components of $\mathbf{f}^{p2}$, $\mathbf{j}^{p2}$ and $\mathbf{k}^{p2}$ are:

$$F_{ge2}^{p2} = \mathbf{f}_g^{p2}.\mathbf{e}_2 \qquad F_{ge4}^{p2} = \mathbf{f}_g^{p2}.\mathbf{e}_4 \qquad F_{ge2\times e4}^{p2} = \mathbf{f}_g^{p2}.(\mathbf{e}_2 \times \mathbf{e}_4) \tag{A.40}$$

$$J_{e2}^{p2} = \mathbf{j}^{p2}.\mathbf{e}_2 \qquad J_{p2e4} = \mathbf{j}^{p2}.\mathbf{e}_4 \qquad J_{e2\times e4}^{p2} = \mathbf{j}^{p2}.(\mathbf{e}_2 \times \mathbf{e}_4) \tag{A.41}$$

$$K_{e2}^{p2} = \mathbf{k}^{p2}.\mathbf{e}_2 \qquad K_{e4}^{p2} = \mathbf{k}^{p2}.\mathbf{e}_4 \qquad K_{e2\times e4}^{p2} = \mathbf{k}^{p2}.(\mathbf{e}_2 \times \mathbf{e}_4) \tag{A.42}$$

Kinetic and Potential Energies of the Wrist Components

Kinetic Energy (E_k):

Kinetic energy relations for the two motors (m_1 and m_2) and four wrist components are given by:

$$E_k^{m1} = 0.5I^{m1}\left[\boldsymbol{\omega}^{p1}(3)\right]^2 \qquad \text{(Motor-I)} \tag{A.43}$$

$$E_k^{m2} = 0.5I^{m2}\left[\boldsymbol{\omega}^{p2}(1)\right]^2 \qquad \text{(Motor-II)} \tag{A.44}$$

$$E_k^t = 0.5\left(\boldsymbol{\omega}^t\right)^T \mathbf{I}^t\boldsymbol{\omega}^t \qquad \text{(Terminal)} \tag{A.45}$$

$$E_k^d = 0.5\left(\boldsymbol{\omega}^d\right)^T \mathbf{I}^d\boldsymbol{\omega}^d \qquad \text{(Distal)} \tag{A.46}$$

$$E_k^{p1} = 0.5 \left(\boldsymbol{\omega}^{p1}\right)^T \mathbf{I}^{p1} \boldsymbol{\omega}^{p1} \qquad \text{(Proximal-I)} \qquad \text{(A.47)}$$

$$E_k^{p2} = 0.5 \left(\boldsymbol{\omega}^{p2}\right)^T \mathbf{I}^{p2} \boldsymbol{\omega}^{p2} \qquad \text{(Proximal-II)} \qquad \text{(A.48)}$$

I^{m1} and I^{m2} being the inertia of motors m_1 and m_2, respectively.

Potential Energy (E_p):

Potential energy relations are given by:

$$E_p^t = -m^t \left[\mathbf{g} \cdot \left(l_{e3}^t \mathbf{e}_3 + l_{e5}^t \mathbf{e}_5 + l_{e3\times e5}^t \mathbf{e}_3 \times \mathbf{e}_5\right)\right] \qquad \text{(Terminal)} \qquad \text{(A.49)}$$

$$E_p^d = -m^d \left[\mathbf{g} \cdot \left(l_{e4}^d \mathbf{e}_4 + l_{e5}^d \mathbf{e}_5 + l_{e4\times e5}^d \mathbf{e}_4 \times \mathbf{e}_5\right)\right] \qquad \text{(Distal)} \qquad \text{(A.50)}$$

$$E_p^{p1} = -m^{p1} \left[\mathbf{g} \cdot \left(l_{e1}^{p1} \mathbf{e}_1 + l_{e3}^{p1} \mathbf{e}_3 + l_{e1\times e3}^{p1} \mathbf{e}_1 \times \mathbf{e}_3\right)\right] \qquad \text{(Proximal-I)} \qquad \text{(A.51)}$$

$$E_p^{p2} = -m^{p2} \left[\mathbf{g} \cdot \left(l_{e2}^{p2} \mathbf{e}_2 + l_{e4}^{p2} \mathbf{e}_4 + l_{e2\times e4}^{p2} \mathbf{e}_2 \times \mathbf{e}_4\right)\right] \qquad \text{(Proximal-II)} \qquad \text{(A.52)}$$

B Position and Acceleration of the Orthoglide Leg Elements

Expressions of $\mathbf{c}_{ji}$, $j = 1 \ldots 6$, a, p and $i = 1, \ldots, 3$, used for the calculations of the shaking forces for the Orthoglide with reference to Fig. 4.6 and discussed in Sec. 4.3.1.2, (C and S respectively stand for *sine* and *cosine* functions):

$$\mathbf{c}_{ai} = [0 \quad 0 \quad q_{1i}]^T \tag{B.1}$$

$$\mathbf{c}_{1i} = \left[0 \quad \frac{L_f}{2}S\lambda \quad q_{1i} + \frac{L_f}{2}C\lambda\right]^T \tag{B.2}$$

$$\mathbf{c}_{2i} = [0 \quad L_f S\lambda \quad q_{1i} + L_f C\lambda]^T \tag{B.3}$$

$$\mathbf{c}_{3i} = \left[\frac{L_b}{2}Cq_{3i}Cq_{2i} \quad L_f S\lambda + \frac{d}{2} - \frac{L_b}{2}Sq_{3i} \quad q_{1i} + L_f C\lambda + \frac{L_b}{2}Cq_{3i}Sq_{2i}\right]^T \tag{B.4}$$

$$\mathbf{c}_{4i} = \mathbf{c}_{3i} + [0 \quad d \quad 0]^T \tag{B.5}$$

$$\mathbf{c}_{5i} = [L_b Cq_{3i}Cq_{2i} \quad L_f S\lambda - L_b Sq_{3i} \quad q_{1i} + L_f C\lambda + L_b Cq_{3i}Sq_{2i}]^T \tag{B.6}$$

$$\mathbf{c}_{6i} = \mathbf{c}_{5i} + [0 \quad 0 \quad e/2]^T \tag{B.7}$$

$$\mathbf{c}_{pi} = \mathbf{c}_{5i} + [0 \quad 0 \quad e]^T \tag{B.8}$$

Twice differentiating Eqs. B.1 to B.8, result:

$$\ddot{\mathbf{c}}_{ai} = [0 \quad 0 \quad \ddot{q}_{1i}]^T \tag{B.9}$$

$$\ddot{\mathbf{c}}_{1i} = \ddot{\mathbf{c}}_{ai} \tag{B.10}$$

$$\ddot{\mathbf{c}}_{2i} = \ddot{\mathbf{c}}_{ai} \tag{B.11}$$

$$\ddot{\mathbf{c}}_{3i} = \begin{bmatrix} \frac{L_b}{2}(-\dot{q}_{2i}^2 Cq_{3i}Cq_{2i} - \ddot{q}_{2i}Cq_{3i}Sq_{2i} + 2\dot{q}_{2i}\dot{q}_{3i}Sq_{2i}Sq_{3i} - \dot{q}_{3i}^2 Cq_{2i}Cq_{3i} - \ddot{q}_{3i}Cq_{2i}Sq_{3i}) \\ \frac{L_b}{2}\left(\dot{q}_{3i}^2 Sq_{3i} - \ddot{q}_{3i}Cq_{3i}\right) \\ \ddot{q}_{1i} + \frac{L_b}{2}(-\dot{q}_{3i}^2 Cq_{3i}Sq_{2i} - \ddot{q}_{3i}Sq_{3i}Sq_{2i} - 2\dot{q}_{2i}\dot{q}_{3i}Sq_{3i}Cq_{2i} - \dot{q}_{2i}^2 Cq_{3i}Sq_{2i} + \ddot{q}_{2i}Cq_{3i}Cq_{2i}) \end{bmatrix} \tag{B.12}$$

$$\ddot{\mathbf{c}}_{4i} = \ddot{\mathbf{c}}_{3i} \tag{B.13}$$

$$\ddot{\mathbf{c}}_{5i} = \begin{bmatrix} L_b(-\dot{q}_{2i}^2 Cq_{3i}Cq_{2i} - \ddot{q}_{2i}Cq_{3i}Sq_{2i} + 2\dot{q}_{2i}\dot{q}_{3i}Sq_{2i}Sq_{3i} - \dot{q}_{3i}^2 Cq_{2i}Cq_{3i} - \ddot{q}_{3i}Cq_{2i}Sq_{3i}) \\ L_b\left(\dot{q}_{3i}^2 Sq_{3i} - \ddot{q}_{3i}Cq_{3i}\right) \\ \ddot{q}_{1i} + L_b(-\dot{q}_{3i}^2 Cq_{3i}Sq_{2i} - \ddot{q}_{3i}Sq_{3i}Sq_{2i} - 2\dot{q}_{2i}\dot{q}_{3i}Sq_{3i}Cq_{2i} - \dot{q}_{2i}^2 Cq_{3i}Sq_{2i} + \ddot{q}_{2i}Cq_{3i}Cq_{2i}) \end{bmatrix} \tag{B.14}$$

$$\ddot{\mathbf{c}}_{6i} = \ddot{\mathbf{c}}_{5i} \tag{B.15}$$

$$\ddot{\mathbf{c}}_{pi} = \ddot{\mathbf{c}}_{5i} \tag{B.16}$$